Three-Dimensional Finite Difference Analysis of Geosynthetic Reinforcement Used in Column-Supported Embankments

By

Brenton Michael Jones

Thesis submitted to the faculty of the
Virginia Polytechnic Institute and State University
in partial fulfillment of the requirements for the degree of

Master of Science
In
Civil Engineering

Raymond H. Plaut, Chair
George M. Filz
Elisa D. Sotelino

November 28, 2007
Blacksburg, Virginia

Keywords: geosynthetic reinforcement, plate, embankment, finite difference, pile support

Three-Dimensional Finite Difference Analysis of Geosynthetic Reinforcement Used in Column-Supported Embankments

By Brenton M. Jones

Dr. Raymond H. Plaut, Chairman

Charles E. Via, Jr. Department of Civil and Environmental Engineering

(ABSTRACT)

Column-supported, geosynthetic-reinforced embankments provide effective geotechnical foundations for applications in areas of weak subgrade soils. The system consists of a soil bridging layer with one or more embedded layers of geosynthetic reinforcement supported by driven or deep mixed columnar piles. The geosynthetic promotes load transfer within the bridging layer to the columns, allowing for larger column spacings and varied alignments. This technique is generally used when differential settlements of the embankment or adjacent structures are a concern and to minimize construction time.

Recent increase in the popularity of this composite system has generated the need to further investigate its behavior and soil-structure interaction. Current models of geosynthetics are oversimplified and do not represent the true three-dimensional nature of the material. Such simplifications include treating the geosynthetic as a one-dimensional cable as well as neglecting stress concentrations and pile orientations. In this thesis, a complete three-dimensional analysis of the geosynthetic is performed.

The geosynthetic was modeled as a thin flexible plate in a single square unit cell of the embankment. The principle of minimum potential energy was then applied, utilizing central finite difference equations. Energy components from vertical loading, soil and column support, as well as bending and membrane stiffness of the geosynthetic are considered. Three pile orentation types were implemented: square piles, circular piles, and square piles rotated 45° to the edges of the unit cell. Each of the pile orientations was analyzed using two distinct

parameter sets that are investigated in previously published and ongoing research. Vertical and in-plane deflections, stress resultants, and strains were determined and compared to other geosynthetic models and design guides. Results of each parameter set and pile orientation were also compared to provide design recommendations for geosynthetic-reinforced column-supported embankments.

Acknowledgements

I would like to express sincere gratitude to Dr. Raymond Plaut for serving as my advisor and committee chairman. Dr. Plaut's guidance and support was invaluable throughout the research process. I would also like to thank my committee members: Dr. George Filz for his practical background in geotechnical engineering; and Dr. Elisa Sotelino for her knowledge in structural analysis and always bright personality. The suggestions and encouragement provided by the committee truly helped make this research a success.

I would also like to thank my friends in the Structures Department for their academic and social backing. In particular, I would like to thank Kyle Halvordson for the frequent geogrid discussions and occasional jam session, Scott Cirmo for never passing up lunch on campus, Mike Woodworth for his witty humor, and Ashley Warren for the friendly college football feud. I am undoubtedly grateful to my fellow graduate students for making my experience at Virginia Tech the most enjoyable time of my life.

Special thanks go to my girlfriend Katie Smith for being with me through everything. Her support and understanding is sincerely appreciated.

Most importantly, I would like to thank my family for their love and encouragement. I would especially like to thank my Dad for introducing me to the field of engineering and inspiring me to pursue a higher education.

Financial support for this research was provided by the National Science Foundation under Grant No. CMS-0408281.

Table of Contents

List of Figures x

List of Tables xv

Chapter 1 Introduction and Literature Review 1

1.1 Introduction 1

1.1.1 Introduction 1

1.1.2 Objective and Scope of Research 2

1.2 Literature Review 3

1.2.1 Geosynthetics 3

1.2.2 Soil Arching 4

1.2.3 Deformation Based Design 5

1.2.4 Determination of Vertical Loads 6

1.2.5 Column Support 7

1.2.6 Previous Research 8

1.3 Thesis Overview 9

Chapter 2 Geogrid Testing 13

2.1 Introduction 13

2.2 Test Procedure 13

2.3 Test Results 16

2.3.1 Discussion of Results 16

2.3.2 Result Plots 16

Chapter 3 Finite Difference Model 19

3.1 Introduction 19

3.2 Geometry 19

3.3 Assumptions 21

3.4 Pile Orientations 22
3.5 Definition of Terms 24
3.6 Dimensional Equations 27
3.6.1 Energy Equations 27
3.6.2 Stress Resultant and Strain Equations 28
3.7 Non-Dimensional Equations 30
3.7.1 Non-Dimensionalization 30
3.7.2 Non-Dimensional Energy Equations 31
3.7.3 Non-Dimensional Stress Resultant and Strain Equations 32
3.8 Finite Difference Equations 33

Chapter 4 Model Implementation 36

4.1 Introduction 36
4.2 Program Development 36
4.2.1 Utilization of Symmetry 36
4.2.2 Boundary Conditions 38
4.2.3 Solution Technique 40
4.3 Results 41
4.4 Verification Studies 42
4.4.1 1st Example 42
4.4.2 2nd Example 44
4.5 Finite Difference Convergence Study 47

Chapter 5 Pile Orientation Study 51

5.1 Introduction 51
5.2 True Membrane Analysis 52
5.3 Standard Case 53
5.4 Square Piles 55
5.4.1 Deflections 55
5.4.2 Strains 59

5.4.3 Stress Resultants 61
5.5 Circular Piles 65
5.5.1 Deflections 65
5.5.2 Strains 69
5.5.3 Stress Resultants 70
5.6 Square Piles Rotated 45° 75
5.6.1 Deflections 75
5.6.2 Strains 79
5.6.3 Stress Resultants 80
5.7 Discussion of Results 84
5.7.1 Comparison of Pile Orientations 84
5.7.2 Comparison to Halvordson Cable Net Model 85
5.7.3 Comparison to Parabolic Design Guide 86
5.7.4 Effectiveness of Geosynthetic Support 87

Chapter 6 Alternative Parameter Model 89

6.1 Introduction 89
6.2 Alternative Parameter Case 89
6.3 Square Piles 91
6.3.1 Deflections 91
6.3.2 Strains 96
6.3.3 Stress Resultants 97
6.4 Circular Piles 101
6.4.1 Deflections 101
6.4.2 Strains 106
6.4.3 Stress Resultants 107
6.5 Square Piles Rotated 45° 111
6.5.1 Deflections 111
6.5.2 Strains 116
6.5.3 Stress Resultants 117
6.6 Discussion of Results 121

6.6.1 Comparison of Pile Orientations 121
6.6.2 Comparison to Mazursky Rayleigh-Ritz Model 122
6.6.3 Comparison to Parabolic Design Guide 122
6.6.4 Effectiveness of Geosynthetic Support 123

Chapter 7 Alternative Modeling Attempts 124

7.1 Introduction 124
7.2 Rayleigh-Ritz Model 124
7.2.1 Rayleigh-Ritz Method 124
7.2.2 Basic Model 125
7.2.3 Mathematica Implementation 127
7.2.4 Problems Encountered 127
7.3 Nonlinear Plate Equations Using Finite Differences 128
7.3.1 Nonlinear Plate Analysis 128
7.3.2 Basic Model 129
7.3.3 Mathematica Implementation 131
7.3.4 Problems Encountered 131

Chapter 8 Summary and Conclusions 132

8.1 Research Summary 132
8.2 Conclusions 134
8.3 Suggestions for Future Research 136

References 139

Appendix A Supporting Information for Program Development 143
A.1 Printout of Final Program Mathematica Notebook 143

Appendix B Supporting Information for Verification Studies 156

B.1 Printout of Mathematica Notebook for 1st Example 156
B.2 Printout of Mathematica Notebook for 2nd Example 159

Appendix C Supporting Information for Convergence Study 163
C.1 Printout of Mathematica Notebook for Convergence Study 163

Appendix D Supporting Information for Alternative Models 167
D.1 Printout of Mathematica Notebook for Rayleigh-Ritz Model 167
D.2 Printout of Mathematica Notebook for Nonlinear Membrane Model .. 169

Appendix E Supporting Information for Geogrid Testing 172
E.1 Tension Test Results 172

Vita 186

List of Figures

Figure 1.1 Reinforced Geotechnical Composite Foundation System 2

Figure 2.1 Universal Tensile Test Apparatus 14
Figure 2.2 Typical Geogrid Specimen During Testing 15
Figure 2.3 Fortrac 110 Geogrid Test Results in the Long Direction 18
Figure 2.4 Fortrac 110 Geogrid Test Results in the Cross Direction 18

Figure 3.1 Typical Column Layout Emphasizing a Unit Cell 20
Figure 3.2 Unit Cell with Square Piles with 0° rotation 21
Figure 3.3 Unit Cell with Square Piles Oriented at 45° 23
Figure 3.4 Unit Cell with Circular Piles 23
Figure 3.5 Elevation View of Composite System 25
Figure 3.6 Three – Dimensional View of Geosynthetic with Coordinate Systems 26
Figure 3.7 Visual Representation of Finite Differences 34

Figure 4.1 Progression of Symmetry in the Unit Cell 37
Figure 4.2 Finite Difference Discretization on a One-Eighth Symmetrical Section 38
Figure 4.3 Convergence Study Test Case 1 48
Figure 4.4 Convergence Study Test Case 2 49
Figure 4.5 Convergence Study Test Case 3 49
Figure 4.6 Convergence Study Test Case 4 50
Figure 4.7 Convergence Study Test Case 5 50

Figure 5.1 Three – Dimensional Plot of W Deflection 55
Figure 5.2 Three – Dimensional Plot of U Deflection 55
Figure 5.3 Three – Dimensional Plot of V Deflection 56
Figure 5.4 Three – Dimensional Plot of Deflected Shape 56
Figure 5.5 Contour Plot of W Deflection 57

Figure 5.6 Contour Plot of U Deflection 57
Figure 5.7 Two – Dimensional Plot of W Deflection Versus X 58
Figure 5.8 Two – Dimensional Plot of U Deflection Versus X 58
Figure 5.9 Three – Dimensional Plot of Ex 59
Figure 5.10 Contour Plot of Ex 60
Figure 5.11 Three – Dimensional Plot of Nx 61
Figure 5.12 Contour Plot of Nx 61
Figure 5.13 Three – Dimensional Plot of Nmax 62
Figure 5.14 Contour Plot of Nmax 62
Figure 5.15 Three – Dimensional Plot of Nmin 63
Figure 5.16 Contour Plot of Nmin 63
Figure 5.17 Contour Plot of Nmin Highlighting Region of Compressive Stress 64
Figure 5.18 Three – Dimensional Plot of W Deflection 65
Figure 5.19 Three – Dimensional Plot of U Deflection 65
Figure 5.20 Three – Dimensional Plot of V Deflection 66
Figure 5.21 Total Deflected Shape 66
Figure 5.22 Contour Plot of W Deflection 67
Figure 5.23 Contour Plot of U Deflection 67
Figure 5.24 Two – Dimensional Plot of W Deflection Versus X 68
Figure 5.25 Two – Dimensional Plot of U Deflection Versus X 68
Figure 5.26 Three – Dimensional Plot of Ex 69
Figure 5.27 Contour Plot of Ex 70
Figure 5.28 Three – Dimensional Plot of Nx 70
Figure 5.29 Contour Plot of Nx 71
Figure 5.30 Three – Dimensional Plot of Nmin 71
Figure 5.31 Contour Plot of Nmin 72
Figure 5.32 Three-Dimensional Plot of Nmax 72
Figure 5.33 Contour Plot of Nmax 73
Figure 5.34 Contour Plot of Nmin Highlighting Region of Compressive Stress 73
Figure 5.35 Three – Dimensional Plot of W Deflection 75
Figure 5.36 Three – Dimensional Plot of U Deflection 75

Figure 5.37 Three – Dimensional Plot of V Deflection 76
Figure 5.38 Total Deflected Shape 76
Figure 5.39 Contour Plot of W Deflection 77
Figure 5.40 Contour Plot of U Deflection..... 77
Figure 5.41 Two – Dimensional Plot of W Deflection Versus X 78
Figure 5.42 Two – Dimensional Plot of U Deflection Versus X 78
Figure 5.43 Three-Dimensional Plot of Ex 79
Figure 5.44 Contour Plot of Ex 80
Figure 5.45 Three-Dimensional Plot of Nx 80
Figure 5.46 Contour Plot of Nx 81
Figure 5.47 Three-Dimensional Plot of Nmax 81
Figure 5.48 Three-Dimensional Plot of Nmax 82
Figure 5.49 Three-Dimensional Plot of Nmin 82
Figure 5.50 Three-Dimensional Plot of Nmin 83
Figure 5.51 Contour Plot of Nmin Highlighting Region of Compressive Stress 83

Figure 6.1 Three – Dimensional Plot of W Deflection 91
Figure 6.2 Three – Dimensional Plot of U Deflection 91
Figure 6.3 Three – Dimensional Plot of V Deflection 92
Figure 6.4 Total Deflected Shape 92
Figure 6.5 Contour Plot of W Deflection 93
Figure 6.6 Contour Plot of U Deflection 93
Figure 6.7 Two – Dimensional Plot of W Deflection Versus X 94
Figure 6.8 Two – Dimensional Plot of U Deflection Versus X 94
Figure 6.9 Three – Dimensional Plot of Ex 96
Figure 6.10 Contour Plot of Ex 96
Figure 6.11 Three – Dimensional Plot of Nx 97
Figure 6.12 Contour Plot of Nx 98
Figure 6.13 Three – Dimensional Plot of Nmin 98
Figure 6.14 Contour Plot of Nmin 99
Figure 6.15 Three – Dimensional Plot of Nmax 99

Figure 6.16 Contour Plot of Nmax 100
Figure 6.17 Contour Plot of Nmin Highlighting Region of Compressive Stress 100
Figure 6.18 Three – Dimensional Plot of W Deflection 101
Figure 6.19 Three – Dimensional Plot of U Deflection 102
Figure 6.20 Three – Dimensional Plot of V Deflection 102
Figure 6.21 Total Deflected Shape 103
Figure 6.22 Contour Plot of W Deflection 103
Figure 6.23 Contour Plot of U Deflection 104
Figure 6.24 Two – Dimensional Plot of W Deflection Versus X 104
Figure 6.25 Two – Dimensional Plot of U Deflection Versus X 105
Figure 6.26 Three – Dimensional Plot of Ex 106
Figure 6.27 Contour Plot of Ex 106
Figure 6.28 Three – Dimensional Plot of Nx 107
Figure 6.29 Contour Plot of Nx 107
Figure 6.30 Three – Dimensional Plot of Nmax 108
Figure 6.31 Contour Plot of Nmax 108
Figure 6.32 Three – Dimensional Plot of Nmin 109
Figure 6.33 Contour Plot of Nmin 109
Figure 6.34 Contour Plot of Nmin Highlighting Region of Compressive Stress 110
Figure 6.35 Three – Dimensional Plot of W Deflection 111
Figure 6.36 Three – Dimensional Plot of U Deflection 112
Figure 6.37 Three – Dimensional Plot of V Deflection 112
Figure 6.38 Total Deflected Shape 113
Figure 6.39 Contour Plot of W Deflection 113
Figure 6.40 Contour Plot of U Deflection 114
Figure 6.41 Two – Dimensional Plot of W Deflection Versus X 114
Figure 6.42 Two – Dimensional Plot of U Deflection Versus X 115
Figure 6.43 Three – Dimensional Plot of Ex 116
Figure 6.44 Contour Plot of Ex 116
Figure 6.45 Three – Dimensional Plot of Nx 117
Figure 6.46 Contour Plot of Nx 117

Figure 6.47 Three – Dimensional Plot of Nmin 118
Figure 6.48 Contour Plot of Nmin 118
Figure 6.49 Three – Dimensional Plot of Nmax 119
Figure 6.50 Contour Plot of Nmin 119
Figure 6.51 Contour Plot of Nmin Highlighting Region of Compressive Stress 120

Figure 7.1 Rayleigh-Ritz Shape Function for w with n = m = 1.0 126
Figure 7.2 Rayleigh-Ritz Shape Function for u with n = m = 1.0 127

List of Tables

Table 1.1 Calculated SRR Values (Filz and Smith 2006) 7

Table 2.1 Geogrid Test Results 17

Table 5.1 Deflections for Standard Case Square Piles 59
Table 5.2 Stress and Strain for Standard Case Square Piles 64
Table 5.3 Deflections for Standard Case Circle Piles 69
Table 5.4 Stress and Strain for Standard Case Circle Piles 74
Table 5.5 Deflections for Standard Case Rotated Square Piles 79
Table 5.6 Stress and Strain for Standard Case Rotated Square Piles 84
Table 5.7 Comparison of Maximum Values for Standard Case 85
Table 5.8 Comparison of Cable Net Model Results (Halvordson 2007) 86

Table 6.1 Deflections for Alternate Case Square Piles 95
Table 6.2 Stress and Strain for Alternate Case Square Piles 101
Table 6.3 Deflections for Alternate Case Circle Piles 105
Table 6.4 Stress and Strain for Alternate Case Circle Piles 111
Table 6.5 Deflections for Alternate Case Rotated Square Piles 115
Table 6.6 Stress and Strain for Alternate Case Rotated Square Piles 121
Table 6.7 Comparison of Maximum Values for Alternate Case 121
Table 6.8 Comparison of Rayleigh-Ritz Model Results (Mazursky 2006) 122

Chapter 1

Introduction and Literature Review

1.1 Introduction

1.1.1 Introduction

Geosynthetic-reinforced, column-supported embankments provide effective geotechnical composite systems for use in the construction of civil engineering works over regions of soft soil. The system offers a cost-effective solution to minimize settlements of structures founded on the embankment as well as any adjacent structures susceptible to movement. Construction time is also minimized when timely excavation or soil improvement would otherwise be necessary.

These reinforced embankments consist of strong columns, a coarse grained bridging layer, and one or more layers of geosynthetic reinforcement. Columns are founded on a hard-bearing stratum below the embankment and rise up through the soft soil to the bridging layer. These columns can be implemented through a variety of methods and may or may not have pile caps of various sizes and geometries. Several feet of coarse-grained soil or aggregate is used in the bridging layer, which is placed above the columns. In order to encourage load transfer within the bridging layer, geosynthetics are sometimes utilized to help transfer the embankment loads. One or more layers of geosynthetic, usually in the form of geogrids, are placed in the bridging layer and enhance the load transfer into the columns and away from the soft soil. The use of geosynthetics therefore efficiently allows for the design of smaller column diameters and wider spacings. A model of a typical geosynthetic-reinforced, column-supported embankment can be seen in Figure 1.1.

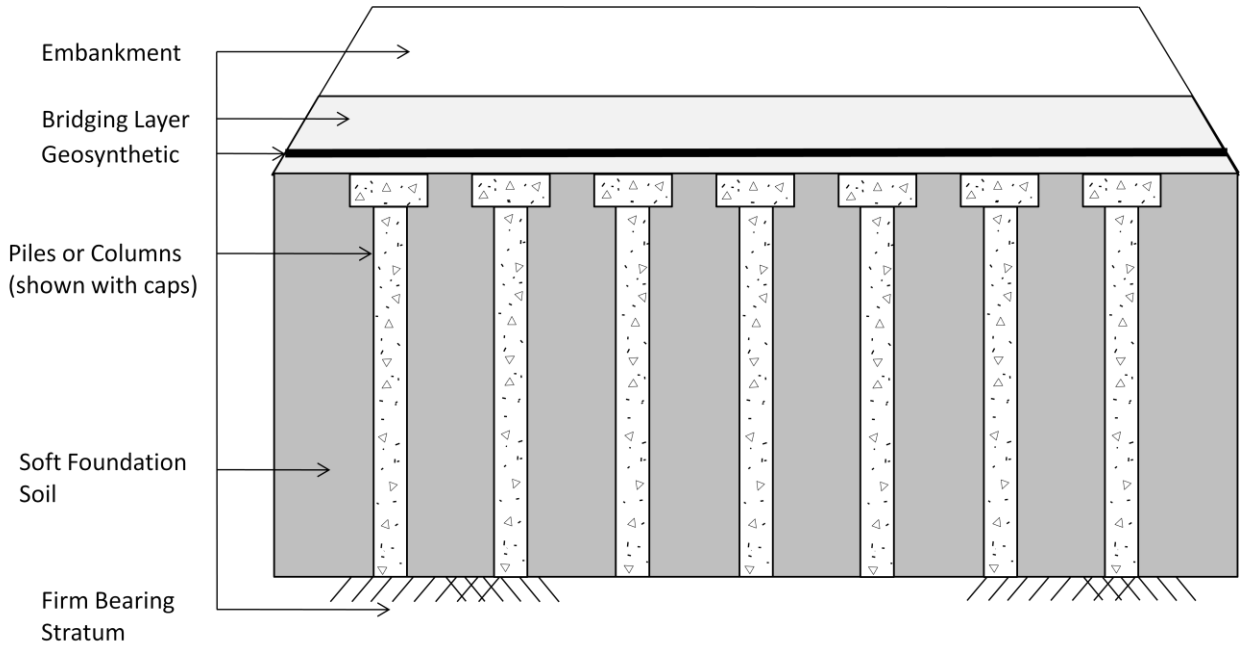

Figure 1.1 Reinforced Geotechnical Composite Foundation System

1.1.2 Objective and Scope of Research

Current design methods for geosynthetic-reinforced embankments are based on a wide range of conservative assumptions, which give rise to conflicting results. Most of the them rely on an equal-strain method that assumes equal vertical strains over the columns and weak soil. This assumption contradicts vertical stress equilibrium in which strains in the geosynthetic, and stress concentrations over the piles, are not fully realized. Another source of error is in the determination of vertical loads transmitted to the geosynthetic. Several methods are available for these calculations and can be shown to yield different results. This discrepancy was addressed in Filz and Smith (2006), in which a new method was presented that accounts for the effects of the soft soil.

Previous modeling of the geosynthetic layer has also been oversimplified and subsequently inaccurate to represent the true nature of the material. The majority of the prior studies treat the geosynthetic as a one-dimensional cable. However, this approximation neglects the three-dimensional, orthotropic behavior of geosynthetics in applications of column-supported embankments.

Recent increases in the popularity of this composite system has generated the need to further investigate its behavior and soil-structure interaction. Current models of geosynthetics are oversimplified and do not represent the true three-dimensional othotropic nature of the material. Such simplifications include treating the geosynthetic as a one-dimensional cable as well as neglecting stress concentrations and pile orientations. Previous studies at Virginia Tech by Miriam Stewart and Laurie Mazursky on the subject have eliminated certain assumptions regarding the analysis and design of geosynthetic embankments. The purpose of this research is to continue to examine the three-dimensional nature of geosynthetics through established numerical and mathematical techniques. In this thesis, a new method based on finite differences and utilizing energy methods is developed.

1.2 Literature Review

1.2.1 Geosynthetics

Geosynthetics are polymeric planar materials that are used in conjunction with geotechnical materials such as soil and rock in civil engineering applications (Pinto 2003). In general, there are eight types of geosynthetics: geotextiles, geogrids, geonets, geomembranes, geosynthetic clay liners, geopipes, geofoam, and geocomposites (Koerner 2005). The use of these materials began in the 1970's and their popularity is steadily increasing today. Currently geosynthetics are used in roadway and railways, foundations, embankments, steep slopes, and retaining walls. In these applications, geosynthetics can function as a barrier, or provide drainage, filtration, separation, protection, surface erosion, or reinforcement (Pinto 2003).

Advantages for the use of geosynthetics are numerous and benefit several job sectors. Geosynthetics afford beneficial construction applications such as rapid installation, weather resistance, reduction of earthwork volume, and increased potential of soft-soil work sites. Similarly, geosynthetics are attractive to designers in the sense that they provide a uniform material in which quality control and assurance are ensured. Construction and maintenance costs are also typically lower as well, providing an attractive alternative to clients under tight budgets (Pinto 2003).

Important properties of geosynthetics include tensile strength, tensile modulus, and shear strength. Tensile strength is essential to resist the tensile stresses induced in the material when used as anchorage or reinforcement. Also imperative is the tensile modulus which must be sufficient to resist deformations consistent within the surrounding soil or aggregate. Shear strength is the capacity of the material to interact and bond to the adjacent soil layer to provide pullout resistance. In applications of reinforcement, the geosynthetic often acts as a tensioned membrane in which normal and planar stresses are generated (Pinto 2003). However, when modeling the geosynthetic as a membrane, normal stresses are typically assumed to be zero.

The development of geosynthetics with high-modulus polymeric materials gave rise to their use in areas of reinforcement. Geogrids are generally used in this role, as they contain apertures that allow for good interlocking in the soil and aggregates. Longitudinal and transverse ribs of various materials are machined together to create geogrids of various orientation. Two types of geogrids exist: uniaxial geogrids, which are used when the direction of stress is known, and biaxial geogrids, where stresses are applied from multiple directions (Koerner 2005). Biaxial geogrids are most commonly used in applications of pavement and embankment foundations. Custom geogrids are also commercially available for unique applications (Huesker 2006).

1.2.2 Soil Arching

Soil arching is a phenomenon that has been described by Karl Terzaghi through a simple experiment. In the experiment, a bed of sand was situated above a support containing a removable strip. Before yielding, the state of stress is constant throughout the sand layer. When the "trap door" is lowered from its initial position, however, the sand just above the strip will travel downward. This lowering induces friction and subsequent shear stresses along the vertical plane of the sand layer still over the support. The shear stresses in the system cause a decrease in pressure throughout the sand in the unsupported layer, of intensity equal to that of the shearing resistance along the boundary. Terzaghi therefore noted that the decrease in vertical pressure over the unsupported region must be associated with a sharp increase in pressure at the boundary of the rigid support. This phenomenon is termed soil arching effect and is defined by Terzaghi

as the “transfer of pressure from a yielding mass of soil onto adjoining stationary parts” (Terzaghi 1943).

Soil arching is an important factor in column-supported embankments over soft soil. In particular, similar results as in Terzaghi’s experiment occur when the soft soil of the embankment consolidates and settles relative to the stronger piles. The piles will then act as the rigid support and a portion of the vertical stress in the soft soil will be transmitted to the piles due to arching. A significant number of factors have been shown to influence the degree of soil arching in column-supported embankments. Horgan and Sarsby (2002) stated that in order for soil arching in the embankment to occur, the depth of the fill over the void must be sufficiently large. Also, Lawson (1992) showed that the degree of arching is influenced by the distance between columns, embankment height, and soil and pile properties. Soil arching is the basis for several design procedures that model the vertical load attributed to the geosynthetic bridging layer.

1.2.3 Deformation Based Design

Foundation engineering uses a deformation based design approach in a variety of applications such as piles, footings, drilled shafts, and embankments. In order to effectively use a deformation based approach, differential settlements in the foundation system of interest must be accurately known. In geosynthetic-reinforced column-supported embankments, differential settlements are not readily attainable.

Current design procedures for geosynthetic-reinforced foundations use several assumptions that complicate the prediction of differential settlements. In particular, an equal-strain assumption is commonly used. The equal-strain approach assumes that vertical stresses are constant with depth throughout the column and soft-soil regions (Broms 1999). Under this assumption, stress concentrations can be seen to develop over the columns, which have much larger modulus values. Also notable is the fact that the columns are said to be founded on a hard bearing stratum. The equal-strain method would then yield equal settlement over the soft soil as the columns. This uniform settlement suggests that stress concentrations are not possible within the bridging layer, inconsistent with the stress concentrations that can be seen to develop over the

columns. The equal-strain method therefore violates vertical stress equilibrium and is not accurate for use in column-supported embankments.

1.2.4 Determination of Vertical Loads

Several different methods for calculating the vertical loading on geosynthetic reinforcement exist. Each method is based on different approaches to influential factors such as soil arching, loading, and material parameters. Examples of the design methods currently in use are the British Standard BS8006, Terzaghi, Hewlett and Randolph, and Guido methods. Each of these methods is inherently flawed, as they assume no resistance of the soft-soil layer (Russell and Pierpoint 1997). A new method, however, has been presented by Smith (2005), which incorporates compressibility of the soft soil between the columns.

Inconsistencies in the British Standard BS8006, Terzaghi, Hewlett and Randolph, and Guido methods are notable and have been examined in Love (1994), Russell and Pierpoint (1997), Love and Milligan (2003), and Filz and Smith (2006). Russell and Pierpoint (1997) suggest that the development of a consistent design method is essential and that three-dimensional analysis is the most reliable approach.

In order to evaluate each of the proposed design methods, a stress reduction ratio (SRR) value is introduced. The calculated SRR value from each of the design methods represents the proportion of the total load that will be carried by the geosynthetic. SRR values were calculated for a variety of design methods by Filz and Smith (2006) and their results can be seen in Table 1.1. The variation in each method is apparent in Table 1.1, further revealing the need for a more consistent design of geosynthetic-reinforced embankments. In this analysis, “a” denotes the pile cap width, “s” denotes the center to center column spacing, and “H” represents the embankment height.

Table 1.1 Calculated SRR Values (Filz and Smith 2006)

Method	SRR					
	a/s = 0.25		a/s = 0.333		a/s = 0.50	
	H/s = 1.5	H/s = 4.0	H/s = 1.5	H/s = 4.0	H/s = 1.5	H/s = 4.0
BS8006	0.92	0.34	0.62	0.23	0.09	0.02
Adapted Terzaghi, Kt=1.0	0.60	0.32	0.50	0.23	0.34	0.13
Adapted Terzaghi Kt=0.5	0.77	0.52	0.69	0.42	0.54	0.26
Kempfert et al.	0.55	0.46	0.43	0.34	0.23	0.15
Hewlett & Randolph	0.52	0.48	0.43	0.31	0.30	0.13
Adapted Guido	0.12	0.04	0.10	0.04	0.08	0.03
Carlsson	0.47	0.18	0.42	0.16	0.31	0.12

1.2.5 Column Support

Reinforced embankments are generally strengthened using column elements that are embedded in the soft-soil region. Column support can be achieved by driven concrete piles, vibro concrete columns, stone columns, concrete drilled shafts, or other soil improvement techniques. A commonly used soil stabilization method with applications to reinforced embankments is the deep mixing method. The method is widely used in port facilities, embankments, and excavations in Japan and is currently emerging in the United States (CDIT 2002). In particular, the method has been used at the I-95/Route 1 interchange in Alexandria, Virginia (Smtih 2005).

The deep mixing method uses stabilizing agents, such as cement or slaked lime, to create strong columns. Stabilizing agents are introduced either in "wet" form mixed with water, or by the "dry" method in which the *in situ* soil chemically reacts with the agents and hardens. Soft clays and organic soils are common soils in which the method is utilized. The stabilized columns can also be arranged in a variety of layouts and orientations for specific applications. Groups of deep mixed columns have successfully been used to reduce deformation and increase bearing capacity in embankments or retaining walls (CDIT 2002).

Another commonly used type of column support is achieved by deep vibratory techniques. Vibratory compacted columns provide high compressive strength and stiffness, increasing bearing capacity and reducing settlement in regions of soft soils (Kempfert and Gebreselassie 2006). This method uses a cylindrical, horizontally vibrating shaft to introduce and compact stone aggregates or concrete into the soil. Stone piles can be created using a replacement process in which the vibrator tip jettisons water through the shaft, flushing loosened soil to the surface. The stone aggregate is then embedded as the vibrator is removed, preventing collapse of the shaft. Columns can also be created using a concrete tremie system in which concrete is delivered at positive pressure via the vibrator tip. The vibrator is raised as the concrete fills the shaft and is re-entered to reach a desired resistance (Mosely and Kirsch 2004).

Vibratory columns have been used widely in geotechnical applications of soil reinforcement around the world. In particular, construction of a highway embankment and bridge abutment in Putrajaya Malaysia, in 2001, utilized this technique. The in-situ method was chosen as an economical and environmentally friendly alternative that averted the need to excavate and dispose of the soft soil on-site. Over 420,000 meters of stone columns were successfully created in the project, validating the method. It was also shown that the method is acceptable for use in soft cohesive soils with shear strengths as low as 4 kPa (Mosely and Kirsch 2004).

1.2.6 Previous Research

Significant research has been conducted in the analysis of geosynthetics and their applications to soil reinforcement in column-supported embankments. In most of these previous studies, however, the analysis has been oversimplified. Conservative assumptions have been made for the geosynthetic and soil parameters, vertical load calculation, and modeling technique. Some previous models of geosynthetics have treated the system as a one-dimensional cable, which fails to represent the true behavior of the material. A three-dimensional, orthotropic model is necessary to fully represent factors which are not apparent in a one-dimensional model. Such parameters include the ability of the geosynthetic to carry compressive and tensile forces, stress concentrations in areas of high strains, and the orientation of the geogrid itself. Several sources

on the topic are summarized here to emphasize the ongoing nature of the research and to present other potential models.

A study by Agaiby and Jones (1995) provides an example of one-dimensional cable analysis of geosynthetic-reinforced soil. In particular, their analysis dealt with the formation of voids under roadway and railway embankments. This would be analogous to a reinforced embankment with super soft foundation soils. The reinforcement was modeled with a series of cable elements that had no flexural rigidity and were only capable of carrying tensile forces. A parametric study was conducted, which yielded values for maximum surface displacement and mobilized tension of the reinforcement as well as the width of depression zones.

A two-dimensional model of geosynthetic reinforcement was investigated by Burd (1995). In this case, the geosynthetic was modeled as a plane-strain membrane sheet. Stress values were assumed to act monotonically on the reinforcement, which was then utilized in formulating and solving the membrane equations. Also included was the allowance of relative slip between the reinforcement and subgrade soil. Physical testing by Love et al. (1987) and Love (1994) as well as finite element modeling were used to validate the proposed model. It is important to note that the finite element modeling highlighted the magnitude of the membrane action that is prevalent at large deformations.

A three-dimensional analysis was conducted by Villard and Giroud (1998) to investigate geotextile sheets used in road and rail infrastructure. In particular, the membrane behavior of flat sheets under uniform pressure was studied. A three-node, three-dimensional geotextile element was created specifically for use in the finite element applications. This element allows for different orientations of threads most often found in geogrids. The threads are interwoven in the formulation to prevent relative slip between the nodes. In their analysis, a uniformly distributed vertical load was used with a nonlinear stress behavior. Although not presented in the paper, soil behavior, soil and geotextile interaction, and other stress aspects could be included in the model to create a more specific and focused analysis.

Another detailed study was performed by Fakher and Jones (2001), in which the central focus was to determine the importance of bending resistance in geosynthetic reinforcement. In this model, super soft clay was overlain by a variable cohesionless sand layer with and without a

layer of geosynthetic. It should be noted that the authors denoted super soft clay as a clay with high water content and little shear resistance. The geosynthetic was represented in two ways: as cable elements with no bending stiffness, and as beam elements with elastic bending stiffness. The reinforcement was also not vertically fixed to any boundary so as to avoid any unrealistic pullout behavior. A surface loading was applied to the system in the form of a rigid plate acting on the sand bearing layer. The finite difference program FLAC was used for the analysis of the two models to determine the effects of the inclusion of bending resistance. The resulting analysis showed that when the footing settles over a layer of super soft clay, the material attempts to move laterally, resulting in heave. Bearing capacity is directly affected by this heave action and is an important factor in construction on super soft clays. The inclusion of bending stiffness within the reinforcement was shown to significantly reduce heave action and to spread the effects over a greater area. Most importantly, it was shown that geosynthetics with bending resistance and tensile stiffness overlaying super soft clays provide a superior form of support when compared with the membrane support system used in Burd (1995).

1.3 Overview of Thesis

The following seven chapters discuss the proposed finite difference model, its implementation in Mathematica, and subsequent analysis results. Chapter one provides an introduction for the stated problem and outlines the research objectives. A thorough literature review was also conducted and presented in Chapter one to determine the current state of knowledge on the subject.

Chapter two discusses the tensile material testing conducted on several geogrid samples. The material samples and following testing procedure are outlined according to ASTM guidelines. Pertinent results are presented in text in Chapter two which include ultimate strain and plots of the approximate linear elastic behavior exhibited by the geogrids. These tests were used to gain an understanding of the behavior of the material under load in order to confidently make modeling assumptions.

Chapter three discusses the proposed finite difference model. The nomenclature, modeling assumptions, geometry, layout, and parameters are outlined. Also included, are all requisite energy and finite difference equations used in the formulation.

Chapter four continues the discussion of the finite difference model development. Emphasis in this chapter is placed on programming in Mathematica 5.2. Symmetry and boundary conditions are presented and their implementation discussed. Once the finite difference program was established, two verification studies were performed based on published literature on plate analysis. Each of the two test problems analyzed in the finite difference method yielded similar results to the published analytical results. A convergence study on the finite differences was also conducted to determine the required number of node divisions.

Chapter five and six each discuss the results obtained from the analysis of the standard and alternative parameter cases respectively. In particular, three-dimensional plots were generated for the vertical and in-plane displacements, total deflected shape, stress resultants, and strains. Contour plots were also utilized to emphasize highly variable regions within the unit cell. Tables were generated to show maximum values for deflections, stress resultants, and strains.

Also provided in Chapters five and six, are comparisons to other models such as a cable net analysis conducted by Halvordson (2007) and a Rayleigh-Ritz analysis performed in Mazursky (2006). A current design method in which a parabolic approximation is made for the geosynthetic is also evaluated. Relative effectiveness of the geosynthetic reinforcement is calculated for each pile orientation and parameter case. These values represent the portion of the total load being carried by the geosynthetic.

Chapter seven discusses two analysis methods attempted at the outset of this research. Specifically, the Rayleigh-Ritz method and finite difference method using nonlinear plate equilibrium equations were investigated. Each method yielded undesirable results and ultimately proved to be inefficient for the required analysis. The development of these methods as well as the problems encountered is discussed.

Lastly, Chapter eight provides a summary of the research conducted and conclusions drawn. The overall procedure and progression of the analysis is discussed. The results in Chapters five and

six are also evaluated of which conclusions and design suggestions are determined. Suggestions for future work are also discussed with respect to the proposed model as well as other techniques.

Appendix A contains a final printout of the Mathematica notebook used in the finite difference analysis. Also included in Appendix B, are printouts of the Mathematica notebooks used for each of the verification examples. Appendix C contains the printout of the Mathematica notebook used in the convergence study for the finite differences. The failed model attempts including Rayleigh-Ritz and finite difference analysis with nonlinear plate equations are included in Appendix D. Finally, the supporting data from the geogrid tensile testing is provided in Chapter E. Figures for each test are presented including geogrid type and material direction.

Chapter 2

Geogrid Testing

2.1 Introduction

Several specimens of Fortrac and Fornit (Huesker geogrids) were tested in the Virginia Tech Engineering Science and Mechanics laboratory. The objective of the tests was to observe the behavior of commonly used geogrids under tensile load. Knowledge of the material's behavior was then used to make necessary modeling assumptions with confidence. Twenty-seven small samples of geogrid in a variety of sizes and orientations were used in the tests.

Each of the two brands of geogrids tested are manufactured by Huesker, Inc., a subsidiary of Huesker Synthetics. Fortrac geogrids are constructed in a grid pattern with interwoven polyester yarns. The grid is coated in PVC and commonly used in the reinforcement of retaining walls and steep slopes, and as landfill liner systems. The orientation of the ribs and the aperture size allow for interaction between the geogrid and surrounding soil in the development of full tensile capacity of the material (Huesker 2007).

A collection of Fornit brand Huesker geogrid was also tested. Fornit geogrids are comprised of polypropylene yarns woven into an interlocking pattern. They are also coated to produce a stable construction material that is resistant to damage during installation. Fornit geogrids have been shown to resist freeze-thaw conditions, harsh soil chemicals, and ultra-violet exposure. Applications of the material include stabilizing poor soils by increasing tensile reinforcement and providing soil separation (Huesker 2007).

2.2 Test Procedure

The geogrid testing procedure was based on the American Society for Testing Materials ASTM D6637-01 standard for determining tensile properties of geogrids by the single or multi-rib tensile method. The D6637-01 standard covers three methods of determining the properties of

geogrids under tensile load. Method A was adopted here, which involves the testing of a single geogrid rib. Although tests were conducted using two ribs, the ASTM designated methods B and C require that three ribs be tested (ASTM 2007).

Sample geogrids were obtained from Huesker, Inc., in a variety of layouts and sizes in 3" by 5" specimens. The exact dimensions of the specimens did not meet ASTM standards, but were constructed to provide the most accurate data possible. The samples were placed in a universal tensile testing machine with various gage lengths. Soft, compressible paper was placed in the grips of the machine clamps to help alleviate the drastic cutting stresses induced during testing. Once each of the specimens was securely fastened in the testing apparatus, loading was applied.

Figure 2.1 Universal Tensile Test Apparatus (used with permission)

A data acquisition system recorded the applied tensile load and overall head displacement of the clamps. The testing apparatus and acquisition system can be seen in Figure 2.1. Each specimen was loaded at slow rates of strain until rupture occurred. It is important to note that an initial slack displacement region occurred in several of the tests. ASTM D6637-01 discusses this

behavior and suggests that slack occurs during test setup or due to the testing equipment. Data retrieved from the acquisition system were used to produce plots of applied load versus strain. Ultimate load and strains were also attainable from these plots and are discussed in the following section.

Sample geogrids were tested in both the machine direction and cross directions specified here by L and X, respectively. In general, the machine direction contains larger rib sizes, which affords it greater strength than the cross direction. Table 2.1 illustrates which of the tests involved testing in the machine and cross directions. A typical geogrid specimen setup for testing is shown in Figure 2.2.

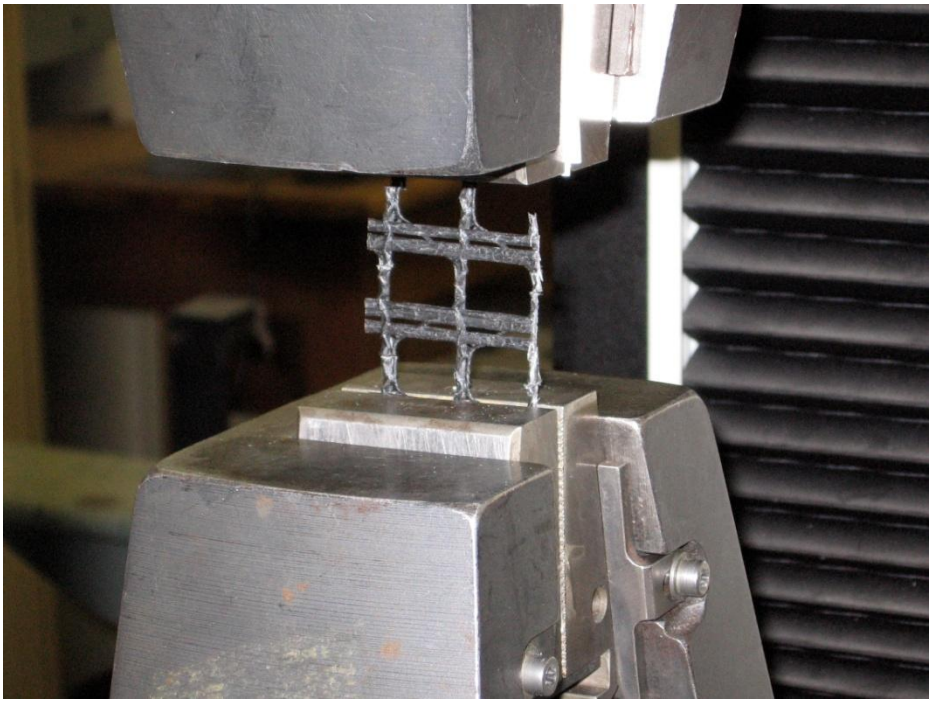

Figure 2.2 Typical Geogrid Specimen During Testing (used with permission)

2.3 Test Results

2.3.1 Discussion of Results

As can be seen in Appendix E, test results vary greatly depending on brand, direction of loading, and number of strands tested. This contradicts design information provided in Huesker (2007). Errors potentially arise when using the modified test procedure other than one specified by ASTM D6637-01. In all of the samples tested, only one or two ribs of the grid were loaded. Although the results are not ideal and do not necessarily agree with given proprietary design information, key facts can still be extracted from these data.

One main assumption used in computer modeling of the geosynthetic is that the material behaves linear elastically for the strains that occur. This behavior is shown to approximately exist as seen in Figures 2.3 and 2.4. Each geogrid tested exhibited an approximately linear increase in strain with an equivalent increase in load. The assumption of linear elastic behavior allowed the geosynthetic to be modeled as an isotropic plate with a specific modulus of elasticity.

Another significant conclusion that can be derived from the test results is the ultimate strain capacity of the material. Most design guides limit the workable strain capacity of geosynthetic reinforcements to 5% elongation (Huang et al. 2006). This limitation is enforced for serviceability reasons to prevent tear or punching failures. The ultimate strain capacity of each test can be seen in Appendix E when a sharp decrease in load occurs. Most of the specimens reached an ultimate strain capacity around 10%, which is slightly more than allowed in practice. Although the test results yielded ultimate strain capacity of each geogrid, the tests performed were not intended to provide exact values as more reliable proprietary data is readily available.

2.3.2 Result Plots

Results from the geogrid testing program are displayed in Table 2.1. Noted in the table are ultimate strain, ultimate load, geogrid brand, and the number of ribs tested. Figures 2.3 and 2.4 also graphically represent load versus strain for a typical specimen in the machine and cross directions, respectively.

Table 2.1 Geogrid Test Results

Test No.	Geogrid Type	Ultimate Load kN	Ultimate Strain %	No. Ribs Tested
1	Fortrac 110	3.191	19.94	2L
2	Fortrac 110	2.052	12.19	2L
3	Fortrac 110	1.459	26.80	1L
4	Fortrac 110	0.250	8.12	1X
5	Fortrac 110	0.454	11.41	1X
6	Fortrac 80	1.195	49.52	1L
7	Fortrac 80	1.046	12.83	1L
8	Fortrac 80	0.652	9.79	2X
9	Fortrac 80	0.905	9.32	2X
10	Fortrac 80	0.952	10.47	2X
11	Fortrac 55	0.885	26.42	1L
12	Fortrac 55	0.846	24.21	1L
13	Fortrac 35	0.533	43.57	2L
14	Fortrac 35	0.403	43.35	2L
15	Fortrac 35	0.444	22.53	1L
16	Fornit 30	0.510	19.58	1L
17	Fornit 30	0.953	10.67	1L
18	Fornit 30	0.475	12.82	1L
19	Fornit 30	0.490	17.13	1L
20	Fornit 30	0.596	7.12	1X
21	Fornit 30	0.597	5.77	1X
22	Fornit 30	0.840	10.02	1X
23	Fornit 20	0.360	11.16	1L
24	Fornit 20	0.330	10.07	1L
25	Fornit 20	0.557	9.76	1X
26	Fornit 20	0.417	6.74	1X
27	Fornit 20	0.291	53.78	1X

Both Figures 2.3 and 2.4 exhibit the initial slack displacement behavior discussed previously. It is also apparent that the long direction was able to sustain a greater applied load than the cross direction. Although results in the tests vary, specimens loaded in the machine direction were capable of reaching higher ultimate strain values then those of specimens loaded in the cross direction.

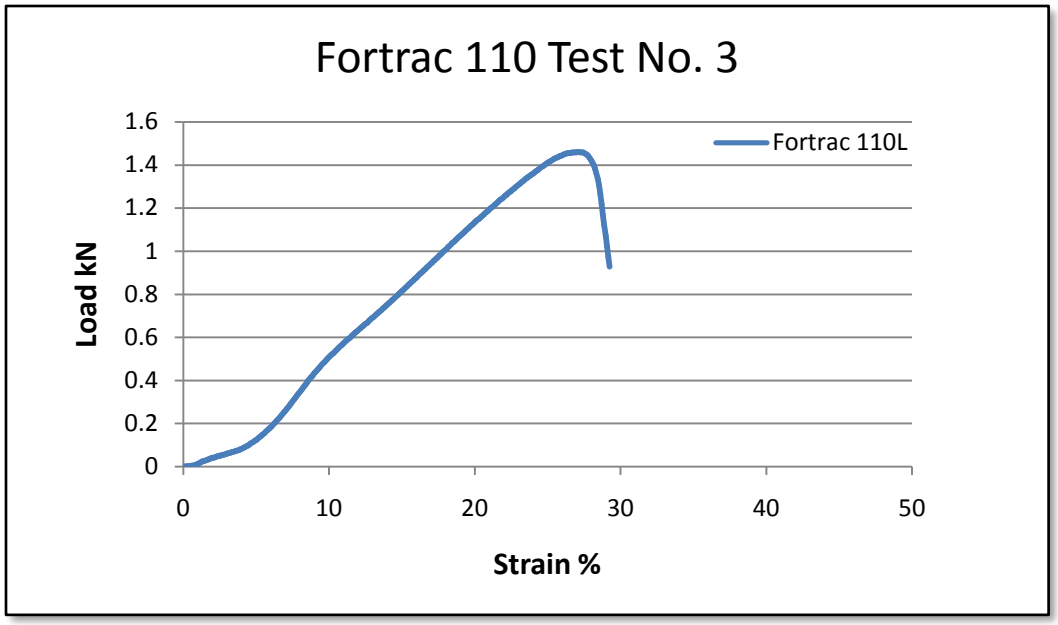

Figure 2.3 Fortrac 110 Geogrid Test Results in the Long Direction

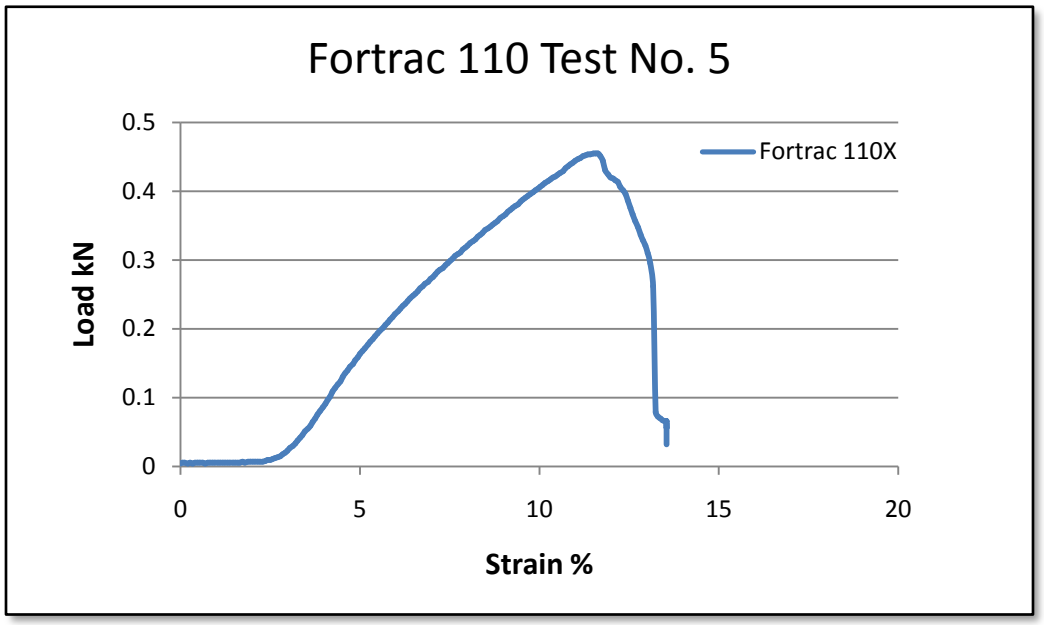

Figure 2.4 Fortrac 110 Geogrid Test Results in the Cross Direction

Chapter 3

Finite Difference Model

3.1 Introduction

A numerical model of the geosynthetic reinforcement was developed based on energy methods employing central finite differences. The mathematical software package Mathematica Version 5.2 was used exclusively to implement the model. Mathematica provides a user-friendly, front-end environment for symbolic expressions and numerical calculations (Wolfram 1996). In developing the program, emphasis was placed on automation allowing for numerous variations in parameters and orientations to be run successively. The software also contains a variety of two- and three-dimensional graphics packages capable of displaying results in visual form. During the course of this thesis, Version 5.2 was used to generate the program, while the latest Version 6.0 was used to create more visually appealing graphics. Mathematica Version 6.0 contains significant graphical improvements to previous versions including the automation of high-fidelity, dynamic, two- and three-dimensional visualizations of functions and data (Wolfram Research 2007).

3.2 Geometry

The focus of this research is to create a more accurate three-dimensional model of the geosynthetic reinforcing layer. As seen in Figure 1.1, the geosynthetic reinforcement lies within a bridging layer just above the column support and soft soil. In practice, several layers of reinforcement at varying depths may be used; however, in this model a single layer is assumed (Yan 2006). A parameter t is defined in the formulation, which denotes the reinforcement thickness. This value can be defined accordingly to represent one or more layers of geosynthetic at a certain depth.

Generally, this composite system is used over a large area in which repetition allows for utilization of symmetry in the model development. A typical grid of columns used in reinforced embankments is shown in Figure 3.1.

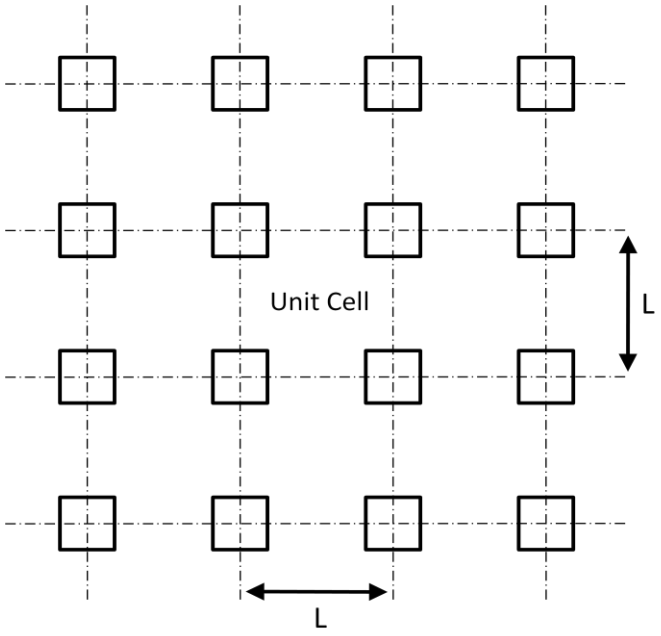

Figure 3.1 Typical Column Layout Emphasizing a Unit Cell

A unit cell concept is adopted here to represent the requisite portion of the system needed for complete analysis. This procedure is common in the analysis of such systems and is used in the calculations of vertical load by the BS8006, Terzaghi, Hewlett and Randolph, and Guido Methods (Russell 1997). Figure 3.2 shows a typical unit cell used in the current model. This representation contains square piles of width 2B spaced a distance L center-to-center. The X-Y coordinate system is also shown, with its origin at the center of the bottom left column.

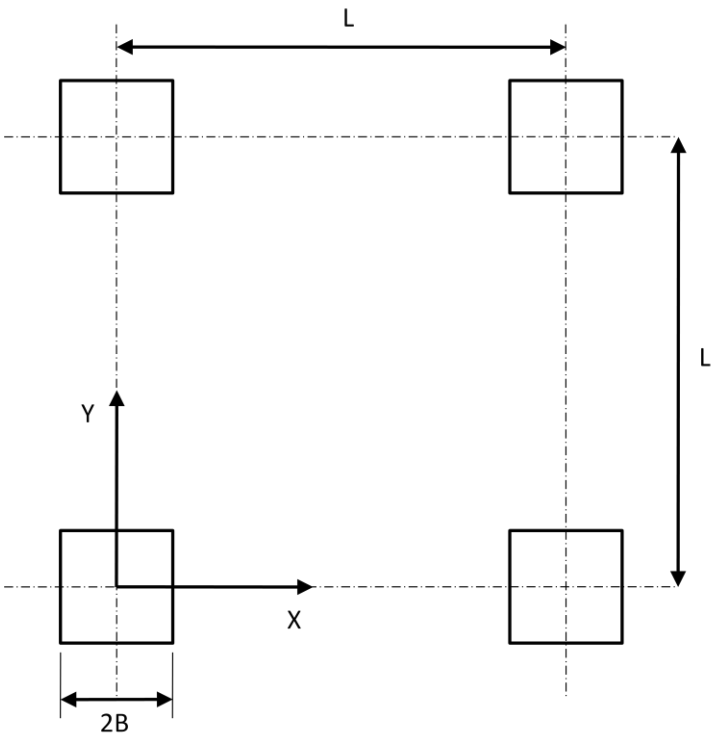

Figure 3.2 Unit Cell with Square Piles with 0° rotation

3.3 Assumptions

A variety of assumptions were necessary to simplify the model and effectively represent its behavior. In this analysis, the geosynthetic reinforcement is treated as a thin, flexible plate. The large-deflection theory of plates is used to account for the magnitude of vertical deflection and subsequent stretching of the mid-plane surface. Szilard (1974) states that for $w \geq .30h$ where w is maximum vertical deflection and h is the thickness of the plate, large-deflection theory should be used. This is the case here, and can be seen in the calculated results. The large-deflection theory of plates also permits resulting deflections that are greater than or equal to the plate thickness but are still small relative to the overall length and width of the plate (Szilard 1974). Elastic plate deflections are accounted for by the nonlinear von Kármán equations given in Chia (1980), Szilard (1974), and Timoshenko and Woinowsky-Krieger (1959). These equations are based on small strains and large rotations of plates that are characterized by small finite

deformations (Ugural 1999). Another key assumption of the von Kármán theory is that the squares of strains and rotations are small in comparison to unity (Chia 1980).

The column and soft soil regions are modeled by an elastic foundation system. The Winkler model is employed in which a spring stiffness k is defined for each region. The elastic half-space is then represented by a distribution of linear vertical springs along the foundation. The values of k are representative of a basic subgrade modulus and are taken to be different over the columns and the soft soil. In this particular model, friction between the geosynthetic and surrounding soil is neglected. Other models such as the Pasternak foundation are capable of representing a horizontal shear layer in addition to the vertical Winkler springs. The Winkler model is extremely popular, with extensive use in the analysis of foundations, and will be adopted here (Scott 1981).

The column support is assumed to be rigid and oriented in a variety of layouts and shapes. To account for soil arching in this system, different values of vertical loading are defined. The load is applied as a uniform pressure with a much higher value over the piles than over the soft soil. The loads used in the basic model are based on previous experience to establish a baseline parameter case.

3.4 Pile Orientations

Three unique pile orientations were investigated with the finite difference based model. Square piles at 0° rotation, square piles at 45° rotation, and circular piles were all examined. Figure 3.2 illustrates a unit cell with square piles at 0° rotation, while Figure 3.3 and Figure 3.4 show a unit cell with square piles rotated 45° and circular piles, respectively. In order to ensure means of comparison between each pile layout, the total pile areas are held constant, resulting in different pile widths. In Figure 3.3, the width is taken as $2\sqrt{2B^2}$ which maintains a total pile area of $4B^2$.

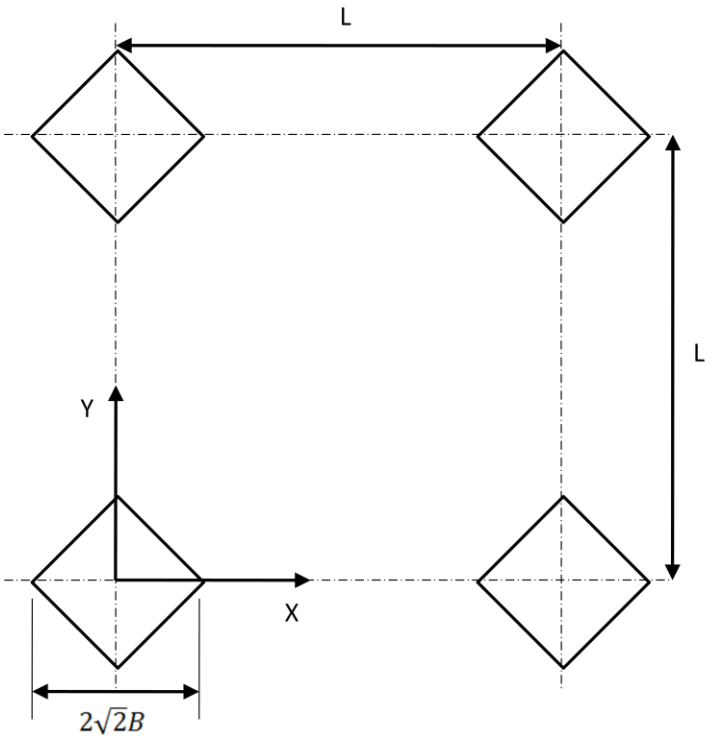

Figure 3.3 Unit Cell with Square Piles Oriented at 45°

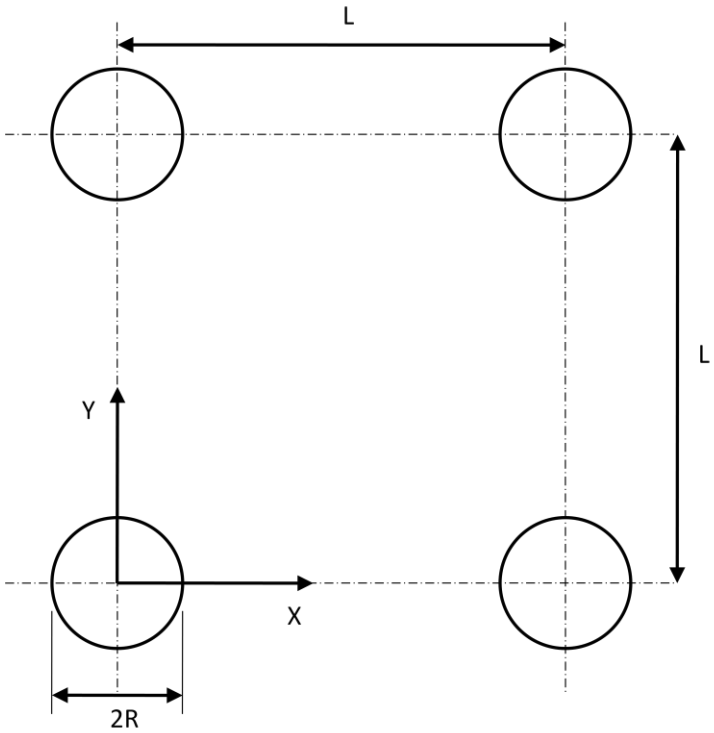

Figure 3.4 Unit Cell with Circular Piles

The unit cell with circular piles is also shown in Figure 3.4. In this representation, the width of the pile is 2R. Again, to ensure that each of the piles has equal area, a new term R is introduced to represent an equivalent pile radius. This variable is obtained by setting the areas of the square piles equal to that of the circular piles and solving for R in terms of B. The resulting value R is given by

$$R = \sqrt{\frac{4B^2}{\pi}} \tag{3.1}$$

where B = half square pile width

R = equivalent circular pile radius

3.5 Definition of Terms

An array of terms is established for the development of equations and dimensions for the geosynthetic composite system. It is important to note that dimensional variables are usually presented with capital letters and subscripts, while non-dimensional parameters are defined using lower-case letters. Figure 3.5 shows a typical elevation view of the system in Figure 3.2 through the piles, including parameters. As can be seen, the column width is 2B, while the center-to-center spacing of the columns is L. The distributed load acting on the soil is Qs, while the load acting over the columns is Qp. Spring constants Ks and Kp are used to define modulus values for the soft soil and the soil over the piles, respectively.

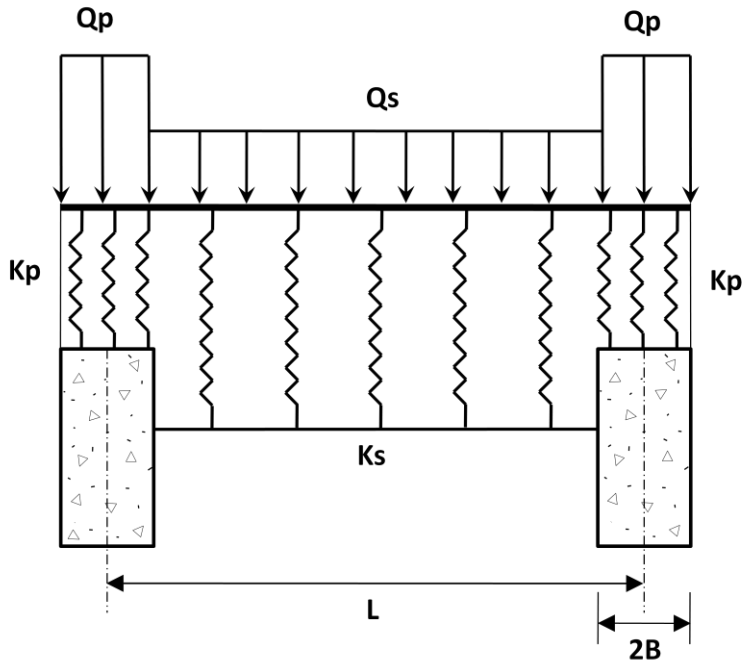

Figure 3.5 Elevation View of Composite System

The geosynthetic itself has an elastic modulus E, thickness t, and Poisson's ratio ν. Figure 3.6 shows a three-dimensional view of the geosynthetic modeled as a plate. Reference axes for the X, Y, Z coordinate system, and deflections U, V, and W in these coordinates, can also be seen in Figure 3.6. The W, U, V deflections are displayed in terms of i and j, which represent the horizontal and vertical locations on the unit cell. W[i,j] represents the dimensional vertical out-of-plane deflection of the plate, assumed positive if downward. Normal in-plane deflection is represented by U[i,j] and is positive in the X direction. Similarly, V[i,j] is the dimensional in-plane deflection, acting positive in the Y direction. Due to symmetry in the plate, the relationship U[i,j] = V[j,i] can be established.

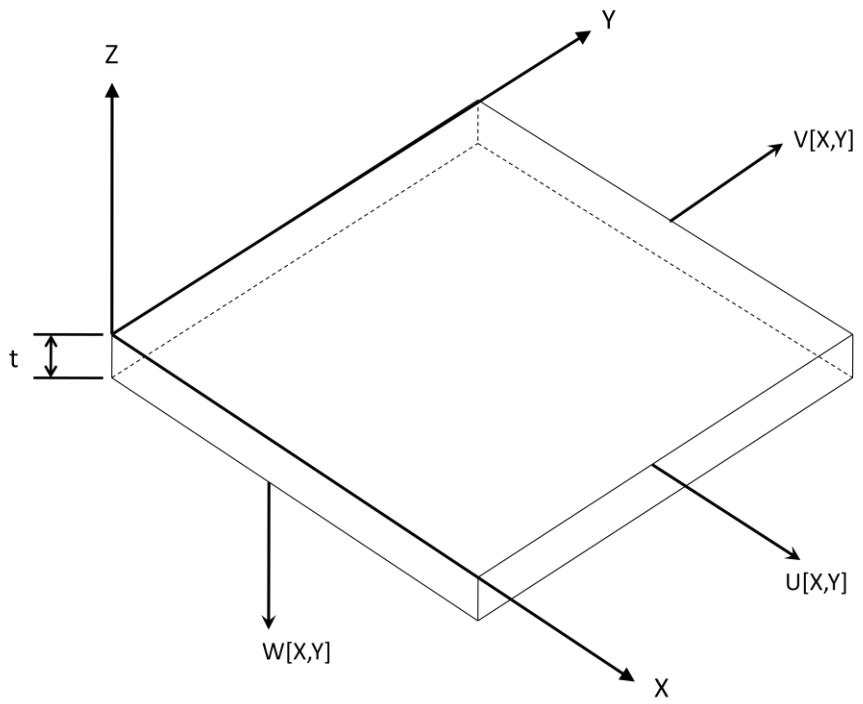

Figure 3.6 Three – Dimensional View of Geosynthetic with Coordinate Systems

Flexural rigidity of the plate is also used in the formulation of bending energy. The definition of this parameter (Szilard 1974) is

$$D = \frac{Et^3}{12(1-\nu^2)} \tag{3.2}$$

where E = elastic modulus of the plate

t = plate thickness

ν = Poisson's ratio of the plate

3.6 Dimensional Equations

3.6.1 Energy Equations

The total energy of the system includes energy expressions due to bending, membrane action, soil foundation, and vertical loading. Each of these components is from Timoshenko and Woinowsky-Krieger (1959) and is expressed in Equations 3.4 – 3.9 in dimensional form. The total energy of the system in Figure 3.2 is given by

$$E_T = E_{Qs} + E_{Qp} + E_{Ks} + E_{Kp} + E_M + E_B \tag{3.3}$$

where E_T = total energy of the system

E_{Qs} = energy due to vertical loading over the soft soil

E_{Qp} = energy due to vertical loading over the piles

E_{Ks} = energy due to the soft soil foundation

E_{Kp} = energy due to the pile foundation

E_M = energy due to membrane action within the plate

E_B = energy due to bending in the plate

$$E_{Ks} = \frac{1}{2} K_S \left[\int_0^L \int_0^L W^2 \, dXdY - 4 \int_0^B \int_0^B W^2 \, dXdY \right] \tag{3.4}$$

$$E_{Kp} = 4 \left[\frac{1}{2} K_P \int_0^B \int_0^B W^2 \, dXdY \right] \tag{3.5}$$

$$E_{Qs} = -Q_S \left[\int_0^L \int_0^L W \, dXdY - 4 \int_0^B \int_0^B W \, dXdY \right] \tag{3.6}$$

$$E_{Qp} = 4\left[-Q_P \int_0^B \int_0^B W\, dXdY\right] \tag{3.7}$$

$$E_B = \frac{D}{2}\int_0^L \int_0^L \left(\frac{\partial^2 W}{\partial X^2} + \frac{\partial^2 W}{\partial Y^2}\right)^2 dXdY \tag{3.8}$$

$$E_M = \frac{Et}{2(1-\nu^2)}\int_0^L \int_0^L [\left(\frac{\partial U}{\partial X} + \frac{1}{2}\left(\frac{\partial W}{\partial X}\right)^2\right)^2 + \left(\frac{\partial V}{\partial Y} + \frac{1}{2}\left(\frac{\partial W}{\partial Y}\right)^2\right)^2 + 2\nu\left(\frac{\partial U}{\partial X} + \frac{1}{2}\left(\frac{\partial W}{\partial X}\right)^2\right)\left(\frac{\partial V}{\partial Y} + \frac{1}{2}\left(\frac{\partial W}{\partial Y}\right)^2\right) + \frac{(1-\nu)}{2}\left(\frac{\partial U}{\partial Y} + \frac{\partial V}{\partial X} + \left(\frac{\partial W}{\partial X}\right)\left(\frac{\partial W}{\partial Y}\right)\right)^2]dXdY \tag{3.9}$$

3.6.2 Stress Resultants and Strain Equations

The large-deflection theory of plates includes effects due to bending and stretching, which must be accounted for in the equations relating stress resultants, strains, and displacements (Szilard 1974). Utilizing compatibility and the nonlinear terms due to stretching of the plate, expressions for stresses and strains may be derived. In terms of the dimensional deflections parallel to the X, Y, and Z axes, Szilard (1974) gives the stress resultants (forces per unit length) as

$$N_X = \frac{Et}{(1-\nu^2)}\left[\frac{\partial U}{\partial X} + \nu\frac{\partial V}{\partial Y} + \frac{1}{2}\left(\left(\frac{\partial W}{\partial X}\right)^2 + \nu\left(\frac{\partial W}{\partial Y}\right)^2\right)\right] \tag{3.10}$$

$$N_Y = \frac{Et}{(1-\nu^2)}\left[\nu\frac{\partial U}{\partial X} + \frac{\partial V}{\partial Y} + \frac{1}{2}\left(\nu\left(\frac{\partial W}{\partial X}\right)^2 + \left(\frac{\partial W}{\partial Y}\right)^2\right)\right] \tag{3.11}$$

$$N_{XY} = \frac{Et}{2(1+\nu)}\left[\frac{\partial U}{\partial Y} + \frac{\partial V}{\partial X} + \left(\frac{\partial W}{\partial X}\right)\left(\frac{\partial W}{\partial Y}\right)\right] \tag{3.12}$$

Nonlinear strains in a plate are also given by Szilard (1974) and Chia (1980). These expressions include components due to stretching of the mid-plane produced by large deflections due to bending (Ugural 1999). General mid-plane strain-displacement relations are expressed in the following equations, which assume that the material is linearly elastic:

$$\varepsilon_X = \frac{\partial U}{\partial X} + \frac{1}{2}\left(\frac{\partial W}{\partial X}\right)^2 \tag{3.13}$$

$$\varepsilon_Y = \frac{\partial V}{\partial Y} + \frac{1}{2}\left(\frac{\partial W}{\partial Y}\right)^2 \tag{3.14}$$

$$\varepsilon_{XY} = \frac{\partial U}{\partial X} + \frac{\partial V}{\partial Y} + \left(\frac{\partial W}{\partial X}\right)\left(\frac{\partial W}{\partial Y}\right) \tag{3.15}$$

Maximum and minimum stress and strains within a plate are given by:

$$N_{Min} = \frac{N_X + N_Y}{2} - \sqrt{\left(\frac{N_X - N_Y}{2}\right)^2 + {N_{XY}}^2} \tag{3.16}$$

$$N_{Max} = \frac{N_X + N_Y}{2} + \sqrt{\left(\frac{N_X - N_Y}{2}\right)^2 + {N_{XY}}^2} \tag{3.17}$$

$$\varepsilon_{Min} = \frac{\varepsilon_X + \varepsilon_Y}{2} - \sqrt{\left(\frac{\varepsilon_X - \varepsilon_Y}{2}\right)^2 + {\varepsilon_{XY}}^2} \tag{3.18}$$

$$\varepsilon_{Max} = \frac{\varepsilon_X + \varepsilon_Y}{2} + \sqrt{\left(\frac{\varepsilon_X - \varepsilon_Y}{2}\right)^2 + {\varepsilon_{XY}}^2} \tag{3.19}$$

These expressions are the vector sum of the stress or strain component in each direction at a particular location in the plate. Each term is a function of individual stress and strain components, which are dependent on the dimensional displacements.

3.7 Non – Dimensional Equations

3.7.1 Non - Dimensionalization

A non-dimensionalization was adopted to reduce the number of parameters and simplify the calculations performed in Mathematica 5.2. Deflections, lengths, soil stiffness, pile stiffness, load over the soil, load over the piles, energy expressions, stress resultants, and strains are all redefined based on the following non-dimensionalization scheme in Equations 3.20-3.36. Each of the new variables is non-dimensional with the exception of β, which has units of length in meters:

$$w = \frac{W}{\beta} \qquad u = \frac{UL}{\beta^2} \qquad v = \frac{VL}{\beta^2} \qquad \text{(3.20, 3.21, 3.22)}$$

$$x = \frac{X}{L} \qquad y = \frac{Y}{L} \qquad b = \frac{B}{L} \qquad \text{(3.23, 3.24, 3.25)}$$

$$q_p = \frac{Q_P}{Q_S} \qquad q_s = 1.0 \qquad \alpha = \frac{t^2}{24\beta^2} \qquad \text{(3.26, 3.27, 3.28)}$$

$$k_s = \frac{K_S\beta}{Q_S} \qquad k_p = \frac{K_P\beta}{Q_S} \qquad n_x = \frac{L^2}{Et\beta^2}N_X \qquad \text{(3.29, 3.30, 3.31)}$$

$$n_y = \frac{L^2}{Et\beta^2}N_Y \qquad n_{xy} = \frac{L^2}{Et\beta^2}N_{XY} \qquad \hat{E}_T = Q_S\beta L^2 E_T \qquad \text{(3.32, 3.33, 3.34)}$$

$$\beta = \left[\frac{Q_S L^4(1-\nu^2)}{Et}\right]^{1/3} \qquad \text{(3.35)}$$

3.7.2 Non – Dimensional Energy Equations

The non-dimensionalization discussed previously is used to reformulate the total energy equation shown in Equation 3.37. Each component of the total energy is non-dimensional and represents energy attributed to load over the soil, load over the piles, soil spring stiffness, pile spring stiffness, bending of the plate, and membrane action in the plate. Individual expressions for the non-dimensional energy are given as follows:

$$\hat{E}_T = \hat{E}_{Qs} + \hat{E}_{Qp} + \hat{E}_{Ks} + \hat{E}_{Kp} + \hat{E}_M + \hat{E}_B \tag{3.36}$$

Equations 3.38 – 3.43 represent the energy components attributed to each component of the total system.

$$\hat{E}_{Ks} = \frac{1}{2} k_s \left[\int_0^1 \int_0^1 w^2 \, dxdy - 4 \int_0^B \int_0^B w^2 \, dxdy \right] \tag{3.37}$$

$$\hat{E}_{Kp} = 4 \left[\frac{1}{2} k_p \int_0^b \int_0^b w^2 \, dxdy \right] \tag{3.38}$$

$$\hat{E}_{Qs} = -q_s \left[\int_0^1 \int_0^1 w \, dxdy - 4 \int_0^b \int_0^b w \, dxdy \right] \tag{3.39}$$

$$\hat{E}_{Qp} = 4 \left[-q_p \int_0^b \int_0^b w \, dxdy \right] \tag{3.40}$$

$$\hat{E}_B = \alpha \int_0^1 \int_0^1 \left(\frac{\partial^2 w}{\partial x^2} + \frac{\partial^2 w}{\partial y^2} \right)^2 dxdy \tag{3.41}$$

$$\hat{E}_M = \frac{1}{2}\int_0^1 \int_0^1 [\left(\frac{\partial u}{\partial x} + \frac{1}{2}\left(\frac{\partial w}{\partial x}\right)^2\right)^2 + \left(\frac{\partial v}{\partial y} + \frac{1}{2}\left(\frac{\partial w}{\partial y}\right)^2\right)^2 + 2\nu\left(\frac{\partial u}{\partial x} + \frac{1}{2}\left(\frac{\partial w}{\partial x}\right)^2\right)\left(\frac{\partial v}{\partial y} + \frac{1}{2}\left(\frac{\partial w}{\partial y}\right)^2\right) + \frac{(1-\nu)}{2}\left(\frac{\partial u}{\partial y} + \frac{\partial v}{\partial x} + \left(\frac{\partial w}{\partial x}\right)\left(\frac{\partial w}{\partial y}\right)\right)^2] dxdy \quad (3.42)$$

3.7.3 Non – Dimensional Stress Resultants and Strain Equations

In a similar procedure, stress resultants and strains can be expressed in terms of the deflections of the plate in the x, y, and z reference system. Equations 3.44-3.48 represent the non-dimensional stress resultants, while Equations 3.49-3.63 give the strains. Maximum and minimum stress and strain values are also attainable with the following equations:

$$n_x = \frac{1}{(1-\nu^2)}\left[\frac{\partial u}{\partial x} + \nu\frac{\partial v}{\partial y} + \frac{1}{2}\left(\left(\frac{\partial w}{\partial x}\right)^2 + \nu\left(\frac{\partial w}{\partial y}\right)^2\right)\right] \quad (3.43)$$

$$n_y = \frac{1}{(1-\nu^2)}\left[\nu\frac{\partial u}{\partial x} + \frac{\partial v}{\partial y} + \frac{1}{2}\left(\nu\left(\frac{\partial w}{\partial x}\right)^2 + \left(\frac{\partial w}{\partial y}\right)^2\right)\right] \quad (3.44)$$

$$n_{xy} = \frac{1}{2(1+\nu)}\left[\frac{\partial u}{\partial y} + \frac{\partial v}{\partial x} + \left(\frac{\partial w}{\partial x}\right)\left(\frac{\partial w}{\partial y}\right)\right] \quad (3.45)$$

$$n_{min} = \frac{n_x+n_y}{2} - \sqrt{\left(\frac{n_x-n_y}{2}\right)^2 + {n_{xy}}^2} \quad (3.46)$$

$$n_{max} = \frac{n_x+n_y}{2} + \sqrt{\left(\frac{n_x-n_y}{2}\right)^2 + {n_{xy}}^2} \quad (3.47)$$

$$\varepsilon_x = \frac{\partial u}{\partial x} + \frac{1}{2}\left(\frac{\partial w}{\partial x}\right)^2 \tag{3.48}$$

$$\varepsilon_y = \frac{\partial v}{\partial y} + \frac{1}{2}\left(\frac{\partial w}{\partial y}\right)^2 \tag{3.49}$$

$$\varepsilon_{xy} = \frac{\partial u}{\partial x} + \frac{\partial v}{\partial y} + \left(\frac{\partial w}{\partial x}\right)\left(\frac{\partial w}{\partial y}\right) \tag{3.50}$$

$$\varepsilon_{min} = \frac{\varepsilon_x + \varepsilon_y}{2} - \sqrt{\left(\frac{\varepsilon_x - \varepsilon_y}{2}\right)^2 + {\varepsilon_{xy}}^2} \tag{3.51}$$

$$\varepsilon_{max} = \frac{\varepsilon_x + \varepsilon_y}{2} + \sqrt{\left(\frac{\varepsilon_x - \varepsilon_y}{2}\right)^2 + {\varepsilon_{xy}}^2} \tag{3.52}$$

3.8 Finite Difference Equations

Central finite difference expressions were used to represent the partial derivatives used in the energy equations. These equations are readily available in any number of numerical analysis or plate theory texts and can be visually represented as in Figure 3.7 for the deflection W. In general, there are three types of finite differences: central, forward, and backward. Central finite differences are deemed the most accurate due to their lower first error terms (Szilard 1974). Central differences are also more convenient in eliminating fictitious nodal points outside of the discretized mesh. As can be seen in the difference equations, the derivatives involve relative displacements at one node prior to and one node after the location in question. Forward and backward differences, however, involve two points outside of the grid for this order of derivatives. Expressions for w, u, and v derivatives in terms of the proposed formulation are displayed in Equations 3.54 – 3.62, where subscripts x and y denote partial derivatives.

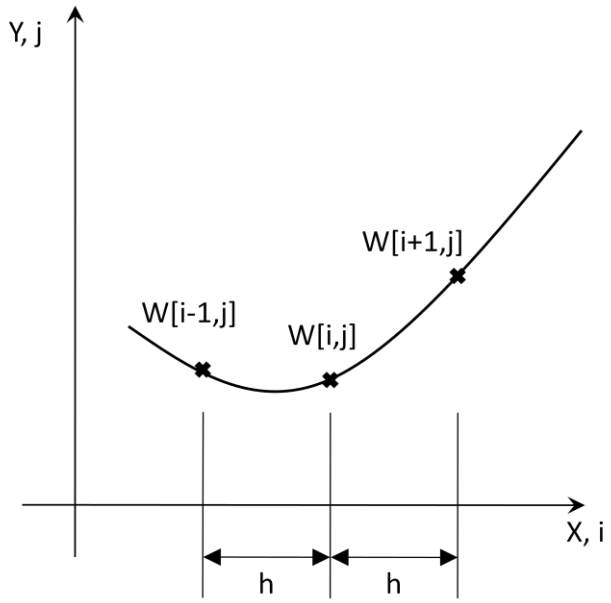

Figure 3.7 Visual Representation of Finite Differences

$$w_x[i,j] = \frac{1}{2h} * (w[i+1,j] - w[i-1,j]) \tag{3.53}$$

$$w_y[i,j] = \frac{1}{2h} * (w[i,j+1] - w[i,j-1]) \tag{3.54}$$

$$w_{xx}[i,j] = \frac{1}{h^2} * (w[i+1,j] - 2w[i,j] + w[i-1,j]) \tag{3.55}$$

$$w_{yy}[i,j] = \frac{1}{h^2} * (w[i,j+1] - 2w[i,j] + w[i,j-1]) \tag{3.56}$$

$$w_{xy}[i,j] = \frac{1}{4h^2} * (w[i+1,j+1] - w[i+1,j-1] - w[i-1,j+1] + w[i-1,j-1]) \tag{3.57}$$

$$u_x[i,j] = \frac{1}{2h} * (u[i+1,j] - u[i-1,j]) \quad (3.58)$$

$$u_y[i,j] = \frac{1}{2h} * (u[i,j+1] - u[i,j-1]) \quad (3.59)$$

$$v_x[i,j] = \frac{1}{2h} * (v[i+1,j] - v[i-1,j]) \quad (3.60)$$

$$v_y[i,j] = \frac{1}{2h} * (v[i,j+1] - v[i,j-1]) \quad (3.61)$$

Chapter 4

Model Implementation

4.1 Introduction

The geosynthetic model developed, based on the equations and assumptions of Chapter 3, was programmed in Mathematica Version 5.2. A variety of techniques was utilized to create the computer program and will be discussed in this chapter. Once the program was formulated, a verification study was performed to ensure its accuracy. Two examples from the published literature were analyzed using similar procedures and assumptions to those used in the geosynthetic model. Also of importance is convergence of the finite differences, in which a suitable number of grid divisions is required. The requisite number of divisions was determined based on consecutive analyses of a base geosynthetic model in Mathematica.

4.2 Program Development

4.2.1 Utilization of Symmetry

Symmetry within the unit cell allowed for simplifications in modeling and most importantly reduced the total number of unknowns. In the analysis of plates, symmetry is often utilized when performing numerical and approximate plate analyses (Szilard 1974). Only a one-eighth portion of the total unit cell was necessary to capture the full composite system.

The method of symmetry adopted is illustrated in Figures 4.1 and 4.2. The one-eighth portion along the left half of the bottom edge in Figure 4.2 was considered. Once the analysis was performed, the results were then unfurled in a similar manner as shown in Figure 4.1, yielding the solution over the entire unit cell.

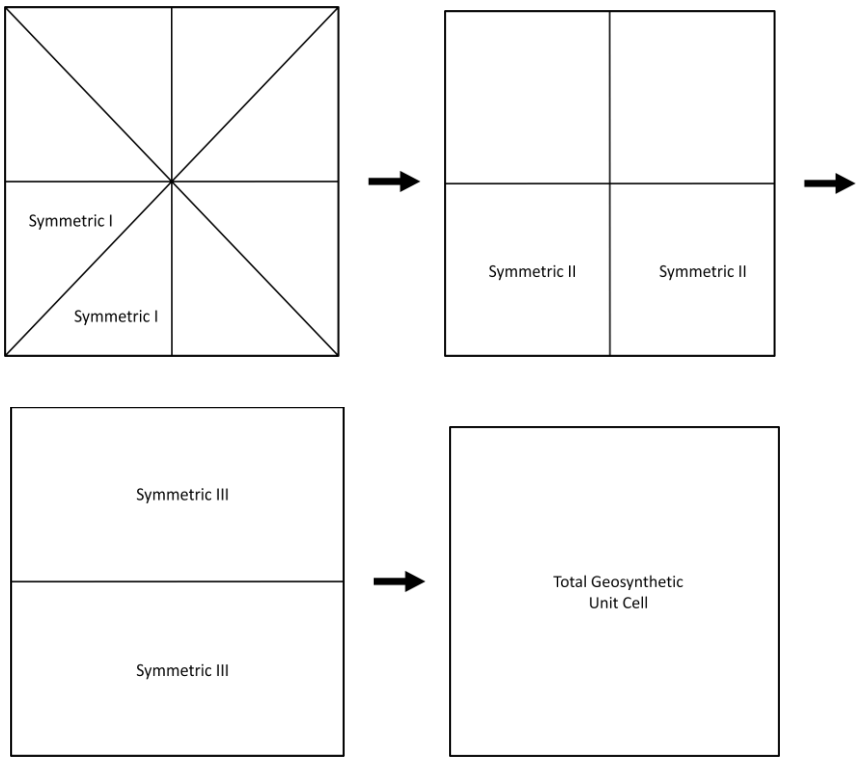

Figure 4.1 Progression of Symmetry in the Unit Cell

A finite difference mesh was applied over the one-eighth portion of the unit cell with interval lengths h. The number of divisions is referenced by the variable n and is the same for the vertical and horizontal directions on the plate. The mesh discretization is shown in Figure 4.2, which illustrates symmetry as well as the finite difference intervals. Relative location of a point anywhere on the grid is described by the coordinates (i,j) representing the horizontal and vertical positions, respectively.

The non-dimensional length and width of the plate are taken to be 1.0, which also results in an area equal to unity. The finite difference interval h therefore can be described by Equation 4.1 in which n is the total number of divisions over the bottom edge of the one-eighth unit cell:

$$h = \frac{1}{2n} \tag{4.1}$$

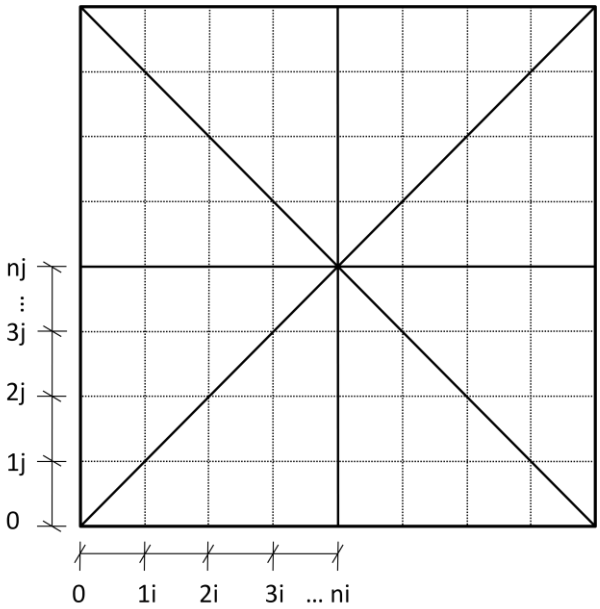

Figure 4.2 Finite Difference Discretization on a One-Eighth Symmetrical Section

4.2.2 Boundary Conditions

Boundary conditions were necessary to represent the behavior of the unit cell and its symmetrical properties. These conditions were programmed in Mathematica with the aid of "do loops". For the total unit cell, the plate was assumed to have no rotation about each edge and no normal in-plane deflection along each edge. These kinematically admissible conditions are shown in dimensional form in Equations 4.2 and 4.3:

$$X = 0 \ldots L: \qquad \frac{\partial W}{\partial X} = 0 \qquad U = 0 \tag{4.2}$$

$$Y = 0 \ldots L: \qquad \frac{\partial W}{\partial Y} = 0 \qquad V = 0 \tag{4.3}$$

As discussed previously, the actual Mathematica program involves the analysis of a non-dimensional one-eighth portion of the unit cell. This technique required additional boundary conditions for each edge of the reduced plate. These conditions are as follows, with Equations 4.4 – 4.19 applied along an edge and Equations 4.20 – 4.21 applied over the entire unit cell:

Non-Dimensional Boundary Conditions in u

$j = 0 - n$: $u[n, j] = 0$ (4.4)

$j = 0 - n$: $u[0, j] = 0$ (4.5)

$i = 0 - n$: $u[i, n + 1] = u[i, n - 1]$ (4.6)

$i = 0 - n$: $u[i, -1] = u[i, 1]$ (4.7)

$j = 0 - n$: $u[-1, j] = -u[1, j]$ (4.8)

$j = 0 - n$: $u[n + 1, j] = -u[n - 1, j]$ (4.9)

Non-Dimensional Boundary Conditions in v

$i = 0 - n$: $v[i, n] = 0$ (4.10)

$i = 0 - n$: $v[i, 0] = 0$ (4.11)

$i = 0 - n$: $v[i, n + 1] = -v[i, n - 1]$ (4.12)

$i = 0 - n$: $v[i, -1] = -v[i, 1]$ (4.13)

$j = 0 - n$: $v[-1, j] = v[1, j]$ (4.14)

$j = 0 - n$: $v[n + 1, j] = v[n - 1, j]$ (4.15)

Non-Dimensional Boundary Conditions in w

$i = 0 - n$: $w[i, n + 1] = w[i, n - 1]$ (4.16)

$i = 0 - n$: $w[i, -1] = w[i, 1]$ (4.17)

$j = 0 - n$: $w[-1, j] = w[1, j]$ (4.18)

$j = 0 - n$: $w[n + 1, j] = w[n - 1, j]$ (4.19)

Non-Dimensional Boundary Conditions over Entire Plate

$$i,j = 0 - 2n: \qquad w[i,j] = w[j,i] \tag{4.20}$$

$$i,j = 0 - 2n: \qquad u[i,j] = v[j,i] \tag{4.21}$$

4.2.3 Solution Technique

The unknown deflections at each nodal point in the w, u, and v directions are computed using the principle of minimum potential energy with the aid of finite differences. Szilard (1974) states that a structure is in a stable equilibrium state when the potential energy of the system has a relative (local) minimum. The total energy of the system is determined here by summing the individual energy components associated with each nodal point on the discretized mesh. This procedure is accomplished through Equation 4.22 by evaluating the energy expressions at each node in terms of bending, membrane stretching, vertical load, and support stiffness, and multiplying by a differential area:

$$E_T[i,j] = \sum_{i=0}^{n} \sum_{j=0}^{i} \left(E_B[i,j] + E_M[i,j] + E_Q[i,j] + E_K[i,j]\right) dxdy \tag{4.22}$$

$$dxdy \approx h^2 \tag{4.23}$$

A tributary area approach was adopted to calculate the energy acting at each node on the finite difference grid. For sufficiently small intervals, which is the case for large values of n, the quantity dxdy can be approximated by Equation 4.23. This quantity is modified along the edges of the one-eighth unit cell area where the differential area is less than the total dxdy. A unique differential area was applied to the nodes along the unit cell edges, while the entire dxdy was applied to the remaining points.

Once the total energy over the unit cell was established, the principle of minimum potential energy was applied. This task is generally accomplished by taking the partial derivative of the

total energy with respect to each unknown, setting the expression equal to zero, and solving for each of the unknowns. Another acceptable method of applying the theorem is to minimize the total energy expression with respect to each of the variables. In Mathematica, this is handled by several built-in minimization functions. Such operators include FindMinimum, NMinimize, and Minimize. For this analysis, the total energy expression was minimized with respect to the non-dimensional node deflections.

FindMinimum was chosen to carry out the analysis, due to its ability to accept initial-guess values as well as a range of values for each variable in which to search for a minimum. Presenting Mathematica with a search range greatly increased the computational speed in which a stable local minimum was found. Several other features of FindMinimum were applied, including the AccuracyGoal option and MaxIterations limit. Throughout the analysis, an AccuracyGoal of seven was selected, to yield results accurate to seven significant figures. Also, the MaxIterations constraint was set to 100,000 total iterations in order to prevent Mathematica from encountering convergence issues.

4.3 Results

Results were obtained from the output of the FindMinimum operation on the system total energy in Mathematica. The solution to the energy minimization contains the non-dimensional deflections at each nodal point in the one-eighth unit cell in the u, v, and w directions. Once the non-dimensional deflections are known, they are transformed into dimensional form using the scheme presented in Chapter 3. With dimensional deflections at each node point established, stress resultants and strains are calculated using Equations 3.15-3.19. Two- and three-dimensional plots were also created to visually display the results of the analysis. A Mathematica notebook containing all applicable equations and types of analysis is presented in Appendix A for the base geosynthetic case containing each pile orientation.

4.4 Verification Studies

Verification studies were performed in Mathematica 5.2 with a similar energy-based approach utilizing central finite differences. The examples are similar in formulation and application as those of the geosynthetic modeling. Two basic examples from plate theory in the literature were used to validate the proposed model.

4.4.1 First Example

The first example problem analyzed is from Ugural (1999) and consists of a clamped square plate under uniform vertical pressure. The boundary conditions are such that no rotations or vertical deflections are allowed at the plate edges, as illustrated by Equations 4.24-4.25:

$$X = 0, L: \qquad \frac{\partial W}{\partial X} = 0 \qquad W = 0 \tag{4.24}$$

$$Y = 0, L: \qquad \frac{\partial W}{\partial Y} = 0 \qquad W = 0 \tag{4.25}$$

A finite difference mesh was established for the plate using 100 total vertical and horizontal divisions, i.e., with n equal to 100. The finite difference equations from Equations 3.53-3.61 are valid here and were used to generate the total energy in terms of the relative deflections at each nodal point. Boundary conditions were also required to eliminate fictitious finite difference grid points, and are:

$$X = 0 - L: \qquad w[i, n+1] = w[i, n-1] \tag{4.26}$$

$$X = 0 - L: \qquad w[i, -1] = w[i, 1] \tag{4.27}$$

$$Y = 0 - L: \qquad w[-1, j] = w[1, j] \tag{4.28}$$

$$\text{Y} = 0 - L: \qquad w[n+1, j] = w[n-1, j] \tag{4.29}$$

The parameters used in the example problem were chosen based on similar values of the geosynthetic model. Also, Equation 3.2 was used to calculate the flexural rigidity of the plate based on the following:

E = 100.0 MPa

t = 1.0 mm

ν = 0.25

Q = 1.0 Pa

L = 1.0 m

Due to the simplicity of the example and subsequent computer programming, the entire plate was analyzed. The energy of the system is formulated by Equations 4.31 and 4.32. In this example, only energy due to bending and uniform load is considered, neglecting any effect due to stretching. The total energy of the system therefore is given by

$$E_T = E_B + E_Q \tag{4.30}$$

$$E_Q = -Q \int_0^L \int_0^L W \, dXdY \tag{4.31}$$

$$E_B = \frac{D}{2} \int_0^L \int_0^L \left(\frac{\partial^2 W}{\partial X^2} + \frac{\partial^2 W}{\partial Y^2} \right)^2 dXdY \tag{4.32}$$

The maximum deflection of the plate occurs at the center, and the analytical solution is given by Ugural (1999) as

$$W_{Max} = 0.00126\frac{Qa^4}{D} \tag{4.33}$$

where Wmax = maximum vertical deflection

Q = uniform pressure

a = length and width of the plate

D = flexural rigidity (Equation 3.2)

The maximum vertical deflection obtained by the finite difference program was 0.14251. This value corresponds well to the analytical deflection calculated by Equation 4.33, which was found to be 0.14175. The total error in the finite difference analysis is therefore 0.53%, indicating that this modeling technique is valid for plate analysis. The Mathematica notebook used for this first example can be found in Appendix B.

4.4.2 Second Example

The second example analyzed is similar to the previous model in which a clamped square plate is subjected to uniform vertical pressure. This model, however, includes the effects due to stretching of the plate. Equation 3.9 is added to the total energy expression shown in Equation 4.30 to formulate the total energy of the system, which accounts for the uniform load as well as bending and stretching of the plate. Equation 4.34 presents the total energy of the system used in the second example:

$$E_T = E_B + E_Q + E_M \tag{4.34}$$

Boundary conditions for this example are the same as in the first example; however, additional requirements are necessary for the dimensional in-plane deflections, U and V. Zero deflections and normal first derivatives were imposed for the in-plane displacements along the clamped edges of the plate. These conditions as well as the expressions needed to eliminate the fictitious finite difference nodes are as follows:

$$X = 0, L: \qquad \frac{\partial U}{\partial X} = \frac{\partial V}{\partial Y} = 0 \qquad U = V = 0 \tag{4.35}$$

$$Y = 0, L: \qquad \frac{\partial U}{\partial Y} = \frac{\partial V}{\partial X} = 0 \qquad U = V = 0 \tag{4.36}$$

The finite difference conditions were obtained by setting the derivates along each edge equal to zero and solving for the fictitious grid points. Symmetry was also applicable in this example and is similar to that used in the geosynthetic program:

$$X = 0 - L: \qquad u[i, n+1] = u[i, n-1] \tag{4.37}$$

$$X = 0 - L: \qquad u[i, -1] = u[i, 1] \tag{4.38}$$

$$Y = 0 - L: \qquad u[-1, j] = -u[1, j] \tag{4.39}$$

$$\text{Y} = 0 - L: \qquad u[n+1, j] = -u[n-1, j] \tag{4.40}$$

$$X = 0 - L: \qquad v[i, n+1] = -v[i, n-1] \tag{4.41}$$

$$X = 0 - L: \qquad v[i, -1] = -v[i, 1] \tag{4.42}$$

$$Y = 0 - L: \qquad v[-1, j] = v[1, j] \tag{4.43}$$

$$\text{Y} = 0 - L: \qquad v[n+1, j] = v[n-1, j] \tag{4.44}$$

The parameters implemented in this example are based on an example problem presented in a report by Levy (1942). In the report, a square clamped plate is investigated with a range of values for the following ratio:

$$\frac{p_o a^4}{E h^4} \text{ with Poisson's ratio } \nu = 0.316$$

where, p_o = uniform vertical pressure

E = modulus of elasticity

a = plate width and length

h = plate thickness

Levy states that for the ratio $\frac{p_o a^4}{E h^4} = 95.0$, the maximum vertical deflection is given by

$$\frac{W_{Max}}{h} = 0.912 \tag{4.45}$$

Representative quantities for the parameters used in the finite difference program were assumed such that the ratio $\frac{p_o a^4}{E h^4} = 95.0$ was maintained. The values were selected as follows:

a = 1.0 m

E = 100.0 MPa

h = 0.01 m

po = 95.0 Pa

The results obtained from the finite difference program are in agreement with Levy's solution for the maximum vertical deflection. The maximum vertical deflection by finite difference analysis was found to be 0.009043 meters, while the analytical solution furnishes 0.00912 meters. This yields only an error of 0.84%, thereby further validating the finite difference based energy method as a reliable means of analysis for large plate deflections. A printout of the Mathematica notebook used for the second example is provided in Appendix B.

4.5 Finite Difference Convergence Study

Errors arise in finite difference analysis when the interval lengths of the discretized mesh are large. Soare (1967) discusses possible errors in the method and concludes that as the interval Δx tends to zero, the approximate values obtained approach an exact solution. It is also shown that the degree of approximation depends greatly on the boundary conditions and form of the problem. In general, there exist several notable variations in finite difference solutions, which include increasing or decreasing monotonic variation, damped oscillatory variation, non-monotonic variation over large intervals, and monotonic variation oscillating between two successive steps (Soare 1967). The last case, in which monotonic variation occurs between two steps, is the dominant source of approximation error apparent in this model. In order to eliminate these errors and to provide a smooth approximation to the overall deflected shape, a convergence study was performed on the base geosynthetic model.

The model analyzed in this section involves a unit cell with square piles at zero rotation to the horizontal. System parameters were selected and the non-dimensionalization scheme presented in Chapter 3 was used. The following dimensional values were used in the convergence study:

$B = 0.6$ m

$L = 3.0$ m

$E = 500$ MPa

$\nu = 0$

$t = 1.5$ mm

Ks = 160 kN/m^3

Kp = 29.2 MN/m^3

Qp = 146 kPa

Qs = 30.6 kPa

Once the model was established, several cases were run, varying the number of grid divisions, n, along the lower edge of the one-eight portion of the unit cell. Values for n were selected as 5, 10, 20, 50, and 100 in order to determine the most efficient number of divisions required to eliminate finite difference approximation errors. Figures 4.3-4.7 reflect each of the five test cases run, showing the vertical edge deflection of the geosynthetic. It was determined that 100 nodal divisions along an edge of the one-eighth portion were sufficient to yield a smooth deflected shape while remaining within the performance capacity of a standard desktop computer. The Mathematica notebook used in the convergence study is presented in Appendix C.

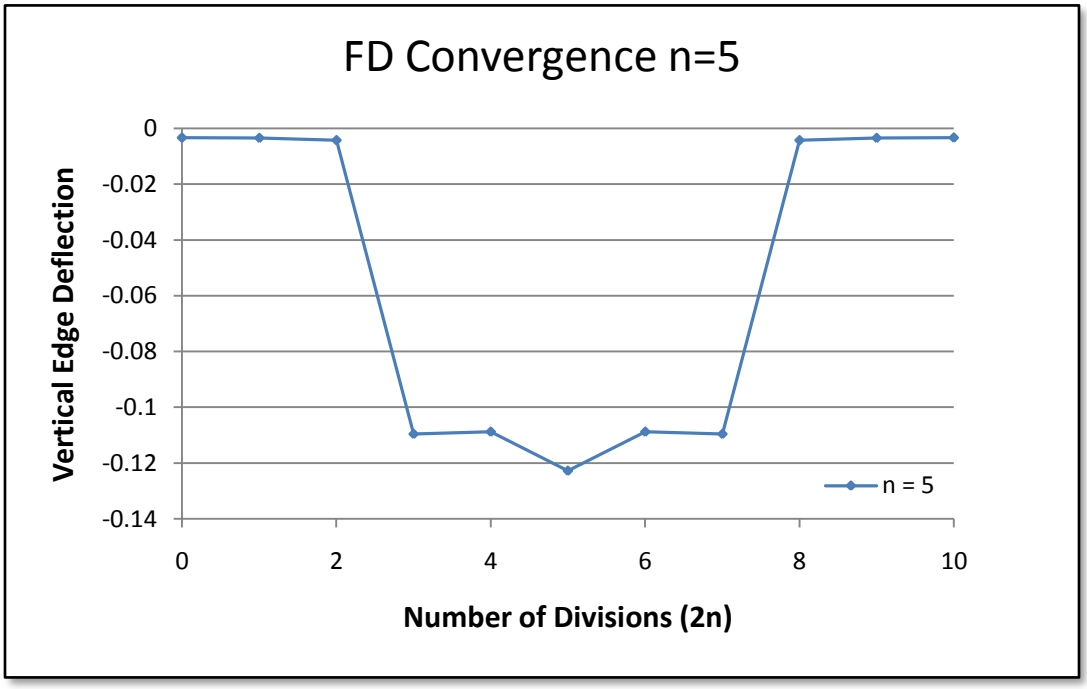

Figure 4.3 Convergence Study Test Case 1

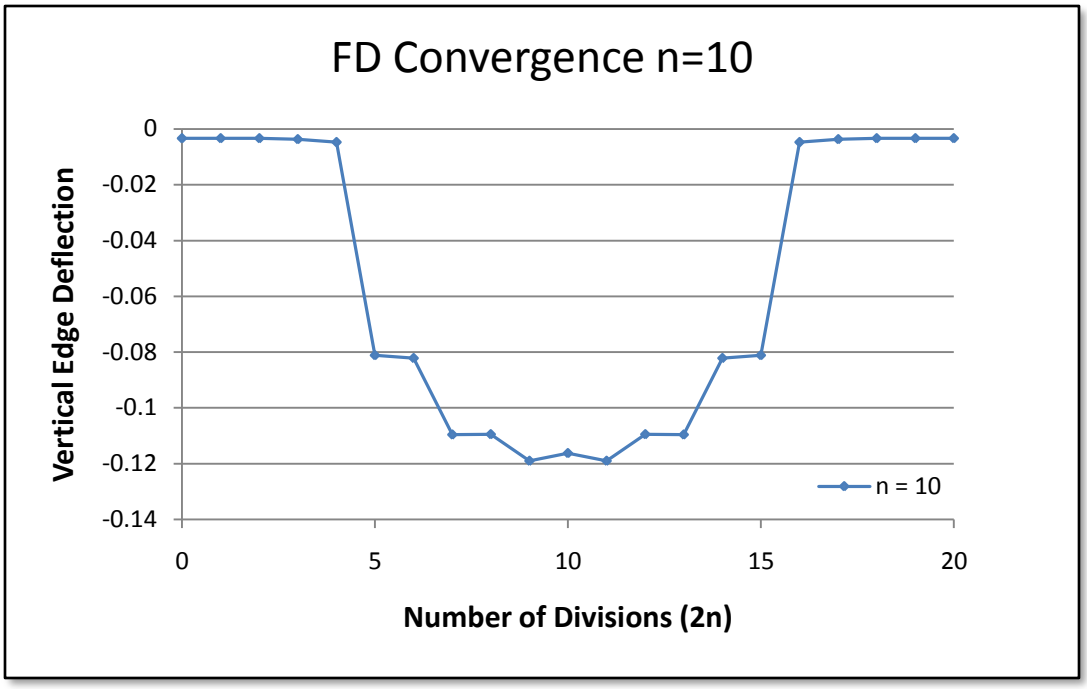

Figure 4.4 Convergence Study Test Case 2

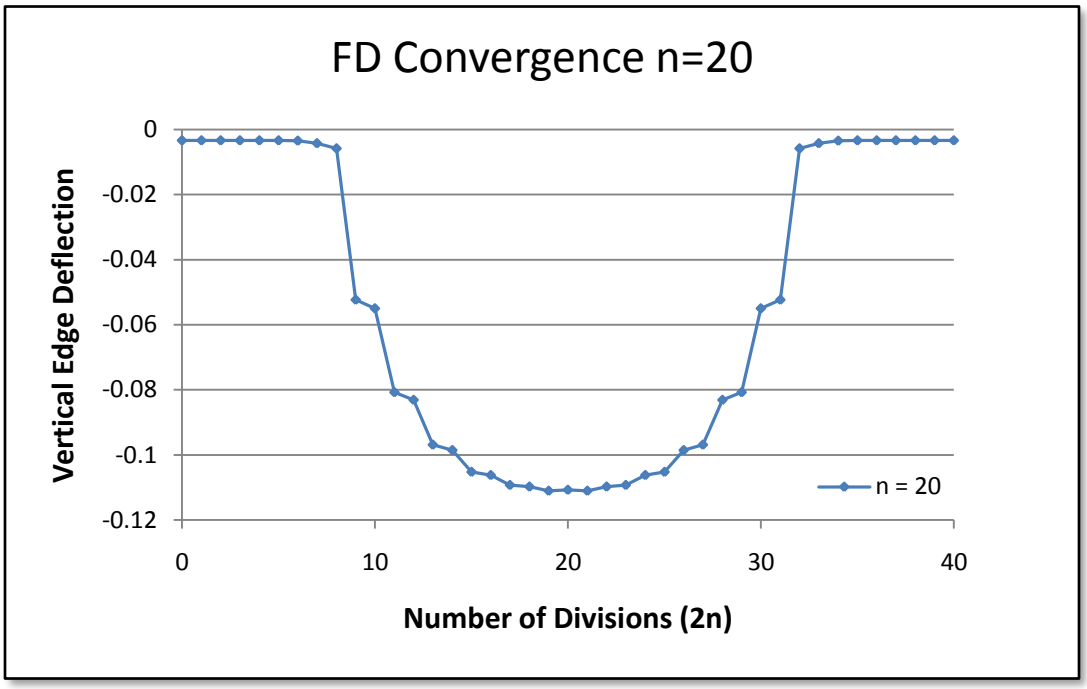

Figure 4.5 Convergence Study Test Case 3

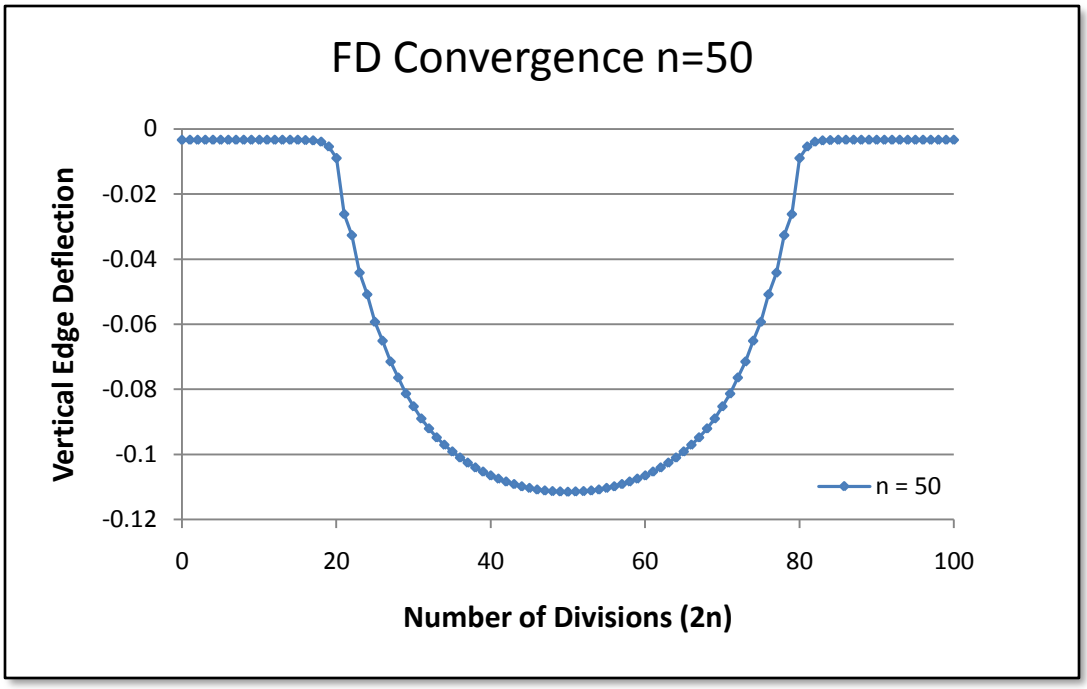

Figure 4.6 Convergence Study Test Case 4

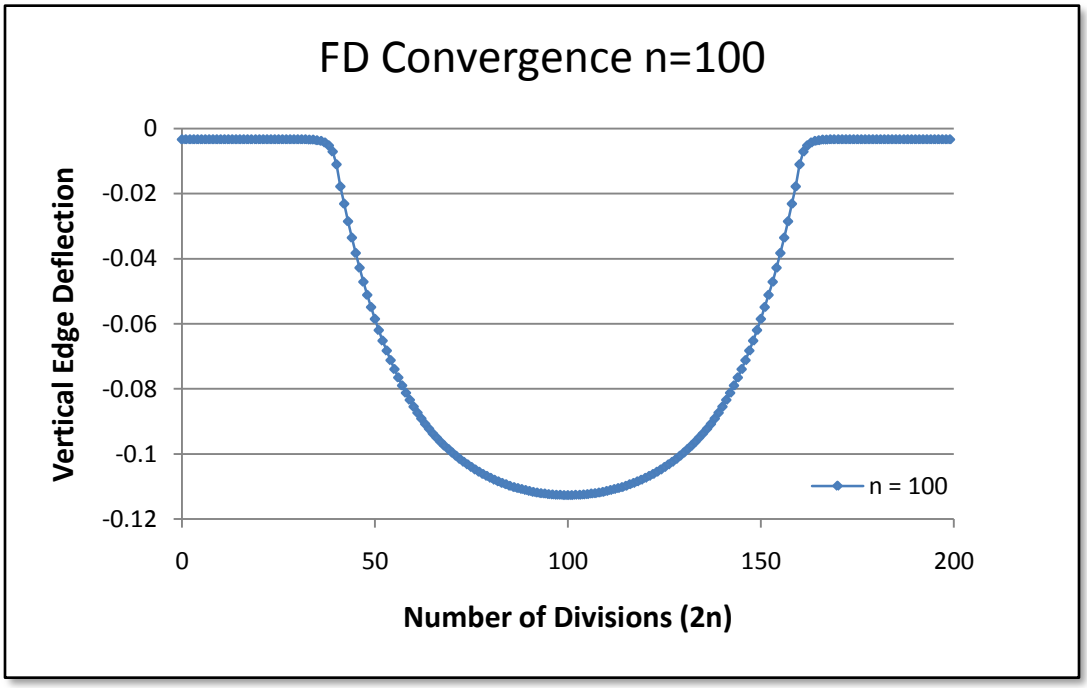

Figure 4.7 Convergence Study Test Case 5

Chapter 5

Pile Orientation Study

5.1 Introduction

Once the Mathematica model was developed and validated, each of the three pile orientation types were analyzed. As discussed previously, these orientations involve square piles, square piles rotated 45° to the horizontal, and circular piles. Separate Mathematica notebooks were created for each pile type and run individually with a standard set of parameters. The notebooks for each pile orientation are combined into a single Mathematica file for presentation in Appendix A. The solutions returned from the subsequent analyses yielded non-dimensional vertical and in-plane deflections. Results over the one-eighth unit cell were extrapolated by symmetry for the entire unit cell area. These results were then placed in dimensional form and used to calculate strains and stress resultants within the geosynthetic. Two- and three-dimensional plots were also generated to visually represent the pertinent findings.

Results from the analysis of each pile orientation type are provided and discussed in detail in the following sections. Included in these results are maximum and minimum values of vertical and in-plane deflections, strains, and stress resultants. Also, the differential settlement of the geosynthetic can be determined by subtracting the vertical deflection over the corner of the pile from the maximum vertical deflection at the center or edge.

Plots of the results were generated with the aid of Mathematica and Excel. Three-dimensional plots of individual dimensional deflections are shown over the entire unit cell by utilization of symmetry. An overall deflected shape of the geosynthetic was also created by including the W, U, and V deflections in one three-dimensional plot. The points used to construct these graphs were obtained by adding the individual deflections at each node to its original position. It is important to note the similarity between the total deflected shape and the plot of vertical deflections only, due to the relatively small magnitude of in-plane dimensional deflections. Therefore it can be deduced that in-plane deflections contribute little to the overall deflected shape of the geosynthetic.

Contour plots are utilized to emphasize the change in magnitude of deflections, strains, and stresses over the unit cell. In these graphs, darker regions denote larger values, while lighter regions represent smaller values. Two-dimensional plots were also created in Excel to express values along the center and edge of the unit cell as well as along the pile edge to emphasize their differences.

5.2 True Membrane Analysis

The analysis of plates is generally divided into four distinct categories: stiff plates, flexible plates, membranes, and thick plates (Szilard 1974). In this research, the geosynthetic was assumed to act as a thin flexible plate. In general, flexible plates behave both as a stiff plate and thin membrane. Applied external loading is carried by a combination of internal moments, transverse and in-plane shear forces, and normal in-plane forces. Alternatively, membranes behave as thin plates with no flexural rigidity and carry lateral loads by axial and central shear forces (Szilard 1974).

True membrane analysis is characterized by the inability of the material to carry compression stresses. Since the membrane can carry no compression, it may be approximated as a network of stressed cables due to their small thickness and inability to resist moment (Szilard 1974). Initially the bending stiffness of the geosynthetic in the finite difference model was neglected, allowing it to be modeled as a membrane. It was found through initial Mathematica models, however, that regions of compressive stresses did exist within the geosynthetic. This violates the requirement of true membrane analysis in which the material is unable to resist compression. In order to accurately account for the regions of compression, the bending resistance of the geosynthetic was included and the geosynthetic was modeled as a thin flexible plate.

Both bending and membrane resistance were included in the total energy formulation of the finite difference program. Although both energy components were included, the contribution due to membrane behavior greatly exceeds that in bending. This is clearly visible when comparing the non-dimensional parameters α and β. For the standard parameter set, β was 1.374 while α was 4.9683×10^{-8}. This suggests that the contribution of bending stiffness to the total energy is several orders of magnitude less than that of the membrane stiffness. Despite this

significant difference, the bending stiffness must be included in the total energy since it was found that regions of compressive stresses exist within the geosynthetic.

An important and highly debated topic in membrane analysis is the formation and behavior of wrinkles in the material. As discussed, membranes inherently cannot sustain compressive stresses and therefore must react accordingly. Compressive stresses are resisted in true membranes by out-of-plane displacements in the form of wrinkles (Ruggiero and Inman 2006). An interesting finding in this research was the formation of wrinkles around the edges of the pile support in each of the three orientations. Figures 5.17, 5.34, and 5.51 visually show these regions of negative minimum stresses enveloping the four piles. Also apparent is the formation of wrinkles in the deflected shapes of the geosynthetic visible in Figures 5.1, 5.18, and 5.35. The wrinkled behavior of membranes under compressive stress therefore is present and a potential concern in geosynthetic reinforcement.

5.3 Standard Case

A standard parameter case was selected and used in the analysis of each pile orientation type. The parameters chosen were based on work currently being conducted on the subject by fellow Master's student Kyle Halvordson. In his research, the geosynthetic is modeled as a cable net and analyzed according to equivalent parameters. A similar parameter set was therefore selected to provide a means of comparison and further validation of the current modeling technique. The following dimensional parameters were used for the standard case:

$B = 0.6$ m

$L = 3.0$ m

$E = 500$ MPa

$\nu = 0$

$t = 1.5$ mm

$Ks = 160$ kN/m^3

$Kp = 29.2$ MN/m^3

Qp = 146 kPa

Qs = 30.6 kPa

Applying the non-dimensionalization described in Chapter 3 the following dimensionless parameters were used in the analysis:

b = 0.20

r = 0.2257

kp = 1,440.27

ks = 7.892

qp = 4.867

qs = 1.0

$\beta = 1.480$

$\alpha = 4.282 \times 10^{-8}$

5.4 Square Piles

5.4.1 Deflections

Deflection results are presented in Figures 5.1-5.8 and Table 5.1.

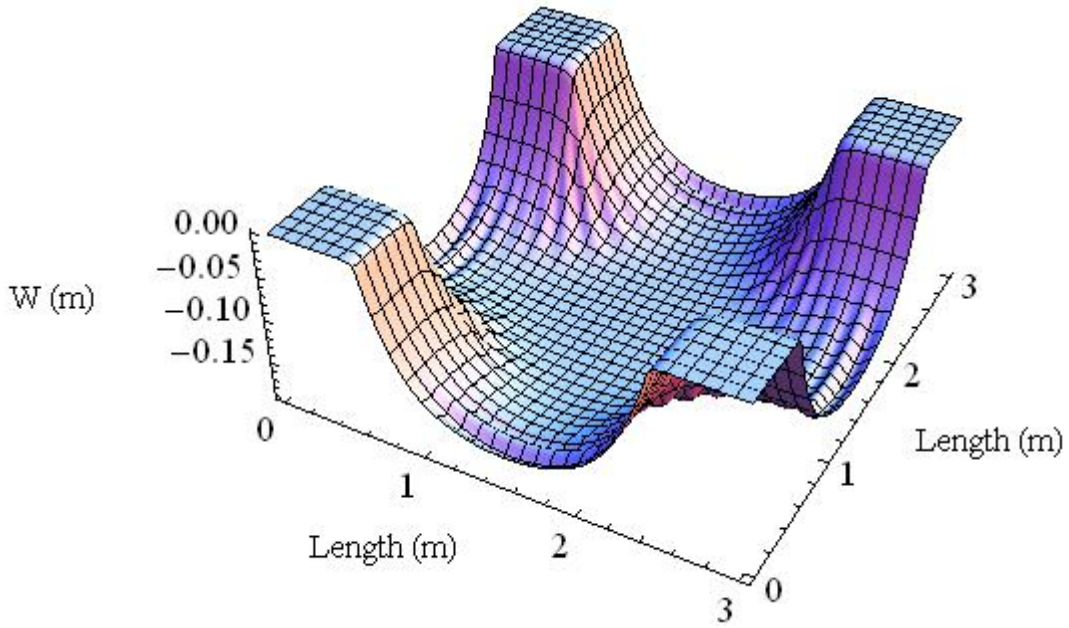

Figure 5.1 Three – Dimensional Plot of W Deflection

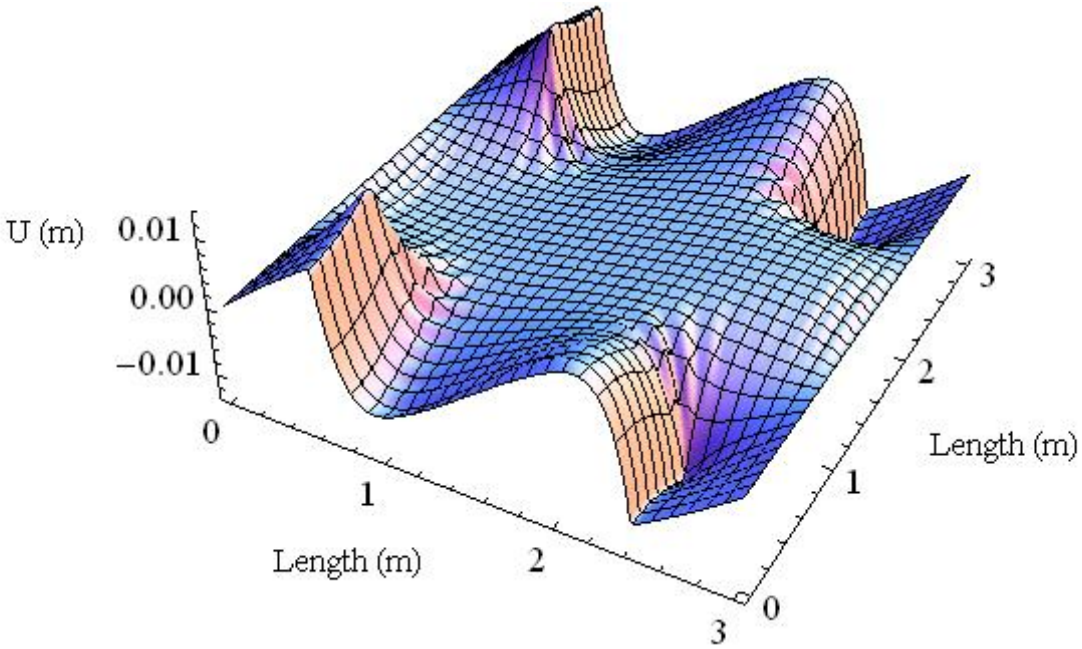

Figure 5.2 Three – Dimensional Plot of U Deflection

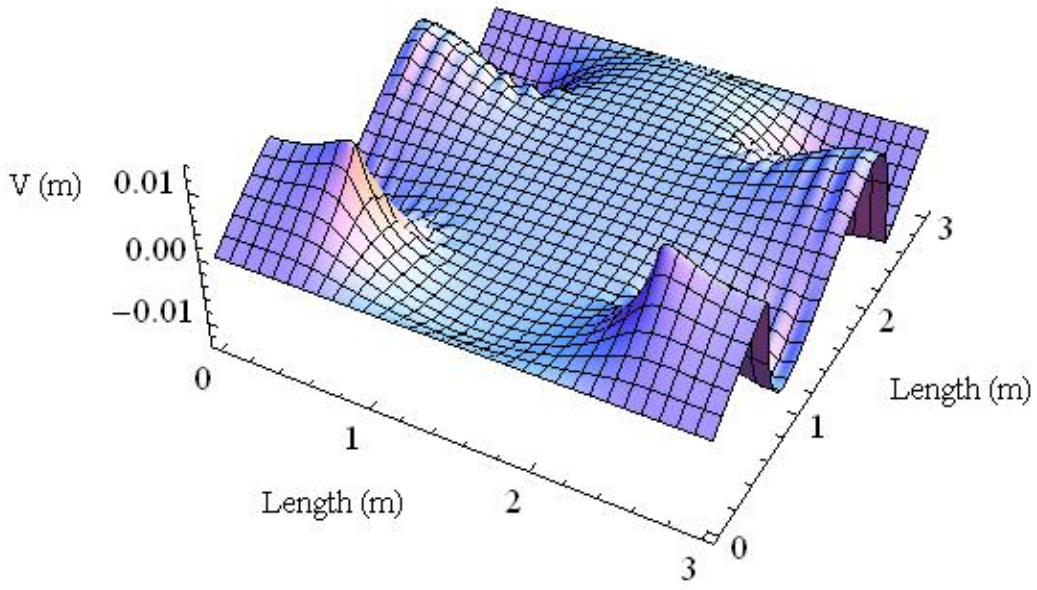

Figure 5.3 Three – Dimensional Plot of V Deflection

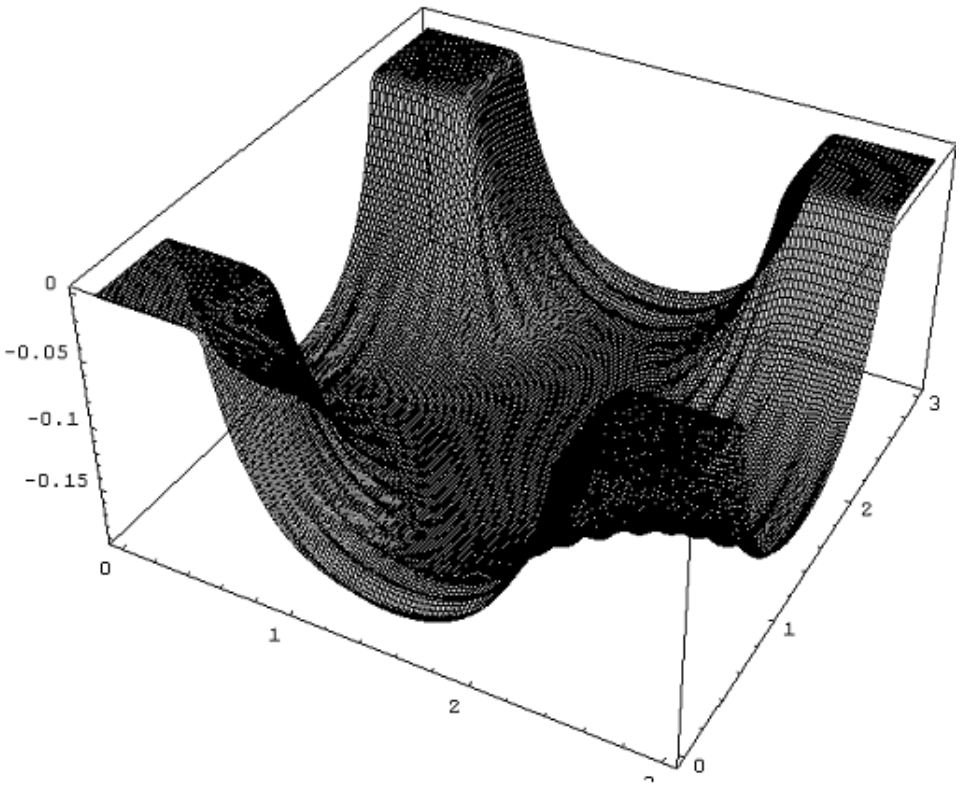

Figure 5.4 Three – Dimensional Plot of Deflected Shape

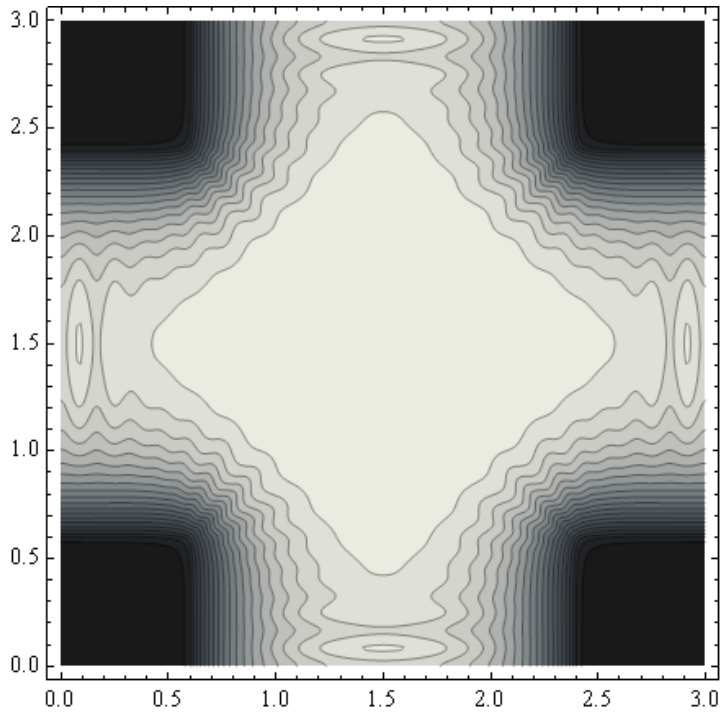

Figure 5.5 Contour Plot of W Deflection

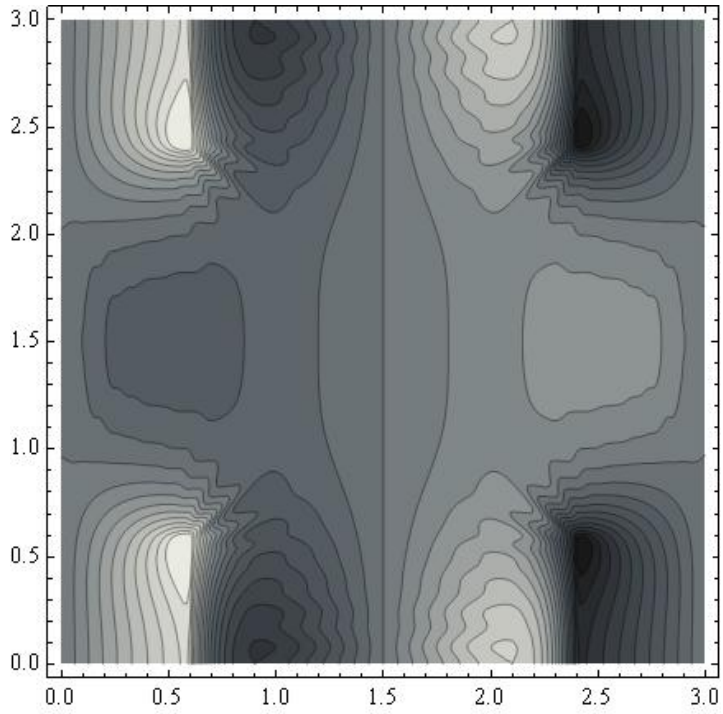

Figure 5.6 Contour Plot of U Deflection

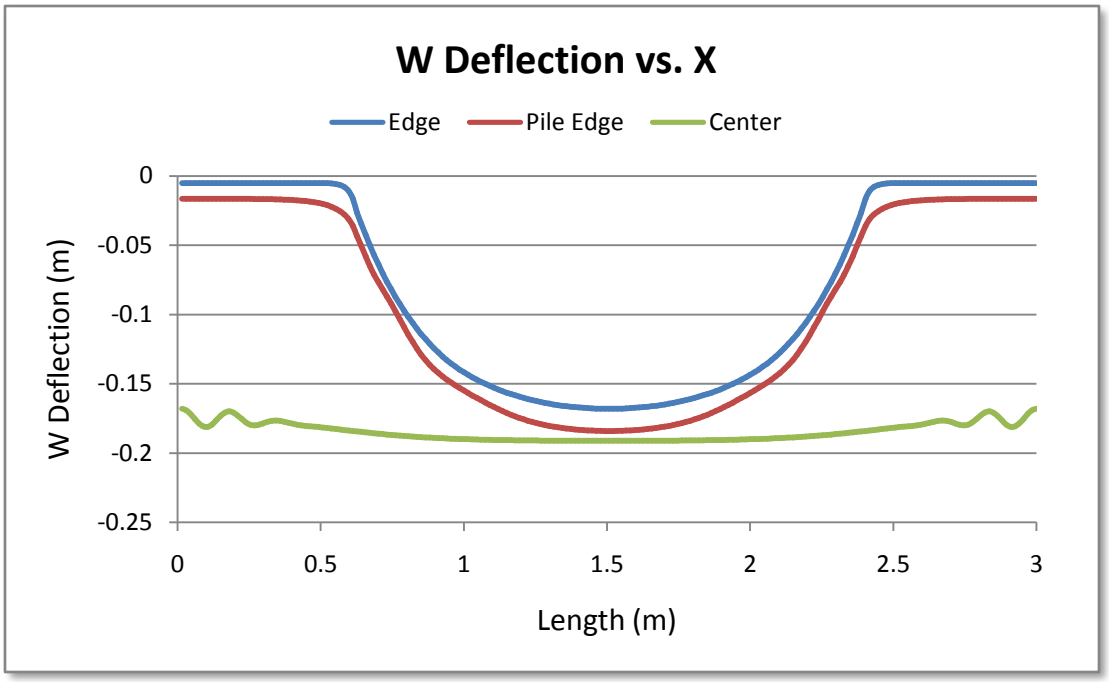

Figure 5.7 Two – Dimensional Plot of W Deflection Versus X

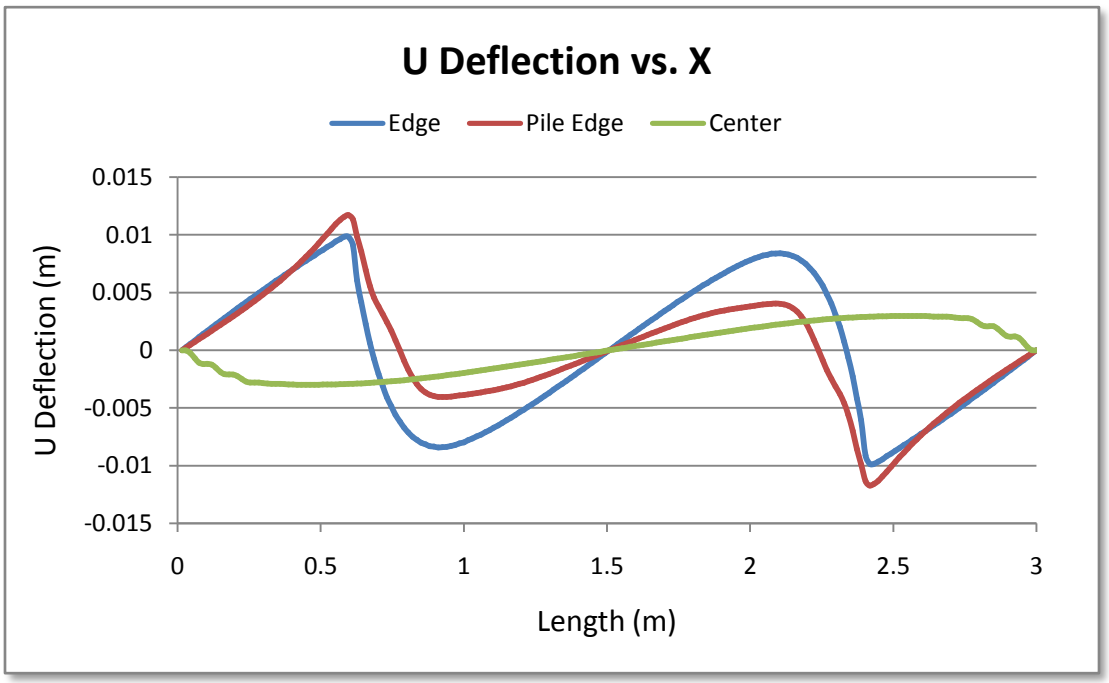

Figure 5.8 Two – Dimensional Plot of U Deflection Versus X

As can be seen in Figures 5.1 and 5.7, the maximum vertical deflection occurs at the center of the geosynthetic and is 0.191 m. The maximum in-plane displacement is along the pile edge and was found to be 0.0117 m. Maximum differential settlements occurring at the edge and center of the geosynthetic were 0.186 m and 0.163 m, respectively. Also, due to symmetry, maximum and minimum displacements are the same in the U and V axes.

Table 5.1 Deflections for Standard Case Square Piles

Square Piles	W (m)	U, V (m)	Ds (m)
Max Center	0.1911	0.0030	0.1861
Max Edge	0.1680	0.0098	0.1630
Max Pile Edge	0.1840	0.0117	0.1676

5.4.2 Strain

Results for strains are presented in Figures 5.9 and 5.10, and in Table 5.2.

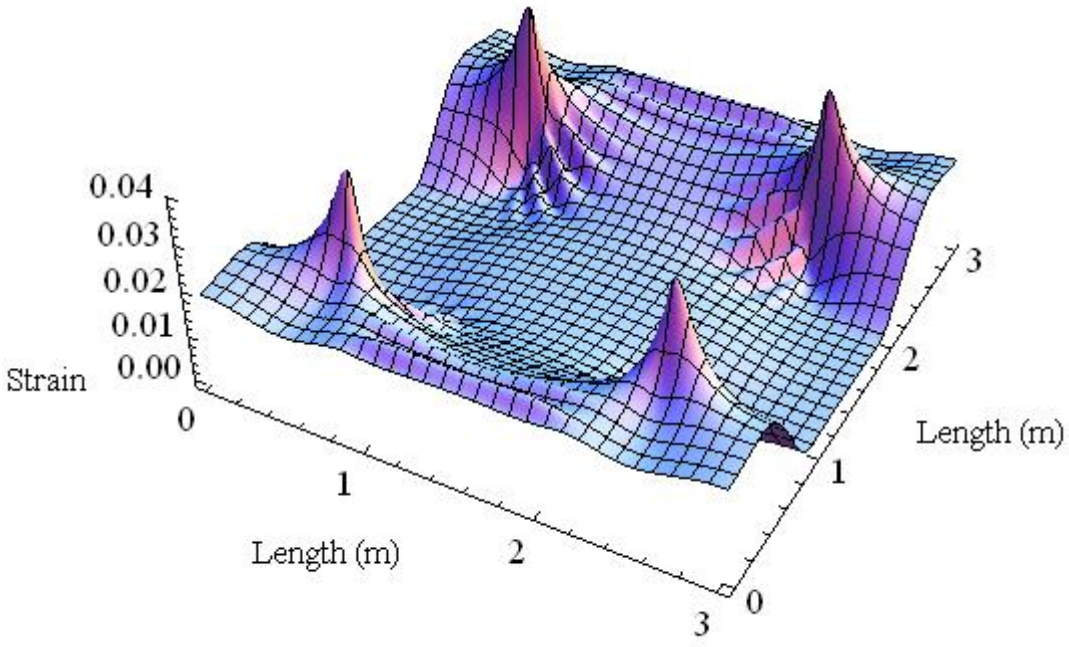

Figure 5.9 Three – Dimensional Plot of Ex

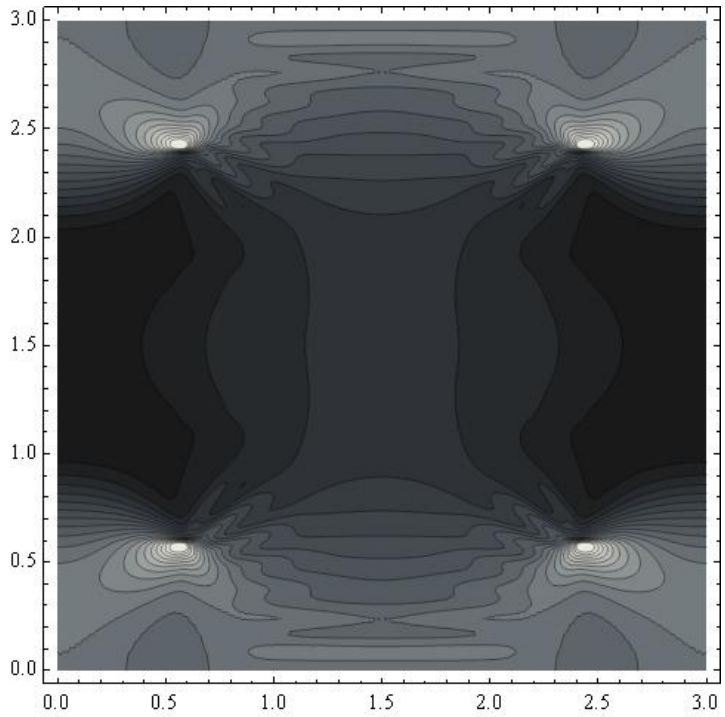

Figure 5.10 Contour Plot of Ex

Strain in the X direction of the geosynthetic for the standard case with square piles ranged from 0.0010 to a maximum value of 0.0395. It is apparent from Figures 5.9 and 5.10 that the maximum strain occurs at the corner of the square pile. The corner of the square pile is a critical location due to the dramatic increase in support stiffness and vertical loading where the soft soil region meets the pile.

5.4.3 Stress Resultants

Results for stresses are presented in Figures 5.11-5.17 and Table 5.2.

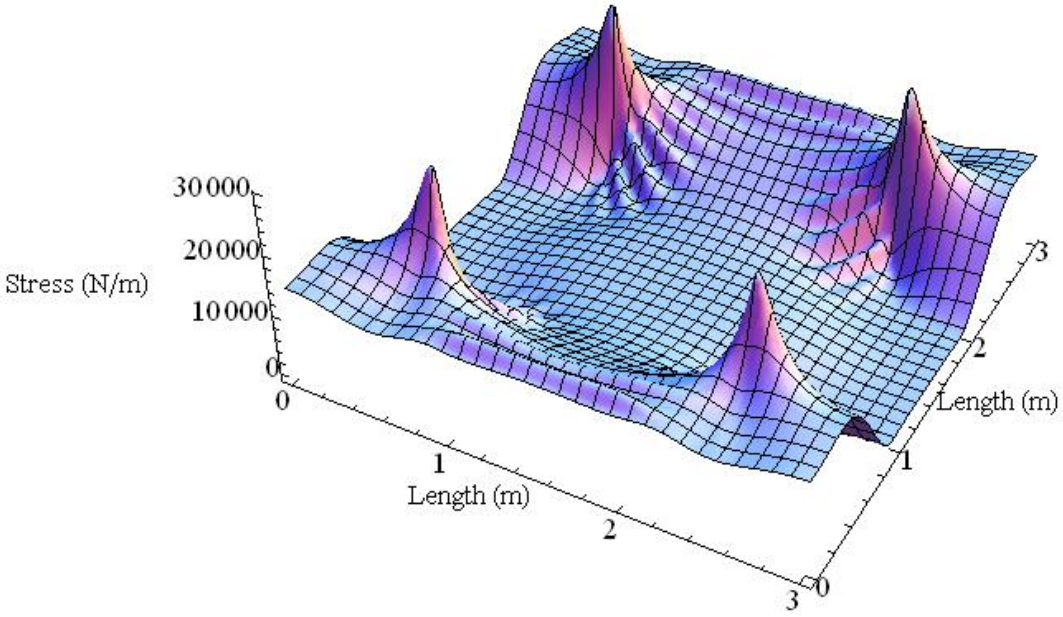

Figure 5.11 Three – Dimensional Plot of Nx

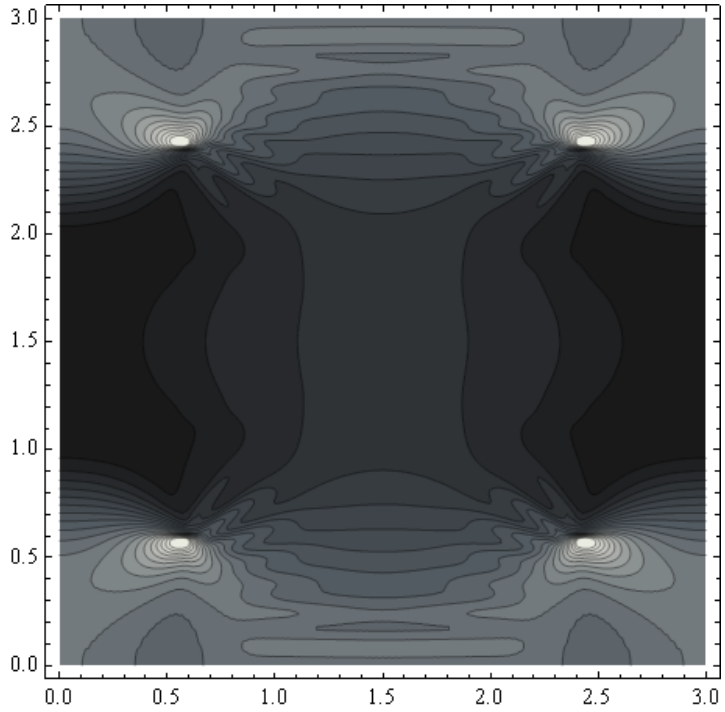

Figure 5.12 Contour Plot of Nx

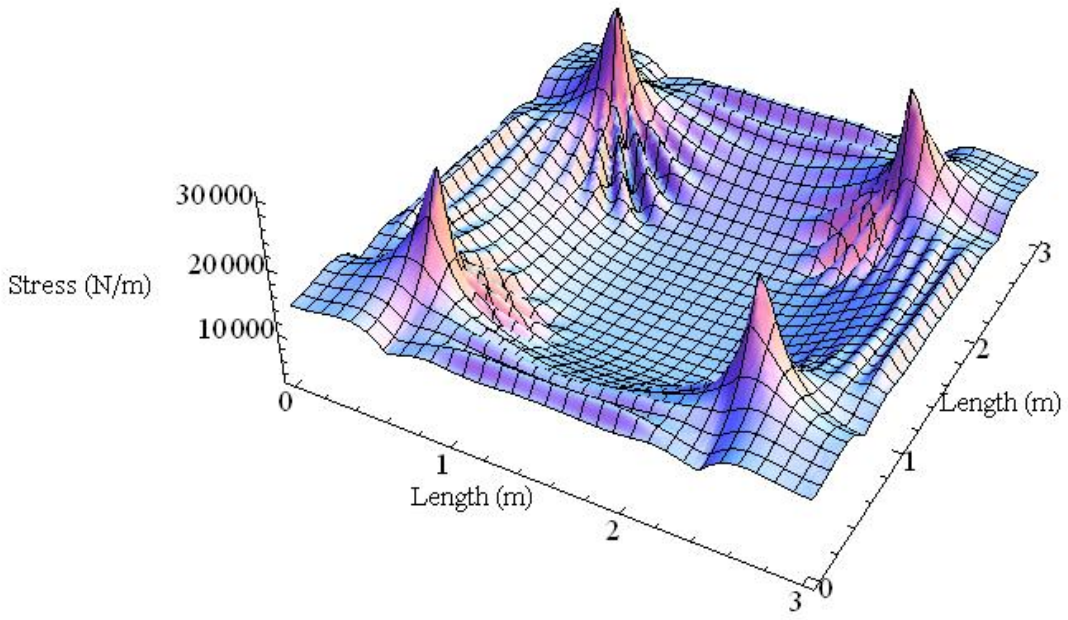

Figure 5.13 Three – Dimensional Plot of Nmax

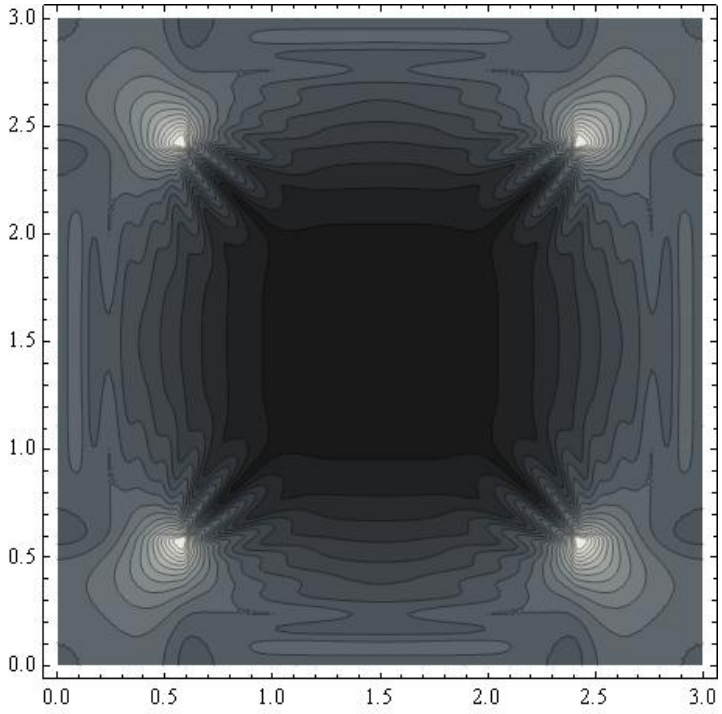

Figure 5.14 Contour Plot of Nmax

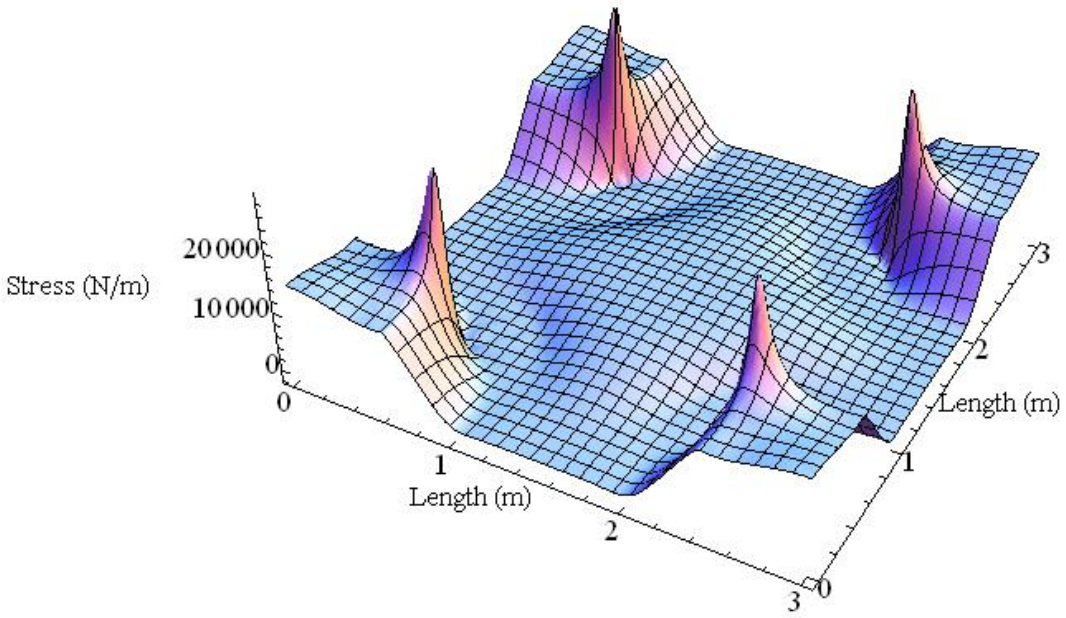

Figure 5.15 Three – Dimensional Plot of Nmin

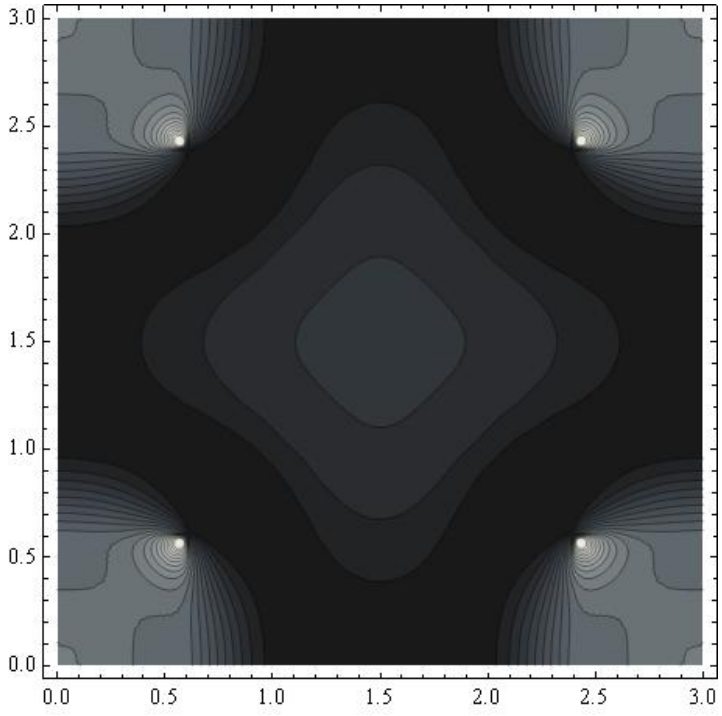

Figure 5.16 Contour Plot of Nmin

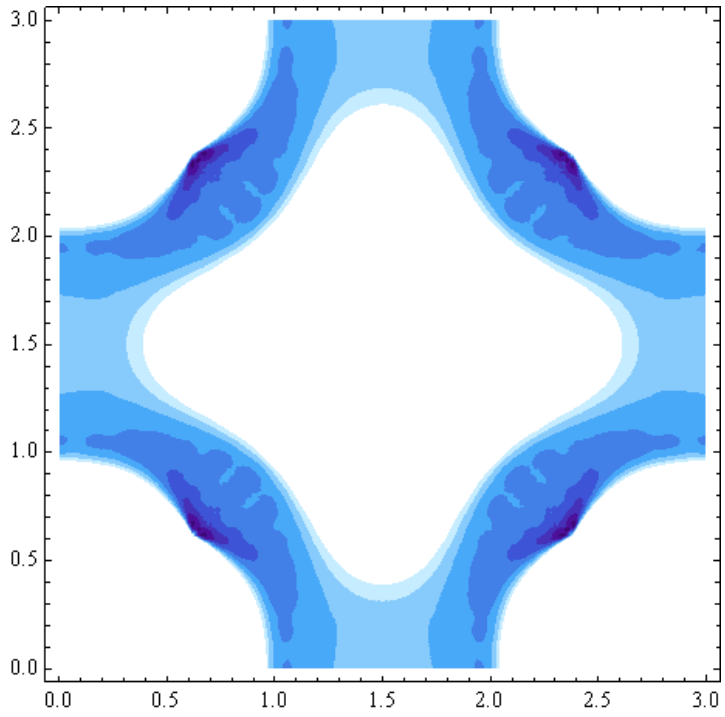

Figure 5.17 Contour Plot of Nmin Highlighting Region of Compressive Stress

Stresses in the geosynthetic were calculated for the X direction, as well as minimum and maximum overall stress. Stress in the X direction reached a maximum of 29,645 N/m and had a compressive minimum value of -743 N/m. The minimum stress at any given node is denoted Nmin and ranged from 29,108 N/m to –1,724.65. As discussed, negative values of minimum stress indicate the potential for wrinkling of the material. Figure 5.17 illustrates the region of the unit cell (in color) in which compressive stresses were found.

Table 5.2 Stress and Strain for Standard Case Square Piles

Square Piles	Ex	Nx (N/m)	Nmin (N/m)	Nmax (N/m)
Max	0.0395	29645.20	29108.40	30641.10
Min	-0.0010	-743.34	-1724.65	2998.75

5.5 Circular Piles

5.5.1 Deflections

Deflection results are presented in Figures 5.18-5.25 and Table 5.3.

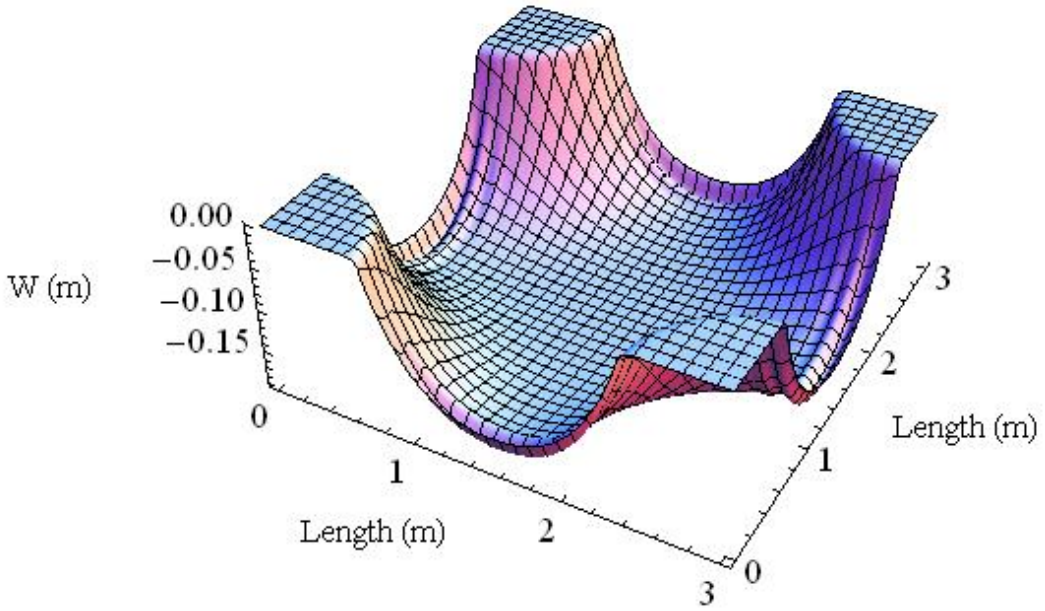

Figure 5.18 Three – Dimensional Plot of W Deflection

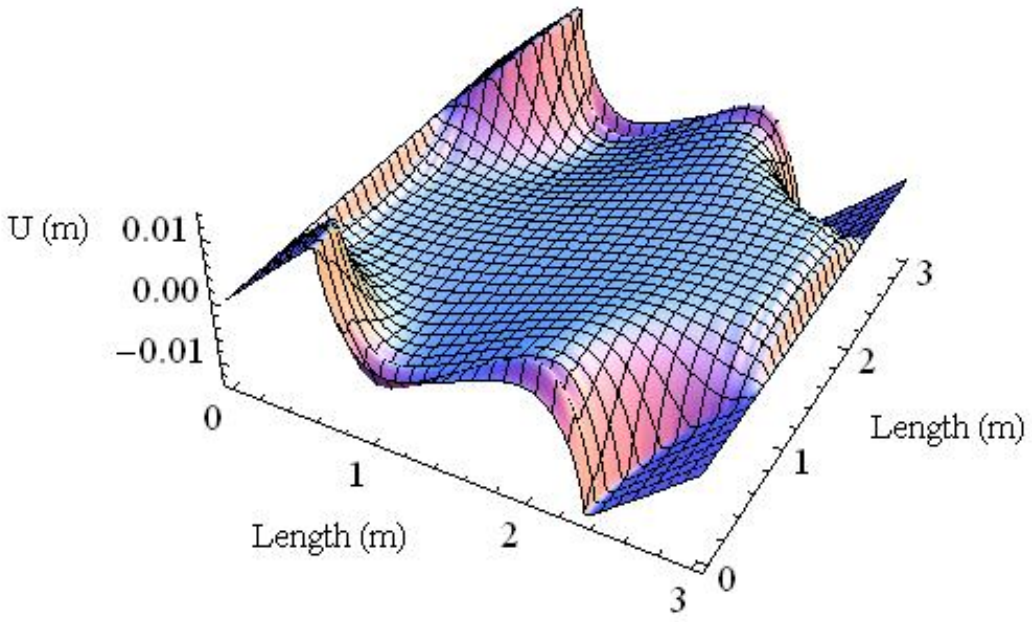

Figure 5.19 Three – Dimensional Plot of U Deflection

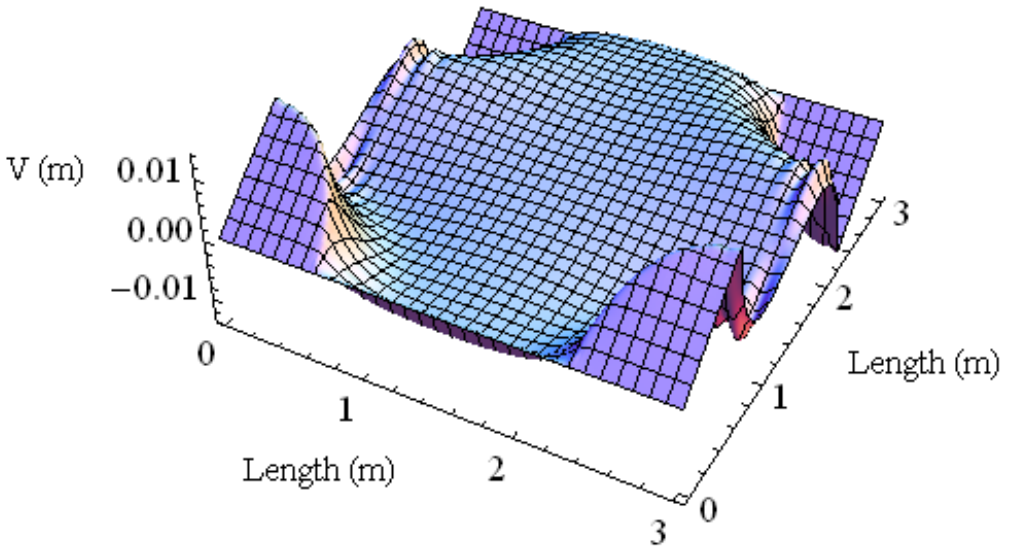

Figure 5.20 Three – Dimensional Plot of V Deflection

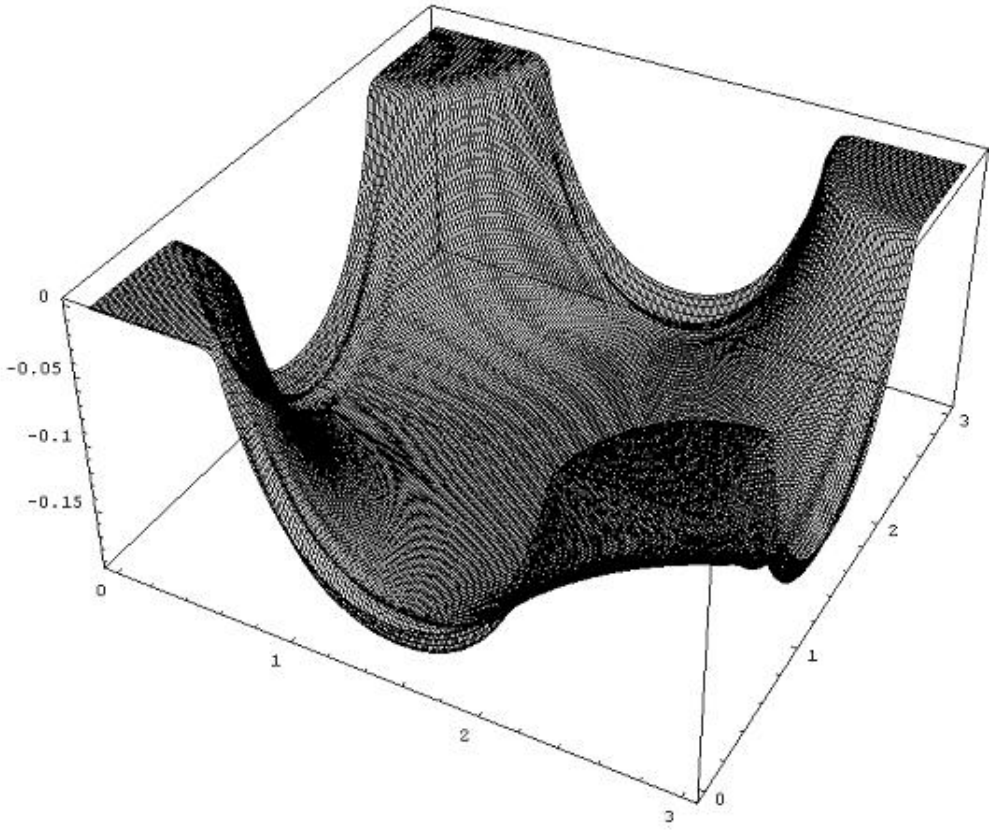

Figure 5.21 Total Deflected Shape

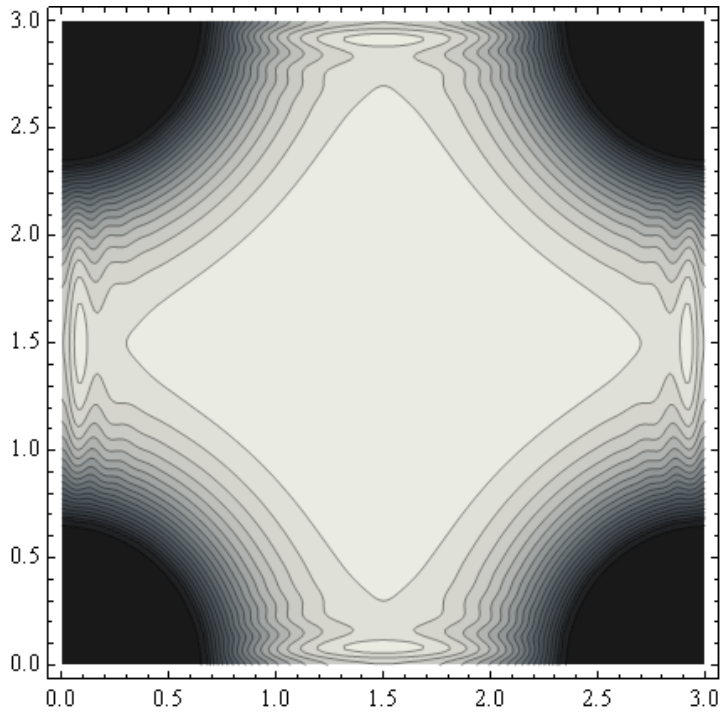

Figure 5.22 Contour Plot of W Deflection

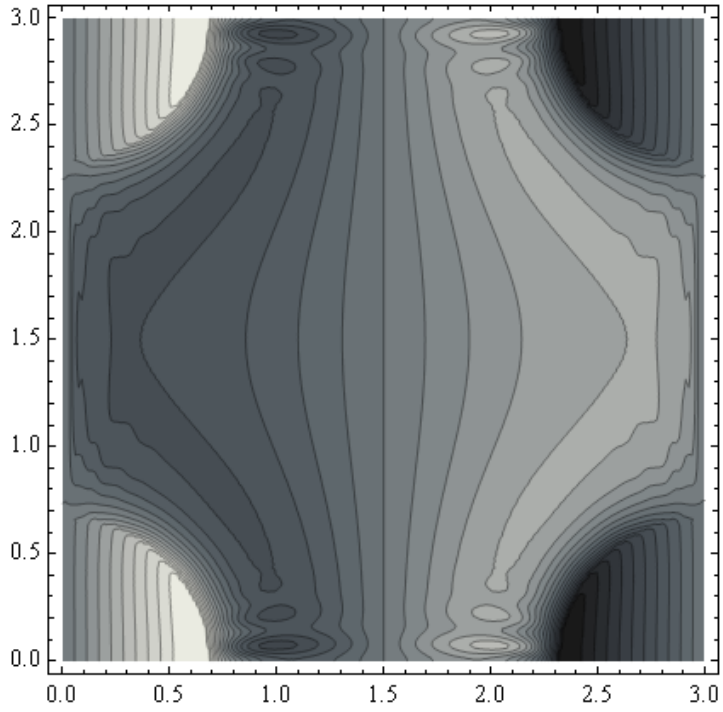

Figure 5.23 Contour Plot of U Deflection

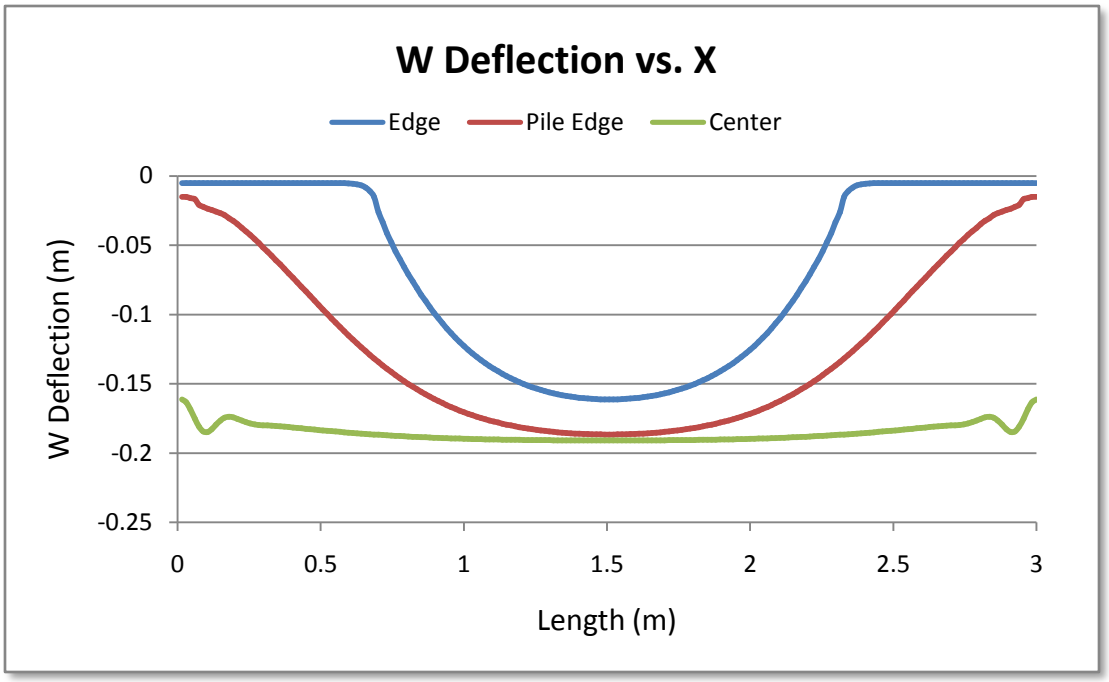

Figure 5.24 Two – Dimensional Plot of W Deflection Versus X

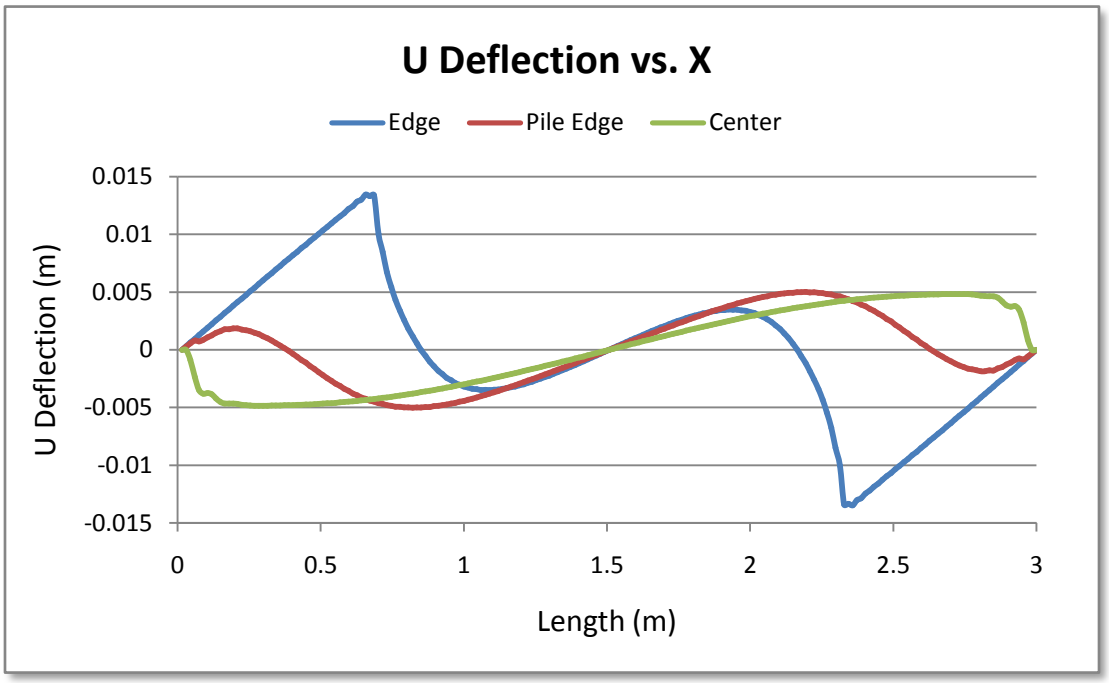

Figure 5.25 Two – Dimensional Plot of U Deflection Versus X

As can be seen in Figures 5.18 and 5.24, the maximum vertical deflection again occurs at the center of the geosynthetic and is of similar magnitude to that of the square piles at 0.1911 m. The maximum in-plane displacement is along the geosynthetic edge and was found to be 0.0135 m. Differential settlement D_s in the unit cell is maximum at 0.186 m and 0.156 m at the center and edge of the geosynthetic, respectively.

Table 5.3 Deflections for Standard Case Circle Piles

Circle Piles	W (m)	U, V (m)	Ds (m)
Max Center	0.1911	0.0048	0.1861
Max Edge	0.1612	0.0135	0.1562
Max Pile Edge	0.1853	0.0050	0.1799

5.5.2 Strains

Results for strains are presented in Figures 5.26 and 5.27, and in Table 5.4.

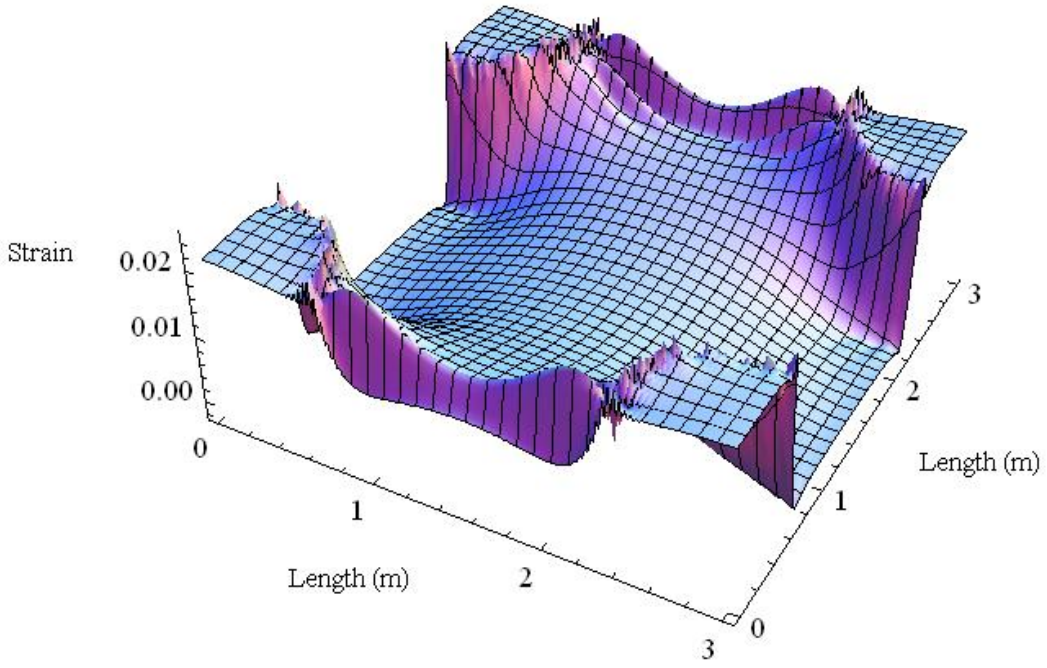

Figure 5.26 Three – Dimensional Plot of Ex

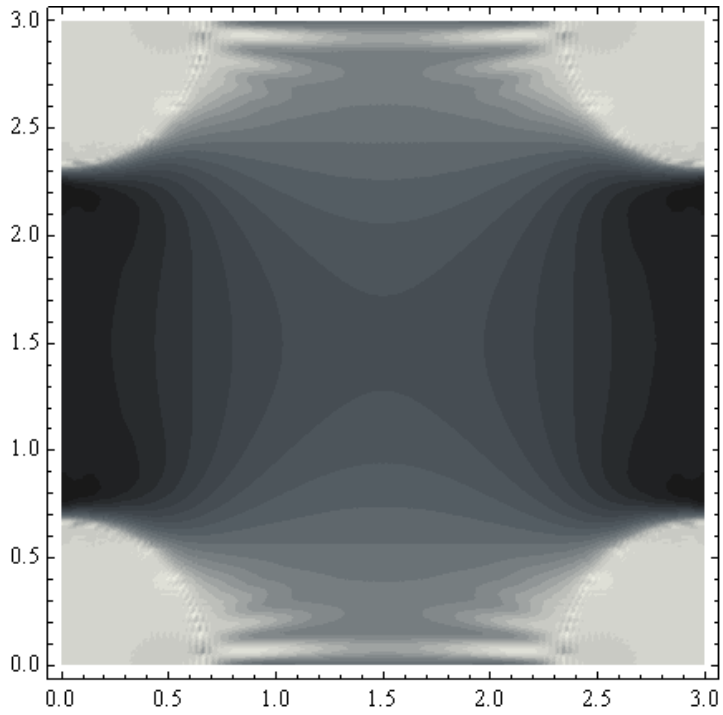

Figure 5.27 Contour Plot of Ex

5.5.3 Stress Resultants

Results for stresses are presented in Figures 5.28-5.34 and Table 5.4.

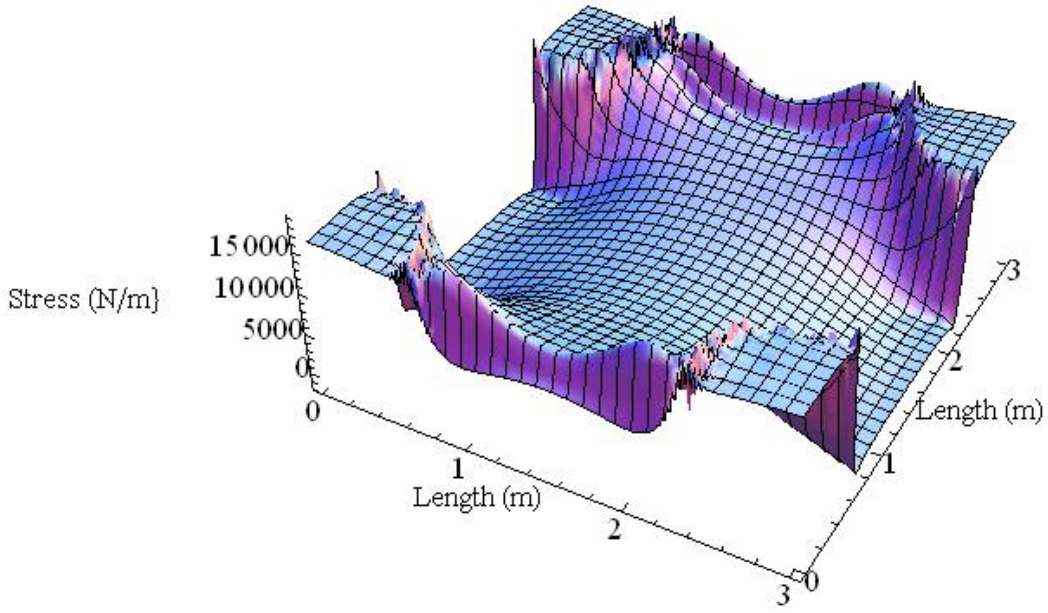

Figure 5.28 Three – Dimensional Plot of Nx

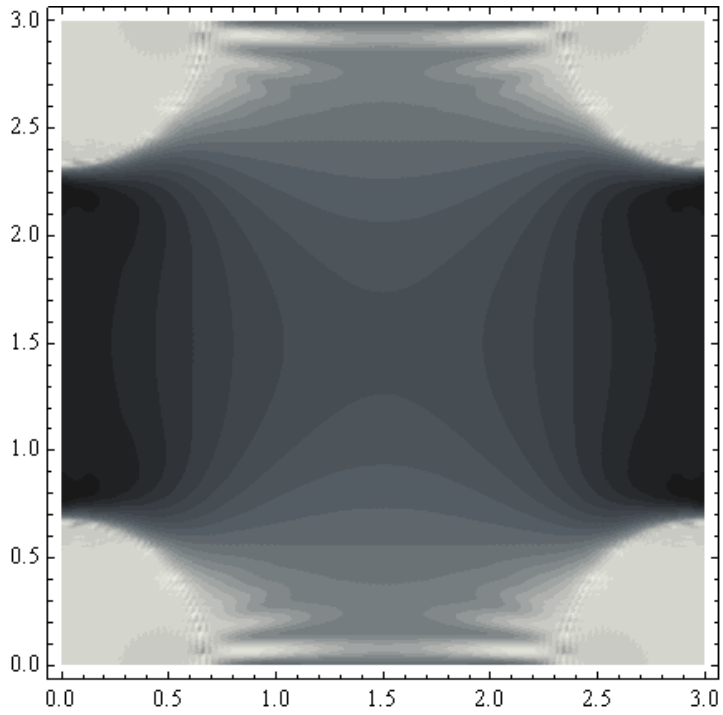

Figure 5.29 Contour Plot of Nx

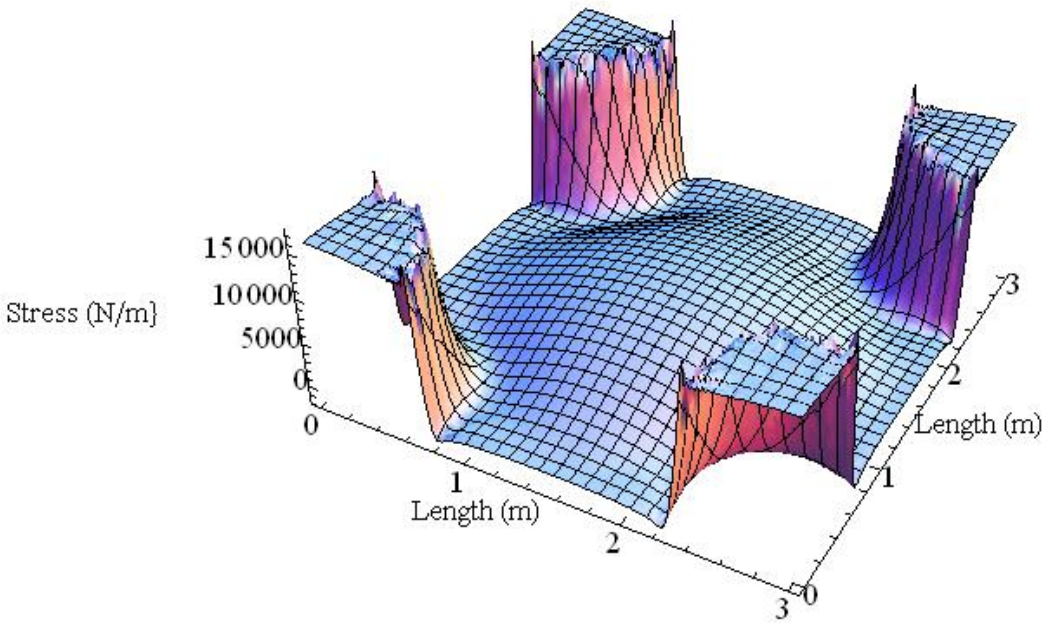

Figure 5.30 Three – Dimensional Plot of Nmin

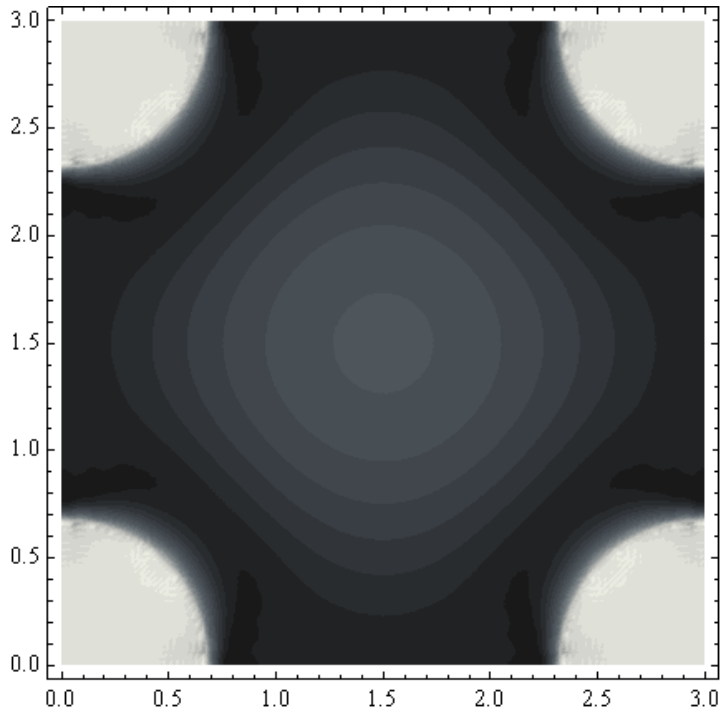

Figure 5.31 Contour Plot of Nmin

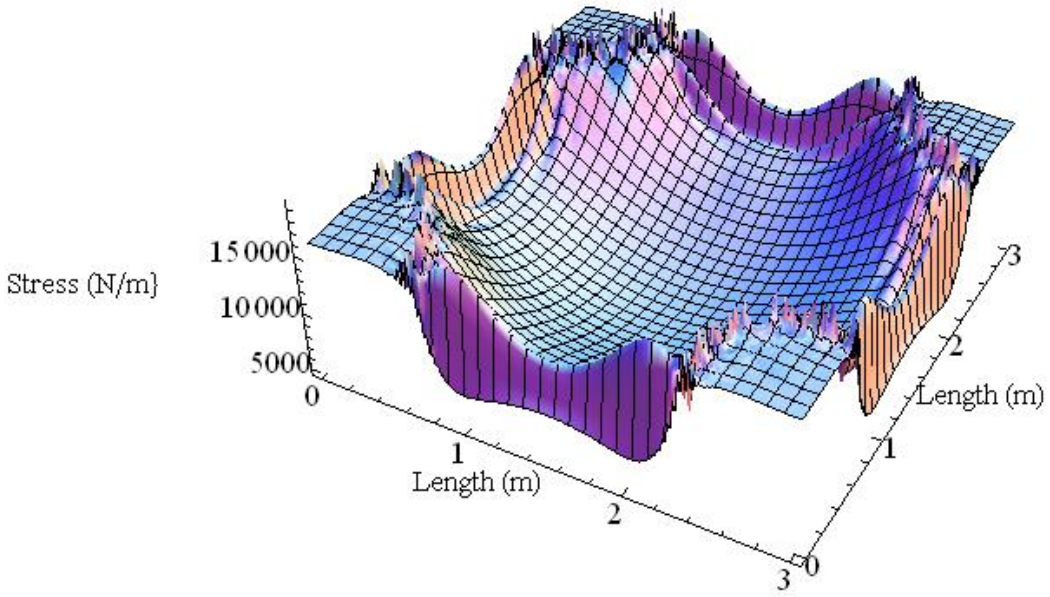

Figure 5.32 Three-Dimensional Plot of Nmax

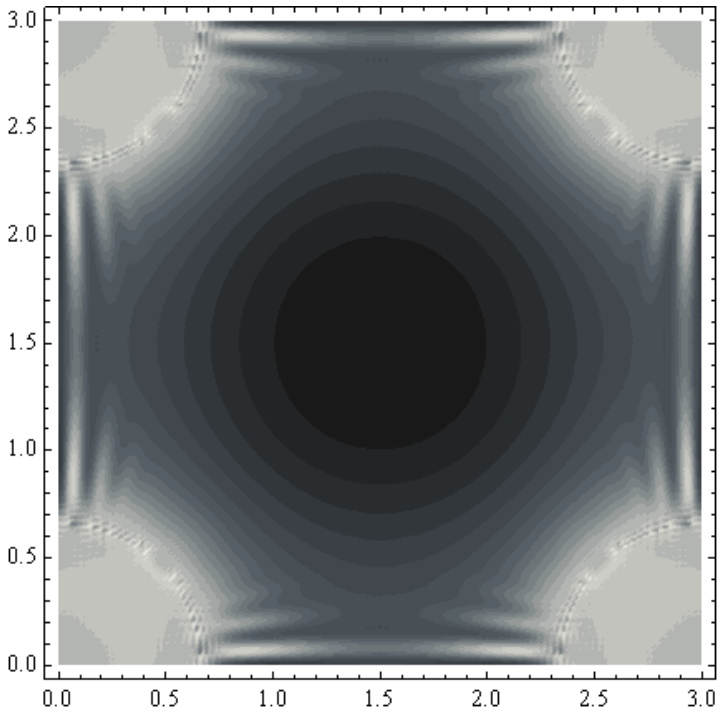

Figure 5.33 Contour Plot of Nmax

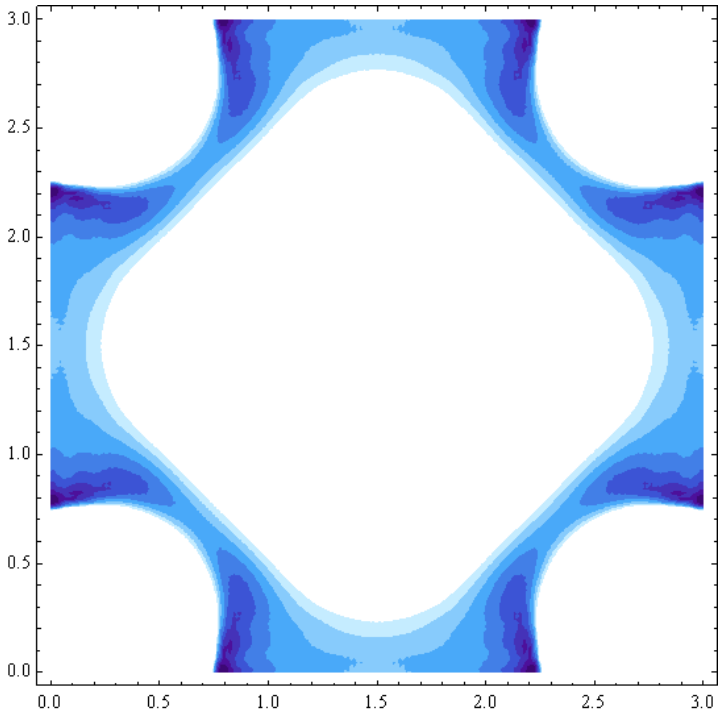

Figure 5.34 Contour Plot of Nmin Highlighting Region of Compressive Stress

The three-dimensional plots of stress and strain of the geosynthetic with a circular pile suggest a potential source of discontinuity. Encircling the pile edge, a region of highly varying stress and strain can be seen to occur. Although the three-dimensional plots of vertical and in-plane deflections appear smooth, plots of stress and strain exhibit erratic behavior. The source of such an error is most likely due to the complexity of modeling a curved pile region with a square finite difference mesh. Equations for stress and strain involve partial derivatives of the deflections at the node in question. In turn, these nodal deflections are based on a finite difference discretization that utilizes the nearby nodal deflections. Although the three-dimensional plots of stress and strain appear flawed, maximum and minimum values can still be reasonably obtained.

Maximum strain in the X direction of the geosynthetic for the standard case with circular piles was 0.0253. This value of strain is significantly less than that of the unit cell containing square piles, suggesting that curved edges have less adverse effects on the geosynthetic. Although slightly obscured, it can be seen in Figure 5.26 that the maximum strain occurs along the circular pile edge.

Stresses in the geosynthetic were calculated for overall maximum and minimum values, and in the X direction. X-direction stress reached a maximum of 18,956 N/m and a minimum of -1,748 N/m. Again, a region of compressive minimum stress was found to exist in the wrinkled region of the geosynthetic near the pile edge. Figure 5.34 illustrates the region in which compressive stress and wrinkling occur.

Table 5.4 Stress and Strain for Standard Case Circle Piles

Circle Piles	Ex	Nx (N/m)	Nmin (N/m)	Nmax (N/m)
Max	0.0253	18956.90	17311.50	19450.40
Min	-0.0023	-1748.57	-1748.57	4697.75

5.6 Square Piles Rotated 45°

5.6.1 Deflections

Deflection results are presented in Figures 5.35-5.42 and Table 5.5.

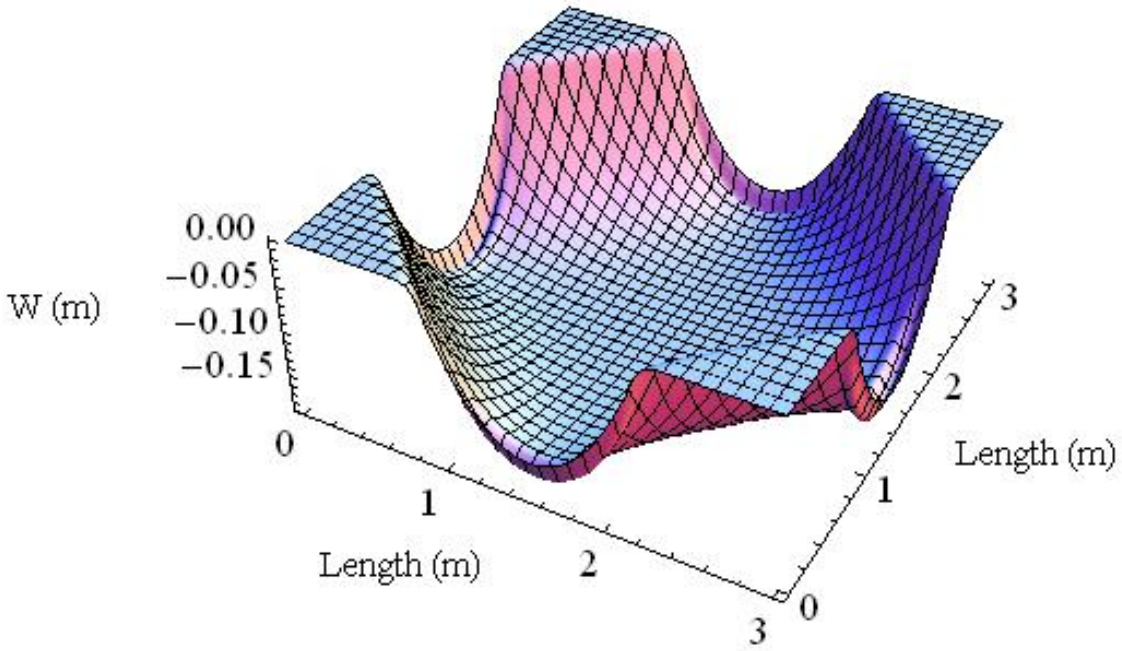

Figure 5.35 Three – Dimensional Plot of W Deflection

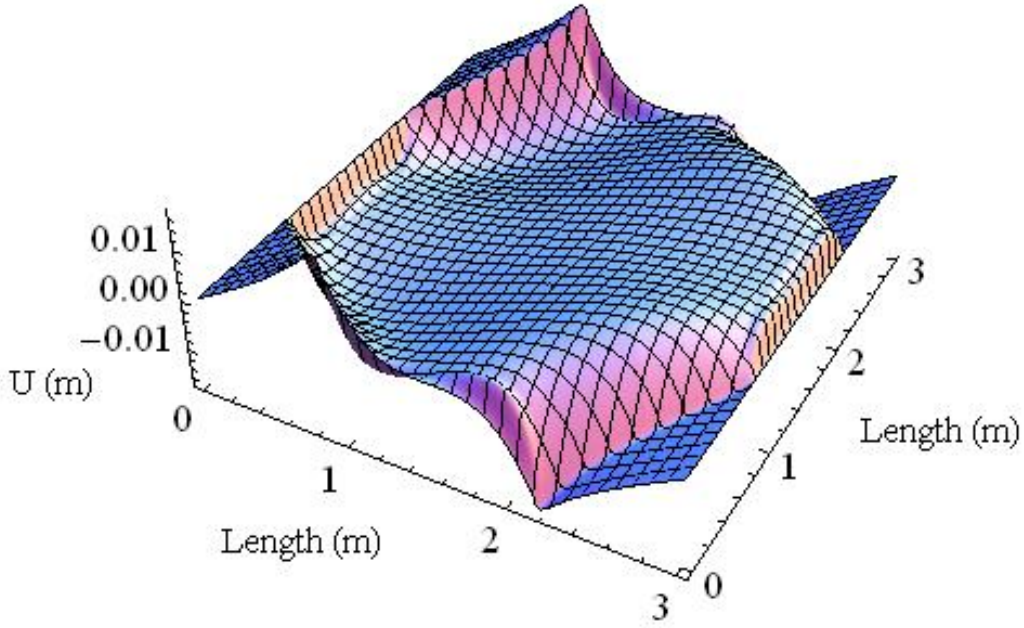

Figure 5.36 Three – Dimensional Plot of U Deflection

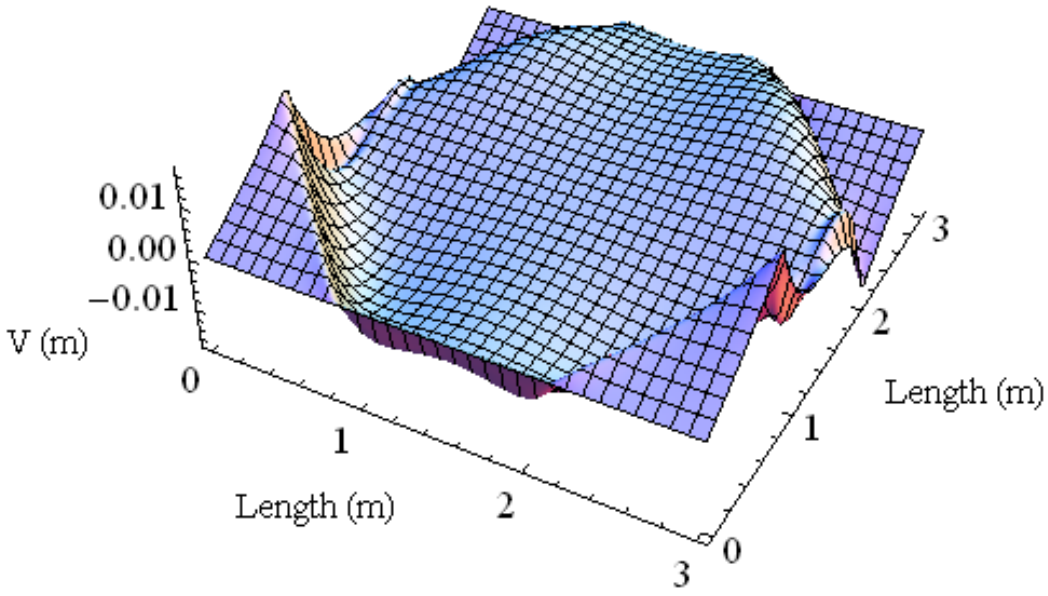

Figure 5.37 Three – Dimensional Plot of V Deflection

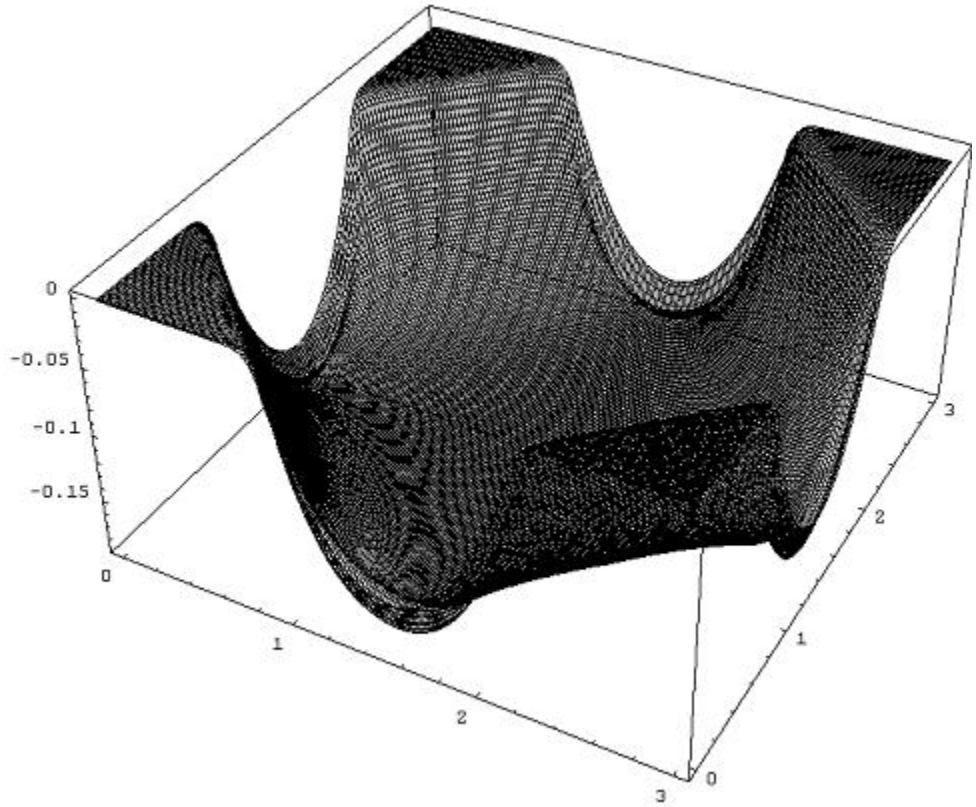

Figure 5.38 Total Deflected Shape

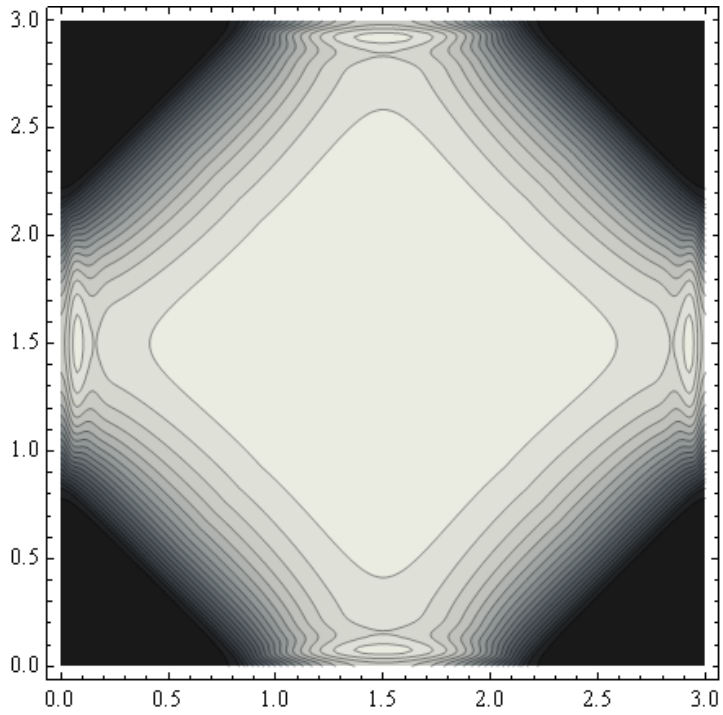

Figure 5.39 Contour Plot of W Deflection

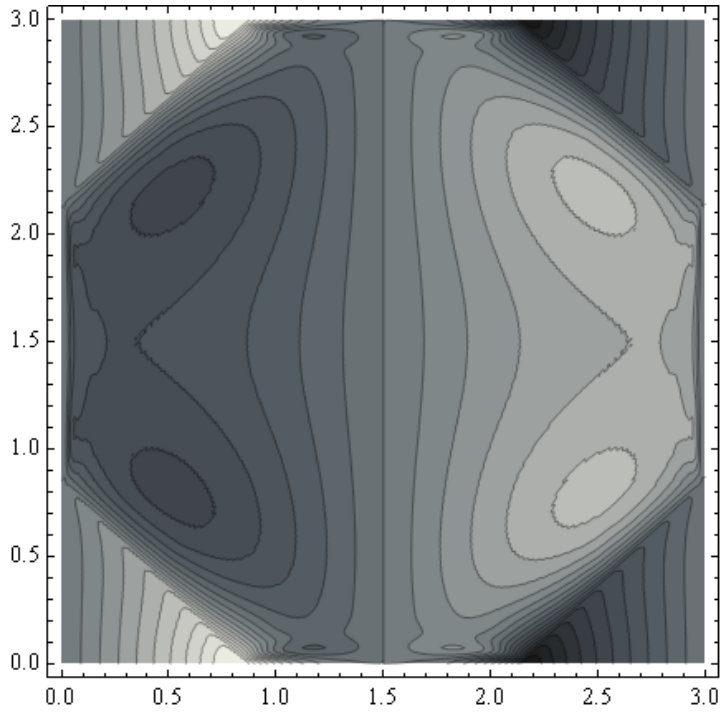

Figure 5.40 Contour Plot of U Deflection

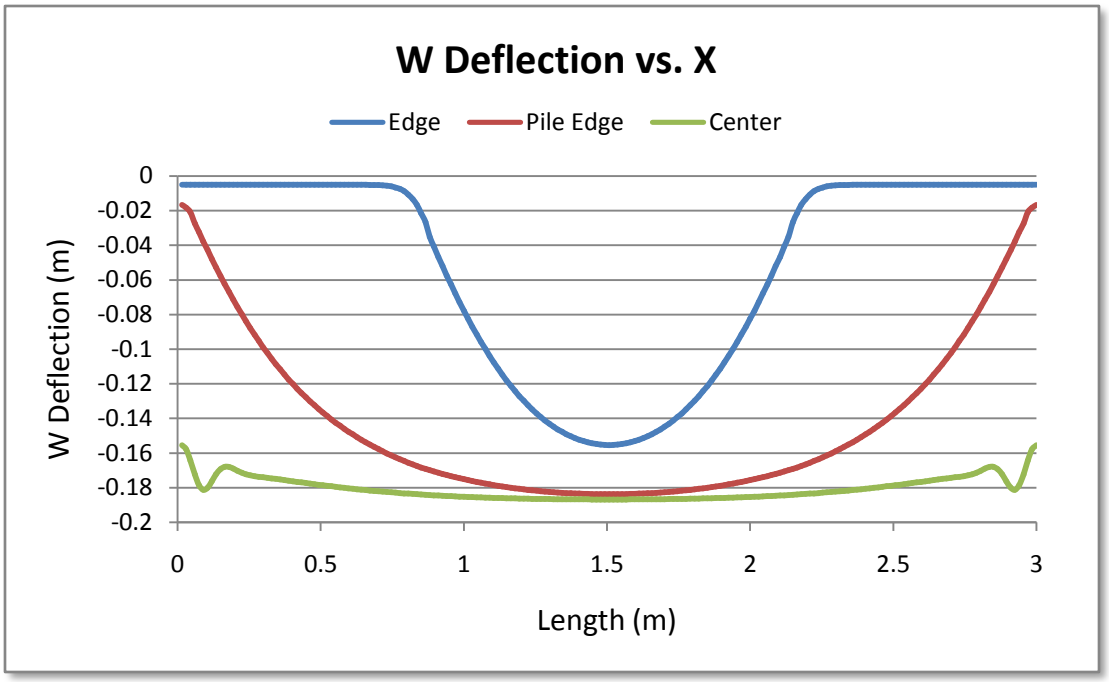

Figure 5.41 Two – Dimensional Plot of W Deflection Versus X

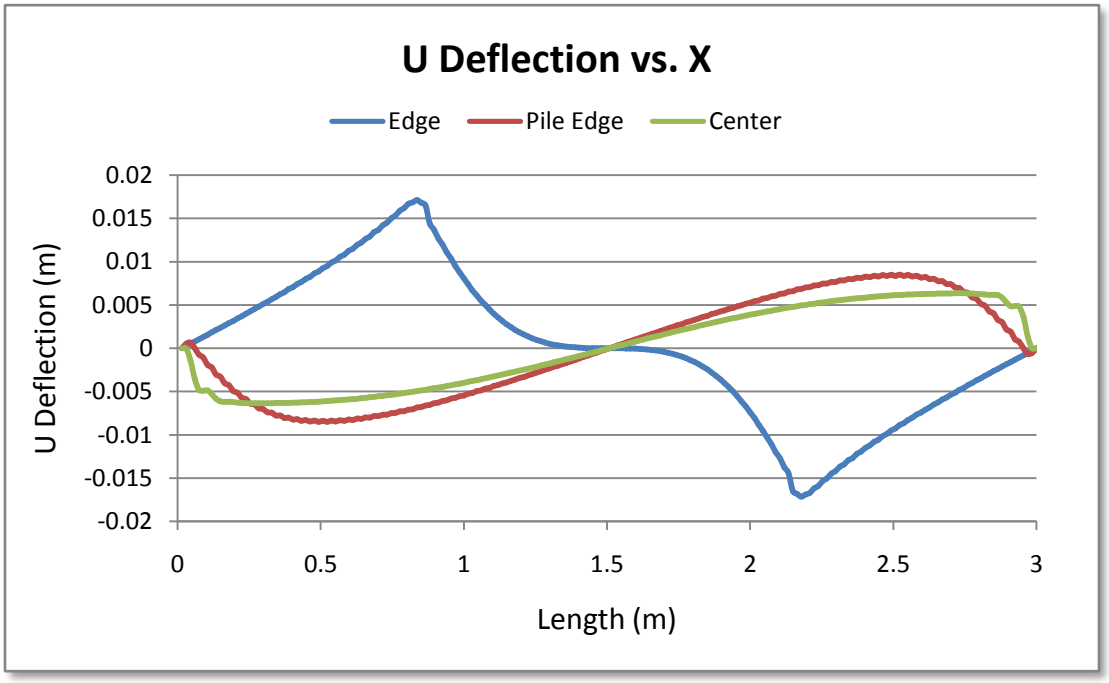

Figure 5.42 Two – Dimensional Plot of U Deflection Versus X

Figures 5.35 and 5.41 indicate that the maximum vertical deflection occurs at the center of the geosynthetic with magnitude 0.1867 m. This amount of displacement is actually the lowest for the three pile types analyzed. In-plane deflections, however, were found to be slightly higher at 0.0171 m near the geosynthetic edge. Differential settlements were 0.1817 m at the center and 0.1503 m near the edge.

Table 5.5 Deflections for Standard Case Rotated Square Piles

Rotated Square Piles	W (m)	U, V (m)	Ds (m)
Max Center	0.1867	0.0064	0.1817
Max Edge	0.1553	0.0171	0.1503
Max Pile Edge	0.1839	0.0084	0.1625

5.6.2 Strains

Results for strains are presented in Figures 5.43 and 5.44, and in Table 5.6.

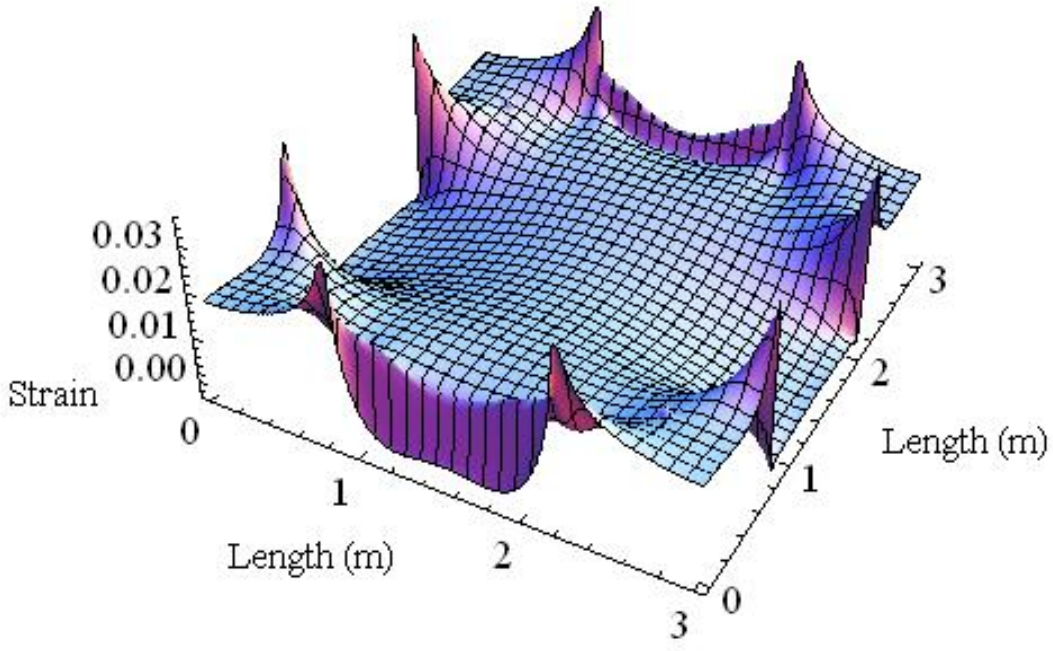

Figure 5.43 Three-Dimensional Plot of Ex

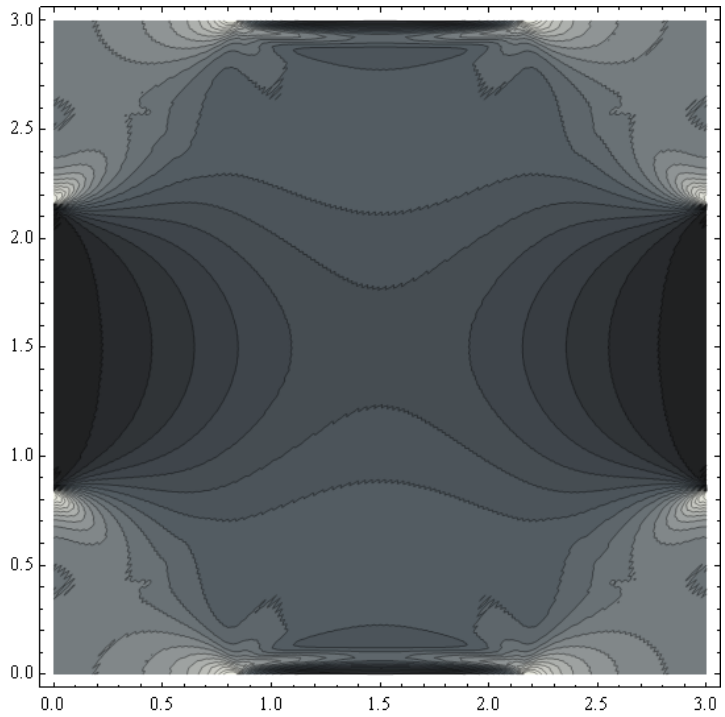

Figure 5.44 Contour Plot of Ex

5.6.3 Stress Resultants

Results for stresses are presented in Figures 5.45-5.51 and Table 5.6.

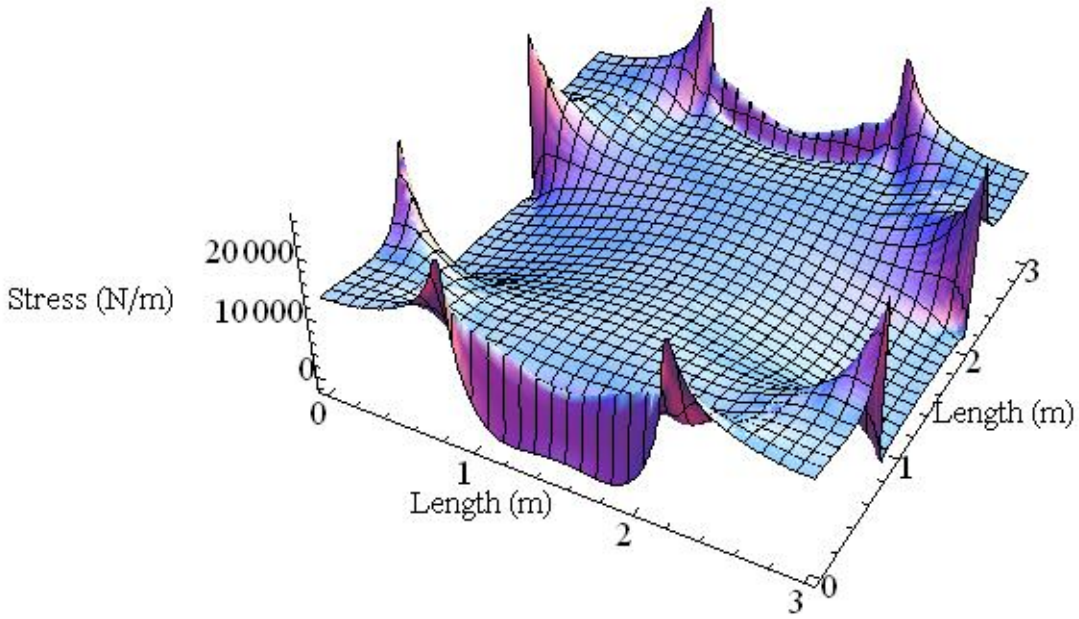

Figure 5.45 Three-Dimensional Plot of Nx

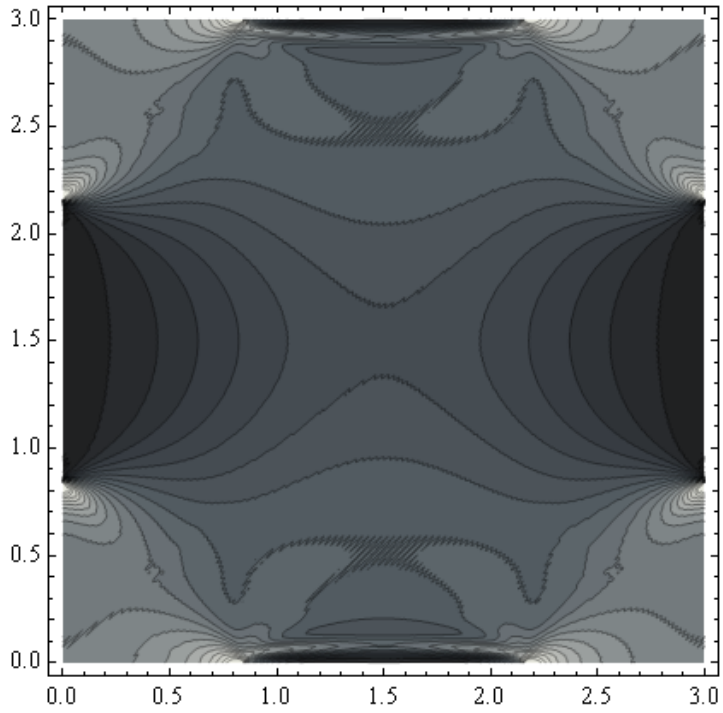

Figure 5.46 Contour Plot of Nx

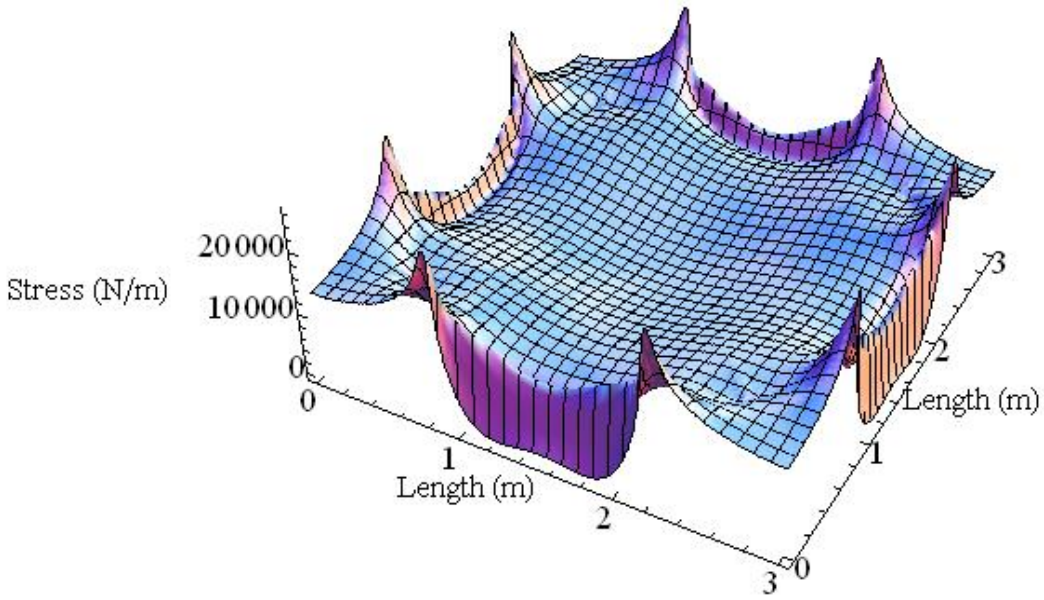

Figure 5.47 Three-Dimensional Plot of Nmax

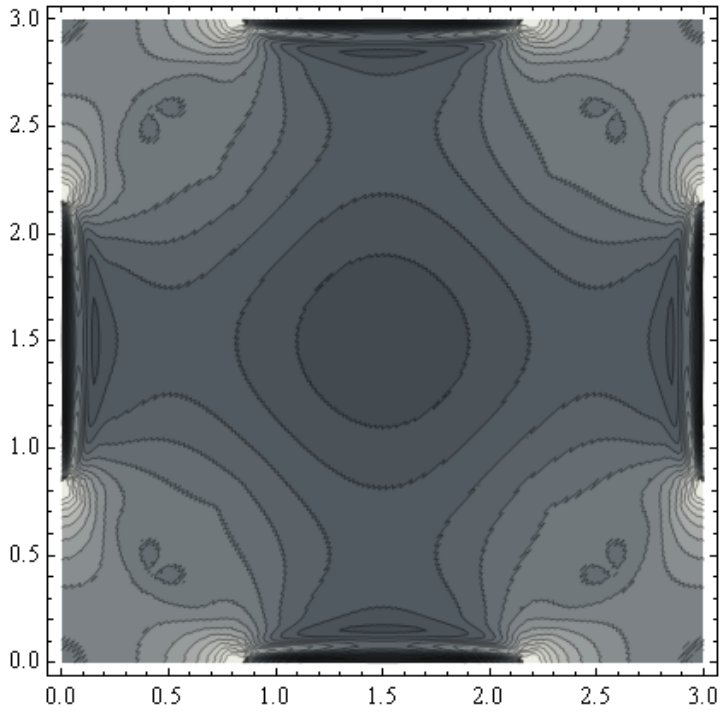

Figure 5.48 Three-Dimensional Plot of Nmax

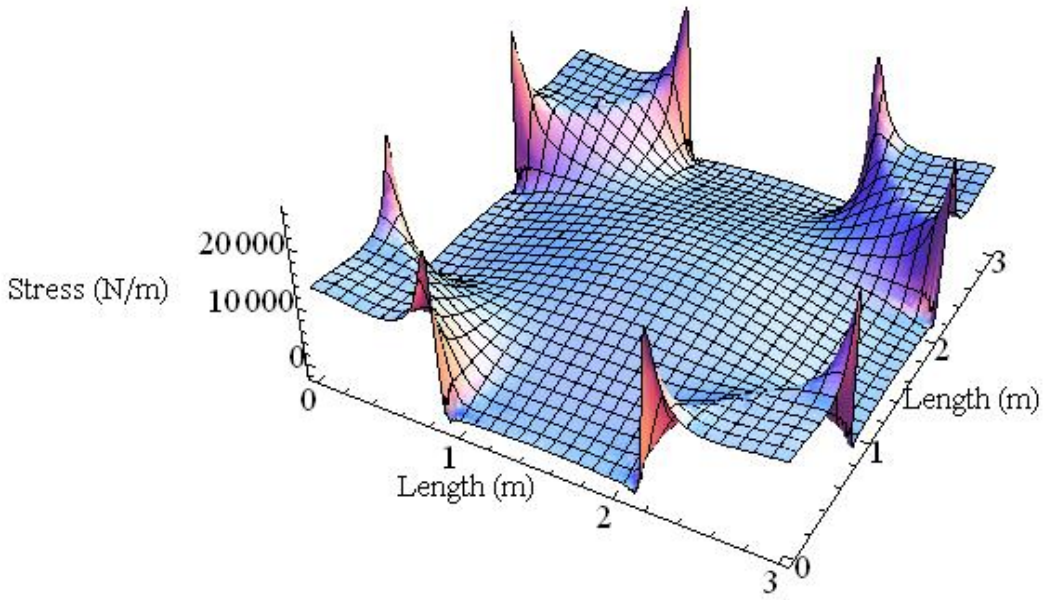

Figure 5.49 Three-Dimensional Plot of Nmin

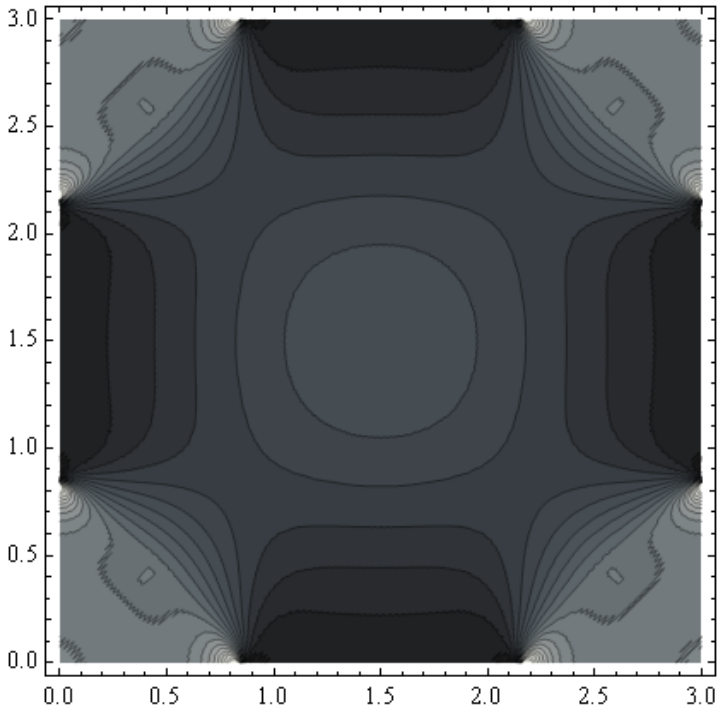

Figure 5.50 Three-Dimensional Plot of Nmin

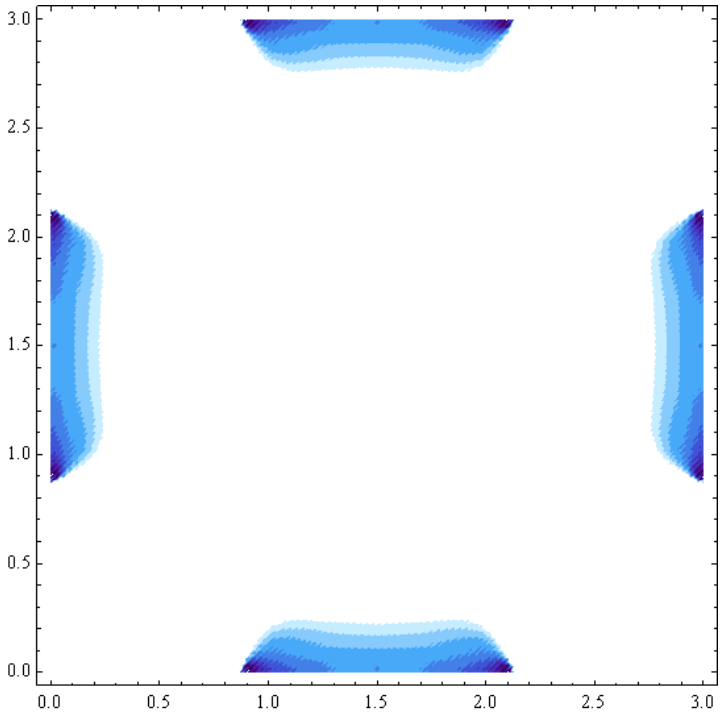

Figure 5.51 Contour Plot of Nmin Highlighting Region of Compressive Stress

Maximum strain in the X direction was found to be 0.0353, slightly lower than that of the standard case with square piles. This magnitude of strain is also larger than that found in the standard case with circular piles, further suggesting that circular piles are best suited for this application. Figure 5.43 shows that the maximum strain still occurs near the corner of the square pile. Since lower X strain was found by using rotated square piles, it can be deduced that this orientation is superior in this respect to regularly spaced square piles.

Stresses in the geosynthetic were found to be maximum at 26,508 N/m in the X direction, 26,450 N/m minimum overall, and 26,508 N/m maximum overall. The location of maximum stress for each case can be seen in Figures 5.45, 5.47, and 5.49. The region of compressive stress seen in Figure 5.51 differs slightly from that for the square pile and circular pile orientations. When utilizing rotated square piles, compression stresses are seen to act in the regions spanning the column corners only. There also is no compressive stress acting around the entire perimeter of the pile as in previous cases.

Table 5.6 Stress and Strain for Standard Case Rotated Square Piles

Rotated Square Piles	Ex	Nx (N/m)	Nmin (N/m)	Nmax (N/m)
Max	0.0353	26508.50	26450.60	26508.50
Min	-0.0030	-2256.56	-2256.56	-661.19

5.7 Discussion of Results

5.7.1 Comparison of Pile Orientations

The standard case was analyzed for each of the three pile orientation types discussed previously. Each analysis yielded varying results for maximum deflection, stress, and strain. Table 5.7 gives the maximum values for vertical and in-plane deflections, as well as stress and strain in the X directions. Maximum vertical deflection is seen to occur with square piles, although each pile orientation showed very similar maximum vertical deflections. In-plane deflection was seen to

be maximum for rotated square piles. Stress and strain values are maximum with square piles due to the concentrations that occur at the pile corners.

Table 5.7 Comparison of Maximum Values for Standard Case

Pile Type	Max W (m)	Max U, V (m)	Max Ex	Max Nx (N/m)
Square	0.1911	0.0134	0.040	29645
Circle	0.1911	0.0135	0.025	18957
Rotated Square	0.1867	0.0171	0.035	26509

5.7.2 Comparison to Cable Net Model

Results obtained by Halvordson (2007) are presented in Table 5.8 for square piles using the standard parameter case. As discussed, his research modeled the geosynthetic layer as a cable net utilizing a similar unit cell approach. Here, the geosynthetic is treated as a geogrid in which the interwoven strands are represented by individual cable elements. The general solution technique involved the minimization of total energy over the unit cell including loading and support components as well as cable resistance. As can be seen in Table 5.8, the results of each model are in close agreement. In particular, the maximum vertical deflection occurring at the center of the geosynthetic is nearly exact. Closely related maximum vertical deflection also results in similar differential settlements.

The cable net and finite difference models yield very similar vertical and in-plane deflections. The stress and strain predicted by each model however differ slightly. The finite difference method yields a maximum strain in the X direction of .0395 while the cable net model show only .0298 strain in X. Stress resultants are calculated for each model of which maximum edge stress is most similar. The finite difference program showed a maximum edge stress of 15,156 N/m, while the cable net model gives 15,200 N/m. Maximum stress resultants over the pile are within in reason but differ somewhat from 21,733 N/m in the cable net model and 29,645 N/m in the finite difference model.

The results obtained by the finite difference and cable net models are in close agreement. The fact that two unique modeling techniques yield such comparable results further validates the assumptions and analysis methods. Although values are quite similar, there still exist certain differences in modeling the geosynthetic as a cable net as opposed to a thin flexible plate. In particular, cable nets inherently cannot withstand compression forces and therefore will not exhibit any of the wrinkling seen to exist in the finite difference model. Since stresses and strains in a plate are dependent upon deflections and the associated changes in deflection, wrinkling could possibly create higher magnitudes of stress and strain within the geosynthetic.

Table 5.8 Comparison of Cable Net Model Results (Halvordson 2007)

Maximum Values	W edge (m)	W center (m)	Ds (m)	U max (m)	Ex	Nx edge (N/m)	Nx pile (N/m)
Cable Net	0.176	0.1910	0.186	0.0105	0.0298	15200.0	21733.3
Finite Difference	0.168	0.1911	0.1861	0.0133	0.0395	15156.3	29645.2

5.7.3 Comparison to Parabolic Design Guide

Several design methods for calculating tension and strain within the geosynthetic exist, which yield conflicting results. One such method investigated by McGuire and Filz (2008) is used in both the British Standard BS8006 and Swedish design guides. In this method the calculations are based on a parabolic approximation of the geosynthetic spanning the region between piles. It is also assumed that the tension is uniform, with critical regions spanning directly between adjacent columns. With these assumptions and a similar unit cell approach to geosynthetic-reinforced embankments, the tension and strain can be determined based on the following:

$$\varepsilon = \frac{T}{J} \tag{5.1}$$

$$96 * T^3 - 6\widehat{K_g}^2 * T - \widehat{K_g}^2 * J = 0 \tag{5.2}$$

$$\widehat{K_g} = \left(\frac{p(s^2-a^2)}{a}\right) \tag{5.3}$$

where, s = center to center spacing of columns
a = pile width
p = net pressure over the soft soil

The standard set of parameters was used in the parabolic design method to calculate an approximate strain. It was found that the parabolic method yields 0.03125 maximum strain, while the finite difference program implemented in this research showed a maximum strain of 0.040. The conflicting results are most likely due to the generalized assumptions made in the parabolic method. Most importantly, the parabolic method does not take into account arching effects caused by the soft soil. A constant vertical pressure is applied over the unit cell, with a single vertical sub-grade support modulus. In the finite difference method, soil arching was included by assigning higher values of sub-grade support and vertical pressure over the piles than over the soft soil region. A dramatic spike in strain was also shown to exist over the square pile corners using the three-dimensional finite difference analysis. This peak is not accurately accounted for when considering the parabolic strain design equation. Also neglected by the parabolic method is the effect of Poisson's ratio. Although a Poisson's ratio of 0 was selected in the standard case of parameters, it can be accurately taken into account in the proposed finite difference formulation.

5.7.4 Effectiveness of Geosynthetic Support

The effectiveness of the geosynthetic reinforcement on embankment performance can be quantified by determining the ratio over the soil of the force supported by the soil to the downward force applied. This was determined using the finite difference program through Equation 5.4. In general, this ratio is Ks times the sum of the vertical displacements of the geosynthetic spanning the soft soil regions, divided by Qs times the area of the soil:

$$\text{Reinforcement Ratio} = \frac{Ks \sum_i \sum_j w[i,j] * h^2}{Qs * \left[\left(\frac{L}{2}\right)^2 - B^2\right]} \quad (5.4)$$

The subsequent ratios obtained for each of the pile orientations are as follows:

Square Piles:	0.807
Circular Piles:	0.819
Rotated Square Piles:	0.712

Based on these findings, it can be deduced that the rotated square piles are most effective at transferring load from the soft soil to the columns. The geosynthetic is therefore providing the most support when used with rotated square piles.

Chapter 6

Alternate Parameter Model

6.1 Introduction

An alternative set of dimensional parameters was selected to further analyze the response of the geosynthetic reinforcement with respect to various pile orientation types. The objective of the analysis was to determine the relative effect that different loading and support stiffness had on the proposed finite difference based model. In Mazursky (2006), an extensive parameter study was performed in which a variety of non-dimensional values were varied. Similar modeling assumptions and approach were used in the analysis. Therefore conducting a similar large-scale parameter study was deemed unnecessary and rather two unique data sets were investigated to provide insight into the geosynthetic behavior.

6.2 Alternative Parameter Case

An alternative parameter case was analyzed to determine the effects that different values had on the geosynthetic response. The parameters chosen were based on previous work done on the subject by Mazursky (2006). In her research, a Rayleigh-Ritz based method was used to model the geosynthetic, with relative success. The values used here were again chosen to provide means of comparison between the various models of geosynthetic reinforcement. The following dimensional parameters were used in the alternative case:

$B = 0.6$ m

$L = 3.0$ m

$E = 500$ MPa

$\nu = 0$

$t = 1.5$ mm

$Ks = 300\ kN/m^3$

$Kp = 150\ MN/m^3$

$Qp = 184\ kPa$

$Qs = 24\ kPa$

Applying the non-dimensionalization described in Chapter 3, the following dimensionless parameters were used in the analysis:

$b = 0.20$

$r = 0.2257$

$kp = 1{,}420.94$

$ks = 7.792$

$qp = 4.766$

$qs = 1.0$

$\beta = 1.490$

$\alpha = 4.221 \times 10^{-8}$

6.3 Square Piles

6.3.1 Deflections

Deflection results are presented in Figures 6.1-6.8 and Table 6.1.

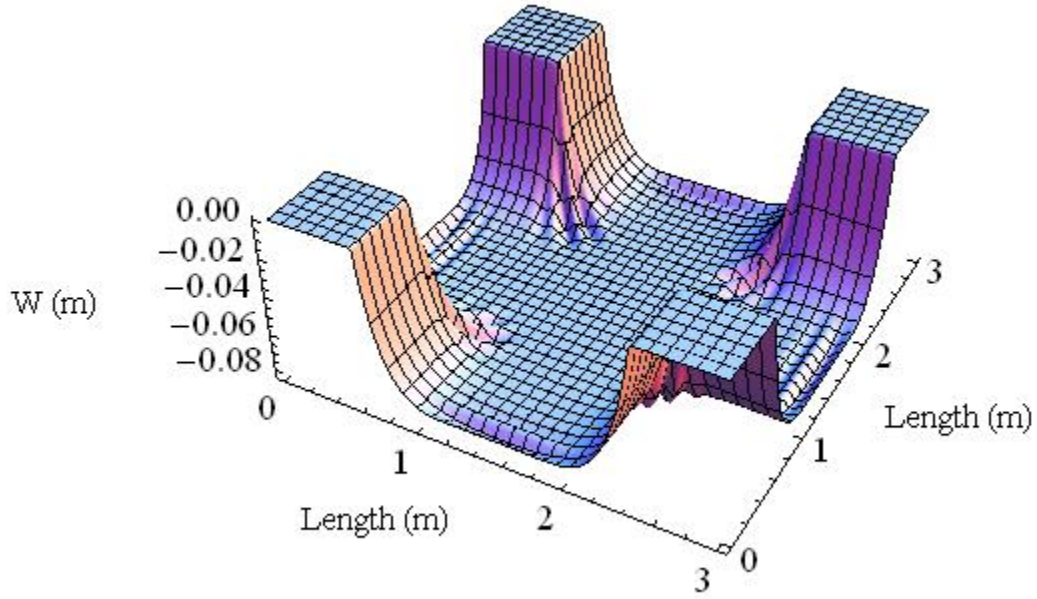

Figure 6.1 Three – Dimensional Plot of W Deflection

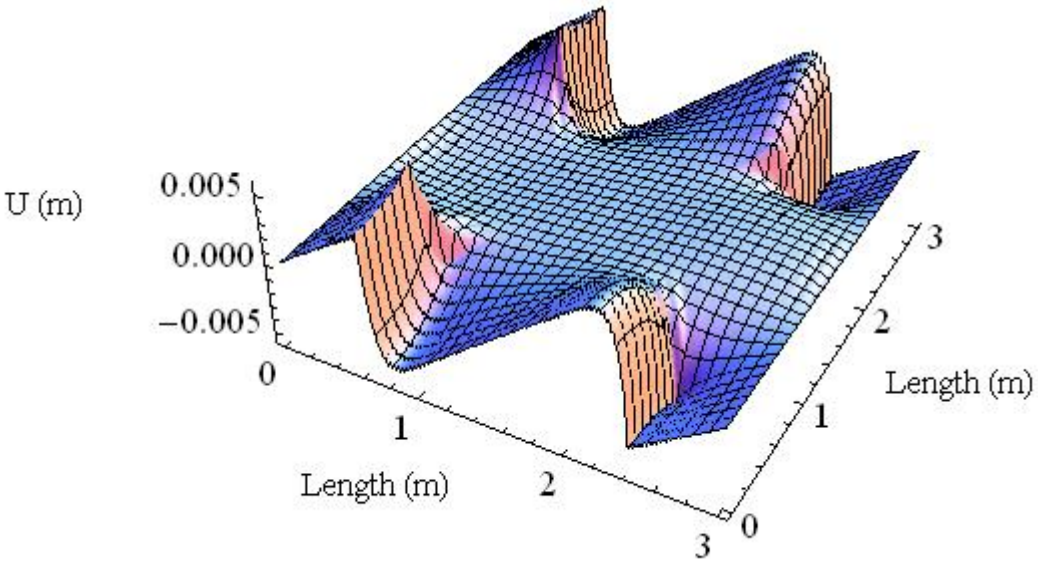

Figure 6.2 Three – Dimensional Plot of U Deflection

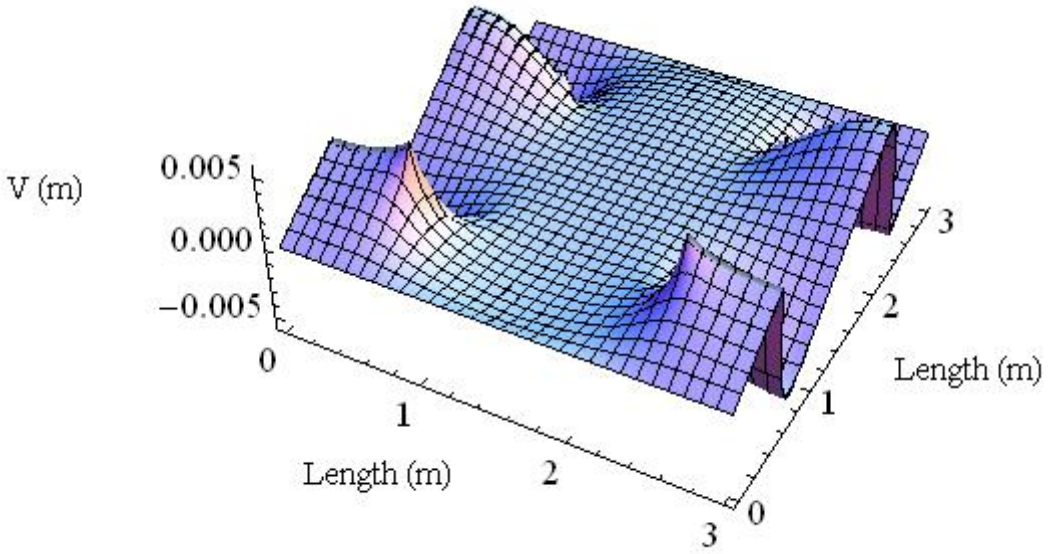

Figure 6.3 Three – Dimensional Plot of V Deflection

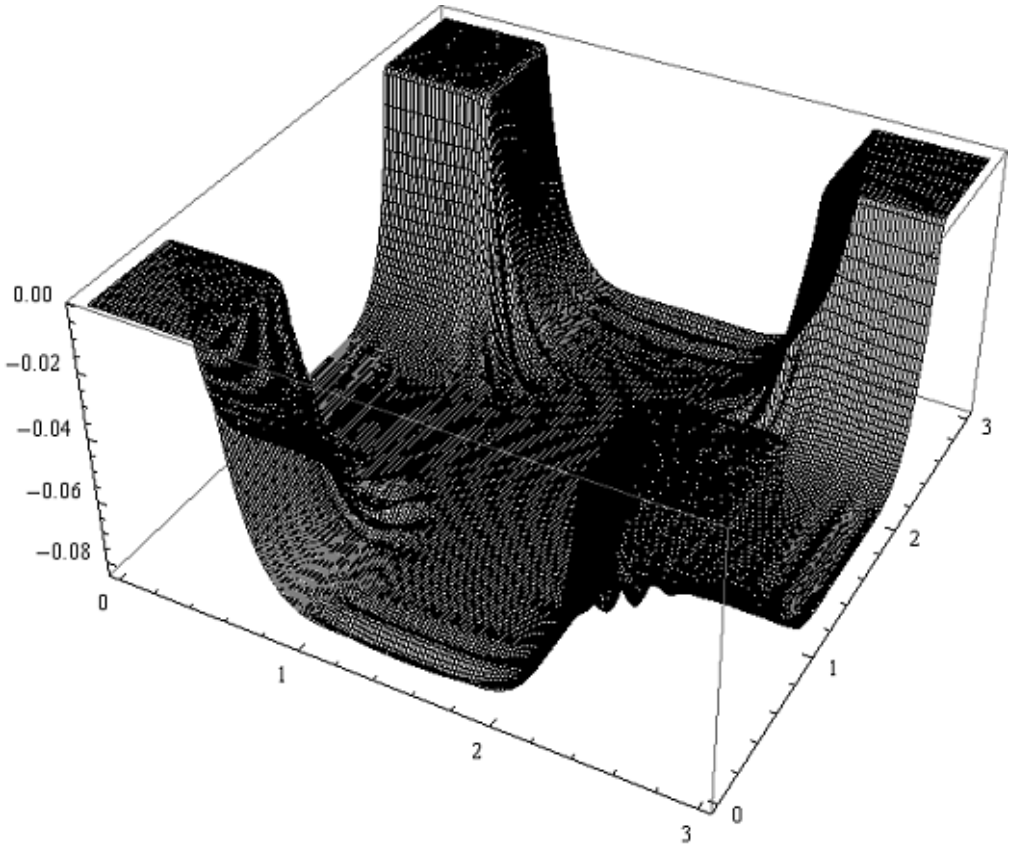

Figure 6.4 Total Deflected Shape

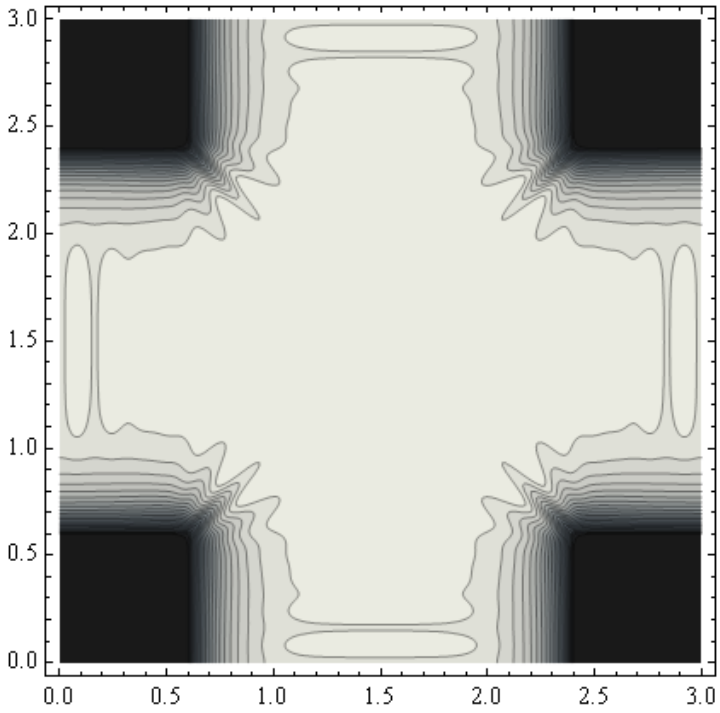

Figure 6.5 Contour Plot of W Deflection

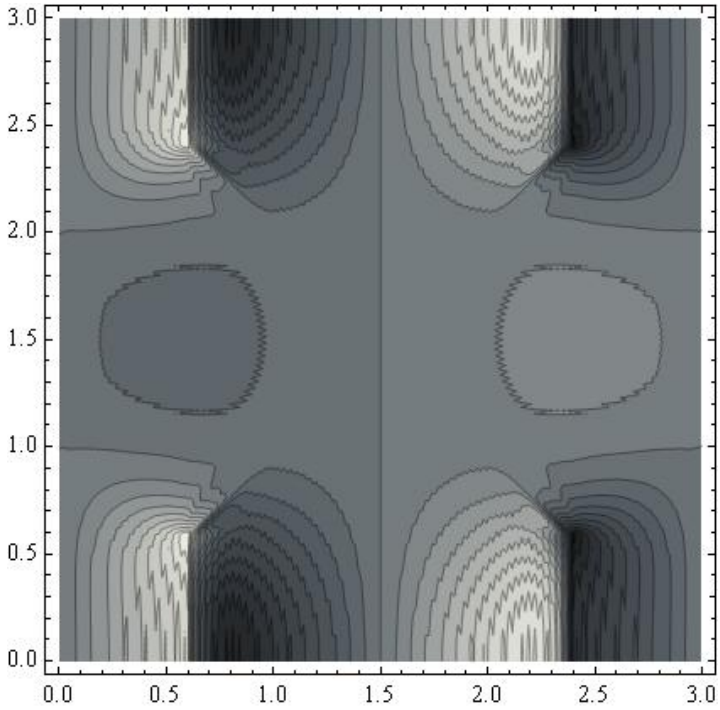

Figure 6.6 Contour Plot of U Deflection

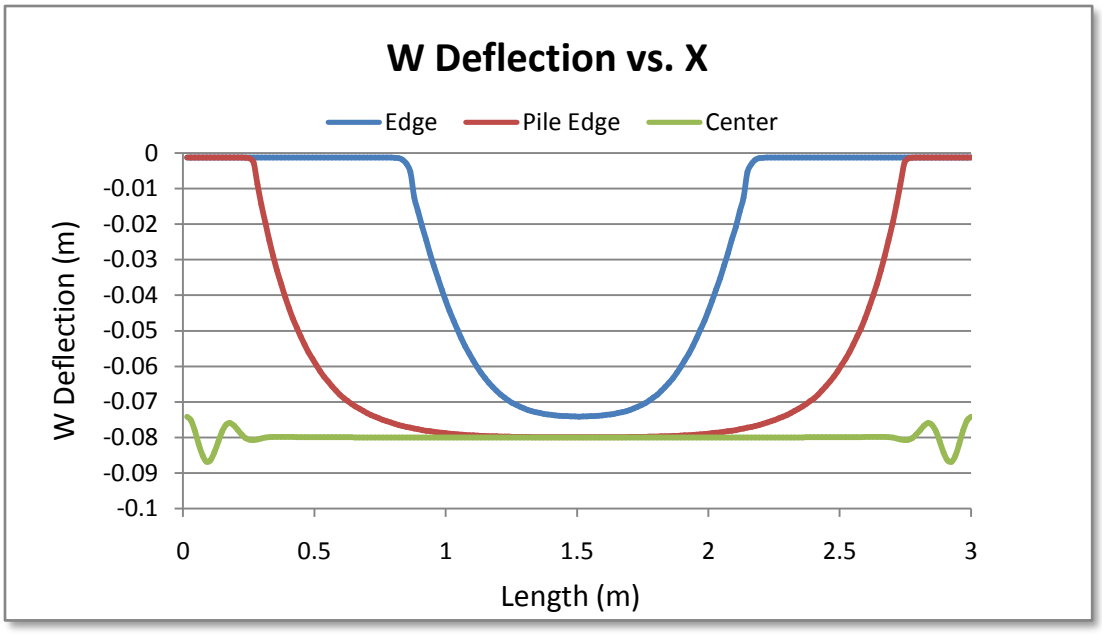

Figure 6.7 Two – Dimensional Plot of W Deflection Versus X

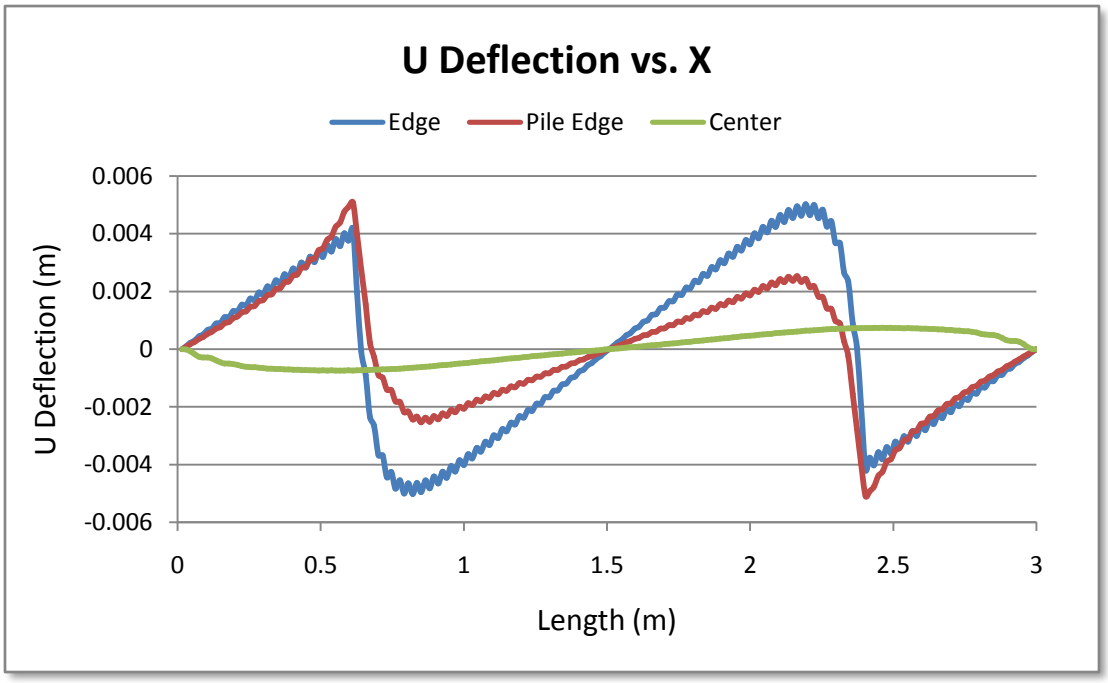

Figure 6.8 Two – Dimensional Plot of U Deflection Versus X

Maximum vertical deflection is seen to occur at the center of the geosynthetic and is 0.0827 m. Similarly, the maximum in-plane deflection is 0.0051 m along the line through the pile edge and parallel to the X axis. This is also similar to the standard parameter case in that the maximum in-plane deflection was found to occur along the pile edge. Maximum differential settlement along the edge was 0.0756 m, and 0.0815 m at the center. Again, due to symmetry, the maximum and minimum U and V displacements are the same.

Slight waviness in the in-plane displacement can be seen in Figure 6.8, resulting from slight finite difference approximation error. As discussed in Chapter 4, errors arise in finite difference analysis when the interval lengths are large. One of the four types of error, monotonic variation between two successive steps, is common in finite difference analysis and is apparent here. Although slight waviness exists, the change in displacement is trivial due to the small interval step. These errors would most likely vanish if a larger n value were selected; however, this would result in an increase in computer expense.

In general, the alternative parameter case tends to yield lower vertical and in-plane displacements than the standard case. This is most likely due to the increase in support stiffness over the soil and column support. Stiffness of the soil and pile were taken to be 29.2 MN/m^3 and 160 kN/m^3 for the standard case, while the alternative case used increased values of 150 MN/m^3 and 300 kN/m^3, respectively. Maximum and minimum displacements as well as differential settlements are summarized in Table 6.1.

Table 6.1 Deflections for Alternate Case Square Piles

Square Piles	W (m)	U, V (m)	Ds (m)
Max Center	0.0827	0.0007	0.0815
Max Edge	0.0768	0.0050	0.0756
Max Pile Edge	0.0799	0.0051	0.0768

6.3.2 Strains

Results for strains are presented in Figures 6.9 and 6.10, and in Table 6.2.

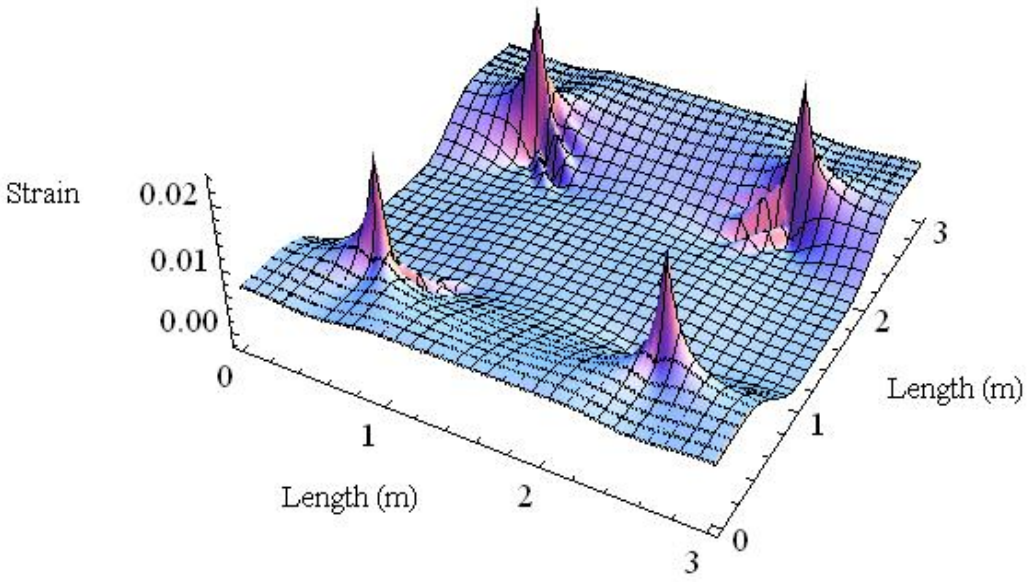

Figure 6.9 Three – Dimensional Plot of Ex

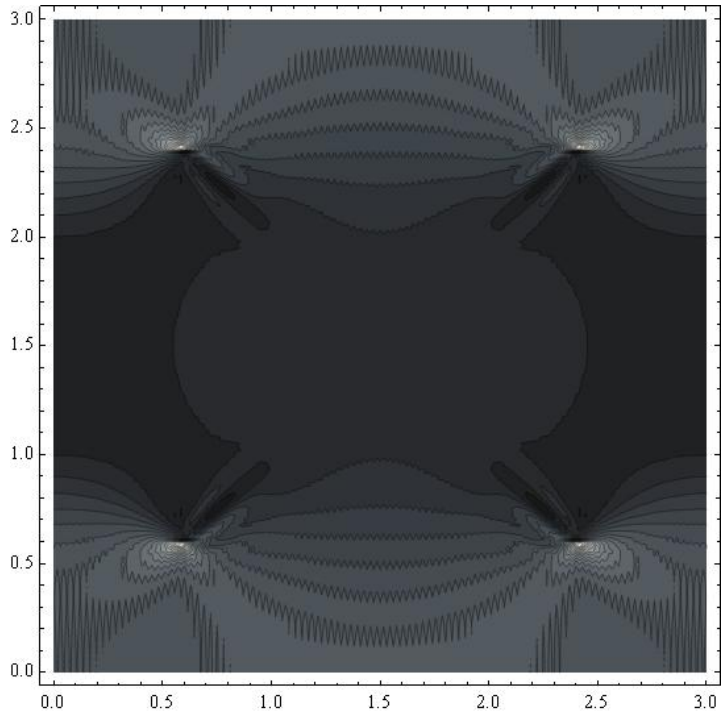

Figure 6.10 Contour Plot of Ex

In the alternative case with square piles, strain in the X direction reached a maximum of 0.024. Figure 6.9 shows that the maximum strain again occurs at the corner of the square pile. The alternative parameter set also yielded lower strain than the standard case. The standard case maximum strain in the X direction for square piles was 0.0395.

6.3.3 Stress Resultants

Results for stresses are presented in Figures 6.11-6.17 and Table 6.2.

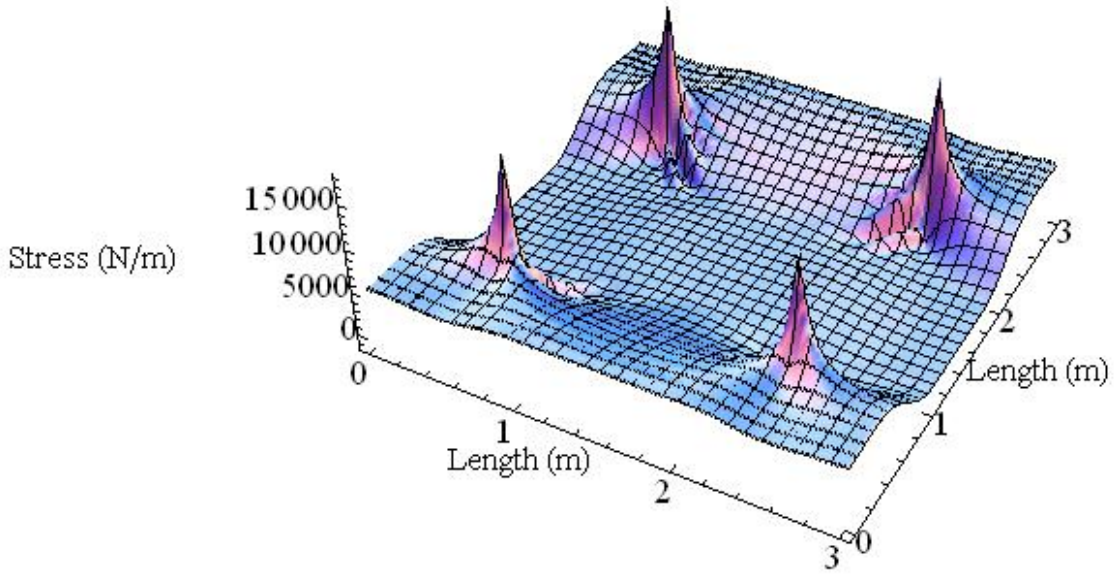

Figure 6.11 Three – Dimensional Plot of Nx

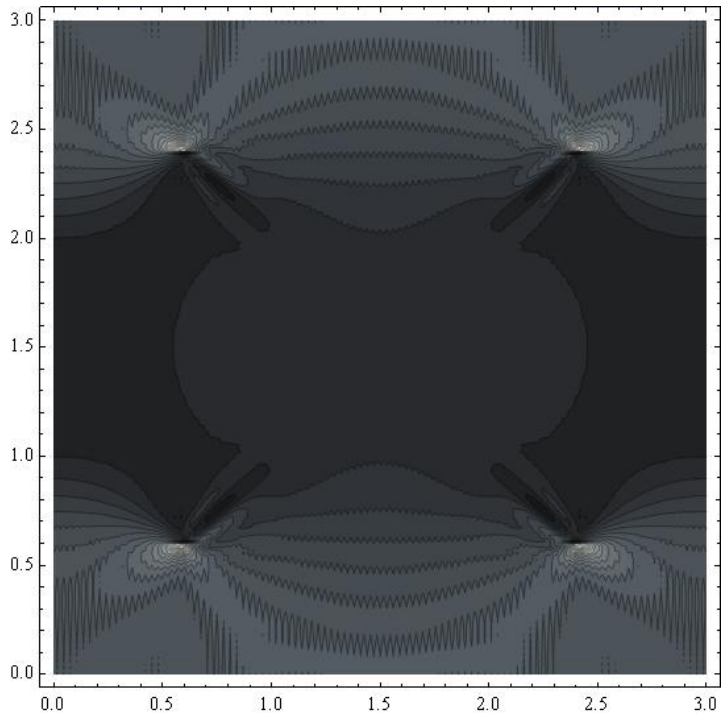

Figure 6.12 Contour Plot of Nx

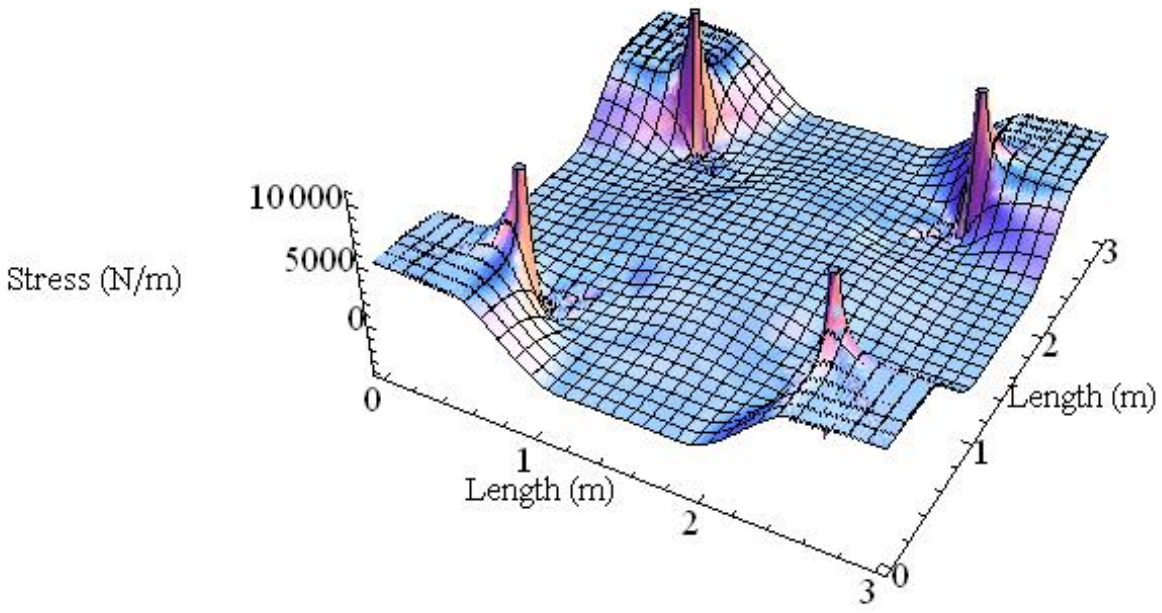

Figure 6.13 Three – Dimensional Plot of Nmin

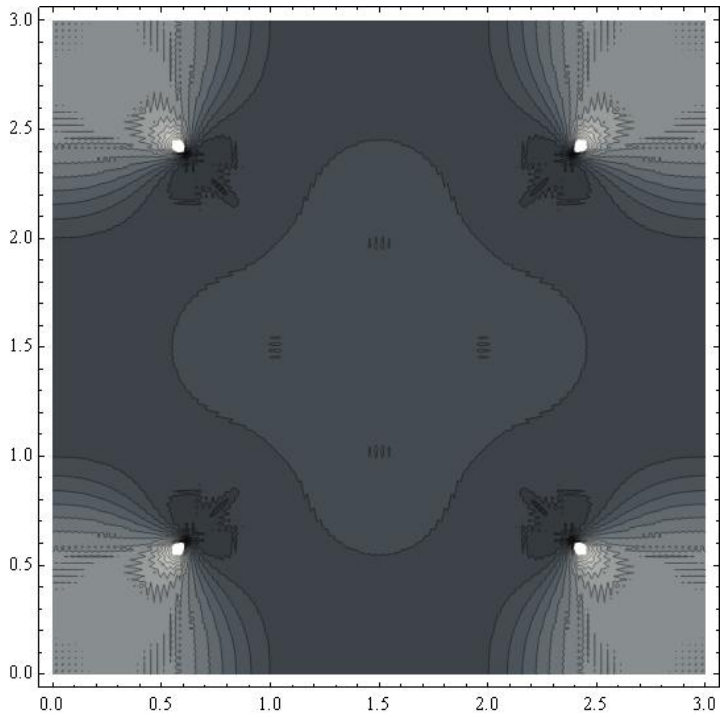

Figure 6.14 Contour Plot of Nmin

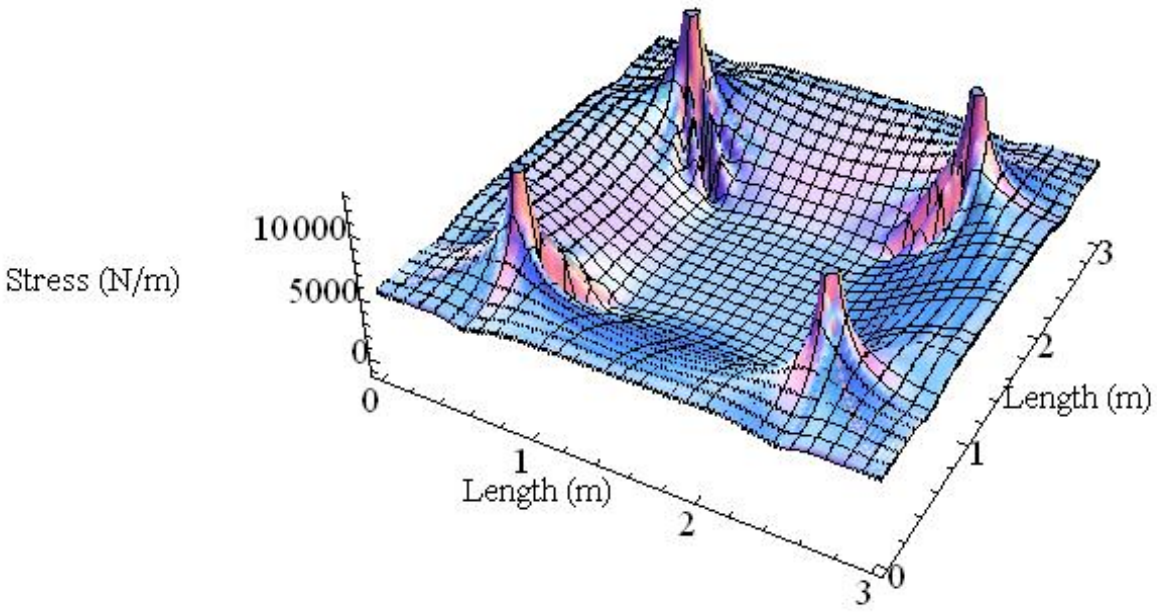

Figure 6.15 Three – Dimensional Plot of Nmax

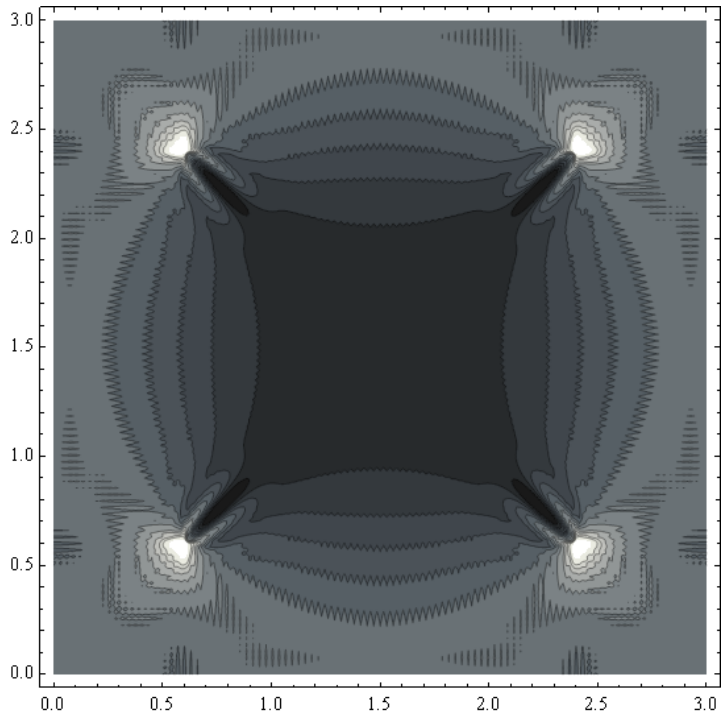

Figure 6.16 Contour Plot of Nmax

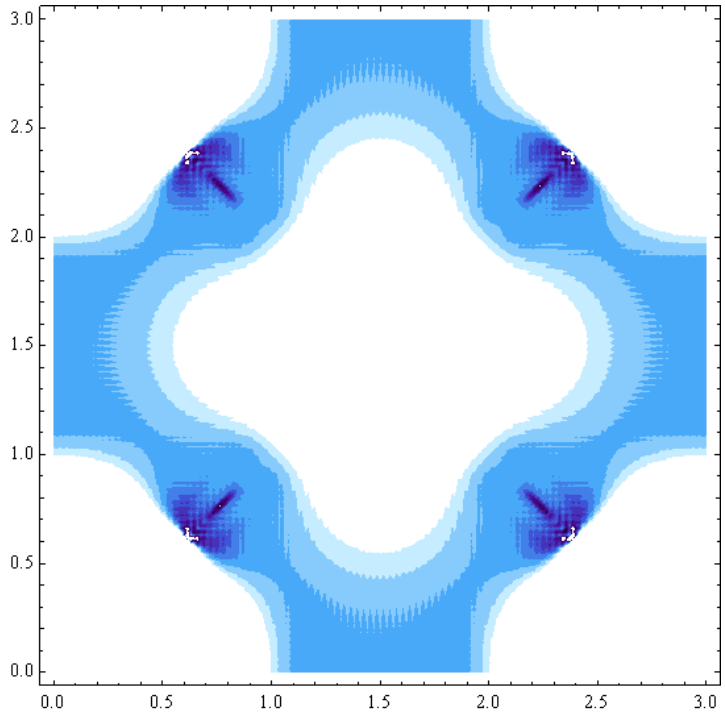

Figure 6.17 Contour Plot of Nmin Highlighting Region of Compressive Stress

Stresses in the geosynthetic were calculated for the X direction, minimum overall, and maximum overall. In the X direction, the maximum stress was 18,026 N/m and the minimum stress was 1,501 N/m. Maximum overall stress ranged from -1,224 N/m to 18,467 N/m and minimum overall stress from -4,049 N/m to 17,584 N/m. Figures 6.13 and 6.15 indicate that the maximum stresses are induced at the square pile corner. Also, Figure 6.17 shows the region in which compressive minimum stresses occur, giving rise to potential wrinkling of the geosynthetic.

Table 6.2 Stress and Strain for Alternate Case Square Piles

Square Piles	Ex	Nx (N/m)	Nmin (N/m)	Nmax (N/m)
Max	0.0240	18026.00	17584.40	18467.50
Min	-0.0020	-1501.03	-4049.58	-1224.64

6.4 Circular Piles

6.4.1 Deflections

Deflection results are presented in Figures 6.18-6.25 and Table 6.3.

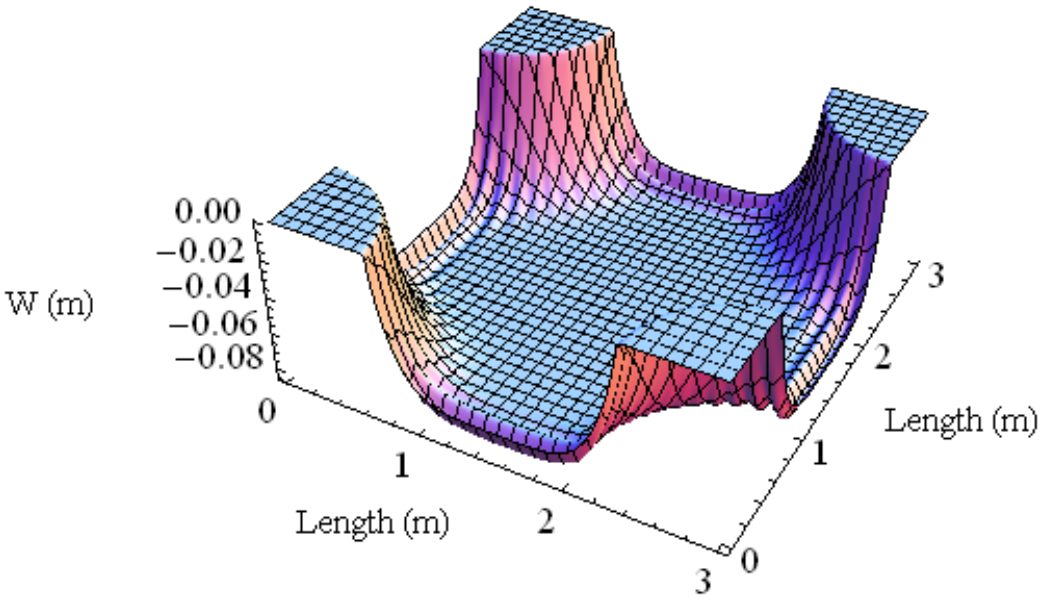

Figure 6.18 Three – Dimensional Plot of W Deflection

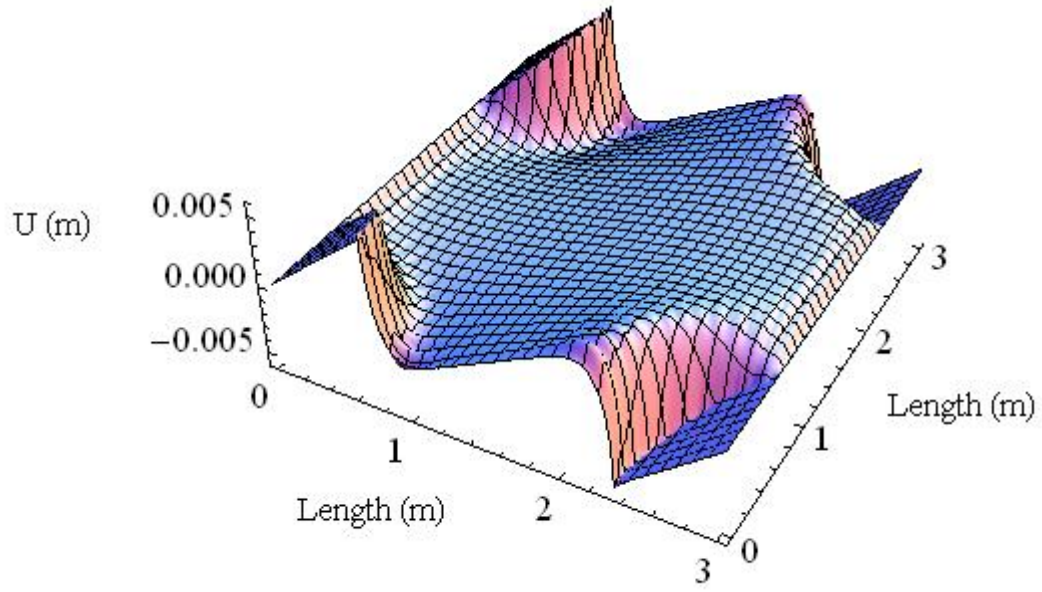

Figure 6.19 Three – Dimensional Plot of U Deflection

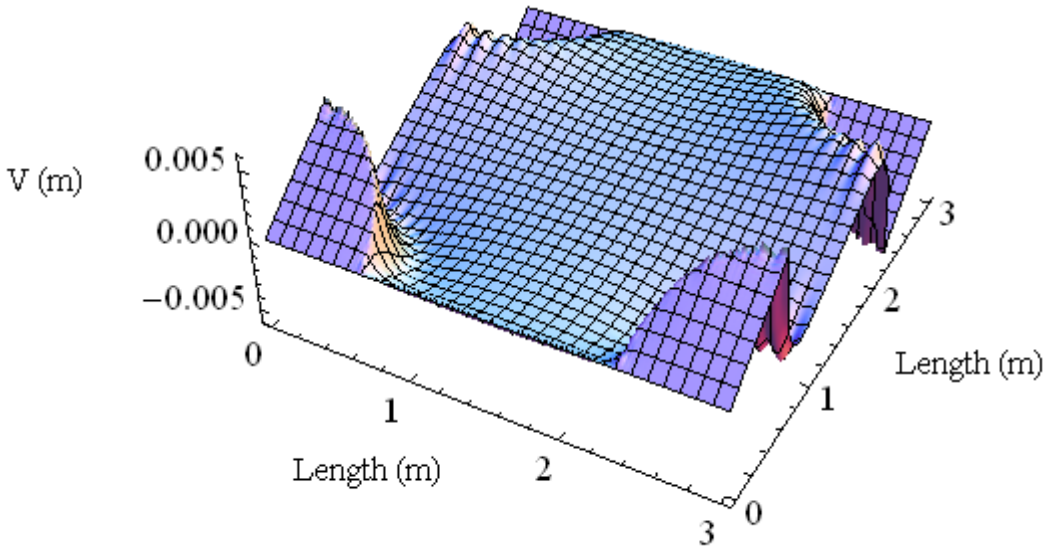

Figure 6.20 Three – Dimensional Plot of V Deflection

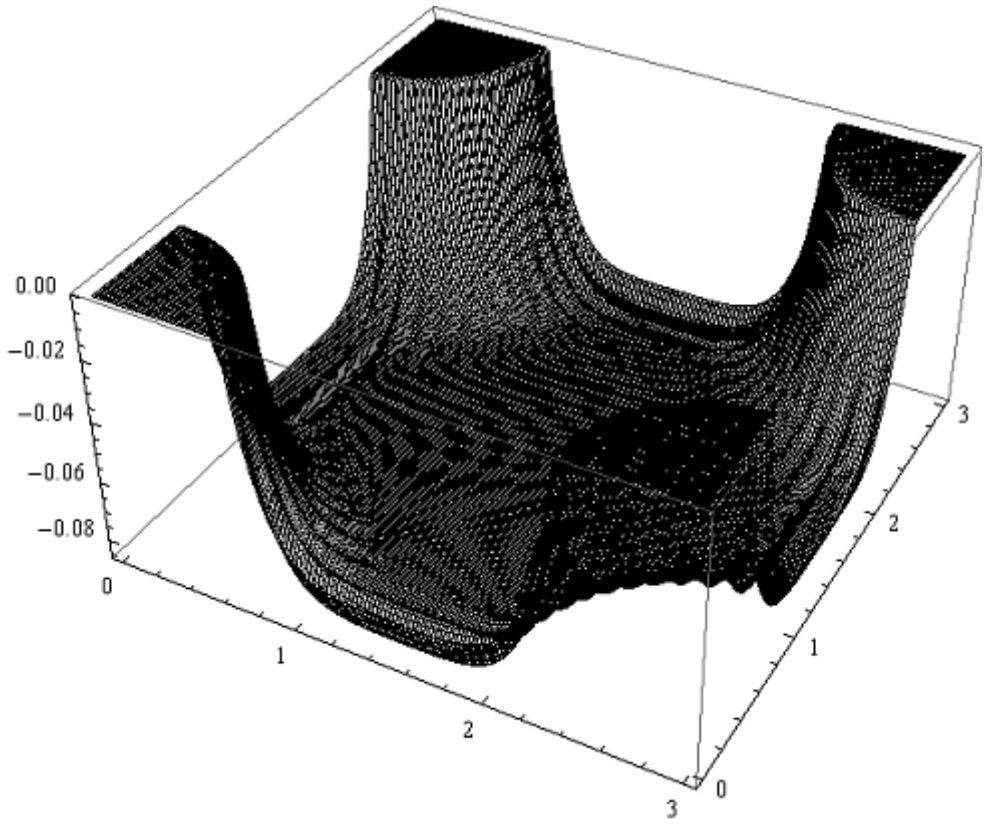

Figure 6.21 Total Deflected Shape

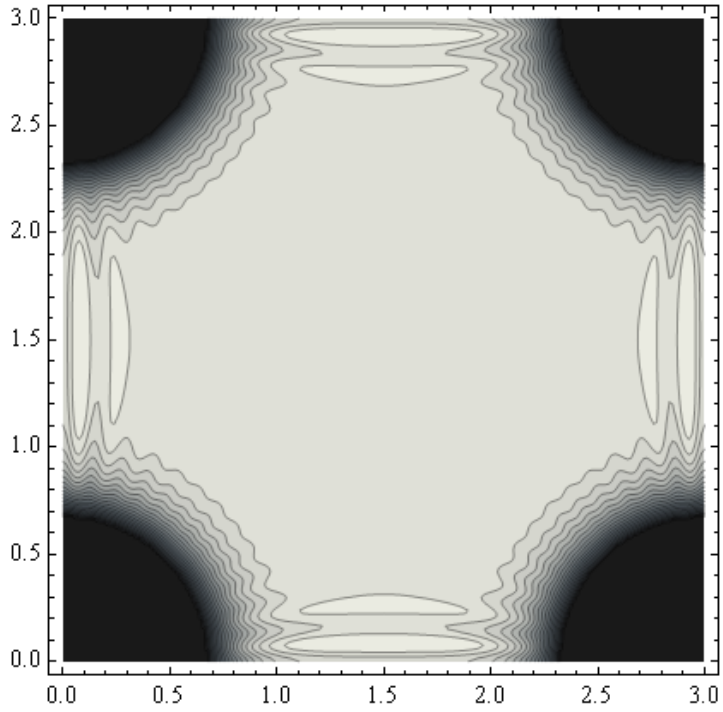

Figure 6.22 Contour Plot of W Deflection

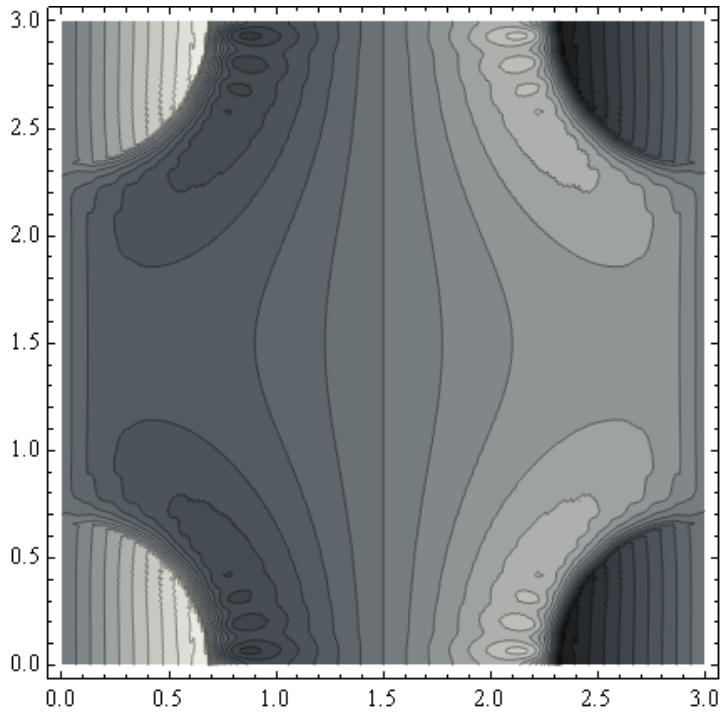

Figure 6.23 Contour Plot of U Deflection

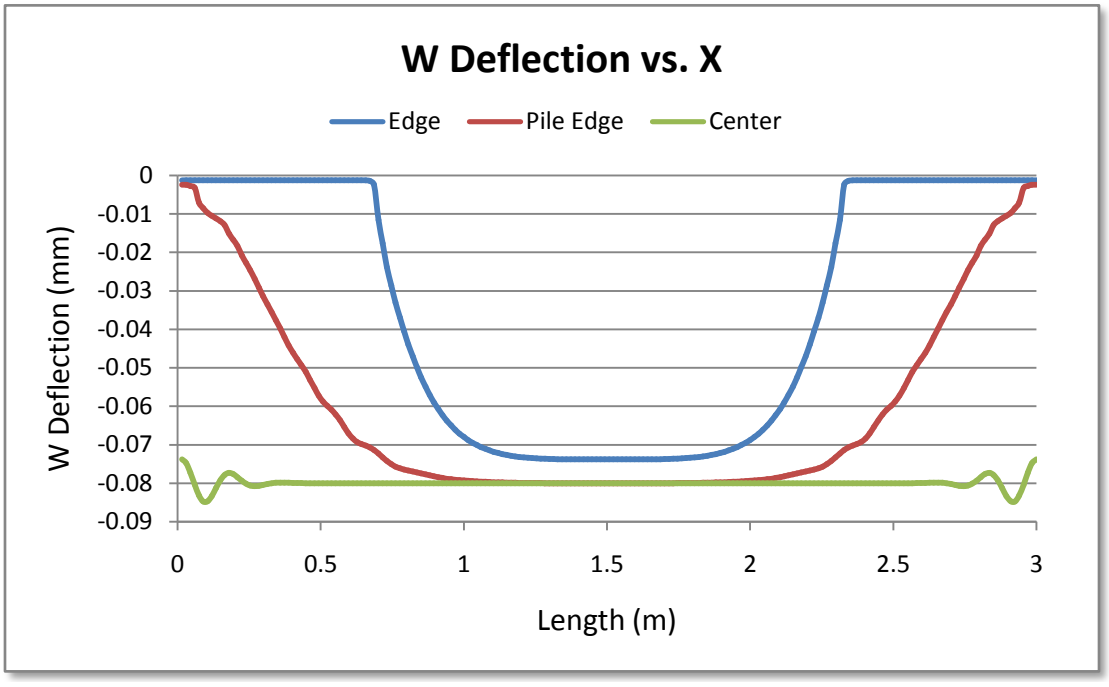

Figure 6.24 Two – Dimensional Plot of W Deflection Versus X

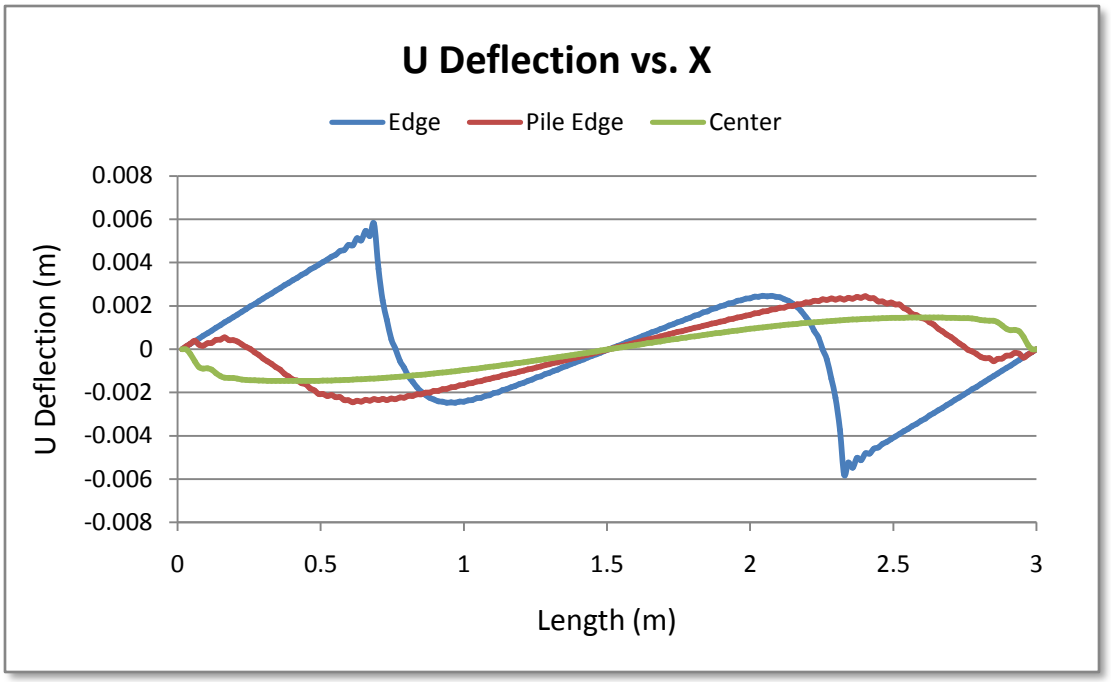

Figure 6.25 Two – Dimensional Plot of U Deflection Versus X

As can be seen in Figures 6.18 and 6.24, the maximum vertical deflection again occurs at the center of the geosynthetic and is 0.0847 m. The maximum in-plane displacement is along the geosynthetic edge and was found to be 0.0058 m. Differential settlement in the unit cell is maximum at 0.0835 m at the center, and at 0.0726 m along the edge of the geosynthetic. Again, the resulting displacements are significantly lower in the alternative parameter case with circular piles than for the standard case.

Table 6.3 Deflections for Alternate Case Circle Piles

Circle Piles	W (m)	U, V (m)	Ds (m)
Max Center	0.0847	0.0015	0.0835
Max Edge	0.0738	0.0058	0.0726
Max Pile Edge	0.0800	0.0024	0.0776

6.4.2 Strains

Results for strains are presented in Figures 6.26 and 6.27, and in Table 6.4.

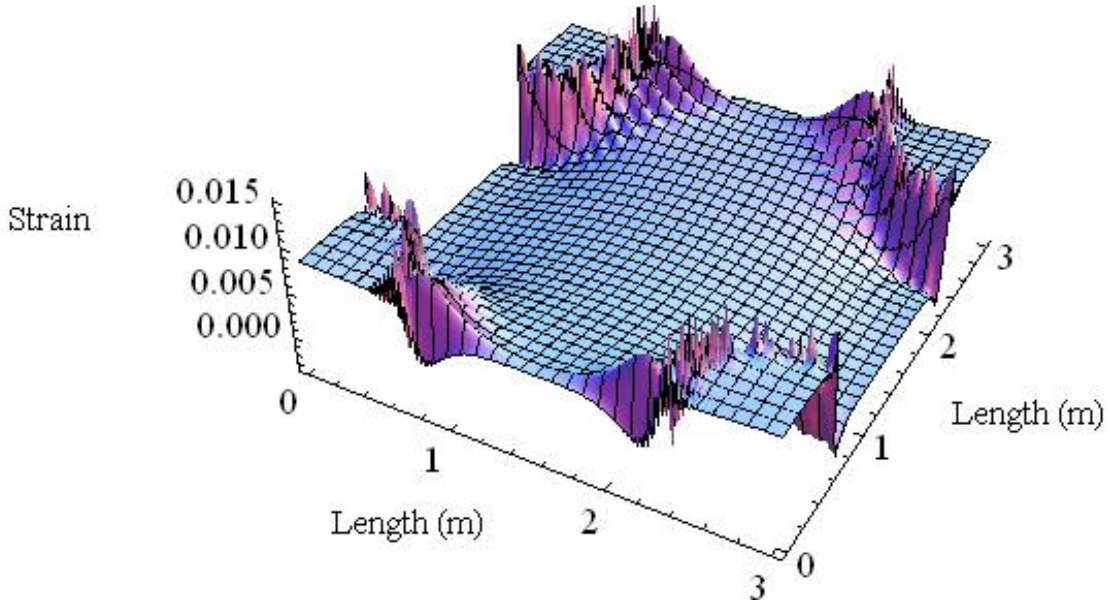

Figure 6.26 Three – Dimensional Plot of Ex

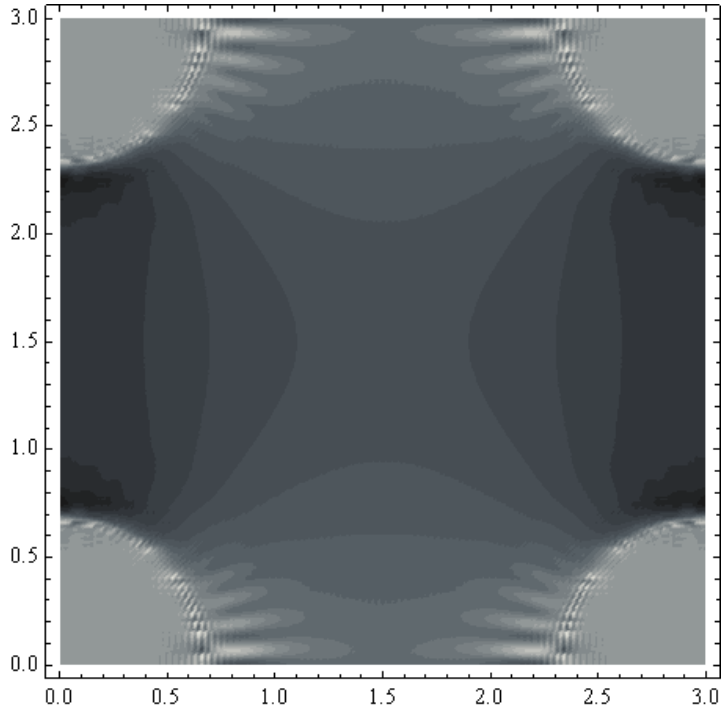

Figure 6.27 Contour Plot of Ex

6.4.3 Stress Resultants

Results for stresses are presented in Figures 6.28-6.34 and Table 6.4.

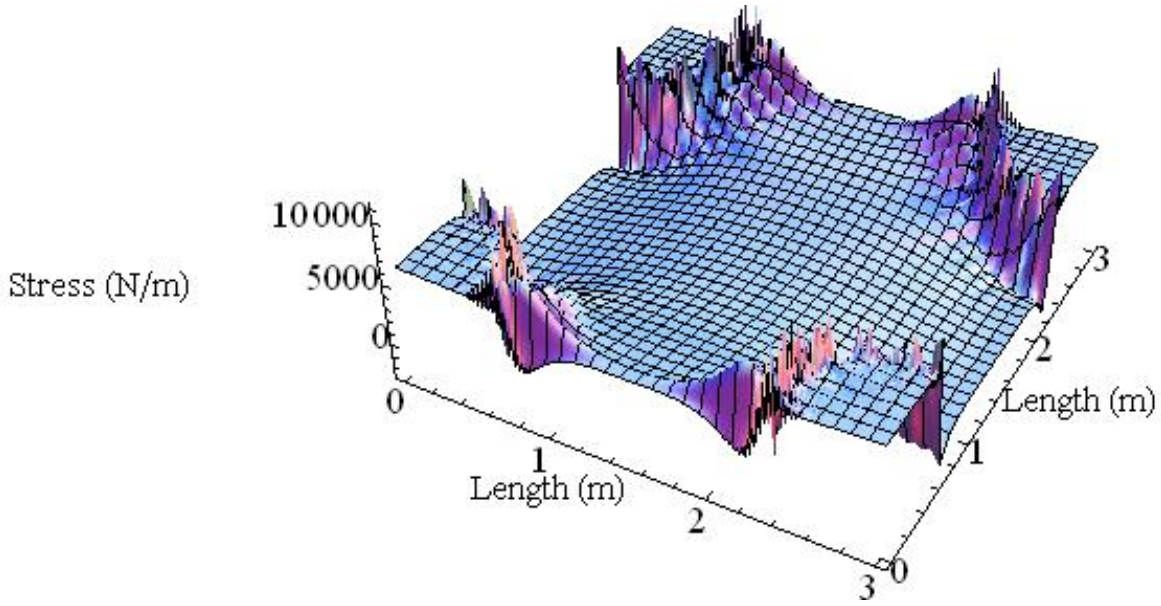

Figure 6.28 Three – Dimensional Plot of Nx

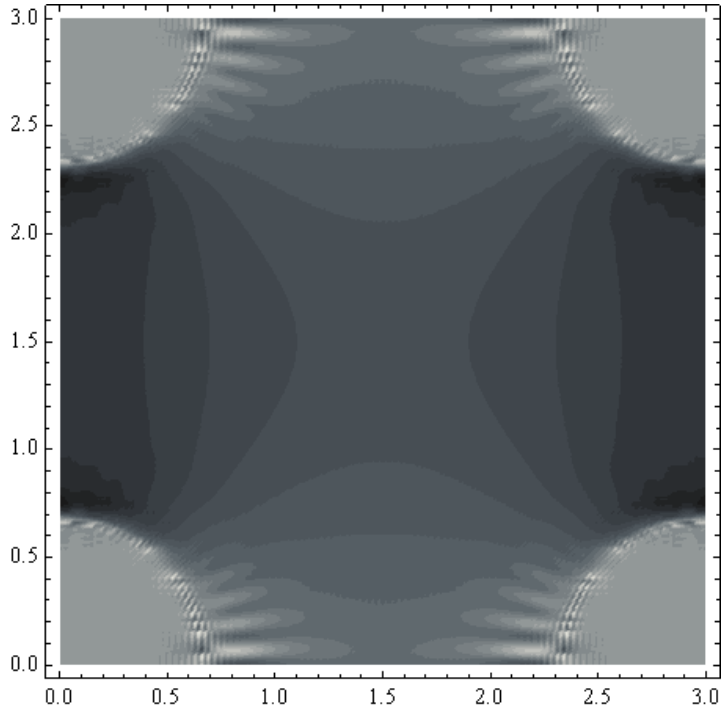

Figure 6.29 Contour Plot of Nx

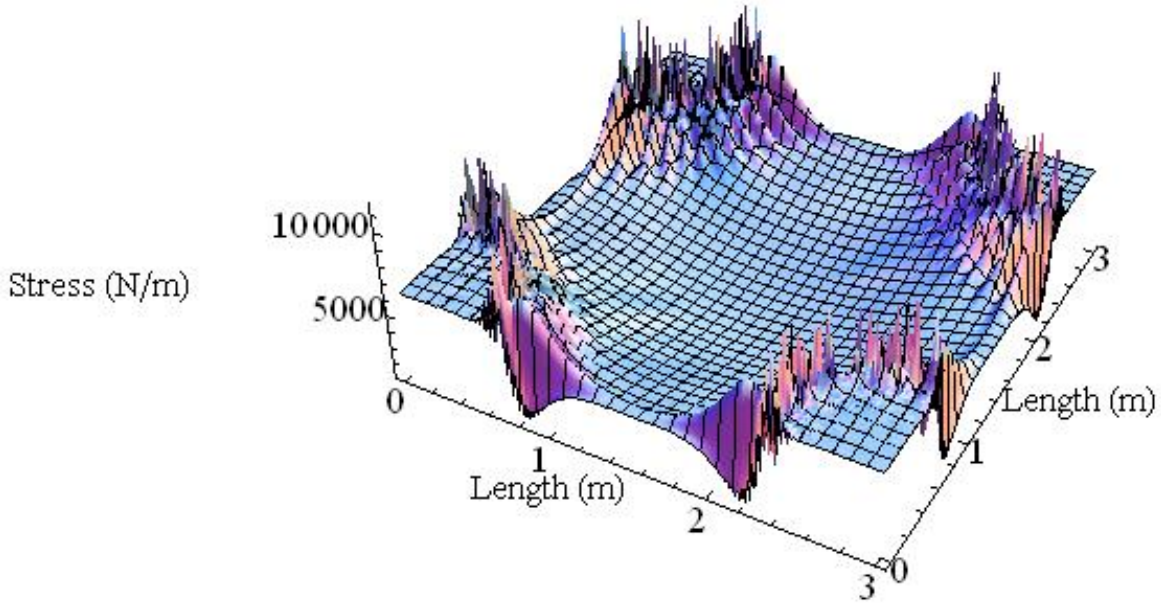

Figure 6.30 Three – Dimensional Plot of Nmax

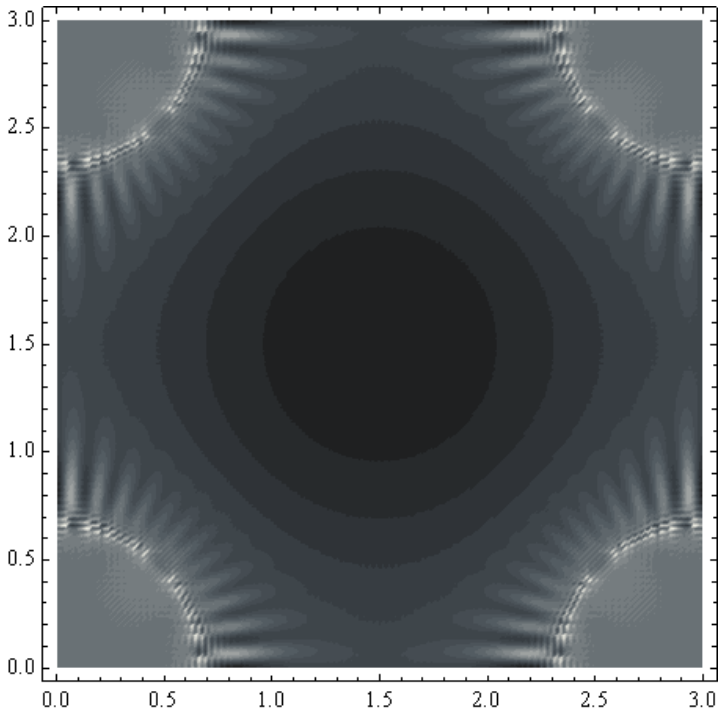

Figure 6.31 Contour Plot of Nmax

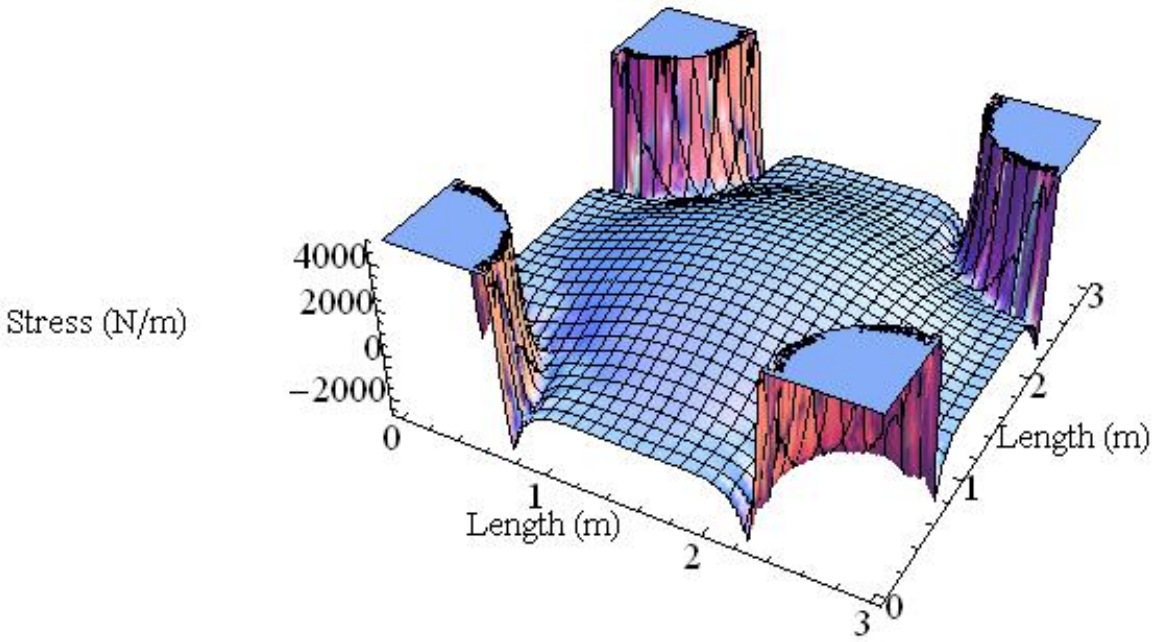

Figure 6.32 Three – Dimensional Plot of Nmin

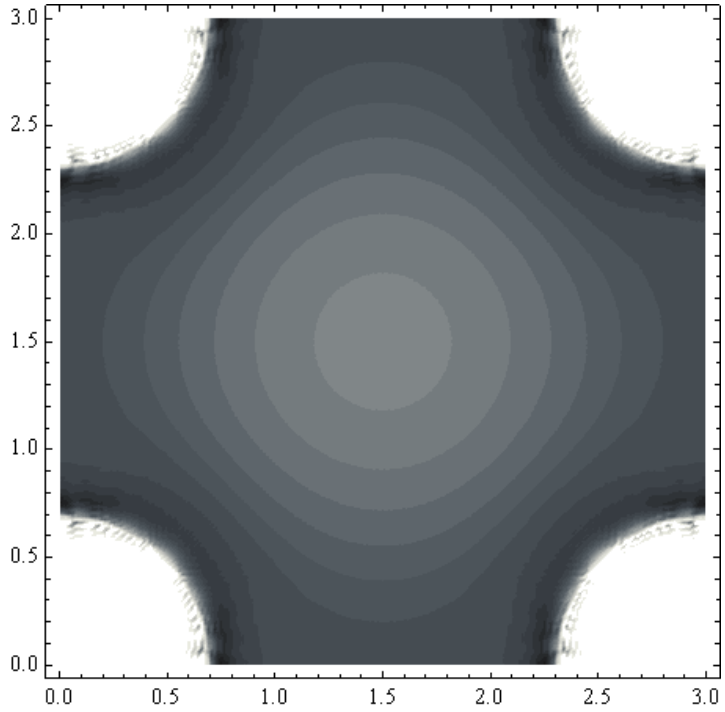

Figure 6.33 Contour Plot of Nmin

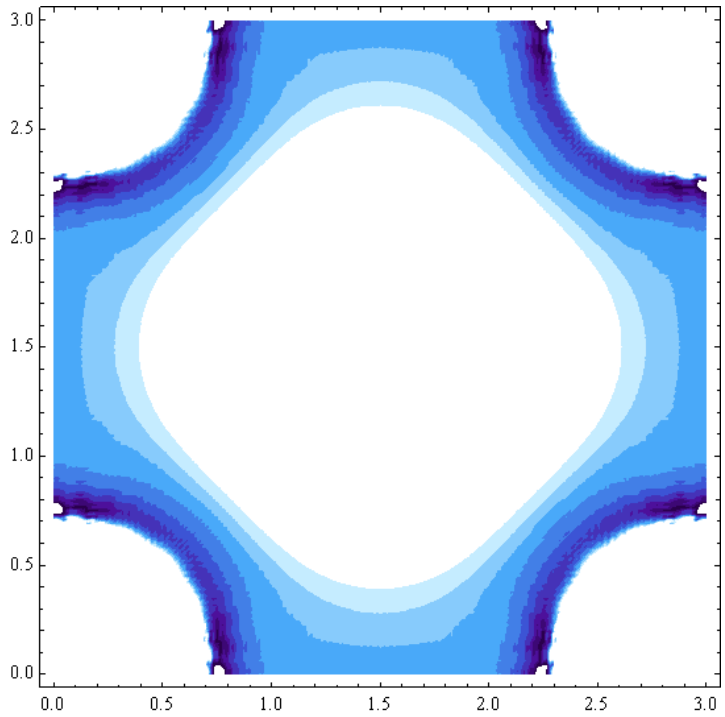

Figure 6.34 Contour Plot of Nmin Highlighting Region of Compressive Stress

Similar discontinuities in Chapter 5 are seen to exist in the three-dimensional plots of stress and strain for the alternative case with circular piles. Around each pile edge, a region of varying stress and strain is present. As discussed previously, representing the circular pile with a square finite difference mesh may be causing such erratic behavior. Three-dimensional plots of vertical and in-plane deflection are smooth and continuous, and therefore maximum stresses and strains can still be extracted from the data.

Maximum X direction strain in the geosynthetic for the alternative case with circular piles was calculated as 0.015. This magnitude of strain is the lowest encountered so far. This low value is most likely a result of implementing higher support stiffness in the alternative case and utilizing circular piles. Figure 6.26 shows that this maximum strain occurs around the pile edge.

Stresses in the X direction range from -2,656 N/m to 11,273 N/m in the geosynthetic. The maximum overall stress was also calculated as 11,529 N/m and the minimum overall stress as 8,487 N/m. Compressive stresses are again seen to exist within the geosynthetic, occurring

around the pile edges. Figure 6.34 explicitly shows the region in which negative stress and potential wrinkling occur.

Table 6.4 Stress and Strain for Alternate Case Circle Piles

Circle Piles	Ex	Nx (N/m)	Nmin (N/m)	Nmax (N/m)
Max	0.0150	11273.00	8486.88	11529.60
Min	-0.0035	-2655.83	-2655.83	1201.16

6.5 Square Piles Rotated 45°

6.5.1 Deflections

Deflection results are presented in Figures 6.35-6.42 and Table 6.5.

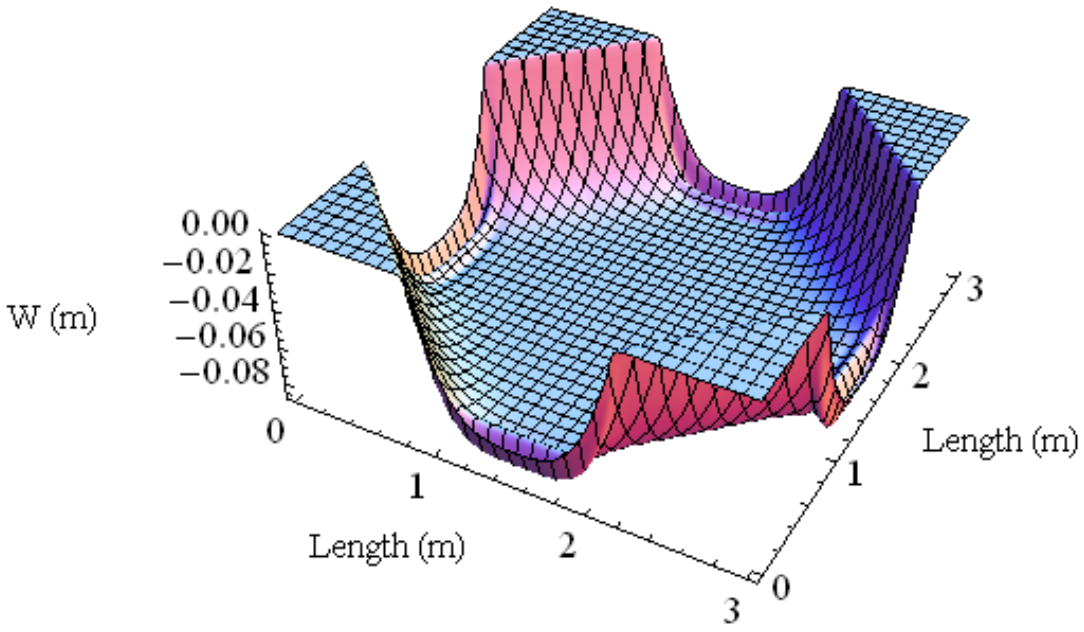

Figure 6.35 Three – Dimensional Plot of W Deflection

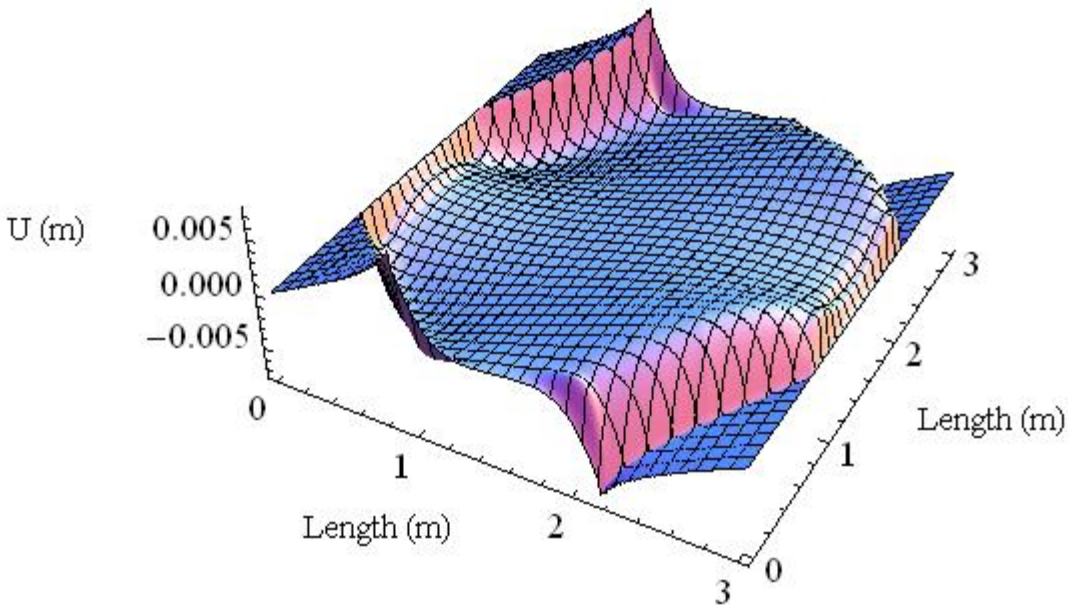

Figure 6.36 Three – Dimensional Plot of U Deflection

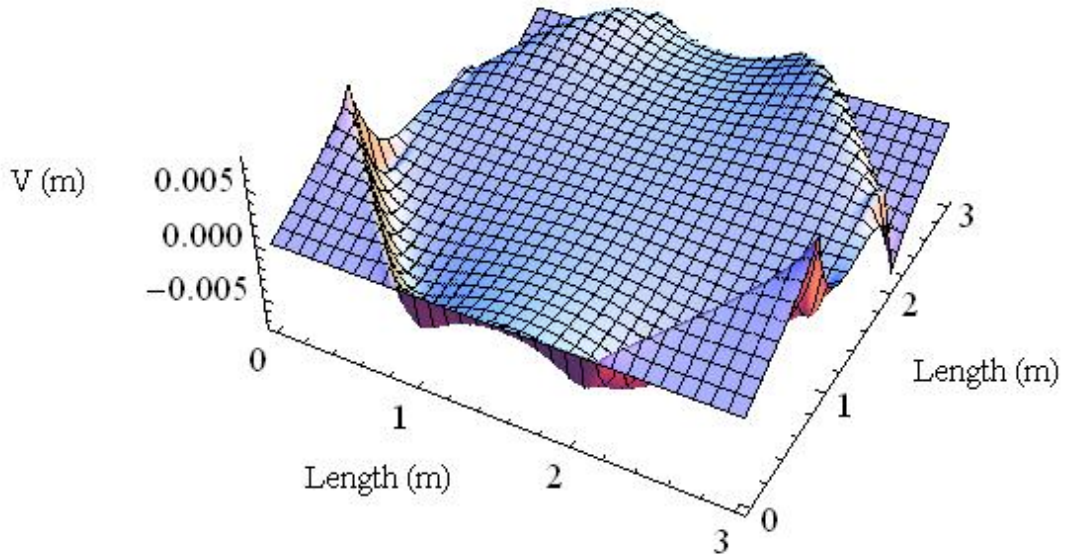

Figure 6.37 Three – Dimensional Plot of V Deflection

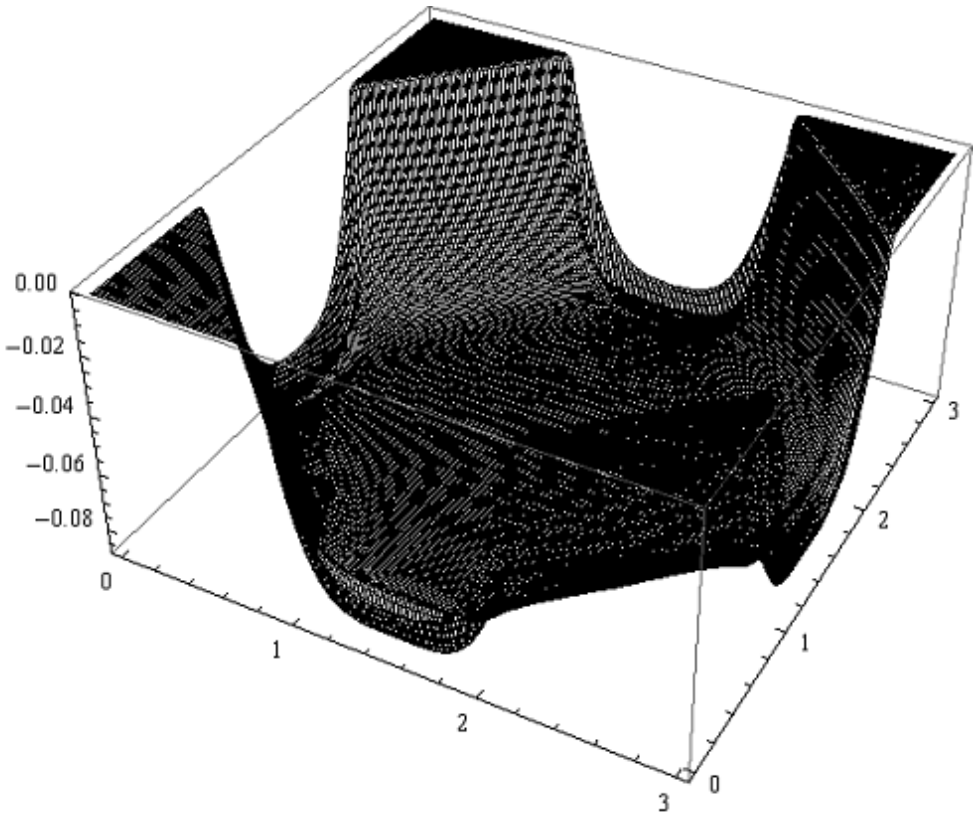

Figure 6.38 Total Deflected Shape

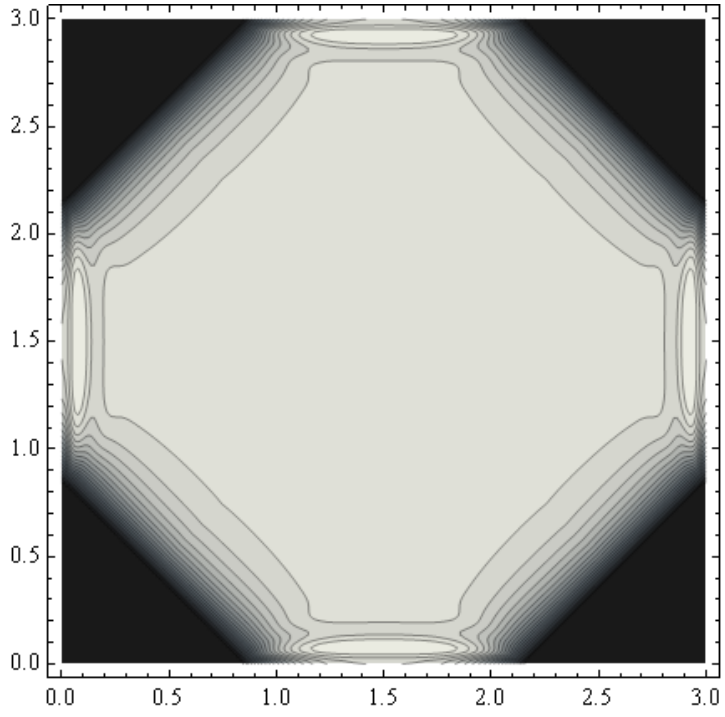

Figure 6.39 Contour Plot of W Deflection

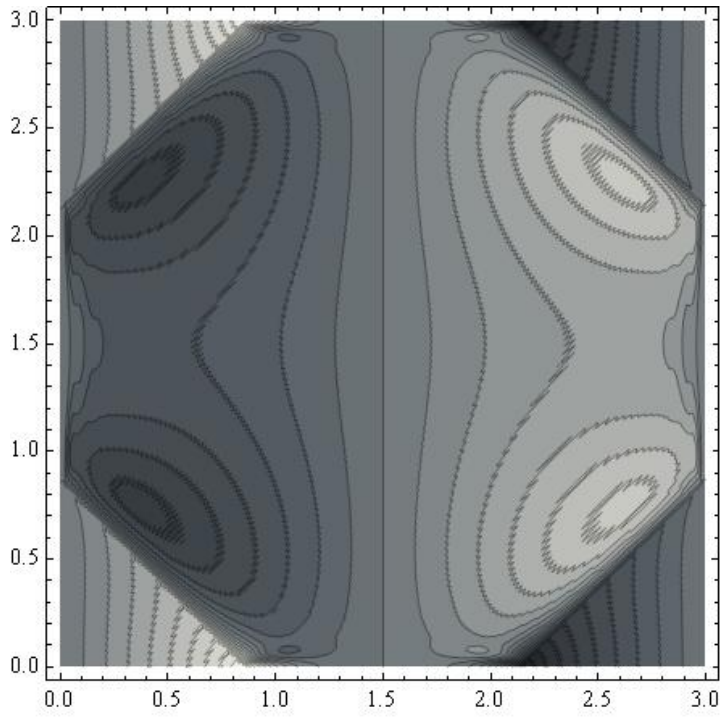

Figure 6.40 Contour Plot of U Deflection

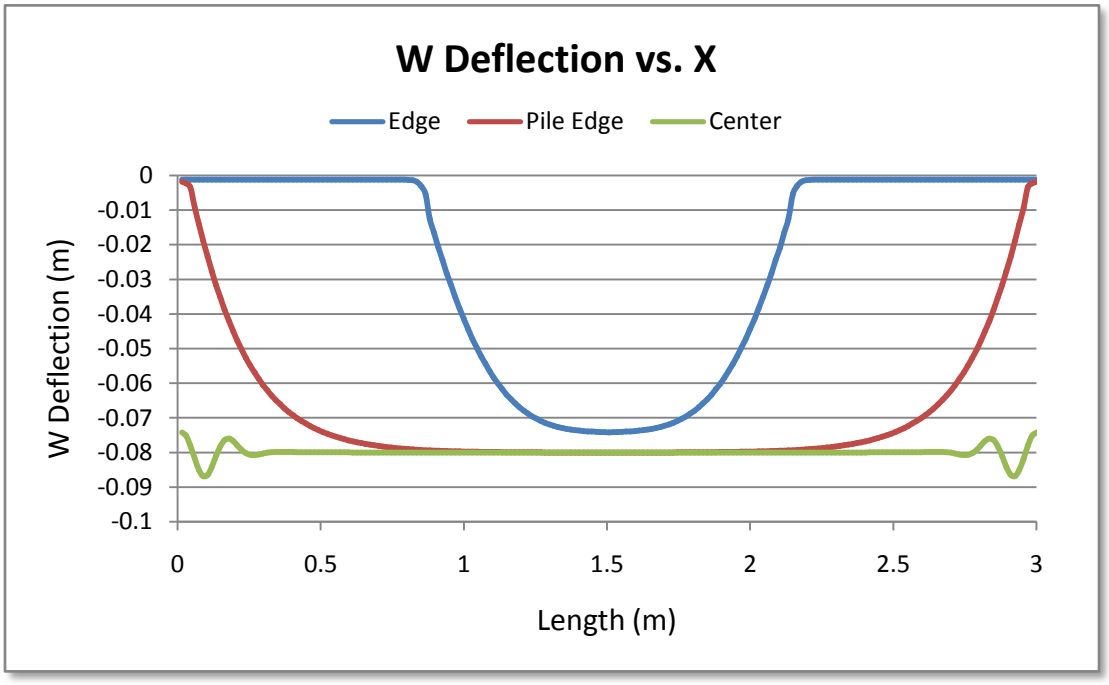

Figure 6.41 Two – Dimensional Plot of W Deflection Versus X

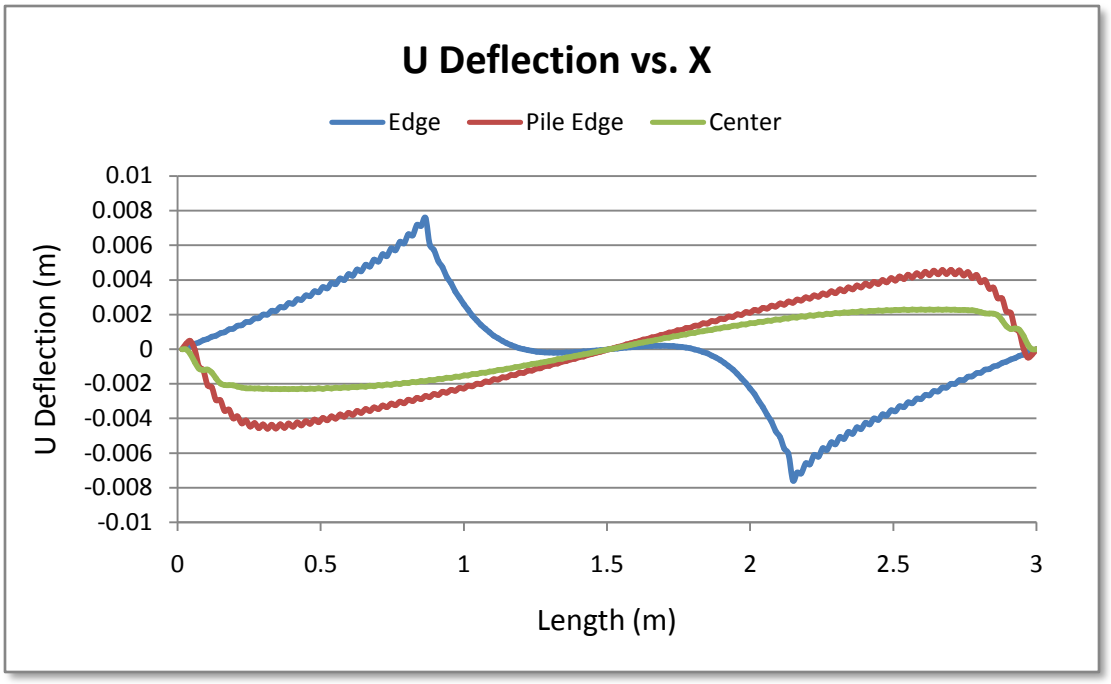

Figure 6.42 Two – Dimensional Plot of U Deflection Versus X

Maximum vertical deflection for the alternative case with rotated square piles was 0.0868 m. Figures 6.35 and 6.41 indicate that this maximum value occurs at the center of the unit cell. This deflection is the highest obtained for the alternative parameter case pile orientations. In the standard case, however, rotated square piles yielded the lowest vertical deflection. In-plane deflection was found to be maximum at 0.0076 m along the geosynthetic edge. Also, differential settlement was 0.0856 m at the center and 0.0729 m along the edge.

Table 6.5 Deflections for Alternate Case Rotated Square Piles

Rotated Square Piles	W (m)	U, V (m)	Ds (m)
Max Center	0.0868	0.0023	0.0856
Max Edge	0.0742	0.0076	0.0729
Max Pile Edge	0.0800	0.0045	0.0769

6.5.2 Strains

Results for strains are presented in Figures 6.43 and 6.44, and in Table 6.6.

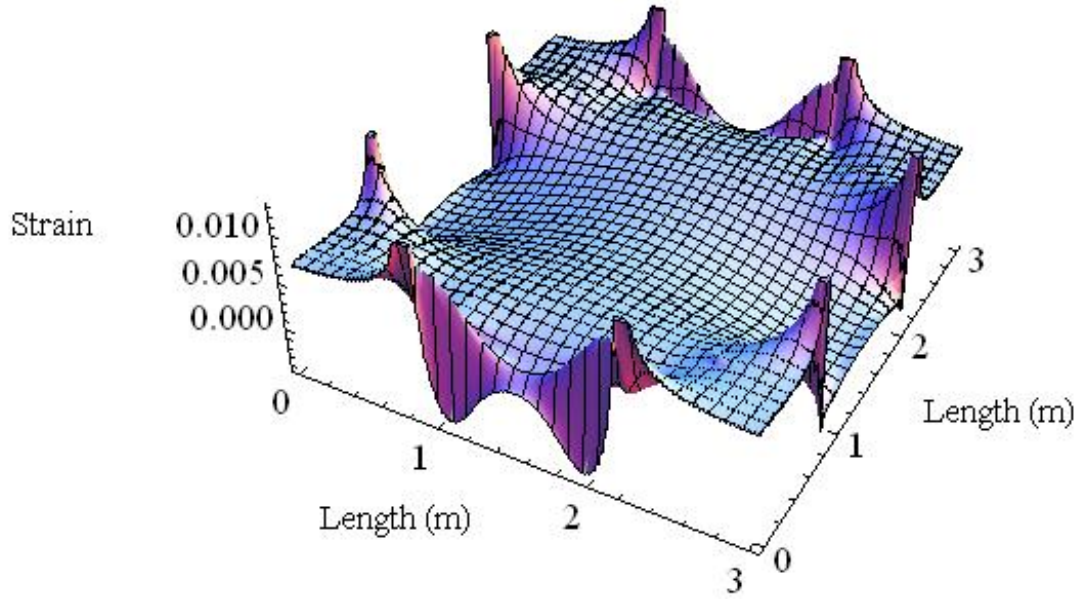

Figure 6.43 Three – Dimensional Plot of Ex

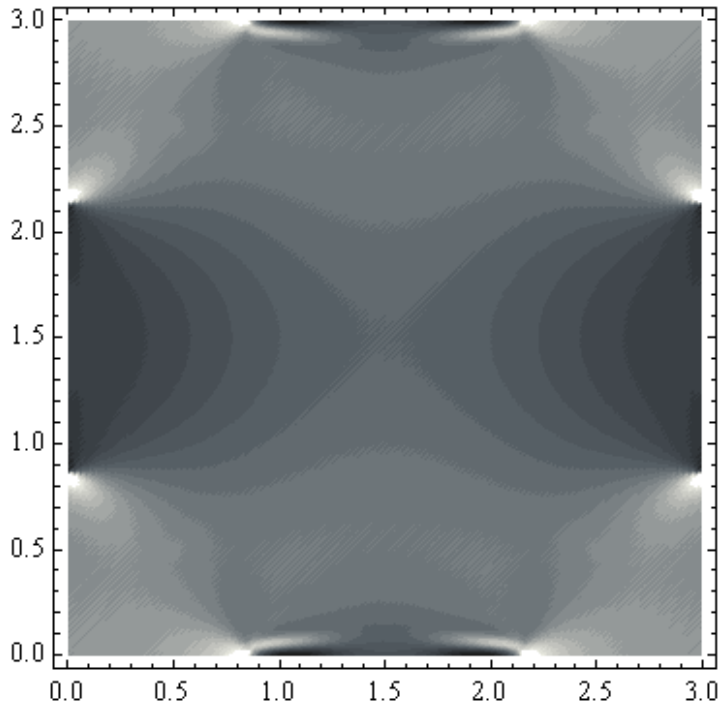

Figure 6.44 Contour Plot of Ex

6.5.3 Stress Resultants

Results for stresses are presented in Figures 6.45-6.51 and Table 6.6

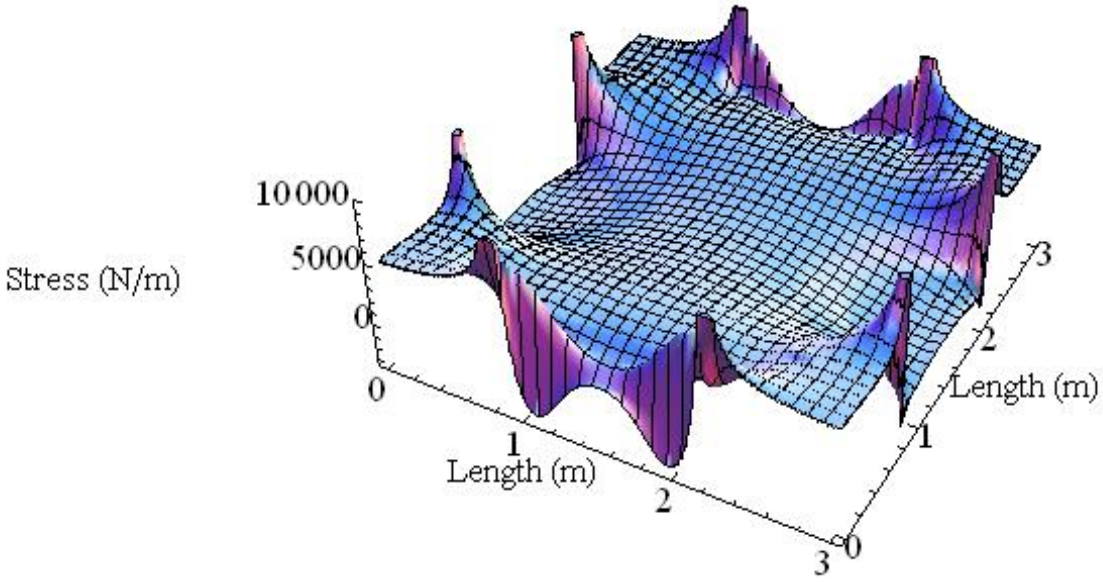

Figure 6.45 Three – Dimensional Plot of Nx

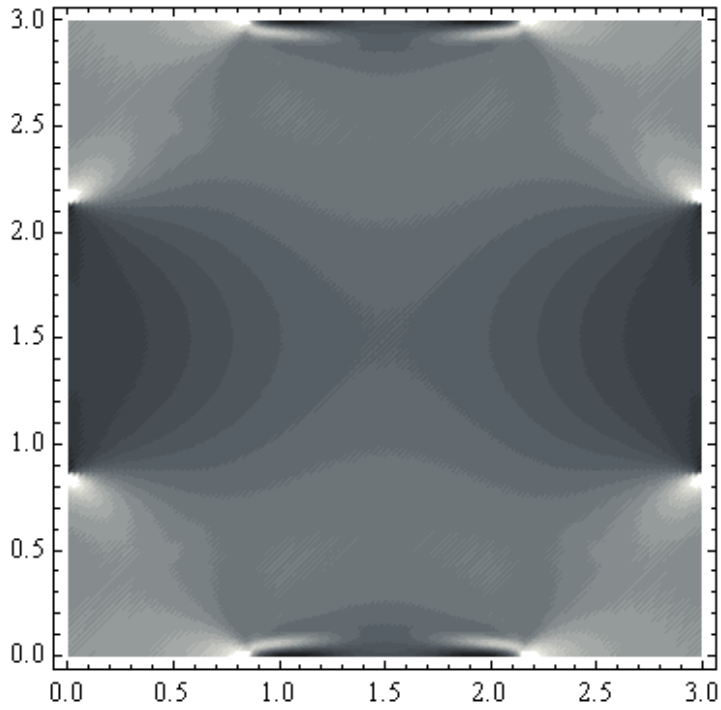

Figure 6.46 Contour Plot of Nx

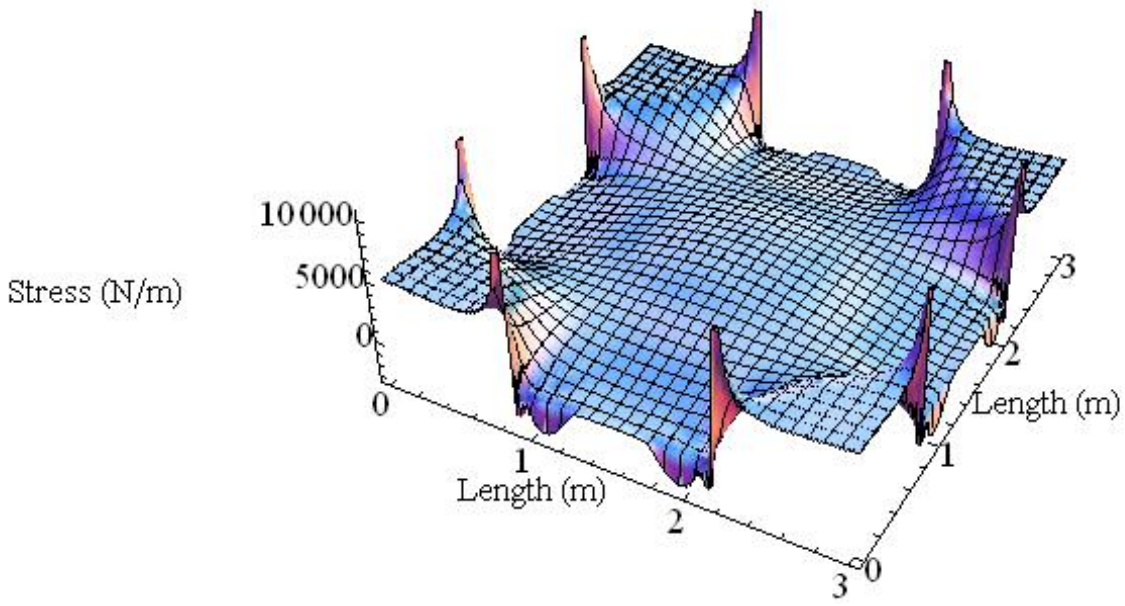

Figure 6.47 Three – Dimensional Plot of Nmin

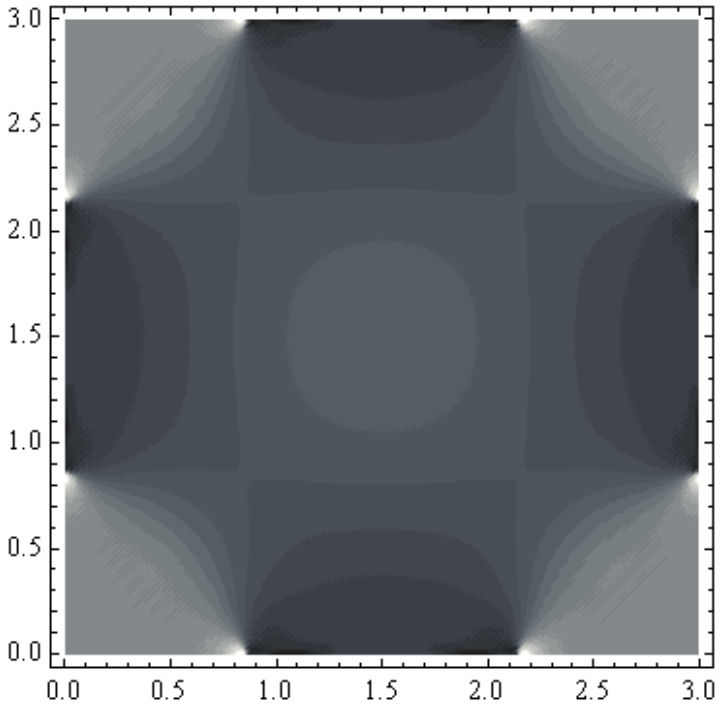

Figure 6.48 Contour Plot of Nmin

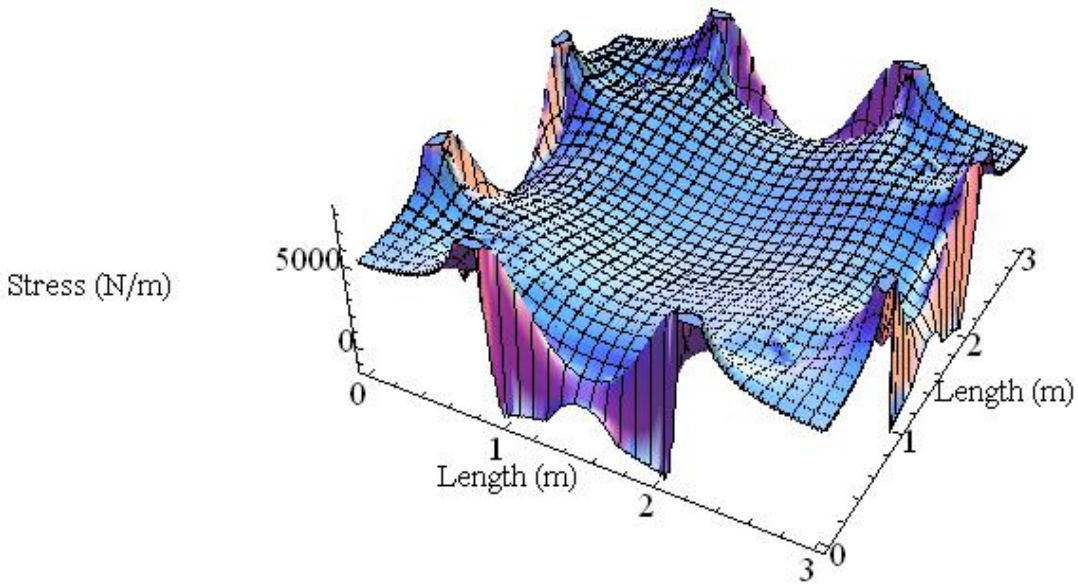

Figure 6.49 Three – Dimensional Plot of Nmax

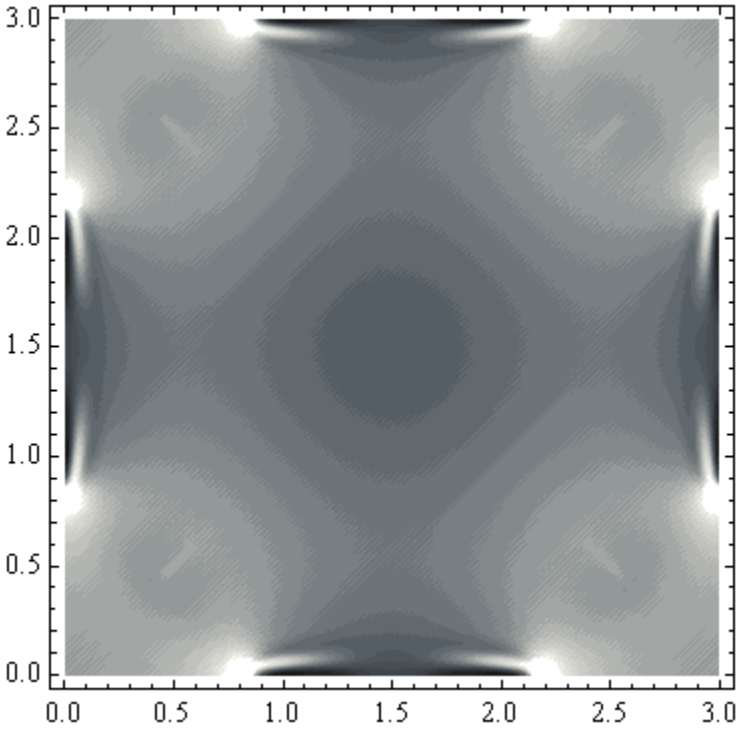

Figure 6.50 Contour Plot of Nmin

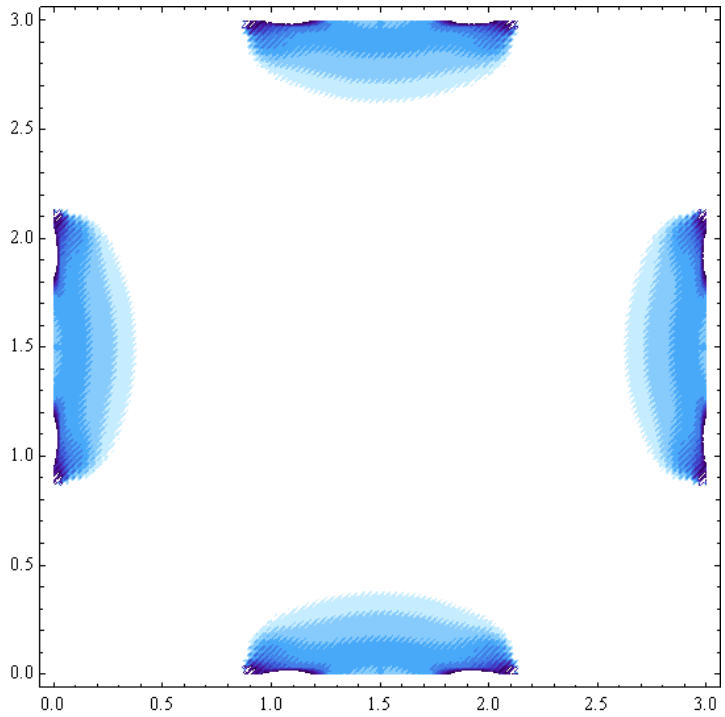

Figure 6.51 Contour Plot of Nmin Highlighting Region of Compressive Stress

Maximum strain in the X direction was 0.0261, the highest obtained in the alternative parameter case. Again, the circular piles yielded the lowest strain of the three pile orientations at 0.015. This result further suggests that circular piles are superior to the square counterpart. Figures 6.43 and 6.44 show that the maximum strain occurs at the square pile corner.

Stresses in the geosynthetic were maximum at 19,578 N/m in the X direction, 15,439 N/m minimum overall, and 19,579 N/m maximum overall. The locations of these maximum stresses can be seen in Figures 6.45, 6.47, and 6.49. Minimum compressive stresses were also found to occur with a minimum of -3,262 N/m. Figure 6.51 indicates the region in which compressive stresses act and wrinkling of the geosynthetic is possible. The rotated square piles again show regions of compressive stress spanning the square column corners only. Compressive stress is not found to act around the entire perimeter for the rotated square columns

Table 6.6 Stress and Strain for Alternate Case Rotated Square Piles

Rotated Square Piles	Ex	Nx (N/m)	Nmin (N/m)	Nmax (N/m)
Max	0.0261	19578.50	15438.60	19578.50
Min	-0.0044	-3261.79	-3261.79	-1428.23

6.6 Discussion of Results

6.6.1 Comparison of Pile Orientations

The alternative parameter set was analyzed with each of the three pile orientation types discussed above. Each pile type yielded different results for maximum deflection, stress, and strain. Table 6.7 illustrates the maximum values obtained in each pile orientation for the alternative case. It can be seen that the maximum vertical deflection occurred using rotated square piles. Although there is a clear maximum deflection, each pile type yielded very similar maximum vertical deflections. Maximum in-plane displacement also occurred in the analysis of rotated square piles.

Table 6.7 Comparison of Maximum Values for Alternate Case

Pile Type	Max W (m)	Max U, V (m)	Max Ex	Max Nx (N/m)
Square	0.0827	0.0057	0.024	18026
Circle	0.0847	0.0058	0.015	11273
Rotated Square	0.0868	0.0076	0.026	19579

6.6.2 Comparison to Mazursky Rayleigh-Ritz Model

Results obtained by Mazursky (2006) are presented in Table 6.8 for circular piles using the alternative parameter case. As previously discussed, her research involved Rayleigh-Ritz approximation of a similar unit cell with square and circular piles. It can be seen that results vary slightly between the finite difference model and the Rayleigh-Ritz model in Mazursky (2006). The finite difference model predicted slightly lower vertical and in-plane displacements along the edge and greater vertical deflection at the center. Although the results differ, they are still within reason for the given parameter case. Each method is a form of approximate plate analysis and therefore could possibly yield dissimilar results.

Table 6.8 Comparison of Rayleigh-Ritz Model Results (Mazursky 2006)

Maximum Values	W edge (m)	W center (m)	Ds (m)	U edge (m)	U center (m)	Nx edge (N/m)	Nx center (N/m)
Rayleigh-Ritz	0.066	0.129	0.126	0.0007	0.0004	2100	2500
Finite Difference	0.0768	0.0827	0.0815	0.0042	0.0057	5329	5552

6.6.3 Comparison to Parabolic Design Guide

The parabolic design method is one commonly used method for calculating strain in geosynthetic reinforcement. To further investigate the effectiveness of this method, the alternative parameter set was used to calculate the parabolic method maximum strain. Equations 5.1 – 5.3 presented in Chapter 5 were used to determine a maximum design strain of 0.01565 based on that method. The finite difference analysis of square piles for the standard case showed a maximum strain of 0.0240. Again these differences are most likely due to the oversimplified nature of the parabolic design method. Poisson's ratio, soil arching, and soil and column support stiffness are all neglected in the method. Also of importance is the peak in strain over the square pile corners predicted by the finite difference analysis. It is therefore apparent that including these parameters indeed has an effect on the maximum strain induced in the geosynthetic.

6.6.4 Effectiveness of Geosynthetic Support

As discussed in Section 5.7.4, the effectiveness of the geosynthetic reinforcement can be obtained by the ratio in Equation 5.4. The ratio represents the force supported by the soil divided by the downward force applied over the soft soil region. Using the alternative parameter set, the finite difference program was used to calculate these ratios for each of the three pile orientation types. The subsequent reinforcement ratios are as follows:

Square Piles:	0.909
Circular Piles:	0.915
Rotated Square Piles:	0.777

Based on these findings, it can be deduced that the rotated square piles are again most effective at transferring load from the soft soil to the columns. The geosynthetic is therefore providing the most support when used with rotated square piles.

Chapter 7

Alternative Modeling Attempts

7.1 Introduction

Various methods of approximate numerical analysis were investigated over the course of this research in an attempt to represent the complex three-dimensional nature of the stated problem. Initially, the Rayleigh-Ritz method was employed as an extension of previous work done by Mazursky (2006). Also, the finite difference method was attempted utilizing nonlinear plate equilibrium equations for large deflections. Although both of these approaches ultimately proved to be inefficient to accurately model the geosynthetic, the procedures and their subsequent development will be discussed briefly.

7.2 Rayleigh-Ritz Model

7.2.1 Rayleigh-Ritz Method

The Rayleigh-Ritz method is an approximate variational method that is often used in plate bending analysis. Variational methods in general are useful techniques in the evaluation of complex boundary value problems. The objective is to utilize a set of admissible functions that closely represent the deflections of an elastic body corresponding to a stable equilibrium configuration. The Rayleigh-Ritz method in particular uses this representation along with the principle of minimum potential energy. Shape functions are chosen based on the required geometric (kinematic) boundary conditions, and the displacements are written in the form:

$$w(x,y) = c_1 f_1(x,y) + c_2 f_2(x,y) + \cdots + c_n f_n(x,y) = \sum_{i=1}^{n} c_i \, f_i(x,y) \tag{7.1}$$

$$u(x,y) = d_1 g_1(x,y) + d_2 g_2(x,y) + \cdots + d_n g_n(x,y) = \sum_{i=1}^{n} d_i \, g_i(x,y) \tag{7.2}$$

$$v(x,y) = e_1 h_1(x,y) + e_2 h_2(x,y) + \cdots + e_n h_n(x,y) = \sum_{i=1}^{n} e_i \, h_i(x,y) \tag{7.3}$$

The selected shape functions must satisfy the geometric boundary conditions and be capable of representing all deflection patterns to be determined. Once a suitable number of shape functions is developed, the total energy of the system is established. The unknown coefficients can then be computed by setting the first partial derivative of the total energy with respect to each coefficient equal to zero (Szilard 1974).

7.2.2 Basic Model

In an attempt to supplement previous research conducted by Mazursky (2006), a set of alternative shape functions was developed. While Mazursky used polynomial shape functions, trigonometric shape functions were used here to represent the approximate plate deflections. These shape functions, shown in Equations 7.4 – 7.6, were selected to satisfy the kinematically admissible boundary conditions of the geosynthetic unit cell stated in Chapter 4:

$$w[x,y] = C_{0,0} + \sum_{m=1}^{i}\sum_{n=1}^{j} C_{m,n} * (2 - \text{Cos}\, 2\pi nx - \text{Cos}\, 2\pi ny)^m \qquad (7.4)$$

$$u[x,y] = A_{0,0} * \text{Sin}\, 2\pi x + \sum_{m=1}^{i}\sum_{n=1}^{j} A_{m,n} * \text{Sin}\, 2\pi nx * \text{Cos}\, 2\pi my \qquad (7.5)$$

$$u[x,y] = v[y,x] \qquad (7.6)$$

In general, these functions satisfy the kinematic boundary conditions:

$$X = 0 \ldots L \qquad \frac{\partial W}{\partial X} = 0 \quad and \quad U = 0$$

$$Y = 0 \ldots L \qquad \frac{\partial W}{\partial Y} = 0 \quad and \quad V = 0$$

Also, by using a similar non-dimensionalization as that used in the proposed finite difference energy method, these boundary conditions become:

$$For\ w(x,y): \quad \frac{\partial W}{\partial X} = 0 \quad x = 0,1 \quad and \quad \frac{\partial W}{\partial y} = 0 \quad y = 0,1$$

$$For\ u(x,y): \quad u = 0 \quad x = 0,1$$

$$For\ v(x,y): \quad v = 0 \quad y = 0,1$$

Once the appropriate shape functions were chosen, the total energy of the system was generated using equations 3.4 – 3.9. A total energy expression for the system was then established in terms of the shape functions and their corresponding coefficients. The principle of minimum potential energy was applied in order to obtain the unknown coefficients. Substituting these coefficients back into the deflection equations yielded the deflected shape corresponding to a stable equilibrium configuration of the system. Examples of the selected shape functions in Equations 7.4 and 7.5 for w and u with m and n equal to one are shown in Figures 7.1 and 7.2, respectively.

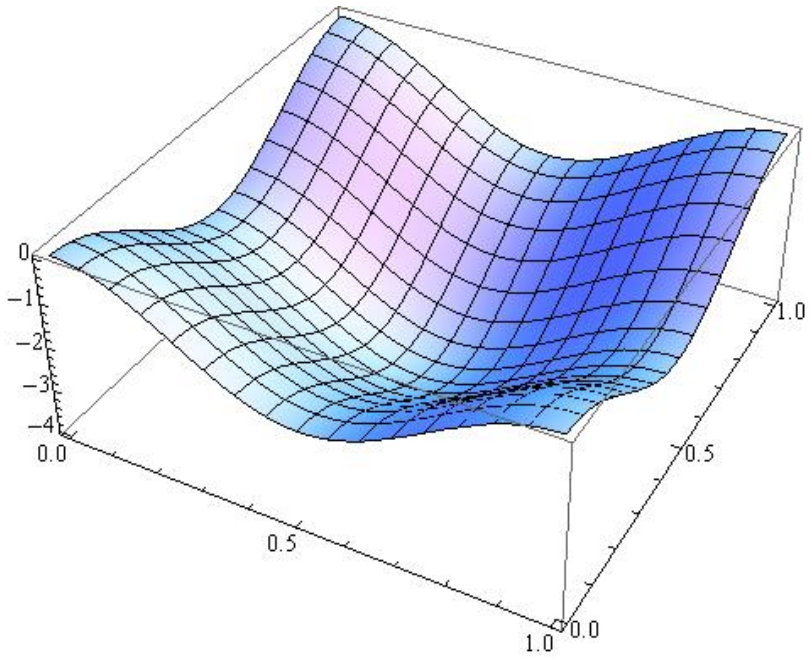

Figure 7.1 Rayleigh-Ritz Shape Function for w with n = m = 1

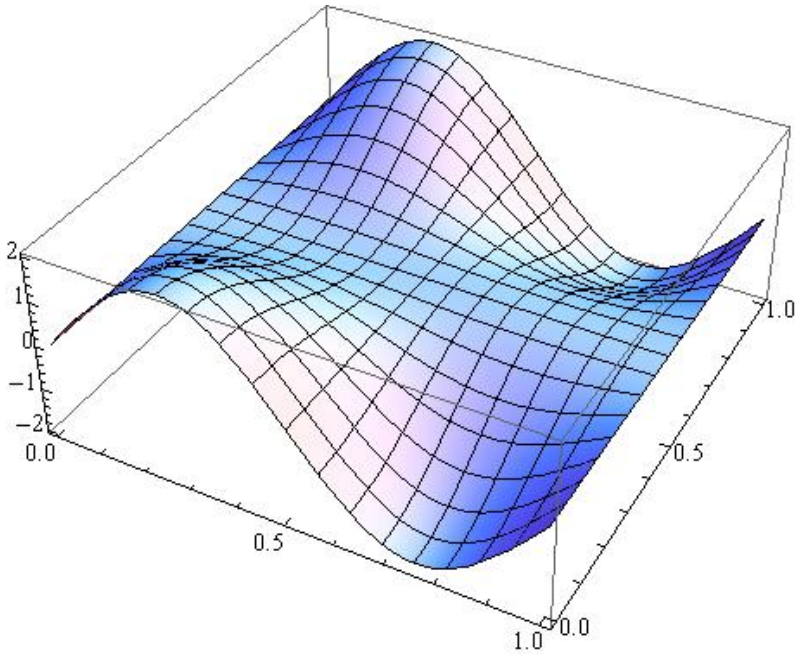

Figure 7.2 Rayleigh-Ritz Shape Function for u with n = m = 1

7.2.3 Mathematica Implementation

Mathematica 5.2 was used exclusively in the development of the Rayleigh-Ritz based model. Specifically, a program was set up that was capable of automating the processes of shape function generation, energy formulation, and minimum potential energy calculations. The built-in operator NMinimize was used to determine the unknown coefficients of the shape functions. Once these values were obtained, they were substituted into the original shape functions to determine the deflected shapes. A copy of the Mathematica notebook used for the Rayleigh-Ritz model is presented in Appendix D.

7.2.4 Problems Encountered

Although the Rayleigh-Ritz method is a well-established and effective means of representing approximate plate deflections in certain cases, several problems were encountered in this formulation. In particular, the resulting deflected shapes and the extreme computer expense proved to be undesirable. The Rayleigh-Ritz method relies on the fact that a significant linear

combination of shape functions should yield an accurate solution. The shape functions chosen to represent the unit cell displacements involved trigonometric functions raised to a variety of powers. In forming the total energy of the system, each shape function was used in the individual energy equations representing soil springs, load on the system, and membrane effect in the geosynthetic. Each of these expressions involves partial derivatives of the w, u, and v shape functions as well as the subsequent double integration over their respective areas. This cascading effect of increasingly complex terms caused the formulation of the total energy expression to be computationally expensive. The total energy expression eventually became prohibitively inefficient and was abandoned before a sufficient number of shape functions could be included.

Other limitations of the Rayleigh-Ritz method were discovered following the successful analysis of the proposed finite difference model. The Rayleigh-Ritz method approximates the shapes of the vertical and in-plane deflections using a linear combination of continuous functions. Because the shape functions are smooth, it became difficult to fully capture the extreme curvature at the edge of the pile regions. The finite difference method, however, was shown to accurately model this behavior of the geosynthetic. Also of importance is that there are regions of compressive stress where wrinkling of the material was found to occur. The finite difference method was able to predict this local behavior of the geosynthetic that was not initially considered in the Rayleigh-Ritz formulation.

7.3 Nonlinear Plate Equations Using Finite Differences

7.3.1 Nonlinear Plate Analysis

Nonlinear analysis of isotropic, orthotropic, and anisotropic plates is discussed by Chia (1980) for moderately large and large deflections. The material covered includes elastic behavior of plates utilizing von Karman's theory. Equations of motion are derived in terms of three-dimensional displacement components as well as transverse deflections and stress functions. Isotropic, orthotropic, and anisotropic plate equations are derived separately and presented for a variety of cases (Chia 1980).

7.3.2 Basic Model

Equilibrium equations for an orthotropic plate with parallel and symmetric material and coordinate axes were used in the model formulation. Chia (1980) gives the governing equilibrium equations of the plate as:

$$E_1 * U_{xx} + \mu * G_{12} * U_{yy} + C * V_{xy} = -W_x * (E_1 * W_{xx} + \mu * G_{12} * W_{yy}) - C * W_y * W_{xy} \quad (7.7)$$

$$C * U_{xy} + \mu * G_{12} * V_{xx} + E_2 * V_{yy} = -W_y * (E_2 * W_{yy} + +\mu * G_{12} * W_{xx}) - C * W_x * W_{xy} \quad (7.8)$$

$$D_1 * W_{xxxx} + 2D_3 * W_{xxyy} + D_2 * W_{yyyy} - Q + K * W = \frac{T}{\mu} * [\left(U_x + \frac{1}{2}{W_x}^2\right) * \left(E_1 * W_{xx} + \upsilon_{12} * E_2 * W_{yy}\right) + \left(V_y + \frac{1}{2}{W_y}^2\right) * \left(\upsilon_{12} * E_2 * W_{xx} + * E_2 * W_{yy}\right) + 2\mu * G_{12} * W_{xy} * (U_y + V_x + W_x * W_y] \quad (7.9)$$

where subscripts denote partial derivatives. These equations can be simplified by a variety of assumptions, decreasing the complexity for the stated problem. In particular, if bending resistance of the plate is neglected, fourth-order derivatives are excluded. Then the highest-order finite difference required to solve the governing equations is second-order. Also, the material is assumed here to be isotropic, which equates Poisson's ratio and the elastic modulus to those of the orthotropic material. By further simplification, Poisson's ratio is set equal to zero, reducing the complexity of the shear modulus G.

A separate, unique non-dimensionalization scheme was adopted for the plate equilibrium equations. The variables are similar in nature to those in the previous non-dimensionalization, except with a slightly different formulation. The equations used to non-dimensionalize Equations 7.7 – 7.9 were as follows:

$$w = \frac{W}{\alpha} \qquad u = \frac{UL}{\alpha^2} \qquad v = \frac{VL}{\alpha^2} \qquad (7.10, 7.11, 7.12)$$

$$x = \frac{X}{L} \qquad y = \frac{Y}{L} \qquad b = \frac{B}{L} \qquad (7.13, 7.14, 7.15)$$

$$q_p = \frac{Qp}{Qs} \qquad q_s = 1.0 \qquad \lambda = \frac{E_2}{E_1} \qquad (7.16, 7.17, 7.18)$$

$$k_s = \frac{K_S \mu L^4}{\alpha^2 E_1 T} \qquad k_p = \frac{K_P \mu L^4}{\alpha^2 E_1 T} \qquad \gamma = \frac{\mu G_{12}}{E_1} \qquad (7.19, 7.20, 7.21)$$

$$\alpha = \left[\frac{Q_S L^4 \mu}{E_1 T}\right]^{1/3} \qquad (7.22)$$

The modeling assumptions and previous non-dimensionalization therefore allow the three governing equilibrium equations of the isotropic plate to be expressed as:

$$u_{xx} + \frac{1}{2}u_{yy} + \frac{1}{2}v_{xy} + \left(w_{xx} + \frac{1}{2}w_{yy}\right) * w_x + \frac{1}{2}w_y * w_{xy} = 0 \qquad (7.23)$$

$$v_{yy} + \frac{1}{2}v_{xx} + \frac{1}{2}u_{xy} + \left(w_{yy} + \frac{1}{2}w_{xx}\right) * w_y + \frac{1}{2}w_x * w_{xy} = 0 \qquad (7.24)$$

$$\left(u_x + \frac{1}{2}{w_x}^2\right) * w_{xx} + \left(v_y + \frac{1}{2}{w_y}^2\right) * w_{yy} + \left(u_y + v_x + w_x * w_y\right) * w_{xy} + \begin{Bmatrix} qp \\ 1 \end{Bmatrix} - \begin{Bmatrix} kp \\ ks \end{Bmatrix} * w = 0 \qquad (7.25)$$

It is important to note that Equation 7.25 contains a column vector with the loading and support stiffness associated with the pile and soft soil regions, respectively. Each of these equations is implemented separately on nodes over the piles and the soft soil.

7.3.3 Mathematica Implementation

Mathematica 5.2 was again used in the development and analysis of the nonlinear plate model with finite differences. A program was created similar to that used in the proposed energy-based model. In particular, the central finite differences presented in Chapter 3 were implemented to form the equilibrium equations at each node.

7.3.4 Problems Encountered

Several methods were attempted to solve the governing equations at each discretized finite difference node. First, the sum of the squares of the equations at each node was minimized with respect to each unknown displacement variable. The minimization was performed in Mathematica utilizing the built-in operators NMinimize, FindMinimum, and Minimize. This method, however, proved to be inadequate, as the relative errors at each node were too large.

Another solution technique implemented involved searching for the root of each equilibrium equation at the discretized nodes. A total equation list was generated including each node with respect to finite differences. The roots of the subsequent equilibrium equations were then computed utilizing built-in operators of Mathematica. Specifically, FindRoot was applied, which allows for an initial guess within a certain range for each unknown variable. Again, the errors encountered were too large to confidently accept the model's results as a valid approximation for the geosynthetic deformation. With a significant number of nodes, the equation list quickly grew to a point where the roots could not be found.

Solving individual equilibrium equations for the in-plane and vertical directions at each node proved to be prohibitively complex. The built-in functions of Mathematica were unable to find the true root of each equation, therefore leading to solution errors. Another potential source of error lies in the finite difference equations themselves. Unlike the energy-based method, the nonlinear equilibrium equations involve first- and second-order differences in the w, u, and v functions. The increased complexity of the finite differences used in the analysis may have contributed to the inadequacies of this particular model. Although some results were obtained, few were ideal and the method therefore was abandoned.

Chapter 8

Summary and Conclusions

8.1 Research Summary

Geosynthetic-reinforced, column-supported embankments provide effective geotechnical foundations for applications in areas of weak subgrade soils. This method provides a cost-effective solution to minimize overall and differential settlements that may adversely affect the embankment or adjacent structures. The composite system consists of a soil bridging layer with one or more embedded layers of geosynthetic reinforcement. Several feet of coarse-grained soil or aggregate are generally used in the bridging layer to promote interaction between the geosynthetic and surrounding material. Support is provided by columns, founded on a firm-bearing stratum, which rise into the bridging layer just below the geosynthetic. The geosynthetic then acts to promote load transfer into the columns and away from the soft soil. Use of geosynthetics as load transfer mechanisms therefore allows for larger column spacings and varied alignments that can reduce construction costs. Current design procedures and analysis methods make a variety of assumptions that obscure the true three-dimensional behavior of the geosynthetic. Recent increases in the popularity of this system have generated the need to further investigate the behavior and soil-structure interaction of geosynthetics used in column-supported embankments.

Current models of geosynthetic reinforcement used in column-supported embankments are oversimplified and incapable of fully representing the true behavior of the material. In particular, the three-dimensional nature and soil interaction of the geosynthetic are not accurately taken into account. Current design methods for geosynthetic-reinforced embankments are based on a wide range of conservative assumptions, which give rise to conflicting results. Most methods rely on an equal-strain approach that contradicts vertical stress equilibrium and overlooks stress concentrations around the piles. Also, models for the reinforcement have sometimes involved one-dimensional cables that only resist tension. Again, the three-dimensional behavior of the geosynthetic is inaccurately neglected in these instances.

The objective of this research was to investigate the behavior of geosynthetic reinforcment used in column-supported embankments and reduce the number of assumptions made in design. Emphasis was placed on developing a three-dimensional model of the material that accounts for soil arching and potential stress concentrations. A single layer of reinforcement with varied thickness was analyzed within a square unit cell shown in Figure 3.1. The geosynthetic was modeled as a thin, isotropic, flexible plate with bending and membrane resistance. Non-uniform vertical loading was considered over the pile and soft soil regions to account for arching effects. Friction between the geosynthetic and soil was ignored and a Winkler-foundation soil model was implemented with different stiffnesses over the soft soil and the columns.

Several approximate plate analysis techniques were explored throughout the course of this research. The Rayleigh-Ritz method as well as nonlinear plate equilibrium equations utilizing finite differences were both attempted, with mixed results. Eventually a finite difference method using the principle of minimum potential energy was succesfully developed.

Mathematica 5.2 was used exclusively in the programming and development of the finite difference based energy method. Through symmetrical properties and boundary conditions, only a one-eighth portion of the unit cell was required for complete analysis. The one-eighth region was then discretized with a uniformly-spaced finite difference mesh. Individual energy components at each node were used to formulate the total system energy. These energy components involve the vertical loading and support stiffness over the piles and soft soil as well as the membrane and bending stiffness of the geosynthetic. Once the total energy was established, the principle of minimum potential energy was applied with respect to each of the unknown nodal displacements. The computed vertical and in-plane displacements at each node were then used to calculate stress resultants and strains within the geosynthetic.

Three unique pile orientation types were investigated using the finite difference energy method developed in Mathematica. In particular, square piles, circular piles, and square piles rotated 45° with respect to the edge of the unit cell were considered. Sizing of each of the pile types was based on equivalent area in order to accurately compare the cases. Vertical and in-plane deflections, stress resultants, and strains were calculated for each pile type and compared.

Two sets of parameters were also analyzed for each of the three pile orientation types. A standard case was selected based on work conducted by fellow Master's student Kyle Halvordson. In his research, the geosynthetic was modeled as a cable net, using similar modeling assumptions and geometry. An alternative set of parameters was also chosen to reflect previous research on the subject by Mazursky (2006). Her research involved Rayleigh-Ritz analysis of the geosynethic, with a comparable modeling procedure. The subsequent results obtained for each parameter set by the finite difference method were then compared to the cable net and Rayleigh-Ritz models. Resulting values for strain were also compared to an existing parabolic design guide to emphasis its highly conservative nature.

8.2 Conclusions

Two sets of parameters were analyzed with the finite difference program developed in Mathematica. As previously discussed, the standard case was selected to reflect a cable net analysis performed by Master's student Kyle Halvordson and the alternative case was based on previous Rayleigh-Ritz analysis by Mazursky (2006). The most apparent difference in the two parameter sets is the magnitude of pile and soil support stiffness. The standard case used 29.2 MN/m^3 and 160.2 kN/m^3, as compared to 150 MN/m^3 and 300 kN/m^3 for the pile and soil stiffness, respectively, in the alternative case. It can be seen from results in Chapters 5 and 6 that the increase in support stiffness greatly affected the maximum vertical and in-plane displacements. For example, the standard case with square piles yielded a maximum vertical deflection of 0.1911 meters, while the alternative case showed 0.0827 meters for the same system layout.

Maximum stress resultants and strain values were also computed for each of the two parameter sets and compared. Again, the alternative case exhibited lower stress and strain values due to the larger support stiffness. Each parameter case also showed regions of compressive stresses around the pile edges in which potential wrinkling of the geosynthetic occurred.

Three unique pile orientations were analyzed for each parameter case to determine the most efficient layout. When implementing the standard parameters, the maximum vertical and in-plane deflections occurred with circular piles. Although the maximum deflections were found in

this case, the peak stress and strain values were actually lowest when using circular piles. This is most likely due to the absence of a sharp pile corner present in the square and rotated square orientations.

When considering the alternative parameter case, the largest vertical and in-plane deflections occurred with the rotated square pile orientation. Although this is contradictory to results obtained in the standard parameter case, the change in support stiffness and loading could potentially create distinct loading interactions. Similar to the standard case, however, the lowest peak values of stress and strain were found with circular piles. The conclusion can therefore be drawn that when concerned with stress and strain in the geosynthetic, circular piles are superior to their square counterpart. It can also be deduced that vertical and in-plane deflections are influenced more by loading and support stiffness parameters than by pile type and orientation.

The results obtained in the finite difference program developed in this thesis were compared to the cable net model by Halvordson as well as the Rayleigh-Ritz model employed in Mazursky (2006). Results for the standard case were shown to be in close agreement with those from the cable net model. Maximum vertical and in-plane deflections as well as differential settlements were nearly identical for each model. Also similar were calculated stress and strain values in the geosynthetic. Maximum strain predicted in the cable net model, however, was slightly lower at 0.0298 in the X direction for square piles than 0.0395 found using the membrane model. Stress values were also similar, which indicates that each of the models provides a reliable means of three-dimensional analysis of geosynthetic reinforcement.

Results obtained by Mazursky (2006) were slightly different than from the finite difference model but were still within reason. (The shape functions used in that study were insufficient to accurately model the high curvatures of the geosynthetic near the pile edges.) The maximum vertical displacement was larger in the Rayleigh-Ritz analysis at 129 mm compared to 84.7 mm using finite differences. In-plane displacements were also lower when compared to Mazursky (2006). Strains were not presented for the Rayleigh-Ritz analysis; however, stress resultants were calculated in the X direction. These values were also larger than those obtained using the finite difference model. These results therefore suggest that the Rayleigh-Ritz model used in

Mazursky (2006) provides a conservative approximation of the geosynthetic reinforcement behavior.

To illustrate the benefits and effectiveness of a three-dimensional analysis, results were compared to an existing design guide approximation. In particular, a parabolic approximation is often used to calculate strain in the geosynthetic for the British Standard BS8006 and Swedish design guides. Strain values were computed for the standard and alternative parameters using the parabolic method. It was subsequently shown that this method under predicts the maximum strain induced in the material for applications of reinforced embankments. In particular, the parabolic method neglects key factors such as arching effects in the embankment soil and Poisson's ratio of the material. Most importantly, localized peaks in strain occurring at the pile edges are not considered when utilizing the parabolic approximation. It can therefore be concluded that a more refined three-dimensional analysis of geosynthetic-reinforced embankments provides the most accurate calculation of strains.

Results obtained in this research have significant impact on the design of composite geotechnical foundations such as reinforced embankments. In general, it was shown that circular columns provide the most efficient columnar support for the geosynthetic. Circular columns yielded the lowest peak strain magnitude for each of the two parameter cases analyzed. All results were also validated through comparison of current and previous models such as Rayleigh-Ritz approximation and cable net analysis. It was also shown that the parabolic approximation currently used in the British Standard BS8006 and Swedish design guides under predicts the maximum strain found in the geosynthetic. The parabolic method in particular is not capable of predicting stress and strain concentrations which develop around the piles. A complete three-dimensional analysis, such as the finite difference model developed in this thesis, provides the most effective method for analysis of geosynthetic-reinforced column-supported embankments.

8.3 Suggestions for Future Research

Continued research in the area of geosynthetic-reinforced column-supported embankments is critical to help further the understanding of this system's behavior and its role in composite foundations. Many supplemental modifications could be made to the proposed finite difference

model to account for various conditions. Also, some of the assumptions and simplifications made in the model development could be changed to reflect specific cases.

One modification that could be made to the current finite difference program would be to treat the material as an orthotropic plate. In this research, the geosynthetic was assumed to act as a thin, flexible, isotropic plate. In many instances, however, biaxial geogrids have machine and cross directions with unique stiffness. An orthotropic model would be capable of representing specific geogrids with preferential material axes.

A single layer of geosynthetic reinforcement of specified thickness was assumed in the presented model. In practice, however, several layers of geosynthetic are often placed above the columns, with a region of coarse grained soil between the layers. A possible avenue of future research then would be to develop a model that accounts for the soil-structure interaction between these layers. The stiffness of the bridging layer as well as the multiple layers of reinforcement could be investigated. Again, in this thesis, soil support was only considered to act beneath the geosynthetic. Including multiple layers of reinforcement as well as the stiffness within the bridging layer over the geosynthetic would most likely have some impact on total deflection and subsequent stress and strain.

Another suggestion for future work would be to use alternative foundation models for the soft soil and bridging layers. In this thesis, a Winkler elastic foundation was assumed, in which the soil is represented by a continuous distribution of linear springs. The Pasternak soil model is another common model, which includes a horizontal shear layer in addition to linear spring support. Shear interaction along the geosynthetic could potentially be important, as materials such as geogrids rely on interlocking in the soil to generate tensile capacity. Also, other nonlinear soil models could be developed in which compressibility and consolidation of the soft soil are taken into account.

The current finite difference model could also be improved by reformulating the circular pile case. As shown in Chapters 5 and 6, some discontinuities exist in the three-dimensional stress and strain plots. This erratic behavior is exhibited around the circular pile edge where stress and strain are most critical. The source of error in these calculations is most likely due to the

uniformly-spaced finite difference discretization over a curved region. A hybrid finite difference mesh could therefore be implemented in this region, capable of accounting for the curved edge.

Other models could be considered for the geosynthetic reinforcement in future work. In this research and in Mazursky (2006), the material was treated as a thin flexible plate. Mazursky also considered small-scale finite element modeling using ABAQUS. Large-scale nonlinear finite element modeling, however, would likely provide an accurate means of comparison between methods. Also, research conducted by fellow Master's student Kyle Halvordson employed a cable net analysis. Results for the cable net analysis and current finite difference method were shown to be in close agreement. Additional models would therefore help to further validate these models as effective tools for analysis.

As discussed, there exist several channels for improved analysis of geosynthetic-reinforced column-supported embankments. The finite difference program presented in this thesis could be supplemented and enhanced through different modeling techniques and formulations. Also, additional analyses could be conducted using finite element or other means to provide supplemental comparison of the previous results. As with any emerging technology, focused and continual research will be necessary to fully grasp the complex behavior of this geotechnical composite foundation system employing geosynthetic reinforcement.

References

Agaiby, S.W. and Jones, C.J.F.P. (1995). "Design of reinforced fill systems over voids," *Canadian Geotechnical Journal*, 32, 939-945.

American Society for Testing and Materials (2007). "ASTM D6337 – 01. Standard Test Method for Determining Tensile Properties of Geogrids by the Single or Multi – Rib Tensile Method. " *Annual Book of ASTM Standards*. West Conshohocken, PA, American Society for Testing and Materials.

Broms, B.B. (1999). "Keynote lecture: Design of lime, lime/cement and cement columns," *International Conference on Dry Mix Methods: Dry Mix Methods for Deep Soil Stabilization*, A. A. Balkema, Rotterdam, 125-153.

Burd, H.J. (1995). "Analysis of membrane action in reinforced unpaved roads," *Canadian Geotechnical Journal*, 32, 946-956.

CDIT (Coastal Development Institute of Technology) (2002). *The Deep Mixing Method: Principle, Design and Construction*. A.A. Balkema, The Netherlands.

Chia, C.Y. (1980). *Nonlinear Analysis of Plates*, McGraw-Hill, New York, 54-79.

Fakher, A. and Jones, C.J.F.P. (2001). "When the bending stiffness of geosynthetic reinforcement is important," *Geosynthetics International*, 8, 445-460.

Filz, G.M. and Smith, M.E. (2006). "Design of Bridging Layers in Geosynthetic-Reinforced Column-Supported Embankments" Virginia Transportation Research Council, Charlottesville, VA.

Halvordson, K.A. (2007). *Three – Dimensional Analysis of Geogrid Reinforcement Used in Pile-Supported Embankments*., M.S. thesis. Virginia Polytechnic Institute and State University, Blacksburg, VA.

Horgan, G.J., and Sarsby, R.W. (2002). "The arching effect of soils over voids and piles incorporating geosynthetic reinforcement." *Proceedings, Geosynthetics - 7th ICG*, Delmas, Gourc & Girard (eds), Lisse, Swets & Zetilinger, 373-78.

Huang, J., Han, J., and Collin, J.G. (2006). "Serviceability analysis of geomembrane in geosynthetic-reinforced column-supported platforms," *Advances in Earth Structures: Research to Practice*, 211-216.

Huesker, Inc. (2006). "Fortrac Geogrids for Soil Reinforcement," Huesker Inc, Charlotte, North Carolina.

Huesker, Inc. (2006). "Fornit Biaxial Geogrid Reinforcement," Huesker Inc, Charlotte, North Carolina.

Kempfert, H.G., and Gebreselassie, B. (2006). *Excavations and Foundations in Soft Soils*, Springer, The Netherlands.

Koerner, R.M. (2005). *Designing with Geosynthetics*. New Jersey, Pearson Education, Inc.

Lawson, C.R. (1992). Soil reinforcement with geosynthetics. *Applied Ground Improvement Techniques, Southeast Asian Geotechnical Society (SEAGS)*, 55-74.

Levy, S. (1942). "Square plate with clamped edges under normal pressure producing large deflections," *National Advisory Committee for Aeronautics TN-847*, Washington, D.C.

Love, J.P. (1984). Model testing of geogrids in unpaved roads. D.Phil. thesis, University of Oxford, Oxford, UK.

Love, J. and Milligan, G. (2003). Design methods for basally reinforced pile-supported embankments over soft ground. *Ground Engineering*, March, 39-43.

Love, J.P. Burd, H.J, Milligan, G.W.E, and Houlsby, G.T (1987). Analytical and model studies of reinforcement of a layer of granular fill on soft clay subgrade. *Canadian Geotechnical Journal*, 24, 611-622.

Mazursky, L.A. (2006). *Three – Dimensional Analysis of Geosynthetic Reinforcement Used in Column-Supported Embankments.*, M.S. thesis. Virginia Polytechnic Institute and State University, Blacksburg, VA.

McGuire, M.P. and Filz, G.M. (2008). "Quantitative comparison of theories for geosynthetic reinforcement of column-supported embankments" *The First Pan American Geosynthetics Conference & Exhibition*, Cancun, Mexico.

Moseley, M.P., and Kirsch, K. (2004). *Ground Improvement.* Spon Press, New York.

Pinto, M.I.M. (2003). "Applications of geosynthetics for soil reinforcement. *Ground Improvement*, 7, 61-72.

Ruggiero, E.J. and Inman, D.J. (2006). "Gossamer spacecraft: Recent trends in design, analysis, experimentation, and control," *Journal of Spacecraft and Rockets*, 43, 10-24.

Russell, D. and Pierpoint, N. (1997). "An assessment of design methods for piled embankments," *Ground Engineering*, November, 39-44.

Scott, R.F. (1981). *Foundation Analysis*, Prentice-Hall, Englewood Cliffs, New Jersey.

Smith, M.E. (2005). *Design of Bridging Layers in Geosynthetic-Reinforced Column-Supported Embankments*, Ph.D. Dissertation. Virginia Polytechnic Institute and State University, Blacksburg, VA.

Soare, M. (1967). *Applications of Finite Difference Equations to Shell Analysis*. Pergamon Press, Bucharest.

Szilard, R. (1974). *Theory and Analysis of Plates: Classical and Numerical Methods*, Prentice-Hall, Englewood Cliffs, New Jersey, 216-217.

Terzaghi, K. (1943). *Theoretical Soil Mechanics*. Wiley, New York.

Timoshenko, S. and Woinowsky-Krieger, S. (1959). *Theory of Plates and Shells, Second Edition*: McGraw-Hill, New York, 259, 419-428.

Ugural, A.C. (1999). *Stresses in Plates and Shells, Second Edition*, McGraw-Hill, New York.

Villard, P. and Giraud, H. (1998). "Three-dimensional modeling of the behavior of geotextile sheets as membranes," *Textile Research Journal*, 68, 797-806.

Wolfram, S. (1996). *The Mathematica Book*, Wolfram Media, Inc, Champaign, Illinois.

Wolfram Research (2007). *Introducing a Computing Revolution: Wolfram Mathematica 6*, Wolfram Research, Incorporated http://www.wolfram.com/products/mathematica/newin6/).

Yan, L., Yang, J.S., and Han, J. (2006). "Parametric Study on Geosynthetic-Reinforced Pile-Supported Embankments," *Advances in Earth Structures: Research to Practice*, 255-261.

Appendix A

Supporting Information for Program Development

A.1 Printout of Final Program Mathematica Notebook

Energy Method/Finite Difference Program for Geosynthetic Reinforcement

```
Clear["@"]
Off[General::spell1];
Start = TimeUsed[];
```

Dimensional Input

```
B = .6; L = 3; t = 1.5 * 10^-3; E = 500 * 10^6; ν = 0; Kp = 29.2183 * 10^6;
Ks = 160.229 * 10^3; Qp = 146.034 * 10^3; Qs = 30.643 * 10^3;
```

Non-Dimensionalization

$$qp = \frac{Qp}{Qs};$$

$$qs = 1.0;$$

$$ks = \frac{Ks * L^4 * (1 - \nu^2)}{\beta^2 * E * t};$$

$$kp = \frac{Kp * L^4 * (1 - \nu^2)}{\beta^2 * E * t};$$

$$\gamma = \frac{(1 - \nu)}{2};$$

$$\alpha = \frac{Dd * \beta}{2 * Qs * L^4};$$

$$\beta = \left(\frac{Qs * L^4 * (1 - \nu^2)}{E * t}\right)^{\frac{1}{3}};$$

$$Dd = \frac{E * t^3}{12 (1 - \nu^2)};$$

$$R = \left(\frac{(2 B)^2}{\pi}\right)^{\frac{1}{2}};$$

$$r = \frac{R}{L};$$

General Input

```
n = 100;
h = 1/(2*n);
H = L/(2*n);
bsquare = Ceiling[.4*n];
bdiamond = Ceiling[0.4*Sqrt[2]*n];
dxdy = h^2;
```

Non-Dimensional Energy Equations

```
Eks[i_, j_] := 1/2 * ks * (w[i, j])^2
Ekp[i_, j_] := 1/2 * kp * (w[i, j])^2
Eqs[i_, j_] := -qs * w[i, j]

Eqp[i_, j_] := -qp * w[i, j]

Emsp[i_, j_] :=
 1/2 * ((ux[i, j] + .5 * wx[i, j]^2)^2 + (vy[i, j] + .5 * wy[i, j]^2)^2 +
    2 * v * (ux[i, j] + 0.5 * wx[i, j]^2) * (vy[i, j] + 0.5 * wy[i, j]^2) +
    (1 - v)/2 * (uy[i, j] + vx[i, j] + (wx[i, j] * wy[i, j]))^2)

Ebsp[i_, j_] := α * (wxx[i, j] + wyy[i, j])^2
```

Non-Dimensional Central Finite Difference Equations

```
ux[i_, j_] := 1/(2 h) (u[i + 1, j] - u[i - 1, j])
uy[i_, j_] := 1/(2 h) (u[i, j + 1] - u[i, j - 1])

vx[i_, j_] := 1/(2 h) (v[i + 1, j] - v[i - 1, j])
vy[i_, j_] := 1/(2 h) (v[i, j + 1] - v[i, j - 1])
```

$$w_x[i\_, j\_] := \frac{1}{2\,h}\,(w[i+1, j] - w[i-1, j])$$

$$w_y[i\_, j\_] := \frac{1}{2\,h}\,(w[i, j+1] - w[i, j-1])$$

$$w_{xx}[i\_, j\_] := \frac{1}{h^2}\,(w[i+1, j] - 2\,w[i, j] + w[i-1, j])$$

$$w_{yy}[i\_, j\_] := \frac{1}{h^2}\,(w[i, j+1] - 2\,w[i, j] + w[i, j-1])$$

$$w_{xy}[i\_, j\_] := \frac{1}{4\,h^2}\,(w[i+1, j+1] - w[i+1, j-1] - w[i-1, j+1] + w[i-1, j-1])$$

Non-Dimensional Boundary Conditions

Boundary Conditions in U

```
Do[u[n, j] = 0, {j, -1, n + 1}]
Do[u[0, j] = 0, {j, -1, n + 1}]
Do[u[i, -1] = u[i, 1], {i, -1, n + 1}]
Do[u[i, n + 1] = u[i, n - 1], {i, -1, n + 1}]
Do[u[n + 1, j] = -u[n - 1, j], {j, -1, n + 1}]
Do[u[-1, j] = -u[1, j], {j, -1, n + 1}]
```

Boundary Conditions in V

```
Do[v[i, 0] = 0, {i, -1, n + 1}]
Do[v[i, n] = 0, {i, -1, n + 1}]
Do[v[i, -1] = -v[i, 1], {i, -1, n + 1}]
Do[v[n + 1, j] = v[n - 1, j], {j, -1, n + 1}]
Do[v[-1, j] = v[1, j], {j, -1, n + 1}]
Do[v[i, n + 1] = -v[i, n - 1], {i, -1, n + 1}]
Do[v[i, j] = u[j, i], {i, 0, n}, {j, 0, n}]
```

Boundary Conditions in W

```
Do[w[n + 1, j] = w[n - 1, j], {j, -1, n + 1}]
Do[w[i, n + 1] = w[i, n - 1], {i, -1, n + 1}]
Do[w[i, -1] = w[i, 1], {i, -1, n + 1}]
Do[w[-1, j] = w[1, j], {j, -1, n + 1}]
Do[w[i, j] = w[j, i], {i, 0, n}, {j, 0, n}]
```

Total Non-Dimensional Energy Equations for Square Piles

Energy Equations

$$EEkp := \frac{1}{8} * dxdy * Ekp[0, 0] + \frac{1}{4} * dxdy * Ekp[b, 0] + \frac{1}{8} * dxdy * Ekp[b, b] +$$
$$Sum[1.0 * dxdy * Ekp[i, j], \{i, 2, b-1\}, \{j, 1, i-1\}] +$$
$$Sum\left[\frac{1}{2} * dxdy * Ekp[i, i], \{i, 1, b-1\}\right] + Sum\left[\frac{1}{2} * dxdy * Ekp[i, 0], \{i, 1, b-1\}\right] +$$
$$Sum\left[\frac{1}{2} * dxdy * Ekp[b, j], \{j, 1, b-1\}\right]$$

$$EEqp := \frac{1}{8} * dxdy * Eqp[0, 0] + \frac{1}{4} * dxdy * Eqp[b, 0] + \frac{1}{8} * dxdy * Eqp[b, b] +$$
$$Sum[1.0 * dxdy * Eqp[i, j], \{i, 2, b-1\}, \{j, 1, i-1\}] +$$
$$Sum\left[\frac{1}{2} * dxdy * Eqp[i, i], \{i, 1, b-1\}\right] + Sum\left[\frac{1}{2} * dxdy * Eqp[i, 0], \{i, 1, b-1\}\right] +$$
$$Sum\left[\frac{1}{2} * dxdy * Eqp[b, j], \{j, 1, b-1\}\right]$$

$$EEks := \frac{1}{4} * dxdy * Eks[b, 0] + \frac{3}{8} * dxdy * Eks[b, b] +$$
$$Sum\left[\frac{1}{2} * dxdy * Eks[b, j], \{j, 1, b-1\}\right] + Sum\left[\frac{1}{2} * dxdy * Eks[i, 0], \{i, b+1, n-1\}\right] +$$
$$\frac{1}{8} * dxdy * Eks[n, n] + \frac{1}{4} * dxdy * Eks[n, 0] + Sum\left[\frac{1}{2} * dxdy * Eks[n, j], \{j, 1, n-1\}\right] +$$
$$Sum[1.0 * dxdy * Eks[i, j], \{i, b+1, n-1\}, \{j, 1, i-1\}] +$$
$$Sum\left[\frac{1}{2} * dxdy * Eks[i, i], \{i, b+1, n-1\}\right]$$

$$EEqs := \frac{1}{4} * dxdy * Eqs[b, 0] + \frac{3}{8} * dxdy * Eqs[b, b] +$$
$$Sum\left[\frac{1}{2} * dxdy * Eqs[b, j], \{j, 1, b-1\}\right] + Sum\left[\frac{1}{2} * dxdy * Eqs[i, 0], \{i, b+1, n-1\}\right] +$$
$$\frac{1}{8} * dxdy * Eqs[n, n] + \frac{1}{4} * dxdy * Eqs[n, 0] + Sum\left[\frac{1}{2} * dxdy * Eqs[n, j], \{j, 1, n-1\}\right] +$$
$$Sum[1.0 * dxdy * Eqs[i, j], \{i, b+1, n-1\}, \{j, 1, i-1\}] +$$
$$Sum\left[\frac{1}{2} * dxdy * Eqs[i, i], \{i, b+1, n-1\}\right]$$

```
EEmsp := 1/8 * dxdy * Emsp[0, 0] + 1/4 * dxdy * Emsp[n, 0] + 1/8 * dxdy * Emsp[n, n] +
  Sum[1/2 * dxdy * Emsp[n, j], {j, 1, n - 1}] + Sum[1/2 * dxdy * Emsp[i, 0], {i, 1, n - 1}] +
  Sum[1.0 * dxdy * Emsp[i, j], {i, 1, n - 1}, {j, 1, i - 1}] +
  Sum[1/2 * dxdy * Emsp[i, i], {i, 1, n - 1}]

EEbsp := 1/8 * dxdy * Ebsp[0, 0] + 1/4 * dxdy * Ebsp[n, 0] + 1/8 * dxdy * Ebsp[n, n] +
  Sum[1/2 * dxdy * Ebsp[n, j], {j, 1, n - 1}] + Sum[1/2 * dxdy * Ebsp[i, 0], {i, 1, n - 1}] +
  Sum[1.0 * dxdy * Ebsp[i, j], {i, 1, n - 1}, {j, 1, i - 1}] +
  Sum[1/2 * dxdy * Ebsp[i, i], {i, 1, n - 1}]

EETot = EEbsp + EEmsp + EEks + EEqs + EEkp + EEqp;
```

Total Non-Dimensional Energy Equations for "Diamond" Piles

```
EEk := Sum[If[(i + j) ≤ b, dxdy * Ekp[i, j], dxdy * Eks[i, j]], {i, 1, n - 1},
    {j, 1, i - 1}] + Sum[If[i ≤ b/2, dxdy * Ekp[i, i], dxdy * Eks[i, i]], {i, 1, n - 1}] +
  Sum[If[i ≤ b, 1/2 * dxdy * Ekp[i, 0], 1/2 * dxdy * Eks[i, 0]], {i, 1, n}] +
  Sum[1/2 * dxdy * Eks[n, j], {j, 1, n - 1}] + 1/4 * dxdy * Eks[n, 0] + 1/8 * dxdy * Ekp[0, 0] +
  1/8 * dxdy * Eks[n, n]

EEq := Sum[If[(i + j) ≤ b, dxdy * Eqp[i, j], dxdy * Eqs[i, j]], {i, 1, n - 1},
    {j, 1, i - 1}] + Sum[If[i ≤ b/2, dxdy * Eqp[i, i], dxdy * Eqs[i, i]], {i, 1, n - 1}] +
  Sum[If[i ≤ b, 1/2 * dxdy * Eqp[i, 0], 1/2 * dxdy * Eqs[i, 0]], {i, 1, n}] +
  Sum[1/2 * dxdy * Eqs[n, j], {j, 1, n - 1}] + 1/4 * dxdy * Eqs[n, 0] + 1/8 * dxdy * Eqp[0, 0] +
  1/8 * dxdy * Eqs[n, n]

EEmsp := 1/8 * dxdy * Emsp[0, 0] + 1/4 * dxdy * Emsp[n, 0] + 1/8 * dxdy * Emsp[n, n] +
  Sum[1/2 * dxdy * Emsp[n, j], {j, 1, n - 1}] + Sum[1/2 * dxdy * Emsp[i, 0], {i, 1, n - 1}] +
  Sum[1.0 * dxdy * Emsp[i, j], {i, 1, n - 1}, {j, 1, i - 1}] +
  Sum[1/2 * dxdy * Emsp[i, i], {i, 1, n - 1}]
```

```
EEbsp := 1/8 * dxdy * Ebsp[0, 0] + 1/4 * dxdy * Ebsp[n, 0] + 1/8 * dxdy * Ebsp[n, n] +
  Sum[1/2 * dxdy * Ebsp[n, j], {j, 1, n - 1}] + Sum[1/2 * dxdy * Ebsp[i, 0], {i, 1, n - 1}] +
  Sum[1.0 * dxdy * Ebsp[i, j], {i, 1, n - 1}, {j, 1, i - 1}] +
  Sum[1/2 * dxdy * Ebsp[i, i], {i, 1, n - 1}]

EETot = EEmsp + EEk + EEq + EEbsp;
```

Total Non-Dimensional Energy Equations for Circle Piles

Energy Equations

```
EEk := Sum[If[(i^2 + j^2) ≤ r^2/h^2, dxdy * Ekp[i, j], dxdy * Eks[i, j]], {i, 1, n - 1},
    {j, 1, i - 1}] + Sum[If[(i^2) ≤ r^2/h^2, 1/2 * dxdy * Ekp[i, 0], 1/2 * dxdy * Eks[i, 0]],
    {i, 1, n - 1}] + Sum[If[(2 i^2) ≤ r^2/h^2, 1/2 * dxdy * Ekp[i, i], 1/2 * dxdy * Eks[i, i]],
    {i, 1, n - 1}] + Sum[1/2 * dxdy * Eks[n, j], {j, 1, n - 1}] + 1/4 * dxdy * Eks[n, 0] +
  1/8 * dxdy * Ekp[0, 0] + 1/8 * dxdy * Eks[n, n]

EEq := Sum[If[(i^2 + j^2) ≤ r^2/h^2, dxdy * Eqp[i, j], dxdy * Eqs[i, j]], {i, 1, n - 1},
    {j, 1, i - 1}] + Sum[If[(i^2) ≤ r^2/h^2, 1/2 * dxdy * Eqp[i, 0], 1/2 * dxdy * Eqs[i, 0]],
    {i, 1, n - 1}] + Sum[If[(2 i^2) ≤ r^2/h^2, 1/2 * dxdy * Eqp[i, i], 1/2 * dxdy * Eqs[i, i]],
    {i, 1, n - 1}] + Sum[1/2 * dxdy * Eqs[n, j], {j, 1, n - 1}] + 1/4 * dxdy * Eqs[n, 0] +
  1/8 * dxdy * Eqp[0, 0] + 1/8 * dxdy * Eqs[n, n]

EEmsp := 1/8 * dxdy * Emsp[0, 0] + 1/4 * dxdy * Emsp[n, 0] + 1/8 * dxdy * Emsp[n, n] +
  Sum[1/2 * dxdy * Emsp[n, j], {j, 1, n - 1}] + Sum[1/2 * dxdy * Emsp[i, 0], {i, 1, n - 1}] +
  Sum[1.0 * dxdy * Emsp[i, j], {i, 1, n - 1}, {j, 1, i - 1}] +
  Sum[1/2 * dxdy * Emsp[i, i], {i, 1, n - 1}]
```

```
EEbsp := 1/8 * dxdy * Ebsp[0, 0] + 1/4 * dxdy * Ebsp[n, 0] + 1/8 * dxdy * Ebsp[n, n] +
  Sum[1/2 * dxdy * Ebsp[n, j], {j, 1, n - 1}] + Sum[1/2 * dxdy * Ebsp[i, 0], {i, 1, n - 1}] +
  Sum[1.0 * dxdy * Ebsp[i, j], {i, 1, n - 1}, {j, 1, i - 1}] +
  Sum[1/2 * dxdy * Ebsp[i, i], {i, 1, n - 1}]

EETot = EEbsp + EEmsp + EEk + EEq;
```

Variable List

```
VarW = Flatten[Table[w[i, j], {i, 0, n}, {j, 0, i}]];
VarV = Flatten[Table[v[i, j], {i, 0, n}, {j, 1, i}]];
VarU = Flatten[Table[u[i, j], {i, 0, n - 1}, {j, 0, i}]];
VarT = Sort[Flatten[Prepend[VarW, {VarU, VarV}]]];
Var = Drop[VarT, (Count[VarT, 0] + Count[VarT, qp / kp])];
VarRed = Union[Var];
VT = Partition[VarRed, 1];
Var1 = Table[Prepend[VT[[i]], .0001], {i, 1, Length[VarRed]}];
Var2 = Partition[Reverse[Flatten[Var1]], 2];
Var3 = Table[Flatten[Append[Var2[[i]], {-1, 1}]], {i, 1, Length[VarRed]}];
VVar = Sort[Var3];
```

Solution by Energy Minimization

```
sol = FindMinimum[EETot, VVar, MaxIterations → 100 000, AccuracyGoal → 7]

Energy = sol[[1]];
```

Extrapolating 1/8 portion to full Grid

```
U1 = Flatten[Table[U[j, i], {i, 0, n}, {j, 0, i}]];
V1 = Flatten[Table[V[i, j] /. sol[[2]], {i, 0, n}, {j, 0, i}]];
Do[U1[[i]] = V1[[i]], {i, 1, Length[U1]}]

V2 = Flatten[Table[V[j, i], {i, 0, n}, {j, 0, i}]];
U2 = Flatten[Table[U[i, j] /. sol[[2]], {i, 0, n}, {j, 0, i}]];
Do[V2[[i]] = U2[[i]], {i, 1, Length[U1]}]
```

Non-Dimensional Strains

$$ex[i\_, j\_] := u_x[i, j] + \frac{1}{2} * w_x[i, j]^2$$

$$ey[i\_, j\_] := v_y[i, j] + \frac{1}{2} * w_y[i, j]^2$$

$$exy[i\_, j\_] := u_x[i, j] + v_y[i, j] + w_x[i, j] * w_y[i, j]$$

$$emin[i\_, j\_] := \frac{ex[i, j] + ey[i, j]}{2} - \left(\left(\frac{ex[i, j] - ey[i, j]}{2}\right)^2 + exy[i, j]^2\right)^{\frac{1}{2}}$$

$$emax[i\_, j\_] := \frac{ex[i, j] + ey[i, j]}{2} + \left(\left(\frac{ex[i, j] - ey[i, j]}{2}\right)^2 + exy[i, j]^2\right)^{\frac{1}{2}}$$

```
xstrain = Table[ex[i, j], {i, 0, n}, {j, 0, n}] /. sol[[2]]
ystrain = Table[ey[i, j], {i, 0, n}, {j, 0, n}] /. sol[[2]]
xystrain = Table[exy[i, j], {i, 0, n}, {j, 0, n}] /. sol[[2]]
minstrain = Table[emin[i, j], {i, 0, n}, {j, 0, n}] /. sol[[2]]
maxstrain = Table[emax[i, j], {i, 0, n}, {j, 0, n}] /. sol[[2]]
```

Non-Dimensional Stress Resultants

$$nx[i\_, j\_] := \frac{E * t}{(1 - v^2)} * \left(u_x[i, j] + v * v_y[i, j] + \frac{1}{2} * \left(w_x[i, j]^2 + v * w_y[i, j]^2\right)\right)$$

$$ny[i\_, j\_] := \frac{E * t}{(1 - v^2)} * \left(v * u_x[i, j] + v_y[i, j] + \frac{1}{2} * \left(v * w_x[i, j]^2 + w_y[i, j]^2\right)\right)$$

$$nxy[i\_, j\_] := \frac{E * t}{2 * (1 + v)} * \left(u_y[i, j] + v_x[i, j] + \left(w_x[i, j] * w_y[i, j]\right)\right)$$

$$nmax[i\_, j\_] := \frac{nx[i, j] + ny[i, j]}{2} + \left(\left(\frac{nx[i, j] - ny[i, j]}{2}\right)^2 + nxy[i, j]^2\right)^{\frac{1}{2}}$$

$$nmin[i\_, j\_] := \frac{nx[i, j] + ny[i, j]}{2} - \left(\left(\frac{nx[i, j] - ny[i, j]}{2}\right)^2 + nxy[i, j]^2\right)^{\frac{1}{2}}$$

```
xstress = Table[nx[i, j], {i, 0, n}, {j, 0, n}] /. sol[[2]]
ystress = Table[ny[i, j], {i, 0, n}, {j, 0, n}] /. sol[[2]]
xystress = Table[nxy[i, j], {i, 0, n}, {j, 0, n}] /. sol[[2]]
minstress = Table[nmin[i, j], {i, 0, n}, {j, 0, n}] /. sol[[2]]
maxstress = Table[nmax[i, j], {i, 0, n}, {j, 0, n}] /. sol[[2]]
```

Dimensional Deflections W,U,V

$$\text{Do}\left[U[i,j] = \frac{\beta^2}{L} * u[i,j] /. \text{sol}[[2]], \{i,0,n\}, \{j,0,n\}\right]$$

$$\text{Do}\left[V[i,j] = \frac{\beta^2}{L} * v[i,j] /. \text{sol}[[2]], \{i,0,n\}, \{j,0,n\}\right]$$

```
Do[W[i, j] = β * w[i, j] /. sol[[2]], {i, 0, n}, {j, 0, n}]
```

Dimensional Boundary Conditions

Boundary Conditions in U

```
Do[U[n, j] = 0, {j, -1, n + 1}]
Do[U[0, j] = 0, {j, -1, n + 1}]
Do[U[i, -1] = U[i, 1], {i, -1, n + 1}]
Do[U[i, n + 1] = U[i, n - 1], {i, -1, n + 1}]
Do[U[n + 1, j] = -U[n - 1, j], {j, -1, n + 1}]
Do[U[-1, j] = -U[1, j], {j, -1, n + 1}]
```

Boundary Conditions in V

```
Do[V[i, 0] = 0, {i, -1, n + 1}]
Do[V[i, n] = 0, {i, -1, n + 1}]
Do[V[i, -1] = -V[i, 1], {i, -1, n + 1}]
Do[V[n + 1, j] = V[n - 1, j], {j, -1, n + 1}]
Do[V[-1, j] = V[1, j], {j, -1, n + 1}]
Do[V[i, n + 1] = -V[i, n - 1], {i, -1, n + 1}]
Do[V[i, j] = U[j, i], {i, 0, n}, {j, 0, n}]
```

Boundary Conditions in W

```
Do[W[n + 1, j] = W[n - 1, j], {j, -1, n + 1}]
Do[W[i, n + 1] = W[i, n - 1], {i, -1, n + 1}]
Do[W[i, -1] = W[i, 1], {i, -1, n + 1}]
Do[W[-1, j] = W[1, j], {j, -1, n + 1}]
Do[W[i, j] = W[j, i], {i, 0, n}, {j, 0, n}]
```

Dimensional Central Finite Difference Equations

$$U_x[i\_, j\_] := \frac{1}{2H}(U[i+1, j] - U[i-1, j])$$

$$U_y[i\_, j\_] := \frac{1}{2H}(U[i, j+1] - U[i, j-1])$$

$$V_x[i\_, j\_] := \frac{1}{2H}(V[i+1, j] - V[i-1, j])$$

$$V_y[i\_, j\_] := \frac{1}{2H}(V[i, j+1] - V[i, j-1])$$

$$W_x[i\_, j\_] := \frac{1}{2H}(W[i+1, j] - W[i-1, j])$$

$$W_y[i\_, j\_] := \frac{1}{2H}(W[i, j+1] - W[i, j-1])$$

$$W_{xx}[i\_, j\_] := \frac{1}{H^2}(W[i+1, j] - 2W[i, j] + W[i-1, j])$$

$$W_{yy}[i\_, j\_] := \frac{1}{H^2}(W[i, j+1] - 2W[i, j] + W[i, j-1])$$

$$W_{xy}[i\_, j\_] := \frac{1}{4H^2}(W[i+1, j+1] - W[i+1, j-1] - W[i-1, j+1] + W[i-1, j-1])$$

Dimensional Results Plots

W Deflections

```
Wp1 := Table[Table[W[i, a], {i, 0, n, 1}], {a, 0, n, 1}]
Wp2 :=
 Table[Flatten[Append[Table[W[i, a], {i, 0, n, 1}],
    Reverse[Table[W[i, a], {i, 0, n - 1}]]]], {a, 0, n, 1}]
WPlot := Join[Take[Wp2, {1, Length[Wp2] - 1}], Reverse[Wp2]] /. sol[[2]]
WDeflection := ListPlot3D[-WPlot];
WDeflection := ListPlot3D[-WPlot];
WContour := ListContourPlot[WPlot, Contours → 20];
```

U & V Deflections

```
Up1 := Table[Table[U[i, a], {i, 0, n, 1}], {a, 0, n, 1}]
Up2 :=
 Table[Flatten[Append[Table[U[i, a], {i, 0, n, 1}],
    -Reverse[Table[U[i, a], {i, 0, n - 1, 1}]]]], {a, 0, n, 1}]
UPlot := Join[Take[Up2, {1, Length[Up2] - 1}], Reverse[Up2]] /. sol[[2]]
UDeflection := ListPlot3D[UPlot]
UContour := ListContourPlot[UPlot]

Vp1 := Table[Table[V[i, a], {i, 0, n, 1}], {a, 0, n, 1}]
Vp2 :=
 Table[Flatten[Append[Table[V[i, a], {i, 0, n, 1}],
    Reverse[Table[V[i, a], {i, 0, n - 1, 1}]]]], {a, 0, n, 1}]
VPlot := Join[Take[Vp2, {1, Length[Vp2] - 1}], -Reverse[Vp2]] /. sol[[2]]
VDeflection := ListPlot3D[VPlot]
VContour := ListContourPlot[VPlot]
```

Total Deflected Shape W,U,V

```
cn = n + 1;
cx = 2 n (2 n + 1);
cy = cx;
fc = cx + cy;
fn = (2 n + 1)^2;

NXYZ =
  Partition[
   Flatten[
    Table[Table[{H * i + U[i, j], j * H + V[i, j], -W[i, j]} /. sol[[2]],
       {i, a, n}, {j, a, a}], {a, 0, n}] // N], 3];

Add = Function[x, a = 0; For[k = 1, k < x, k++, a = a + k]; a];
FullXYZ =
  Table[If[j ≤ i && i ≤ cn && j ≤ cn, n1 = i + (j - 1) cn - Add[j];
    {NXYZ[[n1, 1]], NXYZ[[n1, 2]], NXYZ[[n1, 3]]},
    If[i > cn && 2 cn - i ≥ j && j ≤ cn, n2 = cn - i + j cn - Add[j];
     {3 - NXYZ[[n2, 1]], NXYZ[[n2, 2]], NXYZ[[n2, 3]]},
     If[i ≤ cn && j > i && j ≤ cn, n3 = j + (i - 1) cn - Add[i];
      {NXYZ[[n3, 2]], NXYZ[[n3, 1]], NXYZ[[n3, 3]]},
      If[i > cn && j > 2 cn - i && j ≤ cn, n4 = j + (2 cn - i - 1) cn - Add[2 cn - i];
       {3 - NXYZ[[n4, 2]], NXYZ[[n4, 1]], NXYZ[[n4, 3]]},
       If[i ≤ cn && cn - i ≥ j - cn && j > cn, n5 = cn - j + i cn - Add[i];
        {NXYZ[[n5, 2]], 3 - NXYZ[[n5, 1]], NXYZ[[n5, 3]]},
        If[i ≤ cn && cn - i < j - cn && j > cn, n6 = i + (2 cn - j - 1) cn - Add[2 cn - j];
         {NXYZ[[n6, 1]], 3 - NXYZ[[n6, 2]], NXYZ[[n6, 3]]},
         If[i > cn && i ≤ j && j > cn, n7 = cn - i + (2 cn - j) cn - Add[2 cn - j];
          {3 - NXYZ[[n7, 1]], 3 - NXYZ[[n7, 2]], NXYZ[[n7, 3]]},
          If[i > cn && i > j && j > cn, n8 = cn - j + (2 cn - i) cn - Add[2 cn - i];
           {3 - NXYZ[[n8, 2]], 3 - NXYZ[[n8, 1]], NXYZ[[n8, 3]]}, {0, 0, 0}]]]]]]]],
   {i, 2 n + 1}, {j, 2 n + 1}];
a21 = 1; b21 = 1; a22 = 1;

FullCON =
  Partition[
   Flatten[Append[Table[{If[i == (2 n) a22 + 1, a22 += 1; a21 += 1, a21], a21 += 1},
      {i, 1, cx}], Table[{b21++, b21 + 2 n}, {i, 1, cy}]]], 2];

XYZPlot = Partition[Flatten[FullXYZ], 3];

DeflPlot = Flatten[Table[Line[Table[XYZPlot[[FullCON[[i, j]]]], {j, 2}]], {i, fc}]];

DeflectedShape := Show[Graphics3D[DeflPlot, Axes → True, BoxRatios → {1, 1, .5}]];
```

Dimensional Strains

$$Ex[i\_, j\_] := U_x[i, j] + \frac{1}{2} * W_x[i, j]^2$$

$$Ey[i\_, j\_] := V_y[i, j] + \frac{1}{2} * W_y[i, j]^2$$

$$Exy[i\_, j\_] := U_x[i, j] + V_y[i, j] + W_x[i, j] * W_y[i, j]$$

$$Emin[i\_, j\_] := \frac{Ex[i, j] + Ey[i, j]}{2} - \left(\left(\frac{Ex[i, j] - Ey[i, j]}{2}\right)^2 + Exy[i, j]^2\right)^{\frac{1}{2}}$$

$$Emax[i\_, j\_] := \frac{Ex[i, j] + Ey[i, j]}{2} + \left(\left(\frac{Ex[i, j] - Ey[i, j]}{2}\right)^2 + Exy[i, j]^2\right)^{\frac{1}{2}}$$

```
Xstrain = Table[Ex[i, j], {i, 0, n}, {j, 0, n}] /. sol[[2]]
Ystrain = Table[Ey[i, j], {i, 0, n}, {j, 0, n}] /. sol[[2]]
XYstrain = Table[Exy[i, j], {i, 0, n}, {j, 0, n}] /. sol[[2]]
Minstrain = Table[Emin[i, j], {i, 0, n}, {j, 0, n}] /. sol[[2]]
Maxstrain = Table[Emax[i, j], {i, 0, n}, {j, 0, n}] /. sol[[2]]
```

Dimensional Stress Resultants

$$Nx[i\_, j\_] := \frac{E * t}{(1 - \nu^2)} * \left(U_x[i, j] + \nu * V_y[i, j] + \frac{1}{2} * \left(W_x[i, j]^2 + \nu * W_y[i, j]^2\right)\right)$$

$$Ny[i\_, j\_] := \frac{E * t}{(1 - \nu^2)} * \left(\nu * U_x[i, j] + V_y[i, j] + \frac{1}{2} * \left(\nu * W_x[i, j]^2 + W_y[i, j]^2\right)\right)$$

$$Nxy[i\_, j\_] := \frac{E * t}{2 * (1 + \nu)} * \left(U_y[i, j] + V_x[i, j] + \left(W_x[i, j] * W_y[i, j]\right)\right)$$

$$Nmax[i\_, j\_] := \frac{Nx[i, j] + Ny[i, j]}{2} + \left(\left(\frac{Nx[i, j] - Ny[i, j]}{2}\right)^2 + Nxy[i, j]^2\right)^{\frac{1}{2}}$$

$$Nmin[i\_, j\_] := \frac{Nx[i, j] + Ny[i, j]}{2} - \left(\left(\frac{Nx[i, j] - Ny[i, j]}{2}\right)^2 + Nxy[i, j]^2\right)^{\frac{1}{2}}$$

```
Xstress = Table[Nx[i, j], {i, 0, n}, {j, 0, n}] /. sol[[2]]
Ystress = Table[Ny[i, j], {i, 0, n}, {j, 0, n}] /. sol[[2]]
XYstress = Table[Nxy[i, j], {i, 0, n}, {j, 0, n}] /. sol[[2]]
Minstress = Table[Nmin[i, j], {i, 0, n}, {j, 0, n}] /. sol[[2]]
Maxstress = Table[Nmax[i, j], {i, 0, n}, {j, 0, n}] /. sol[[2]]
```

Export Results to MS Excel

```
Export["WDefl.xls", WPlot]
Export["UDefl.xls", UPlot]
Export["VDefl.xls", VPlot]
```

```
Export["XStrain.xls", ExPlot]
Export["MinStrain.xls", EminPlot]
Export["MaxStrain.xls", EmaxPlot]

Export["XStress.xls", NxPlot]
Export["MinStress.xls", NminPlot]
Export["MaxStress.xls", NmaxPlot]
```

RunTime

```
Finish = TimeUsed[];
Elapsed = (Finish - Start) / 60 "minutes"
```

Appendix B

Supporting Information for Verification Study

B.1 Printout of Mathematica Notebook for 1st Example

1st Example Using Energy Method/Finite Difference Program

Plate Test Ugural pg. 180 Clamped rectangular (square) plate carrying uniform load q.

```
n = 20;
L = 1.0;
h = L/n;
dxdy = h^2;
E = 100 * 10^6;
t = 1 * 10^-3;
v = .25;
q = 1;
Dd = E * t^3 / (12 * (1 - v^2));
```

Boundary Conditions in W

```
Do[w[i, 0] = 0, {i, -1, n + 1}]
Do[w[i, n] = 0, {i, -1, n + 1}]
Do[w[0, j] = 0, {j, -1, n + 1}]
Do[w[n, j] = 0, {j, -1, n + 1}]
Do[w[i, -1] = w[i, 1], {i, -1, n + 1}]
Do[w[i, n + 1] = w[i, n - 1], {i, -1, n + 1}]
Do[w[-1, j] = w[1, j], {j, -1, n + 1}]
Do[w[n + 1, j] = w[n - 1, j], {j, -1, n + 1}]
Do[w[i, j] = w[j, i], {i, 0, n}, {j, 0, n}]
```

Energy Equations

```
Eb[i_, j_] = Dd/2 * ((w_xx[i, j] + w_yy[i, j])^2 - 2 * (1 - v) * (w_xx[i, j] * w_yy[i, j] - w_xy[i, j]^2));

Eq[i_, j_] = -q * w[i, j];
```

Total Energy Formulation

```
EEq := 1/4 * dxdy * Eq[0, 0] + 1/4 * dxdy * Eq[n, 0] + 1/4 * dxdy * Eq[0, n] + 1/4 * dxdy * Eq[n, n] +
  Sum[1/2 * dxdy * Eq[0, j], {j, 1, n - 1}] + Sum[1/2 * dxdy * Eq[n, j], {j, 1, n - 1}] +
  Sum[1/2 * dxdy * Eq[i, 0], {i, 1, n - 1}] + Sum[1/2 * dxdy * Eq[i, n], {i, 1, n - 1}] +
  Sum[1.0 * dxdy * Eq[i, j], {i, 1, n - 1}, {j, 1, n - 1}]
```

$$EEb := \frac{1}{4} * dxdy * Eb[0, 0] + \frac{1}{4} * dxdy * Eb[n, 0] + \frac{1}{4} * dxdy * Eb[0, n] + \frac{1}{4} * dxdy * Eb[n, n] +$$
$$Sum\left[\frac{1}{2} * dxdy * Eb[0, j], \{j, 1, n-1\}\right] + Sum\left[\frac{1}{2} * dxdy * Eb[n, j], \{j, 1, n-1\}\right] +$$
$$Sum\left[\frac{1}{2} * dxdy * Eb[i, 0], \{i, 1, n-1\}\right] + Sum\left[\frac{1}{2} * dxdy * Eb[i, n], \{i, 1, n-1\}\right] +$$
$$Sum[1.0 * dxdy * Eb[i, j], \{i, 1, n-1\}, \{j, 1, n-1\}]$$

```
EETot = EEb + EEq;
```

Central Finite Differences

$$w_x[i\_, j\_] := \frac{1}{2h} (w[i+1, j] - w[i-1, j])$$

$$w_y[i\_, j\_] := \frac{1}{2h} (w[i, j+1] - w[i, j-1])$$

$$w_{xx}[i\_, j\_] := \frac{1}{h^2} (w[i+1, j] - 2\,w[i, j] + w[i-1, j])$$

$$w_{yy}[i\_, j\_] := \frac{1}{h^2} (w[i, j+1] - 2\,w[i, j] + w[i, j-1])$$

$$w_{xy}[i\_, j\_] := \frac{1}{4h^2} (w[i+1, j+1] - w[i+1, j-1] - w[i-1, j+1] + w[i-1, j-1])$$

Variable List

```
Var = Drop[Union[Flatten[Table[w[i, j], {i, 0, n}, {j, 0, i}]]], 1];
Var2 = Table[{Var[[i]], .001}, {i, 1, Length[Var]}];
```

Solution

```
sol = Last[FindMinimum[EETot, Var2, AccuracyGoal → 7, MaxIterations → 10000]];
```

Result Plots

```
WDeflection;
```

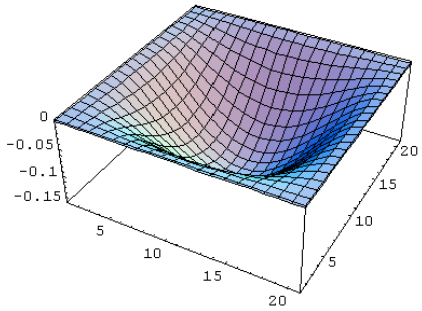


```
WContour;
```

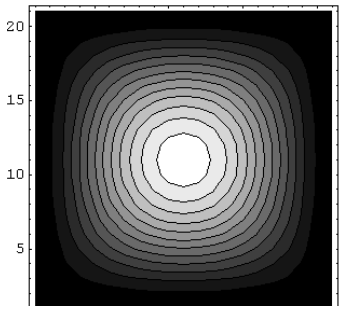

```
W2DCenter;
```

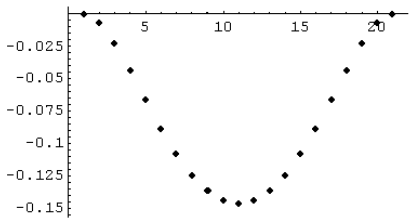

Analytical Solution

$$Wmax = .00126 * \frac{q * L^4}{Dd}$$

```
0.14175
```

```
WFDmax = Max[Flatten[Table[w[i, j], {i, 0, n}, {j, 0, n}] /. sol]]
```

```
0.146634
```

$$Error = Abs\left[\frac{Wmax - WFDmax}{Wmax} * 100\right]$$

```
3.44572
```

Runtime

```
Finish = TimeUsed[];
Elapsed = (Finish - Start) / 60
```

```
0.0151
```

```
Quit
```

B.2 Printout of Mathematica Notebook for 2nd Example

2nd Example Using Energy Method/Finite Difference Program

General Input

```
q = 95;
n = 20;
h = 1/n;
v = .316;
dxdy = h^2;
E = 100 * 10^6;
t = 1.0 * 10^-2;
Dd = E * t^3 / (12 (1 - v^2));
```

Energy Equations

```
Eq[i_, j_] := -q * w[i, j]

Em[i_, j_] :=
  E * t / (2 * (1 - v^2)) *
   ((u_x[i, j] + .5 * w_x[i, j]^2)^2 + (v_y[i, j] + .5 * w_y[i, j]^2)^2 +
    2 * v * (u_x[i, j] + 0.5 * w_x[i, j]^2) * (v_y[i, j] + 0.5 * w_y[i, j]^2) +
    (1 - v)/2 * (u_y[i, j] + v_x[i, j] + (w_x[i, j] * w_y[i, j]))^2)

Eb[i_, j_] := Dd/2 * (w_xx[i, j] + w_yy[i, j])^2
```

Central Finite Difference Equations

```
u_x[i_, j_] := 1/(2 h) (u[i + 1, j] - u[i - 1, j])
u_y[i_, j_] := 1/(2 h) (u[i, j + 1] - u[i, j - 1])
v_x[i_, j_] := 1/(2 h) (v[i + 1, j] - v[i - 1, j])
v_y[i_, j_] := 1/(2 h) (v[i, j + 1] - v[i, j - 1])
w_x[i_, j_] := 1/(2 h) (w[i + 1, j] - w[i - 1, j])
w_y[i_, j_] := 1/(2 h) (w[i, j + 1] - w[i, j - 1])
w_xx[i_, j_] := 1/h^2 (w[i + 1, j] - 2 w[i, j] + w[i - 1, j])
w_yy[i_, j_] := 1/h^2 (w[i, j + 1] - 2 w[i, j] + w[i, j - 1])
w_xy[i_, j_] := 1/(4 h^2) (w[i + 1, j + 1] - w[i + 1, j - 1] - w[i - 1, j + 1] + w[i - 1, j - 1])
```

Boundary Conditions in U

```
Do[u[i, 0] = 0, {i, -1, n + 1}]
Do[u[i, n] = 0, {i, -1, n + 1}]
Do[u[0, j] = 0, {j, -1, n + 1}]
Do[u[n, j] = 0, {j, -1, n + 1}]
Do[u[i, -1] = u[i, 1], {i, -1, n + 1}]
Do[u[i, n + 1] = u[i, n - 1], {i, -1, n + 1}]
Do[u[-1, j] = -u[1, j], {j, -1, n + 1}]
Do[u[n + 1, j] = -u[n - 1, j], {j, -1, n + 1}]
```

Boundary Conditions in V

```
Do[v[i, 0] = 0, {i, -1, n + 1}]
Do[v[i, n] = 0, {i, -1, n + 1}]
Do[v[0, j] = 0, {j, -1, n + 1}]
Do[v[n, j] = 0, {j, -1, n + 1}]
Do[v[i, -1] = -v[i, 1], {i, -1, n + 1}]
Do[v[i, n + 1] = -v[i, n - 1], {i, -1, n + 1}]
Do[v[-1, j] = v[1, j], {j, -1, n + 1}]
Do[v[n + 1, j] = v[n - 1, j], {j, -1, n + 1}]
```

Boundary Conditions in W

```
Do[w[i, 0] = 0, {i, -1, n + 1}]
Do[w[i, n] = 0, {i, -1, n + 1}]
Do[w[0, j] = 0, {j, -1, n + 1}]
Do[w[n, j] = 0, {j, -1, n + 1}]
Do[w[i, -1] = w[i, 1], {i, -1, n + 1}]
Do[w[i, n + 1] = w[i, n - 1], {i, -1, n + 1}]
Do[w[-1, j] = w[1, j], {j, -1, n + 1}]
Do[w[n + 1, j] = w[n - 1, j], {j, -1, n + 1}]

Do[w[i, j] = w[j, i], {i, 0, n}, {j, 0, n}]
Do[u[i, j] = v[j, i], {i, 0, n}, {j, 0, n}]
```

Energy Equations

$$\begin{aligned}
\texttt{EEq} := {} & \frac{1}{4} * \texttt{dxdy} * \texttt{Eq[0, 0]} + \frac{1}{4} * \texttt{dxdy} * \texttt{Eq[n, 0]} + \frac{1}{4} * \texttt{dxdy} * \texttt{Eq[0, n]} + \frac{1}{4} * \texttt{dxdy} * \texttt{Eq[n, n]} + \\
& \texttt{Sum}\left[\frac{1}{2} * \texttt{dxdy} * \texttt{Eq[0, j]}, \{\texttt{j}, 1, \texttt{n} - 1\}\right] + \texttt{Sum}\left[\frac{1}{2} * \texttt{dxdy} * \texttt{Eq[n, j]}, \{\texttt{j}, 1, \texttt{n} - 1\}\right] + \\
& \texttt{Sum}\left[\frac{1}{2} * \texttt{dxdy} * \texttt{Eq[i, 0]}, \{\texttt{i}, 1, \texttt{n} - 1\}\right] + \texttt{Sum}\left[\frac{1}{2} * \texttt{dxdy} * \texttt{Eq[i, n]}, \{\texttt{i}, 1, \texttt{n} - 1\}\right] + \\
& \texttt{Sum[1.0} * \texttt{dxdy} * \texttt{Eq[i, j]}, \{\texttt{i}, 1, \texttt{n} - 1\}, \{\texttt{j}, 1, \texttt{n} - 1\}\texttt{]}
\end{aligned}$$

$$\begin{aligned}
\texttt{EEm} := {} & \frac{1}{4} * \texttt{dxdy} * \texttt{Em[0, 0]} + \frac{1}{4} * \texttt{dxdy} * \texttt{Em[n, 0]} + \frac{1}{4} * \texttt{dxdy} * \texttt{Em[0, n]} + \frac{1}{4} * \texttt{dxdy} * \texttt{Em[n, n]} + \\
& \texttt{Sum}\left[\frac{1}{2} * \texttt{dxdy} * \texttt{Em[0, j]}, \{\texttt{j}, 1, \texttt{n} - 1\}\right] + \texttt{Sum}\left[\frac{1}{2} * \texttt{dxdy} * \texttt{Em[n, j]}, \{\texttt{j}, 1, \texttt{n} - 1\}\right] + \\
& \texttt{Sum}\left[\frac{1}{2} * \texttt{dxdy} * \texttt{Em[i, 0]}, \{\texttt{i}, 1, \texttt{n} - 1\}\right] + \texttt{Sum}\left[\frac{1}{2} * \texttt{dxdy} * \texttt{Em[i, n]}, \{\texttt{i}, 1, \texttt{n} - 1\}\right] + \\
& \texttt{Sum[1.0} * \texttt{dxdy} * \texttt{Em[i, j]}, \{\texttt{i}, 1, \texttt{n} - 1\}, \{\texttt{j}, 1, \texttt{n} - 1\}\texttt{]}
\end{aligned}$$

```
EEb := 1/4 * dxdy * Eb[0, 0] + 1/4 * dxdy * Eb[n, 0] + 1/4 * dxdy * Eb[0, n] + 1/4 * dxdy * Eb[n, n] +
  Sum[1/2 * dxdy * Eb[0, j], {j, 1, n - 1}] + Sum[1/2 * dxdy * Eb[n, j], {j, 1, n - 1}] +
  Sum[1/2 * dxdy * Eb[i, 0], {i, 1, n - 1}] + Sum[1/2 * dxdy * Eb[i, n], {i, 1, n - 1}] +
  Sum[1.0 * dxdy * Eb[i, j], {i, 1, n - 1}, {j, 1, n - 1}]

EETot = EEm + EEq + EEb;
```

Variable List

```
VarW = Flatten[Table[w[x, y], {x, 1, n - 1}, {y, 1, n - 1}]];
VarV = Flatten[Table[v[x, y], {x, 1, n - 1}, {y, 1, n - 1}]];
VarU = Flatten[Table[u[x, y], {x, 1, n - 1}, {y, 1, n - 1}]];
VarT = Sort[Flatten[Prepend[VarW, {VarU, VarV}]]];
Var = Drop[VarT, Count[VarT, 0]];
VarRed = Union[Var];
VVar = Table[{VarRed[[i]], .01}, {i, 1, Length[VarRed]}];
```

Solution

```
sol = FindMinimum[EETot, VVar, MaxIterations → 100000, AccuracyGoal → 7];
```

Result Plots

```
WDeflection;
```

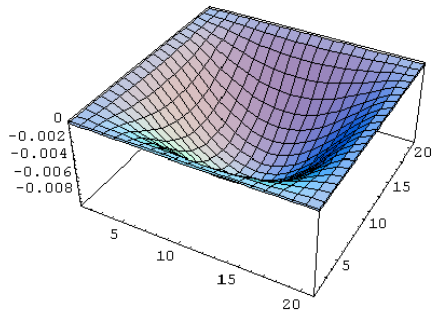


```
WContour;
```

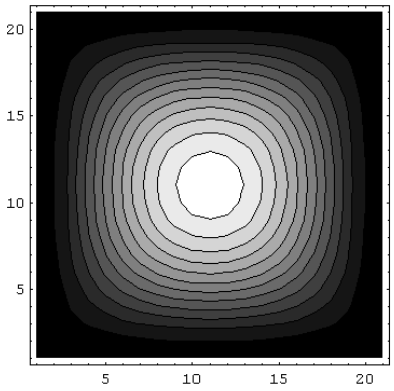

```
W2DCenter;
```

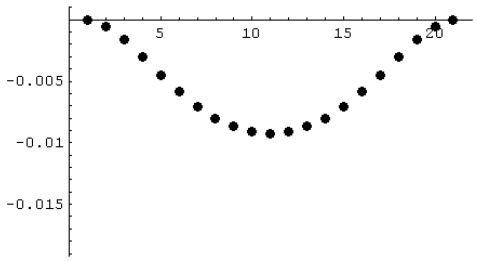

Analytical Solution

```
WFDmax = Max[Flatten[Table[w[i, j], {i, 0, n}, {j, 0, n}] /. sol[[2]]]]
```

```
0.00926031
```

```
Wmax = t * .912
```

```
0.00912
```

$$\text{Error} = \text{Abs}\left[\frac{\text{Wmax} - \text{WFDmax}}{\text{Wmax}} * 100\right]$$

```
1.53847
```

Runtime

```
Finish = TimeUsed[];
Elapsed = (Finish - Start) / 60 "minutes"
```

```
0.207817 minutes
```

```
Quit
```

Appendix C

Supporting Information for Convergence Study

C.1 Printout of Mathematica Notebook for Convergence Study

Convergence of Energy Method/Finite Difference Program for Geosynthetic Reinforcement

Non-Dimensionalization

```
B = .6; L = 3; t = 1.5*10^-3; E = 500*10^6; v = 0; Kp = 29.2183*10^6; Ks = 160.229*10^3; Qp = 146.034*10^3;
Qs = 30.643*10^3;

β = ((Qs*L^4*(1 - v^2))/(E*t))^(1/3);

qp = Qp/Qs;

qs = 1.0;

ks = (Ks*L^4*(1 - v^2))/(β^2*E*t);

kp = (Kp*L^4*(1 - v^2))/(β^2*E*t);

γ = (1 - v)/2;

α = (Dd*β)/(2*Qs*L^4);

Dd = (E*t^3)/(12 (1 - v^2));
```

General Input

```
n = 20;

h = 1/(2*n);

H = L/(2*n);

b = Ceiling[.4*n];

dxdy = h^2;
```

NonDimensional Energy Equations

```
Eks[i_, j_] := 1/2*ks*(w[i, j])^2

Ekp[i_, j_] := 1/2*kp*(w[i, j])^2

Eqs[i_, j_] := -qs*w[i, j]

Eqp[i_, j_] := -qp*w[i, j]
```

```
Emsp[i_, j_] :=
 1/2 * ((u_x[i, j] + .5 * w_x[i, j]^2)^2 + (v_y[i, j] + .5 * w_y[i, j]^2)^2 +
    2 * ν * (u_x[i, j] + 0.5 * w_x[i, j]^2) * (v_y[i, j] + 0.5 * w_y[i, j]^2) +
    (1 - ν)/2 * (u_y[i, j] + v_x[i, j] + (w_x[i, j] * w_y[i, j]))^2)

Ebsp[i_, j_] := α * (w_xx[i, j] + w_yy[i, j])^2
```

NonDimensional Central Finite Difference Equations

```
u_x[i_, j_] := 1/(2 h) (u[i + 1, j] - u[i - 1, j])
u_y[i_, j_] := 1/(2 h) (u[i, j + 1] - u[i, j - 1])
v_x[i_, j_] := 1/(2 h) (v[i + 1, j] - v[i - 1, j])
v_y[i_, j_] := 1/(2 h) (v[i, j + 1] - v[i, j - 1])
w_x[i_, j_] := 1/(2 h) (w[i + 1, j] - w[i - 1, j])
w_y[i_, j_] := 1/(2 h) (w[i, j + 1] - w[i, j - 1])
w_xx[i_, j_] := 1/h^2 (w[i + 1, j] - 2 w[i, j] + w[i - 1, j])
w_yy[i_, j_] := 1/h^2 (w[i, j + 1] - 2 w[i, j] + w[i, j - 1])
w_xy[i_, j_] := 1/(4 h^2) (w[i + 1, j + 1] - w[i + 1, j - 1] - w[i - 1, j + 1] + w[i - 1, j - 1])
```

NonDimensional Boundary Conditions

Boundary Conditions in U

```
Do[u[n, j] = 0, {j, -1, n + 1}]
Do[u[0, j] = 0, {j, -1, n + 1}]
Do[u[i, -1] = u[i, 1], {i, -1, n + 1}]
Do[u[i, n + 1] = u[i, n - 1], {i, -1, n + 1}]
Do[u[n + 1, j] = -u[n - 1, j], {j, -1, n + 1}]
Do[u[-1, j] = -u[1, j], {j, -1, n + 1}]
```

Boundary Conditions in V

```
Do[v[i, 0] = 0, {i, -1, n + 1}]
Do[v[i, n] = 0, {i, -1, n + 1}]
Do[v[i, -1] = -v[i, 1], {i, -1, n + 1}]
Do[v[n + 1, j] = v[n - 1, j], {j, -1, n + 1}]
Do[v[-1, j] = v[1, j], {j, -1, n + 1}]
Do[v[i, n + 1] = -v[i, n - 1], {i, -1, n + 1}]
Do[v[i, j] = u[j, i], {i, 0, n}, {j, 0, n}]
```

Boundary Conditions in W

```
Do[w[n + 1, j] = w[n - 1, j], {j, -1, n + 1}]
Do[w[i, n + 1] = w[i, n - 1], {i, -1, n + 1}]
Do[w[i, -1] = w[i, 1], {i, -1, n + 1}]
Do[w[-1, j] = w[1, j], {j, -1, n + 1}]
Do[w[i, j] = w[j, i], {i, 0, n}, {j, 0, n}]
```

Total Energy Equations

```
EEkp := 1/8 * dxdy * Ekp[0, 0] + 1/4 * dxdy * Ekp[b, 0] + 1/8 * dxdy * Ekp[b, b] +
  Sum[1.0 * dxdy * Ekp[i, j], {i, 2, b - 1}, {j, 1, i - 1}] + Sum[1/2 * dxdy * Ekp[i, i], {i, 1, b - 1}] +
  Sum[1/2 * dxdy * Ekp[i, 0], {i, 1, b - 1}] + Sum[1/2 * dxdy * Ekp[b, j], {j, 1, b - 1}]

EEqp := 1/8 * dxdy * Eqp[0, 0] + 1/4 * dxdy * Eqp[b, 0] + 1/8 * dxdy * Eqp[b, b] +
  Sum[1.0 * dxdy * Eqp[i, j], {i, 2, b - 1}, {j, 1, i - 1}] + Sum[1/2 * dxdy * Eqp[i, i], {i, 1, b - 1}] +
  Sum[1/2 * dxdy * Eqp[i, 0], {i, 1, b - 1}] + Sum[1/2 * dxdy * Eqp[b, j], {j, 1, b - 1}]

EEks := 1/4 * dxdy * Eks[b, 0] + 3/8 * dxdy * Eks[b, b] + Sum[1/2 * dxdy * Eks[b, j], {j, 1, b - 1}] +
  Sum[1/2 * dxdy * Eks[i, 0], {i, b + 1, n - 1}] + 1/8 * dxdy * Eks[n, n] + 1/4 * dxdy * Eks[n, 0] +
  Sum[1/2 * dxdy * Eks[n, j], {j, 1, n - 1}] + Sum[1.0 * dxdy * Eks[i, j], {i, b + 1, n - 1}, {j, 1, i - 1}] +
  Sum[1/2 * dxdy * Eks[i, i], {i, b + 1, n - 1}]

EEqs := 1/4 * dxdy * Eqs[b, 0] + 3/8 * dxdy * Eqs[b, b] + Sum[1/2 * dxdy * Eqs[b, j], {j, 1, b - 1}] +
  Sum[1/2 * dxdy * Eqs[i, 0], {i, b + 1, n - 1}] + 1/8 * dxdy * Eqs[n, n] + 1/4 * dxdy * Eqs[n, 0] +
  Sum[1/2 * dxdy * Eqs[n, j], {j, 1, n - 1}] + Sum[1.0 * dxdy * Eqs[i, j], {i, b + 1, n - 1}, {j, 1, i - 1}] +
  Sum[1/2 * dxdy * Eqs[i, i], {i, b + 1, n - 1}]

EEmsp := 1/8 * dxdy * Emsp[0, 0] + 1/4 * dxdy * Emsp[n, 0] + 1/8 * dxdy * Emsp[n, n] +
  Sum[1/2 * dxdy * Emsp[n, j], {j, 1, n - 1}] + Sum[1/2 * dxdy * Emsp[i, 0], {i, 1, n - 1}] +
  Sum[1.0 * dxdy * Emsp[i, j], {i, 1, n - 1}, {j, 1, i - 1}] + Sum[1/2 * dxdy * Emsp[i, i], {i, 1, n - 1}]

EEbsp := 1/8 * dxdy * Ebsp[0, 0] + 1/4 * dxdy * Ebsp[n, 0] + 1/8 * dxdy * Ebsp[n, n] +
  Sum[1/2 * dxdy * Ebsp[n, j], {j, 1, n - 1}] + Sum[1/2 * dxdy * Ebsp[i, 0], {i, 1, n - 1}] +
  Sum[1.0 * dxdy * Ebsp[i, j], {i, 1, n - 1}, {j, 1, i - 1}] + Sum[1/2 * dxdy * Ebsp[i, i], {i, 1, n - 1}]

EETot = EEbsp + EEmsp + EEks + EEqs + EEkp + EEqp;
```

Variable List

```
VarW = Flatten[Table[w[i, j], {i, 0, n}, {j, 0, i}]];
VarV = Flatten[Table[v[i, j], {i, 0, n}, {j, 1, i}]];
VarU = Flatten[Table[u[i, j], {i, 0, n - 1}, {j, 0, i}]];
```

```
VarT = Sort[Flatten[Prepend[VarW, {VarU, VarV}]]];
Var = Drop[VarT, (Count[VarT, 0] + Count[VarT, qp / kp])];
VarRed = Union[Var];
VT = Partition[VarRed, 1];
Var1 = Table[Prepend[VT[[i]], .0001], {i, 1, Length[VarRed]}];
Var2 = Partition[Reverse[Flatten[Var1]], 2];
Var3 = Table[Flatten[Append[Var2[[i]], {-1, 1}]], {i, 1, Length[VarRed]}];
VVar = Sort[Var3];
```

Solution

```
sol = FindMinimum[EETot, VVar, MaxIterations → 100000, AccuracyGoal → 7]
```

W Deflections

```
W2D5 =
 Partition[
  Flatten[{Table[i, {i, 0, 2 n}],
    {-Join[Table[w[i, 0], {i, 0, n}], Reverse[Table[w[i, 0], {i, 0, n - 1}]]] /. sol[[2]]}}], 2 n + 1]

Export["W2D.xls", W2D5]
```

W2D.xls

Appendix D

Supporting Information for Alternative Models

D.1 Printout of Mathematica Notebook for Rayleigh-Ritz Model

Rayleigh - Ritz Method Program for Geosynthetic Reinforcement

```
Clear["@"];
Off[General::spell1];
Start = TimeUsed[];
```

Standard Non-Dimensional Input

```
ks = 17.17;
kp = 500 * ks;
qp = 7 + (2 / 3);
b = 0.2;
v = 0;
```

Shape Functions Including Constant Terms

```
i = 3;
j = 3;
p = 2;
q = 2;
w[x_, y_] := C0,0 + Sum_{m=1}^{i} Sum_{n=1}^{j} Cm,n * (2 - (Cos[2 * π * n * x]) - (Cos[2 * π * n * y]))^m;

u[x_, y_] := A1,0 * Sin[2 * π * x] + Sum_{m=1}^{p} Sum_{n=1}^{q} Am,n * Sin[2 * π * n * x] * Cos[2 * π * m * y]

v[x_, y_] := u[y, x]
```

Energy Equations

$$
\begin{aligned}
\text{Ems} = \text{Expand}\Big[& \frac{1}{2} * \left(\left((D[u[x, y], x]) + \frac{1}{2} * (D[w[x, y], x])^2 \right)^2 \right) + \\
& \frac{1}{2} * \left(\left((D[v[x, y], y]) + \frac{1}{2} * (D[w[x, y], y])^2 \right)^2 \right) + \\
& \frac{1}{4} * ((D[u[x, y], y] + D[v[x, y], x] + (D[w[x, y], x]) * (D[w[x, y], y]))^2) + \\
& 2 * v * \left(D[u[x, y], x] + \frac{1}{2} * (D[w[x, y], x]\,\hat{}\,2) \right) * \left(D[v[x, y], y] + \frac{1}{2} * (D[w[x, y], y]^2) \right) + \\
& \frac{1}{2} * ((1 - v) * (D[u[x, y], y] + D[v[x, y], x] + (D[w[x, y], x]) * (D[w[x, y], y]))^2) \Big];
\end{aligned}
$$

```
Eks = Expand[1/2 * ks * (w[x, y])^2];

Ekp = Expand[2 * (kp - ks) * (w[x, y])^2];

Eqs = Expand[-w[x, y]];

Eqp = Expand[-(4 * (qp - 1) * w[x, y])];

EEms[x_, y_] = Integrate[Ems, {x, 0, 1}, {y, 0, 1}];
EEks[x_, y_] = Integrate[Eks, {x, 0, 1}, {y, 0, 1}];
EEkp[x_, y_] = Integrate[Ekp, {x, 0, b}, {y, 0, b}];
EEqs[x_, y_] = Integrate[Eqs, {x, 0, 1}, {y, 0, 1}];
EEqp[x_, y_] = Integrate[Eqp, {x, 0, b}, {y, 0, b}];
```

Total Energy

```
EETot = EEms[x, y] + EEks[x, y] + EEkp[x, y] + EEqs[x, y] + EEqp[x, y];
```

Coefficients List

```
VarA = Flatten[Flatten[Table[A_{α,β}, {α, 1, p}, {β, 1, q}]]];
VarC = Flatten[Flatten[Table[C_{α,β}, {α, 1, i}, {β, 1, j}]]];
Var = Flatten[{C_{0,0}, A_{1,0}, VarA, VarC}]
```

Numerical Minimization

```
sol = NMinimize[EETot, Var, MaxIterations → 10000, AccuracyGoal → 5]
```

Return Minimimized Coefficients to Shape Functions

```
ww[x_, y_] = w[x, y] /. sol[[2]]
uu[x_, y_] = u[x, y] /. sol[[2]]
vv[x_, y_] = v[x, y] /. sol[[2]]
```

Deflection at Center of Geosynthetic

```
ww[0.5, 0.5] /. sol[[2]]
```

Results Plots

```
Plot3D[-ww[x, y], {x, 0, 1}, {y, 0, 1}, PlotPoints → 50]
```

Runtime

```
Finish = TimeUsed[];
Elapsed = (Finish - Start) / 60 "minutes"
```

D.2 Printout of Mathematica Notebook for Nonlinear Membrane Model

Finite Difference Nonlinear Plate Equations Program for Geosynthetic Reinforcement

```
Clear["@"]
Off[General::spell1];
Start = TimeUsed[];
```

General Input

```
ks = 17.17;
kp = 500 * ks;
qp = 7 + 2/3;
n = 20;
h = 1/(2 n);
b = Ceiling[0.4 n];
```

Initial Guess for FindRoot

```
UGuess = 0; Umin = -.01; Umax = .01;
VGuess = 0; Vmin = -.01; Vmax = .01;
WGuess = 0; Wmin = (qp / kp) - .01; Wmax = (1 / ks) + .01;


Do[v[i, 0] = 0, {i, 0, n}]
Do[u[n, j] = 0, {j, 0, n}]
```

Variable List

```
VarW = Flatten[Table[w[x, y], {x, 0, n}, {y, 0, x}]];
VarV = Flatten[Table[v[x, y], {x, 0, n}, {y, 0, x}]];
VarU = Flatten[Table[u[x, y], {x, 0, n}, {y, 0, x}]];
VarT = Sort[Flatten[Prepend[VarW, {VarU, VarV}]]];
Var = Drop[VarT, (Count[VarT, 0] + Count[VarT, qp / kp])];
VarRed = Union[Var];
BU = Length[Sum[test[i, j], {i, 0, n - 1}, {j, 0, i}]];
BV = BU * 2;
BW = Length[VarRed];
VT = Partition[VarRed, 1];
UU = Table[Prepend[VT[[i]], UGuess], {i, 1, BU}];
UU2 = Partition[Reverse[Flatten[UU]], 2];
UU3 = Table[Flatten[Append[UU2[[i]], {Umin, Umax}]], {i, 1, BU}];
VV = Table[Prepend[VT[[i]], VGuess], {i, BU + 1, BV}];
VV2 = Partition[Reverse[Flatten[VV]], 2];
VV3 = Table[Flatten[Append[VV2[[i]], {Vmin, Vmax}]], {i, 1, BV - BU}];
WW = Table[Prepend[VT[[i]], WGuess], {i, BV + 1, BW}];
WW2 = Partition[Reverse[Flatten[WW]], 2];
WW3 = Table[Flatten[Append[WW2[[i]], {Wmin, Wmax}]], {i, 1, BW - BV}];
VVar = Sort[Join[UU3, VV3, WW3]];
```

Central Finite Difference Equations

$$u_x[i\_, j\_] := \frac{1}{2\,h}\,(u[i+1, j] - u[i-1, j])$$

$$u_y[i\_, j\_] := \frac{1}{2\,h}\,(u[i, j+1] - u[i, j-1])$$

$$u_{xx}[i\_, j\_] := \frac{1}{h^2}\,(u[i+1, j] - 2\,u[i, j] + u[i-1, j])$$

$$u_{yy}[i\_, j\_] := \frac{1}{h^2}\,(u[i, j+1] - 2\,u[i, j] + u[i, j-1])$$

$$u_{xy}[i\_, j\_] := \frac{1}{4\,h^2}\,(u[i+1, j+1] - u[i+1, j-1] - u[i-1, j+1] + u[i-1, j-1])$$

$$v_x[i\_, j\_] := \frac{1}{2\,h}\,(v[i+1, j] - v[i-1, j])$$

$$v_y[i\_, j\_] := \frac{1}{2\,h}\,(v[i, j+1] - v[i, j-1])$$

$$v_{xx}[i\_, j\_] := \frac{1}{h^2}\,(v[i+1, j] - 2\,v[i, j] + v[i-1, j])$$

$$v_{yy}[i\_, j\_] := \frac{1}{h^2}\,(v[i, j+1] - 2\,v[i, j] + v[i, j-1])$$

$$v_{xy}[i\_, j\_] := \frac{1}{4\,h^2}\,(v[i+1, j+1] - v[i+1, j-1] - v[i-1, j+1] + v[i-1, j-1])$$

$$w_x[i\_, j\_] := \frac{1}{2\,h}\,(w[i+1, j] - w[i-1, j])$$

$$w_y[i\_, j\_] := \frac{1}{2\,h}\,(w[i, j+1] - w[i, j-1])$$

$$w_{xx}[i\_, j\_] := \frac{1}{h^2}\,(w[i+1, j] - 2\,w[i, j] + w[i-1, j])$$

$$w_{yy}[i\_, j\_] := \frac{1}{h^2}\,(w[i, j+1] - 2\,w[i, j] + w[i, j-1])$$

$$w_{xy}[i\_, j\_] := \frac{1}{4\,h^2}\,(w[i+1, j+1] - w[i+1, j-1] - w[i-1, j+1] + w[i-1, j-1])$$

Equations per Node

$$FD1[i\_, j\_] :=$$
$$v_{yy}[i, j] + .5\,v_{xx}[i, j] + .5\,u_{xy}[i, j] + (w_{yy}[i, j] + .5\,w_{xx}[i, j]) * w_y[i, j] + .5\,w_x[i, j] * w_{xy}[i, j] == 0$$

$$FD21[i\_, j\_] :=$$
$$(u_x[i, j] + .5\,w_x[i, j]^2) * w_{xx}[i, j] + (v_y[i, j] + .5\,w_y[i, j]^2) * w_{yy}[i, j] +$$
$$(u_y[i, j] + v_x[i, j] + w_x[i, j] * w_y[i, j]) * w_{xy}[i, j] + qp - kp * w[i, j] == 0$$

$$FD22[i\_, j\_] :=$$
$$(u_x[i, j] + .5\,w_x[i, j]^2) * w_{xx}[i, j] + (v_y[i, j] + .5\,w_y[i, j]^2) * w_{yy}[i, j] +$$
$$(u_y[i, j] + v_x[i, j] + w_x[i, j] * w_y[i, j]) * w_{xy}[i, j] + 1 - ks * w[i, j] == 0$$

$$FD3[i\_, j\_] :=$$
$$u_{xx}[i, j] + .5\,u_{yy}[i, j] + .5\,v_{xy}[i, j] + (w_{xx}[i, j] + .5\,w_{yy}[i, j]) * w_x[i, j] + .5\,w_y[i, j] * w_{xy}[i, j] == 0$$

Total Equation List

```
FDS1[i_, j_] = Table[FD1[i, j], {i, 0, n}, {j, 1, i}];
FDS21[i_, j_] = Table[FD21[i, j], {i, b, b}, {j, 0, i}];
FDS22[i_, j_] = Table[FD22[i, j], {i, b + 1, n}, {j, 0, i}];
FDS3[i_, j_] = Table[FD3[i, j], {i, 0, n - 1}, {j, 0, i}];

FDSTot = Flatten[Prepend[FDS1[i, j], {FDS21[i, j], FDS22[i, j], FDS3[i, j]}]];
```

Boundary Conditions in U

```
Do[u[i, -1] = u[i, 1], {i, -1, n + 1}]
Do[u[n + 1, j] = -u[n - 1, j], {j, -1, n + 1}]
Do[u[-1, j] = -u[1, j], {j, -1, n + 1}]
```

Boundary Conditions in V

```
Do[v[i, -1] = -v[i, 1], {i, -1, n + 1}]
Do[v[n + 1, j] = v[n - 1, j], {j, -1, n + 1}]
Do[v[-1, j] = v[1, j], {j, -1, n + 1}]
Do[v[i, i + 2] = u[i + 2, i], {i, 0, n}]
Do[u[i, i + 2] = v[i + 2, i], {i, 0, n}]
Do[u[i, i + 1] = v[i + 1, i], {i, -1, n}]
Do[v[i, i + 1] = u[i + 1, i], {i, -1, n}]
```

Boundary Conditions in W

```
Do[w[n + 1, j] = w[n - 1, j], {j, -1, n + 1}]
Do[w[i, j] = w[j, i], {i, -1, n + 1}, {j, -1, n + 1}]
Do[w[i, -1] = w[i, 1], {i, -1, n + 1}]
Do[w[-1, j] = w[1, j], {j, -1, n + 1}]
u[n + 1, n + 2] = v[n + 1, n + 2] = w[n + 1, n + 2] = 0;
```

Solve for Reduced Variable List VVar

```
sol = FindRoot[FDSTot, VVar, AccuracyGoal → 5, MaxIterations → 10000] // Chop
```

Results Plots

```
wp1 := Table[Table[w[i, a], {i, 0, n}] /. sol, {a, 0, n}]
wp2 := Table[Flatten[Append[Table[w[i, a], {i, 0, n}] /. sol, Reverse[Table[w[i, a], {i, 0, n}] /. sol]]],
  {a, 0, n}]
WPlot := Join[wp2, Reverse[wp2]] /. sol
WPlot // MatrixForm;
wp1 // MatrixForm
ListPlot3D[-WPlot];
ListContourPlot[-WPlot];
```

Appendix E

Supporting Information for Geogrid Testing

E.1 Test Data

Date of Test: 9/29/2006
Temperature: 72 °F
Humidity: 38 %
Tests Conducted: 1, 2, 3, 7, 8, 23, 24

Date of Test: 10/13/2006
Temperature: 72 °F
Humidity: 34 %
Tests Conducted: 4, 5, 6, 9, 10, 11, 12, 13, 14, 15, 16, 17, 18, 19, 20, 21, 22, 25, 26, 27

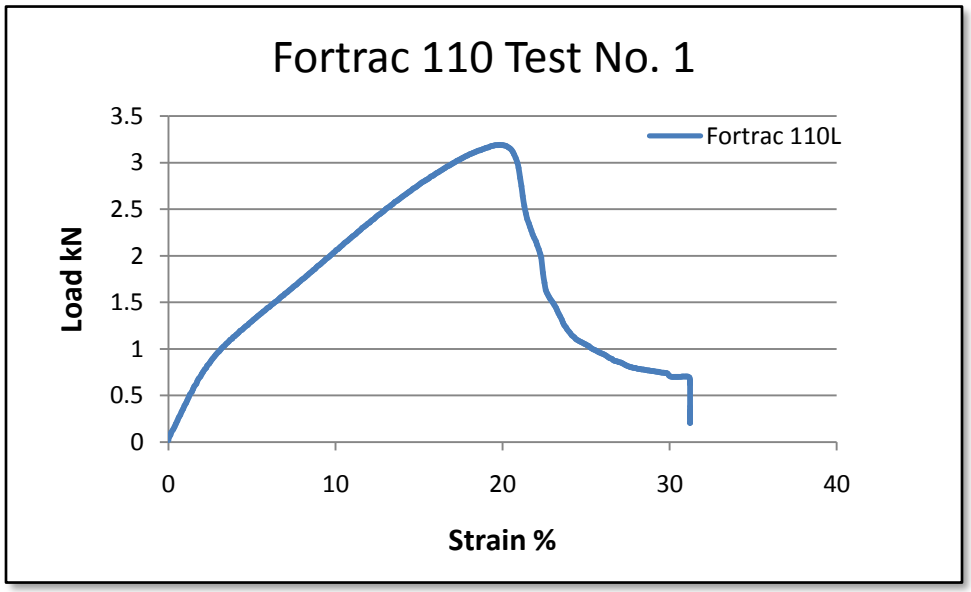

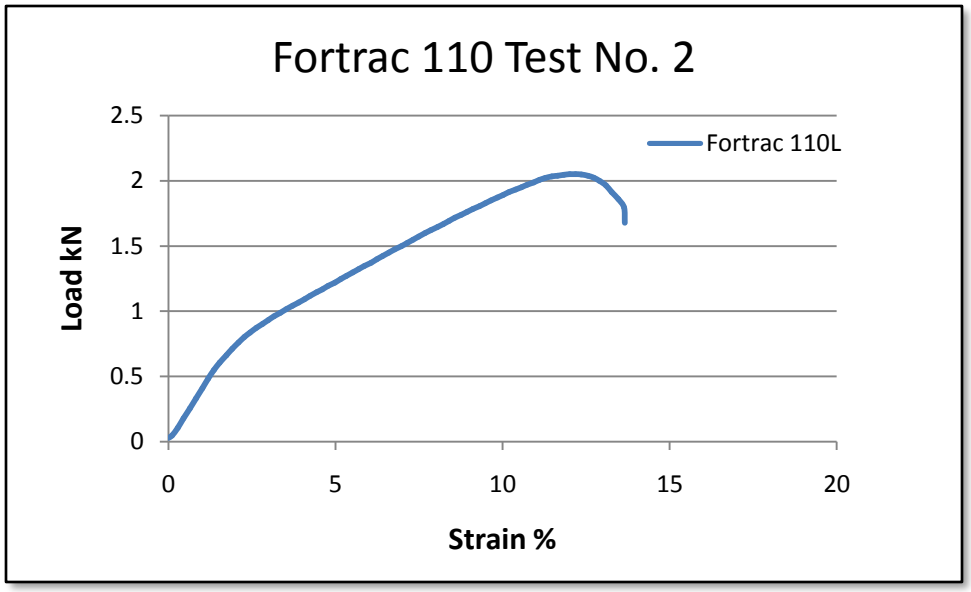
Fortrac 110 Test No. 2
Load kN
2.5
2
1.5
1
0.5
0
0
5
10
15
20
Strain %
Fortrac 110L

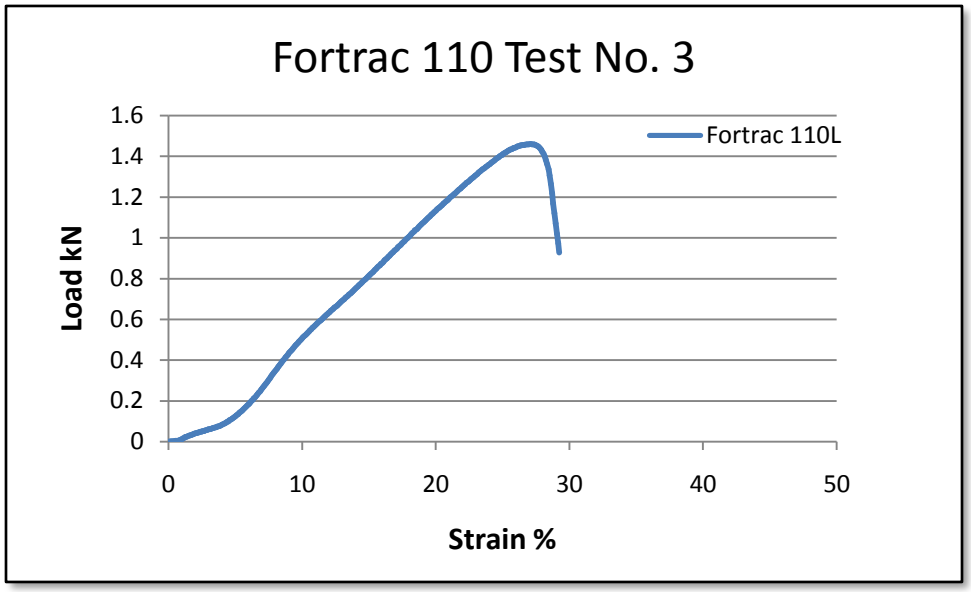
Fortrac 110 Test No. 3
Load kN
1.6
1.4
1.2
1
0.8
0.6
0.4
0.2
0
0
10
20
30
40
50
Strain %
Fortrac 110L

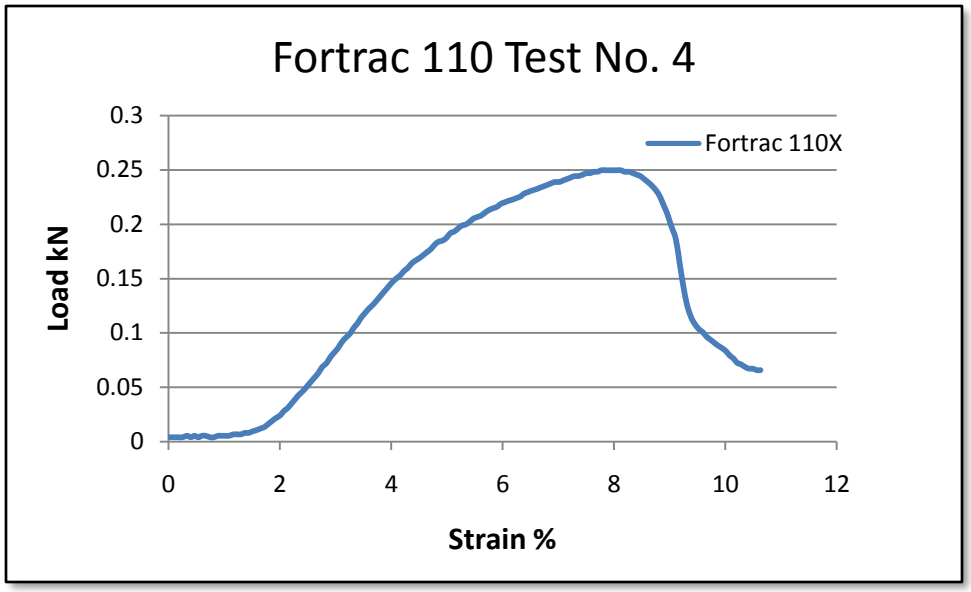
Fortrac 110 Test No. 4
Load kN
0.3
0.25
0.2
0.15
0.1
0.05
0
0
2
4
6
8
10
12
Strain %
Fortrac 110X

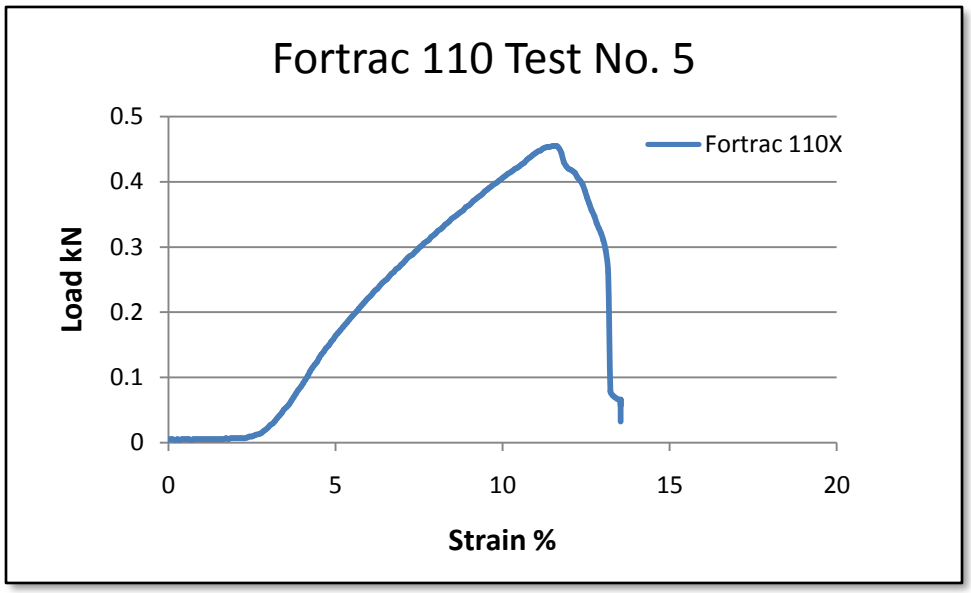
Fortrac 110 Test No. 5
Load kN
0.5
0.4
0.3
0.2
0.1
0
0
5
10
15
20
Strain %
Fortrac 110X

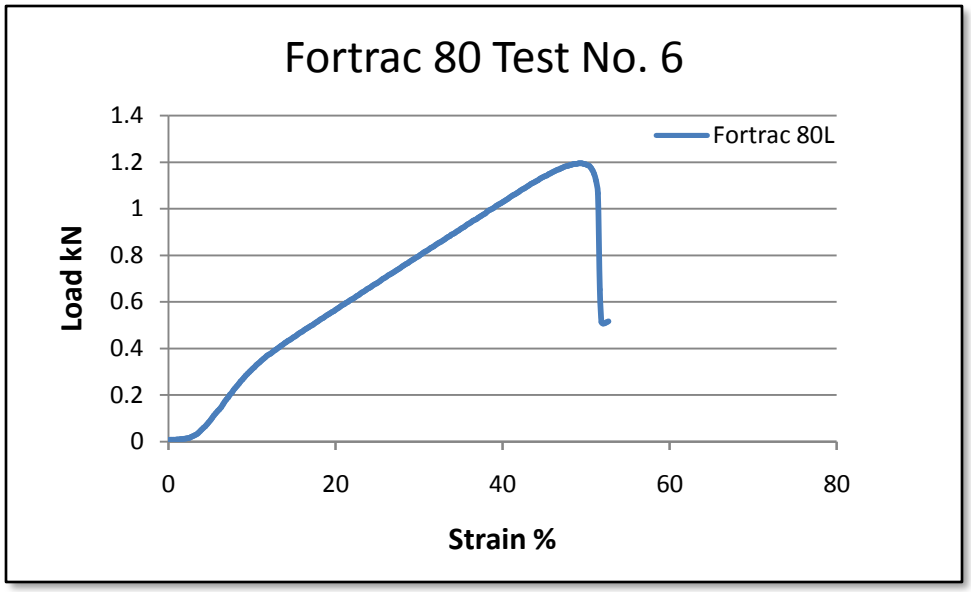
Fortrac 80 Test No. 6
Fortrac 80L
Load kN
1.4
1.2
1
0.8
0.6
0.4
0.2
0
0
20
40
60
80
Strain %

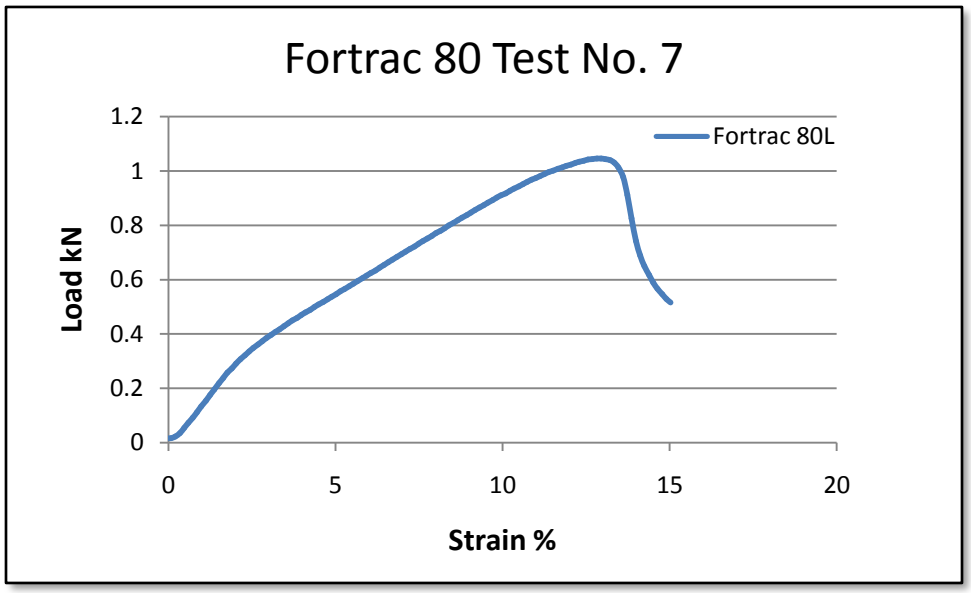
Fortrac 80 Test No. 7
Fortrac 80L
Load kN
1.2
1
0.8
0.6
0.4
0.2
0
0
5
10
15
20
Strain %

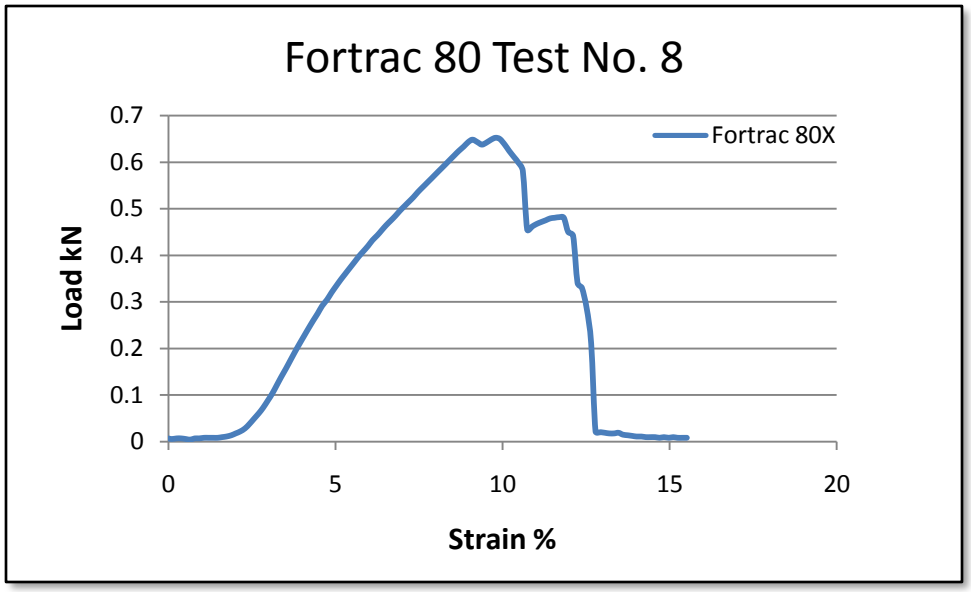
Fortrac 80 Test No. 8
Load kN
0.7
0.6
0.5
0.4
0.3
0.2
0.1
0
0
5
10
15
20
Strain %
Fortrac 80X

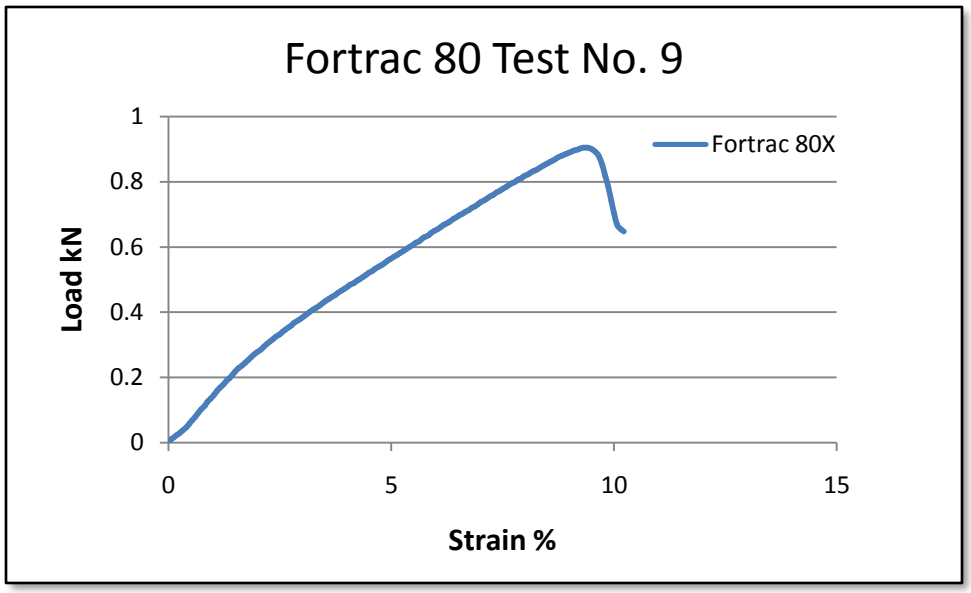
Fortrac 80 Test No. 9
Load kN
1
0.8
0.6
0.4
0.2
0
0
5
10
15
Strain %
Fortrac 80X

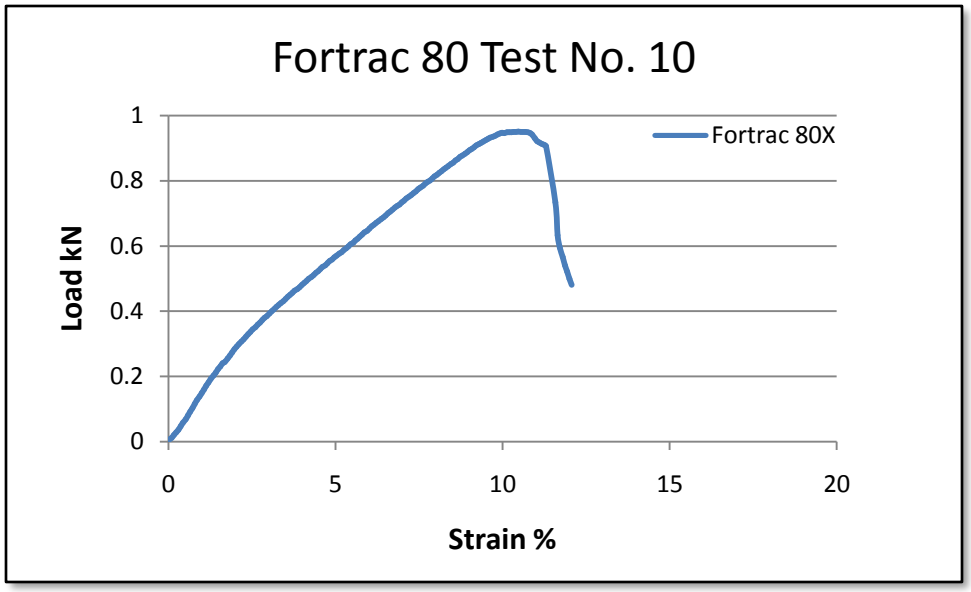
Fortrac 80 Test No. 10
Load kN
1
0.8
0.6
0.4
0.2
0
0
5
10
15
20
Strain %
Fortrac 80X

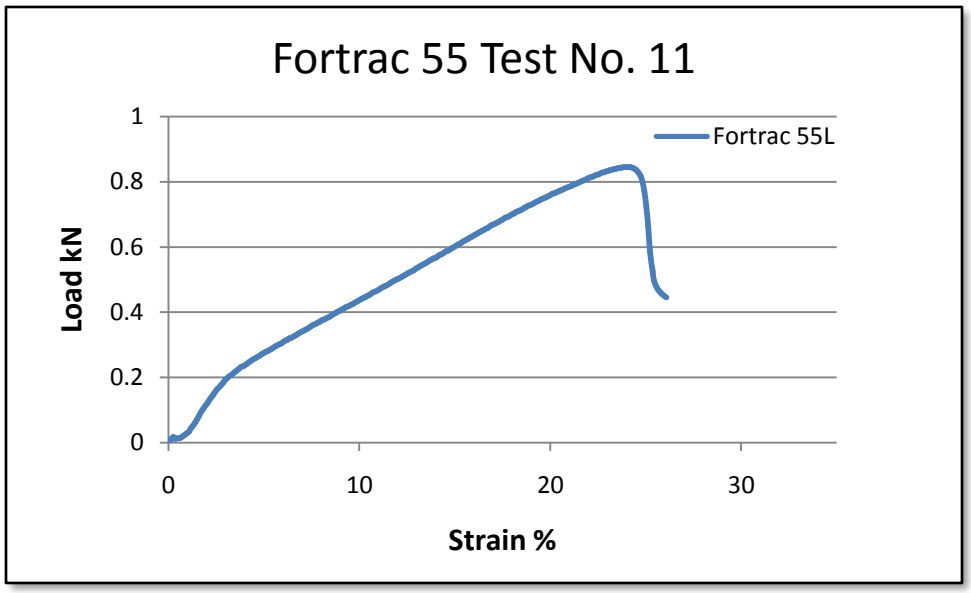
Fortrac 55 Test No. 11
Load kN
1
0.8
0.6
0.4
0.2
0
0
10
20
30
Strain %
Fortrac 55L

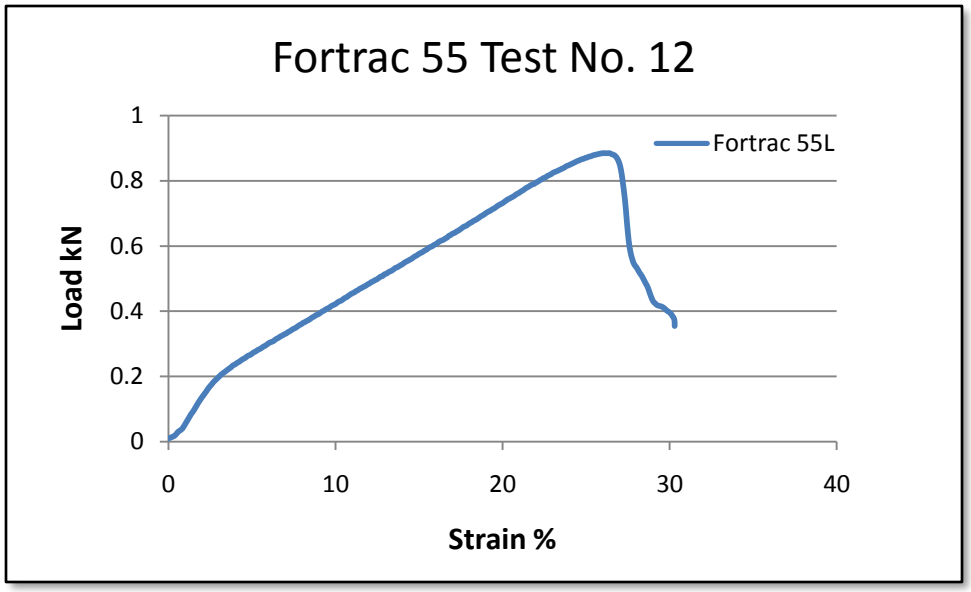
Fortrac 55 Test No. 12
Load kN
1
0.8
0.6
0.4
0.2
0
0
10
20
30
40
Strain %
Fortrac 55L

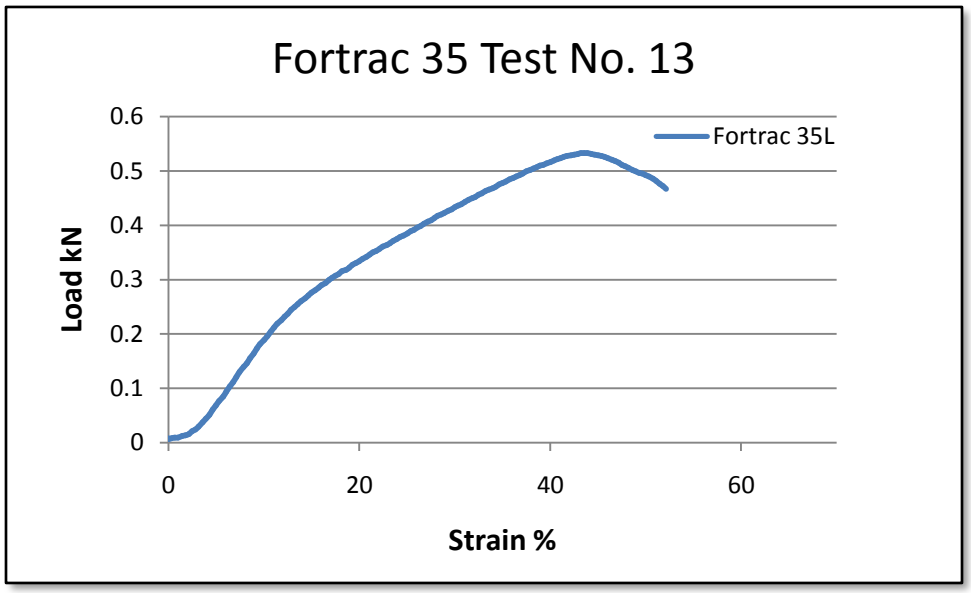
Fortrac 35 Test No. 13
Load kN
0.6
0.5
0.4
0.3
0.2
0.1
0
0
20
40
60
Strain %
Fortrac 35L

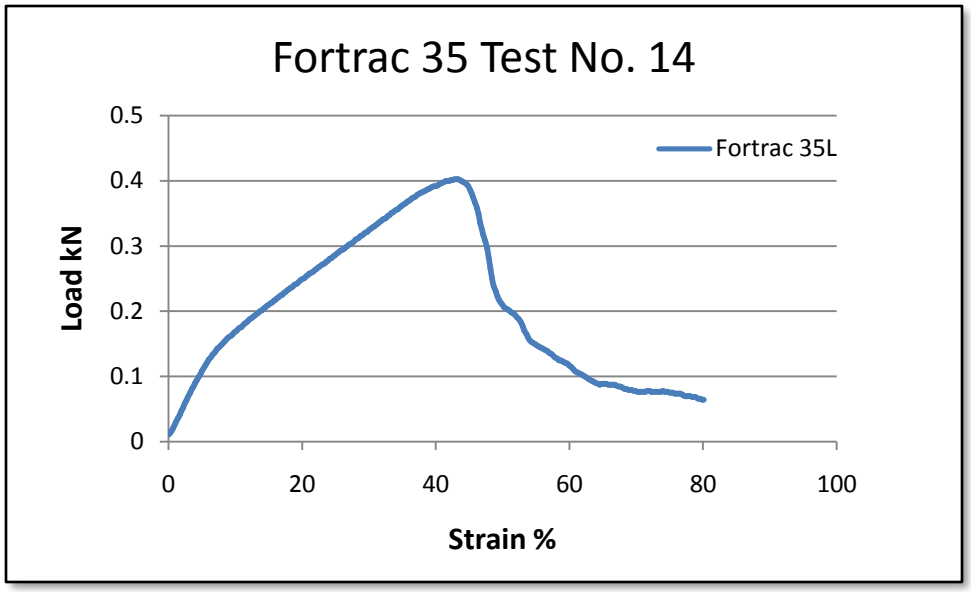
Fortrac 35 Test No. 14
Load kN
0.5
0.4
0.3
0.2
0.1
0
0
20
40
60
80
100
Strain %
Fortrac 35L

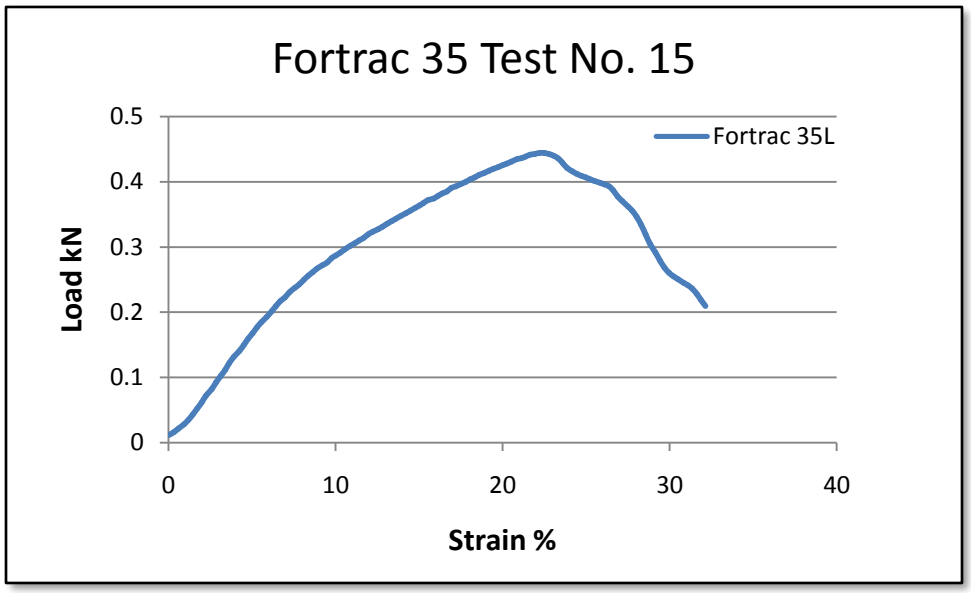
Fortrac 35 Test No. 15
Load kN
0.5
0.4
0.3
0.2
0.1
0
0
10
20
30
40
Strain %
Fortrac 35L

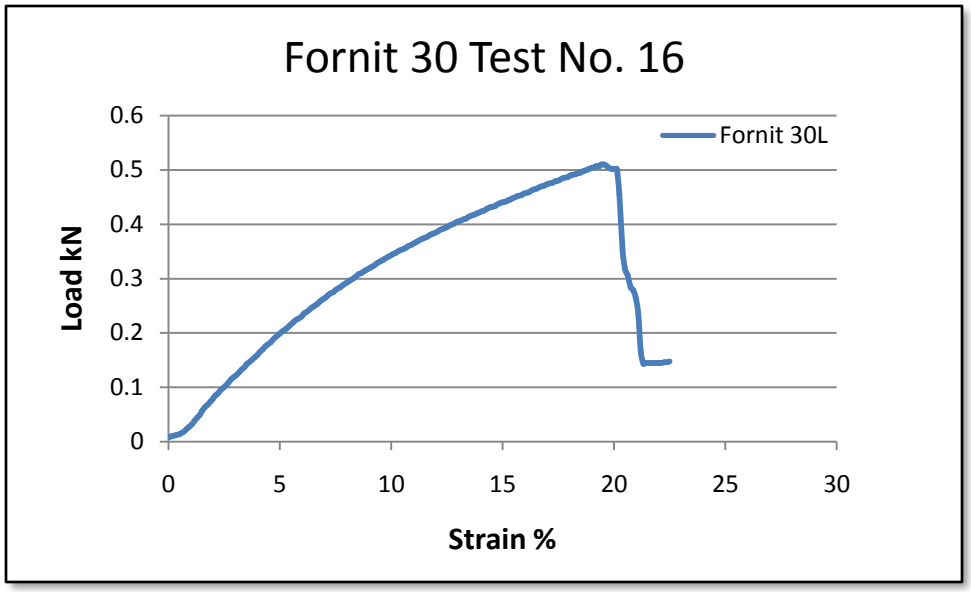
Fornit 30 Test No. 16
Fornit 30L
Load kN
0.6
0.5
0.4
0.3
0.2
0.1
0
0
5
10
15
20
25
30
Strain %

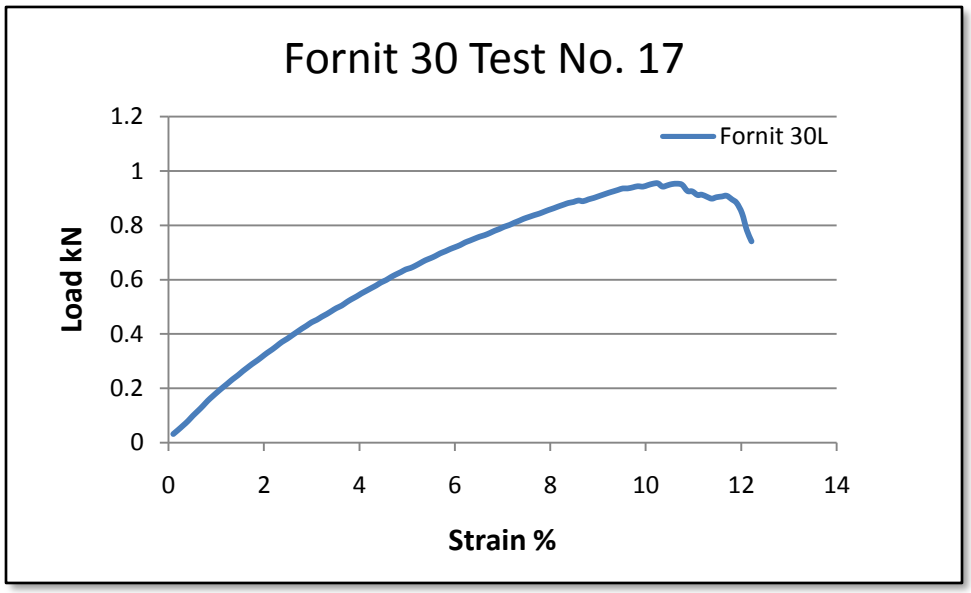
Fornit 30 Test No. 17
Fornit 30L
Load kN
1.2
1
0.8
0.6
0.4
0.2
0
0
2
4
6
8
10
12
14
Strain %

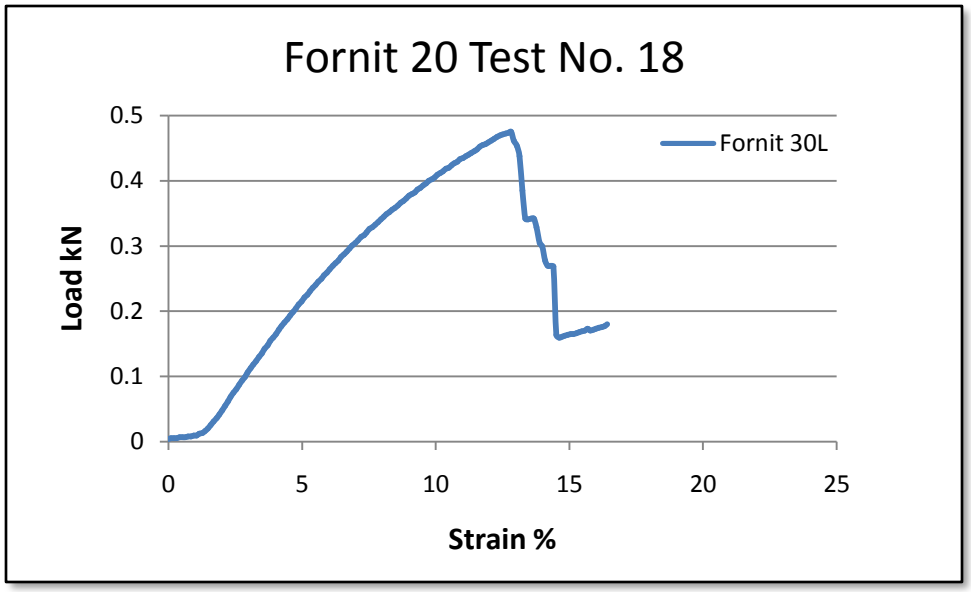
Fornit 20 Test No. 18
Load kN
0.5
0.4
0.3
0.2
0.1
0
0
5
10
15
20
25
Strain %
Fornit 30L

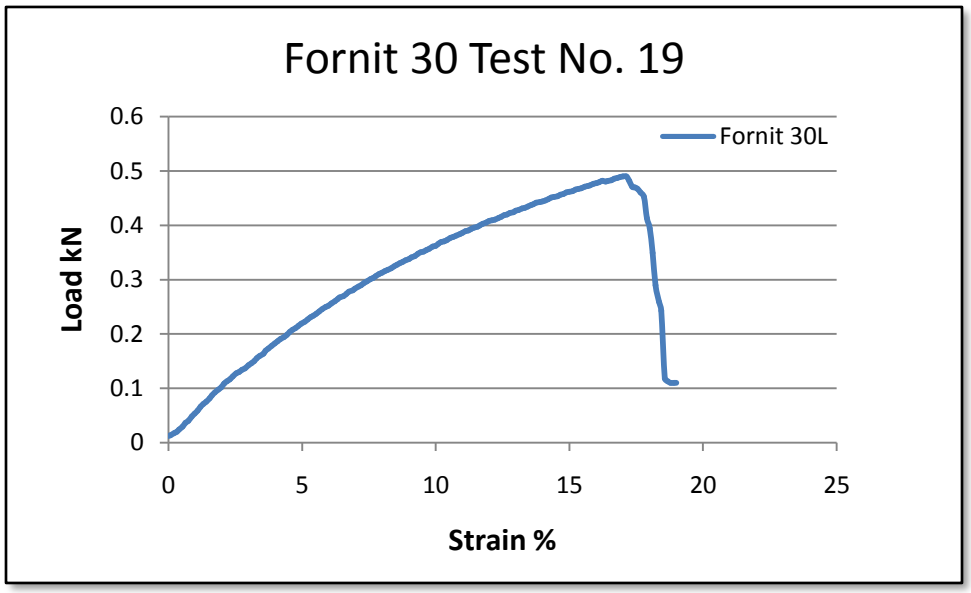
Fornit 30 Test No. 19
Load kN
0.6
0.5
0.4
0.3
0.2
0.1
0
0
5
10
15
20
25
Strain %
Fornit 30L

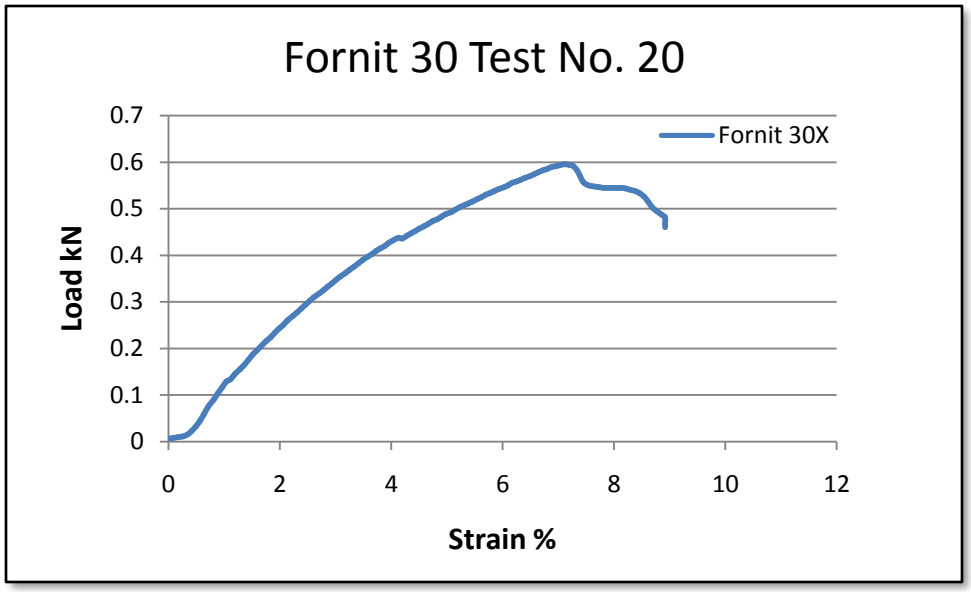
Fornit 30 Test No. 20
Fornit 30X
Load kN
0.7
0.6
0.5
0.4
0.3
0.2
0.1
0
0
2
4
6
8
10
12
Strain %

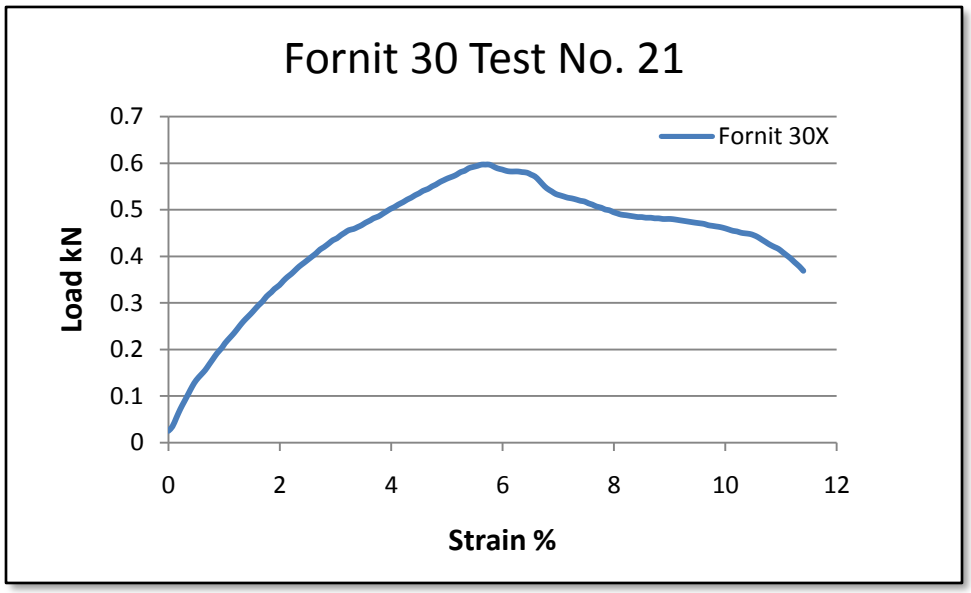
Fornit 30 Test No. 21
Fornit 30X
Load kN
0.7
0.6
0.5
0.4
0.3
0.2
0.1
0
0
2
4
6
8
10
12
Strain %

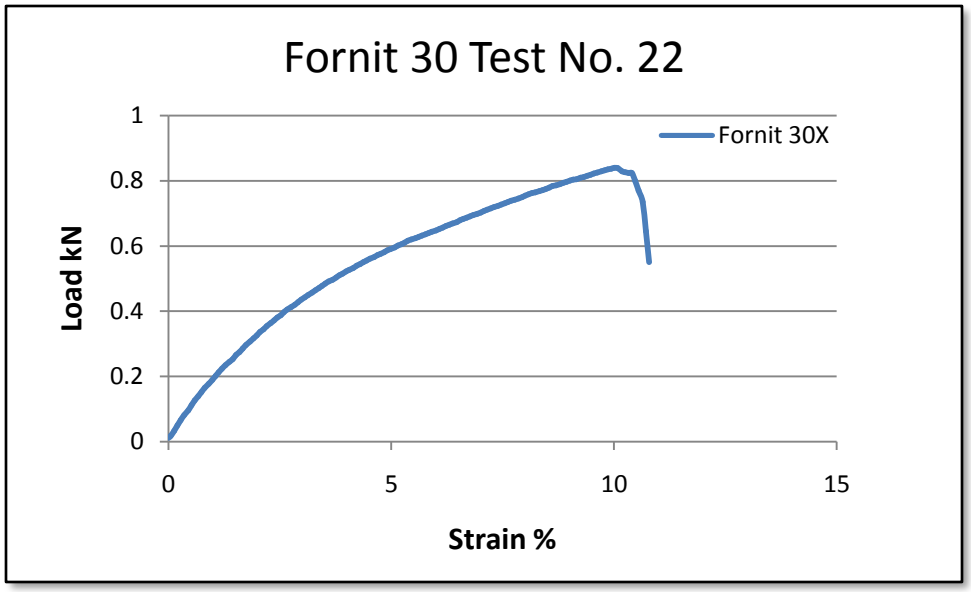
Fornit 30 Test No. 22
Fornit 30X
Load kN
1
0.8
0.6
0.4
0.2
0
0
5
10
15
Strain %

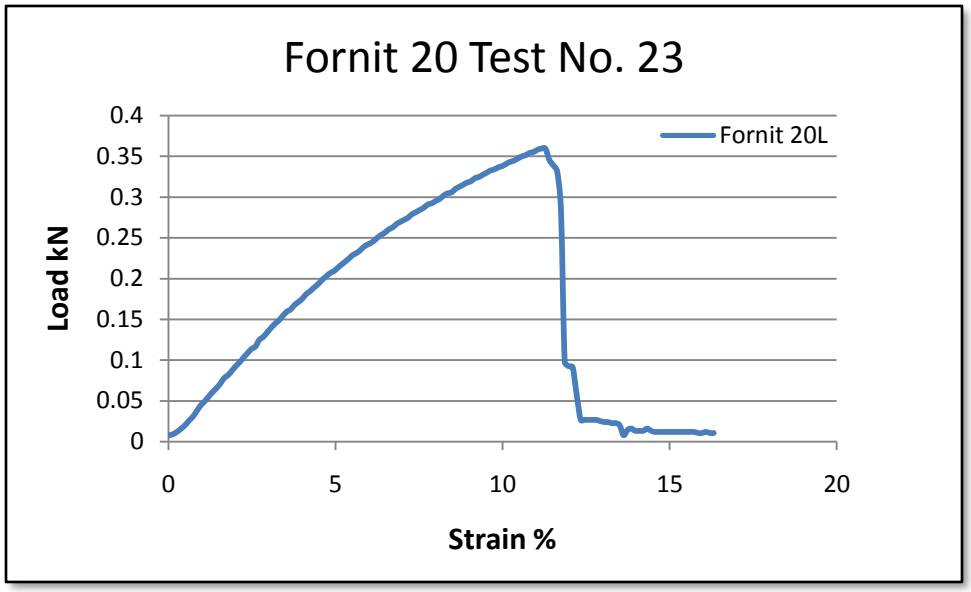
Fornit 20 Test No. 23
Fornit 20L
Load kN
0.4
0.35
0.3
0.25
0.2
0.15
0.1
0.05
0
0
5
10
15
20
Strain %

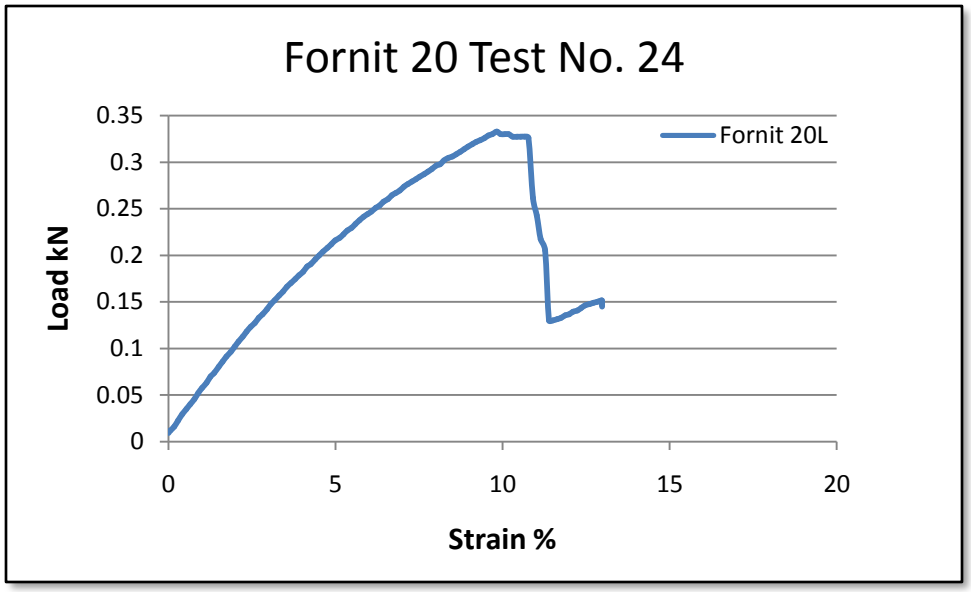
Fornit 20 Test No. 24
Load kN
0.35
0.3
0.25
0.2
0.15
0.1
0.05
0
0
5
10
15
20
Strain %
Fornit 20L

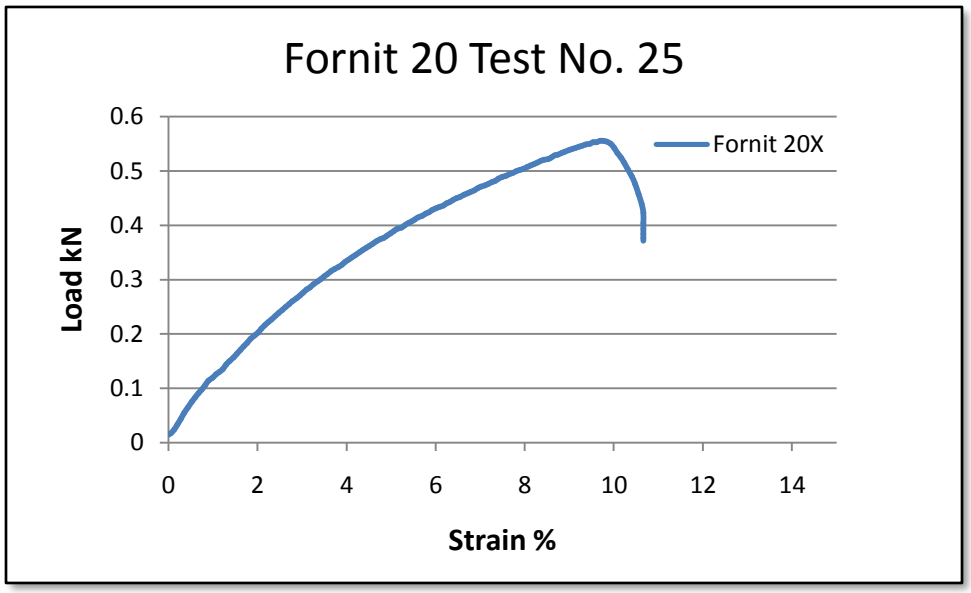
Fornit 20 Test No. 25
Load kN
0.6
0.5
0.4
0.3
0.2
0.1
0
0
2
4
6
8
10
12
14
Strain %
Fornit 20X

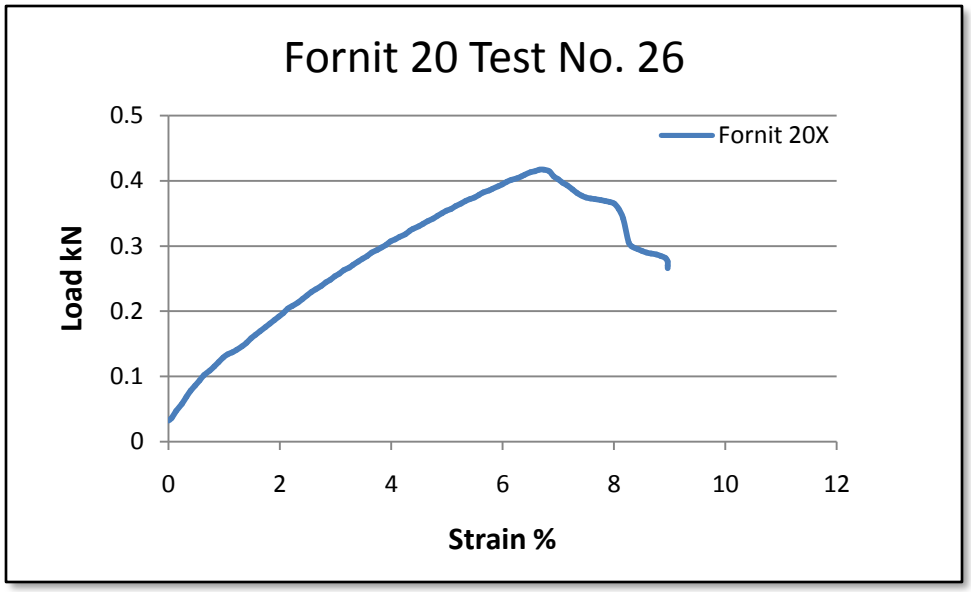
Fornit 20 Test No. 26
Fornit 20X
Load kN
0.5
0.4
0.3
0.2
0.1
0
0
2
4
6
8
10
12
Strain %

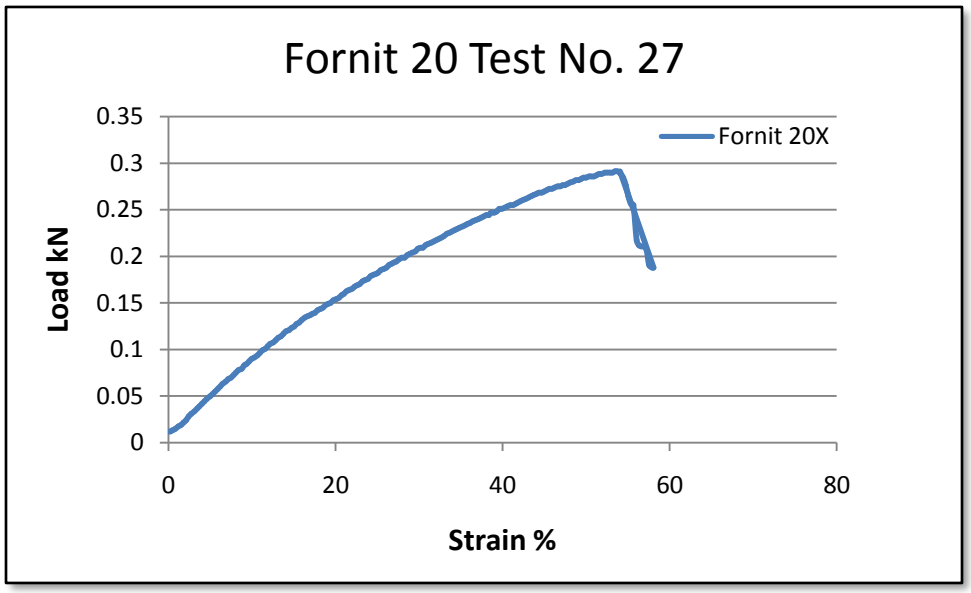
Fornit 20 Test No. 27
Fornit 20X
Load kN
0.35
0.3
0.25
0.2
0.15
0.1
0.05
0
0
20
40
60
80
Strain %

Vita

Brenton Michael Jones was born on the bayou in Lake Charles, Louisiana on March 13, 1984. Brent spent his childhood in Lake Charles where he graduated from Saint Louis Catholic High School in May of 2002. He then attended Louisiana State University in Baton Rouge and graduated in May 2006 with a degree in Civil Engineering. In August 2006, he began graduate studies at Virginia Tech to pursue a Master's of Science degree in Structural Engineering. Upon completion of his degree requirements, Brent will begin his career as a structural design engineer at Stanley D. Lindsey & Associates in Atlanta, Georgia. The research presented in this thesis was successfully defended on November 28, 2007.